PHOTOELECTROCHEMICAL STUDIES OF ELECTRODEPOSITED SEMICONDUCTORS

by Ivor D.J. Howell

CONTENTS

UNIVERSITY OF SOUTHAMPTON

ABSTRACT

FACULTY OF SCIENCE

CHEMISTRY

Master of Philosophy

PHOTOELECTROCHEMICAL STUDIES OF ELECTRODEPOSITED SEMICONDUCTORS

by Ivor D.J. Howell

The theory of operation of a regenerative liquid junction solar cell is explained in terms of energy band interactions between an illuminated semiconductor electrode, the cell's counter electrode, and the redox system of the electrolyte in which they are immersed. The Gärtner model of a semiconductor Schottky barrier photodiode and its extensions are used to describe the semiconductor-electrolyte contact.

The apparatus used to deposit and characterise thin films of cadmium and bismuth sulphides is described, including its automation using a BBC microcomputer and custom designed electronic interfaces. This increased both the accuracy and speed of the experiment.

0.1 to 2.0 micron films of cadmium sulphide and bismuth trisulphide were prepared by cathodic deposition under galvanostatic control, from dimethyl sulphoxide and diethylene glycol respectively, at temperatures up to 160 °C., and at various current densities. The photocurrent conversion efficiencies of these films in 0.1M sodium sulphide were determined, and they were characterised using cyclic voltammetry, interfacial capacitance measurements, electron microscopy, and X-ray diffraction spectroscopy.

A similar investigation was made of the properties of high purity cadmium and bismuth sulphides.

ACKNOWLEDGEMENTS

I am indebted to my Supervisor at the University, Dr. Laurence Peter, for his constant inspiration and encouragement.

I would like to thank my employers at Southampton Institute of Higher Education for granting me day-release, course fees, and an allocation for apparatus; thanks also to those members of the Institute staff who have taken a personal interest in my studies.

I am grateful to Mr. B.A.Bellamy of the Materials Development Division at AERE, Harwell for providing X-ray powder crystallography spectra of my thin-film samples.

CHAPTER 1

INTRODUCTION

Primary non-renewable fuel reserves of coal, oil, gas, wood, and uranium are rapidly being depleted, and their uneven global distribution leads to uncertainties in their supply routes [1,2]. Present designs of nuclear power plant utilise fission reactions of uranium, thorium, etc., which may only be cost-effective to extract for a few decades more. It appears that the development of abundant nuclear fusion power will not take place for a considerable time, and that, although the global per capita energy demand is increasing less rapidly than a decade ago, there may therefore be a shortfall in the world's energy generation capabilities in the first part of the next century.

Solar energy is a renewable resource that is being developed as one possible supplement and alternative to fill this gap.

The factors limiting the use of an energy resource are not only those concerned with its technological difficulties, but also political decisions regarding the level of investment in research and capital provided for generating plant construction; there are social constraints related to the impact of a new technology on the environment and on the redeploymnent of workers; finally, there are natural restrictions, such as the level of cloud cover in high latitudes in the case of solar energy.

The energy reaching the earth from the sun in 2 weeks is equivalent to the estimated initial global resources of fossil fuels. About one third of the incident energy maintains the hydrological cycle, the remainder heating the surface of the oceans and land

masses. Only about 0.03% of the solar input is presently being stored as the products of photosynthesis, from which mankind must obtain all their food, and from which all future reserves of fossil fuels must derive.

The sun's energy may be harnessed indirectly through the power of the winds, waves, tides and water courses. Alternatively, the heating effect of the sun's radiation may be captured in purpose-built absorbers and used for domestic space heating or to raise steam for industrial processes. In the devices we shall consider in more detail shortly, the energy of the sun's photons may be transformed directly to electricity, or converted to chemical fuels.

Electricity holds an increasingly favoured place among the energy currencies in use in a technological society, since it is a clean, convenient, easily transportable, high grade fuel, whose supply is stabilised by the possibility of generating it from many alternative fuel mixes. However, present methods of generation are highly inefficient and wasteful of resources, primarily due to the restrictions of thermodynamics on the conversion of heat to electricity, and often pollute the environment with their by-products, such as carbon dioxide, sulphur dioxide, and waste heat. It is perhaps less due to these factors than a fear of social and political interference with supply lines that has lead recent governments to make some small investments in alternative energy research.

Surface terrestrial solar power densities averaged over a year range from near zero to around 1kW per square metre, and are typically around 200W per square metre in temperate latitudes, with wide daily and seasonal fluctuations. The diffuse nature of the energy, coupled

with a low converter efficiency, requires large areas of collectors to supply the needs of any but the smallest communities, which introduces numerous problems of production costs, maintenance, and environmental impact. The total extinction of the source of power at night, a time in which the peak demand usually occurs, necessitates elaborate energy storage devices. If the solar energy has been converted to heat in some working fluid, then this can be pumped into insulated reservoirs until needed. Electrical energy is more difficult to store. The devices used can range from a small battery or fuel cell through to water pumping schemes and flywheels. Ultimately, it may be possible to avoid the storage problem by having the generators in geosynchronous orbit.

There are a number of good reviews of the alternative energy technologies, and of solar energy in particular, together with their prospects for development, in the recent literature [3-25].

It would seem reasonable to take Nature's example of photosynthesis as a starting point in the search for an industrial solar energy converter. But this natural process is difficult to imitate, being very complex, and having a low efficiency of 0.3 to 3%. So other quite different methods have been developed. Many of the devices for converting sunlight to electricity currently in use and under development depend on the properties of semiconductors for their operation.

The basis of the conversion is the generation of an electron in the conduction band and a hole in the valence band of the semiconductor when an incident photon is absorbed.

The energy of the photon, perhaps with the mediation of some lattice energy, is transferred to an electron residing in an energy state within the uppermost nearly full energy band of the

material, raising its energy across the "forbidden" energy gap to the next highest, nearly empty energy band. The absence of the electron from the lower energy band leaves an excess free positive charge there, which is normally treated as an independent carrier, called a hole. This migrates in the opposite direction to electrons, and has a different mobility and effective mass.

In order for this process to result in useful external work, the two oppositely charged species must be separated further, by transport through the semiconductor to contacts supplying power to a load. Electrons passing through the load give up some of their energy before they recombine with holes upon their arrival back in the semiconductor.

It is the method by which the physical separation of oppositely charged carriers is achieved that distinguishes the various categories of solar cell converters, and it is the competing processes which promote the useless recombination of the charges in the substrate before they reach the external contacts, dissipating their potential energy as heat, that constitute the main problems which must be overcome to improve solar cell efficiencies.

In some cases, the charges are induced to move apart, once they have been separated across the energy gap, by providing a potential gradient in the region of photon absorption, electrons falling towards regions of more positive potential, and holes to regions of more negative potential. The steeper this potential gradient, the more efficient will be the separation of the current carriers, and hence the greater the overall efficiency of the device. A standard method for producing the necessary potential gradient is to form a p-n junction in the semiconducting material by doping the lattices near the interface with small concentrations of foreign atoms

which act as either electron donors or acceptors.

Solid state homojunction devices have a p-n junction within a single basic type of substrate material, e.g. silicon or gallium arsenide.

Solid state heterojunction devices have a p-n junction between two different semiconductor compounds, or between a metal and a semiconductor. The latter type is also known as a Schottky barrier device. A variation on this, the MIS (metal-insulator-semiconductor) type, has a very thin insulating layer of oxide between the conductor and the semiconductor, which can increase the potential gradient across the interface without decreasing the photocurrent.

PEC (photoelectrochemical) devices involve the irradiation of an electrode/electrolyte system to induce charge separation at the "liquid junction" interface (a heterojunction). In some, the potential gradient caused by charge separation across a thin membrane is the driving force. In others, it is the electroactive (redox) species adsorbed on the semiconductor surface, or dissolved in solution that provide the potential gradient by acting as donor or acceptor energy states at potentials different from those of the charge carriers at the interface.

PEC effects are classified as photogalvanic if a net Faradaic charge transfer ensues across the interface i.e. a net chemical change occurs in the region of both of the cell's electrodes, or as photovoltaic when there is no net charge transfer. If the higher energy products of a photogalvanic cell are kept apart, the energy of the incident light may thus be stored as chemical energy, to be released subsequently by a controlled mixing of the products. There has been considerable interest in the development of cells designed

for the photoelectrolysis of water to produce hydrogen fuel. Photovoltaic devices do not have a storage capacity, and their photocurrent output ceases immediately the illumination is discontinued.

CHAPTER 2

THE LIQUID JUNCTION PHOTOELECTROCHEMICAL CELL AND THE THEORY OF THE SEMICONDUCTOR-ELECTROLYTE INTERFACE

(2.1) THE LIQUID JUNCTION CELL

Liquid junction photoelectrochemical cells contain an interface between a semiconductor and an electrolyte, at which charge transfer reactions involving redox systems contribute to the process of separating the electrons which are excited by photons in to the conduction band from the holes left in the valence band. This charge carrier separation is crucial if some of the photon energy is to be made available to do work in an external circuit.

In regenerative liquid junction cells, the counter electrode reaction is the reverse of that at the photoelectrode such that ideally there is no net chemical change, and the only output of the cell, apart from the inevitable waste heat, is electricity.

What are the advantages of these cells over more traditional solid state designs? To answer this, consider the manufacture of a typical solid state p-n junction photocell; this relies on the difficult process of controlled high-temperature diffusion of impurities in to an expensive, extremely pure single crystal substrate material to form the junction. (The junction usually has to be very close to the surface, in the region where most photons will be absorbed, so that the separating field coincides with the region of maximum pair generation.)

The diffusion technique is, unfortunately, not suitable for producing photovoltaic electrodes from (cheaper) polycrystalline substrates, since the diffusion rate of the dopant is often several

orders of magnitude higher along the grain boundaries than through the bulk, causing randomly oriented junctions, and thus shunting the photocurrent to the back contact.

It is also necessary to use (expensive) single crystal material in solid state devices in order to maximise the carrier diffusion lengths, to allow as many as possible of the photogenerated minority carriers to be picked up by finger contacts, and to reduce inefficiences due to electron-hole recombination in areas where the lattice is distorted by grain boundaries. This is particularly important in the case of indirect band-gap materials such as silicon, for which the absorption edge is relatively shallow, so that electron-hole pairs are created from incident photons as much as ten microns from the interface.

For solid state devices, then, the ohmic finger contacts are applied to the illuminated face of the electrode, closely spaced to gather the charge carriers before their energy is dissipated uselessly. In the liquid junction cell, electrical contact between the semiconductor and the electrolyte is made simply by immersion, so the contact to the illuminated surface, close to the region of photon absorption just beneath it, is through the electrolyte, which gathers the charge carriers in its redox energy states.

The lower carrier diffusion lengths and increased recombination losses characteristic of polycrystalline materials typically used in liquid junction cells, compared to those found in e.g. a single crystal silicon homojunction device, should be offset by the reduced distance a carrier needs to travel before it is swept across the (liquid) junction, and by the much reduced manufacturing costs for the liquid junction cell.

We shall see that liquid junction cells, through a suitable combination of semiconductor and electrolyte redox system, allow the reverse leakage current from the semiconductor majority carrier band to be suppressed, by arranging that the reorganisation energy of the redox system is such that ideally, while the minority carrier band overlaps the appropriate redox states, the majority carrier band does not overlap any redox states in the electrolyte.

The electrolyte is chosen on the basis of its carrier mobility, its stability and its ability to inhibit photocorrosion: of course, it should absorb as little of the spectrum of interest as possible, and it may be pumped to extract heat as well as participate in charge transport.

The problems associated with semiconductor electrodes in photoelectrochemical solar cells fall in to two main categories: electron-hole recombination and photocorrosion. We shall consider these in detail later.

(2.2) ENERGY LEVEL STRUCTURE OF LIQUID JUNCTION CELLS IN THE DARK

We will consider the adjustments between the energy bands of the components of the liquid junction cell as they are put together in sequence.

Suppose that, firstly, a semiconductor is deposited on to a metal substrate. The relative magnitudes of the work functions W of the metal and semiconductor determine whether or not an ohmic (non-rectifying) contact is made. Figs 2.1-2.4 show that there are four possibilities, two of which represent ohmic contacts. Essentially, electrons flow from the material of higher electron energy to the material of lower electron energy, until their Fermi

METAL– SEMICONDUCTOR CONTACTS

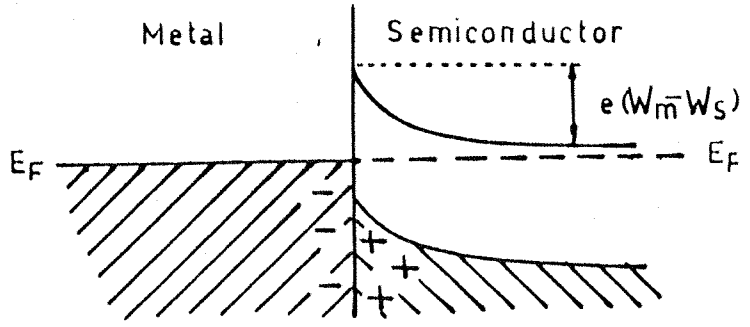

Fig 2.1 n-type, $W_m > W_s$ (non-ohmic)

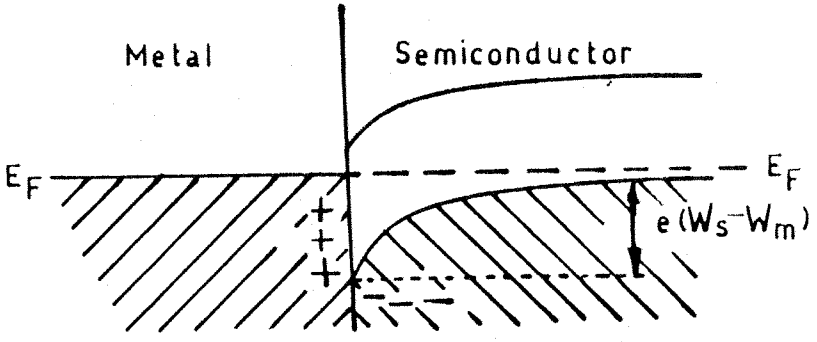

Fig 2.2 p-type, $W_m < W_s$ (non-ohmic)

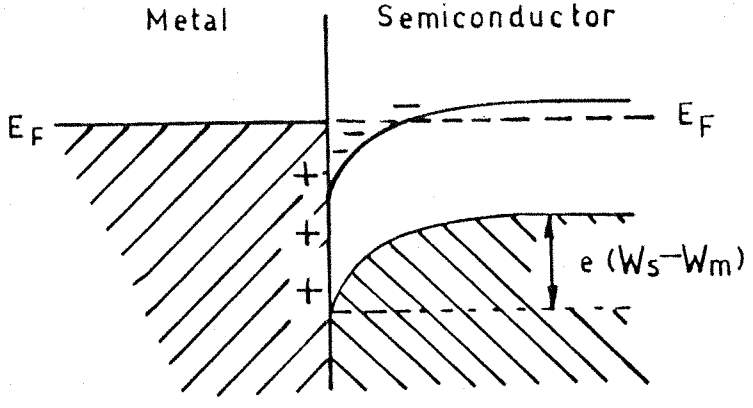

Fig 2.3 n-type, $W_m < W_s$ (ohmic)

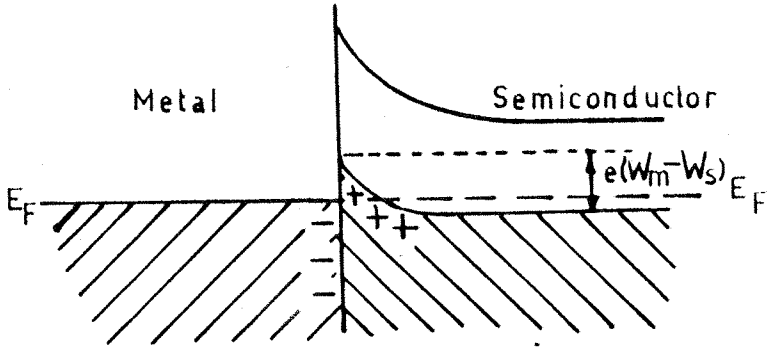

Fig 2.4 p-type, $W_m > W_s$ (ohmic)

levels are equal. Interfacial excess charge causes band bending close to the surface of the semiconductor.

In real systems, some of this local excess charge is accommodated in interfacial states. If there is a high density of these, then the contribution to the band bending by the charge carriers trapped in them may well be enough to produce an ohmic contact even when simple theory predicts a rectifying contact. It is often quite easy to produce an ohmic contact by purposely scratching the surface (to increase the density of surface states). The manufacture of a rectifying contact requires very careful surface preparation or epitaxial growth. Fortunately, this project requires an ohmic contact to be made between the semiconductor under investigation and the metal contact.

Suppose next that the metal-semiconductor electrode is immersed in an electrolyte. Redox couples in solution exchange electrons with the electrode, and changes occur to the original surface state distribution on the semiconductor, involving adsorption and accumulation or dispersion of charged species near the interface, until the Fermi level is the same throughout.

Representing the oxidised form of the redox couple by O and the reduced form by R, we have the following possibilities at the interface:

$$O + e^{-}(cb) \longrightarrow R \qquad \text{at the conduction band edge}$$

$$R + h^{+}(vb) \longrightarrow O \qquad \text{at the valence band edge}$$

Energy distributions of redox couples are usually represented as in fig 2.5, where the reduced form is portrayed at lower energy than the oxidised form. This type of diagram takes into account

Fig. 2.5

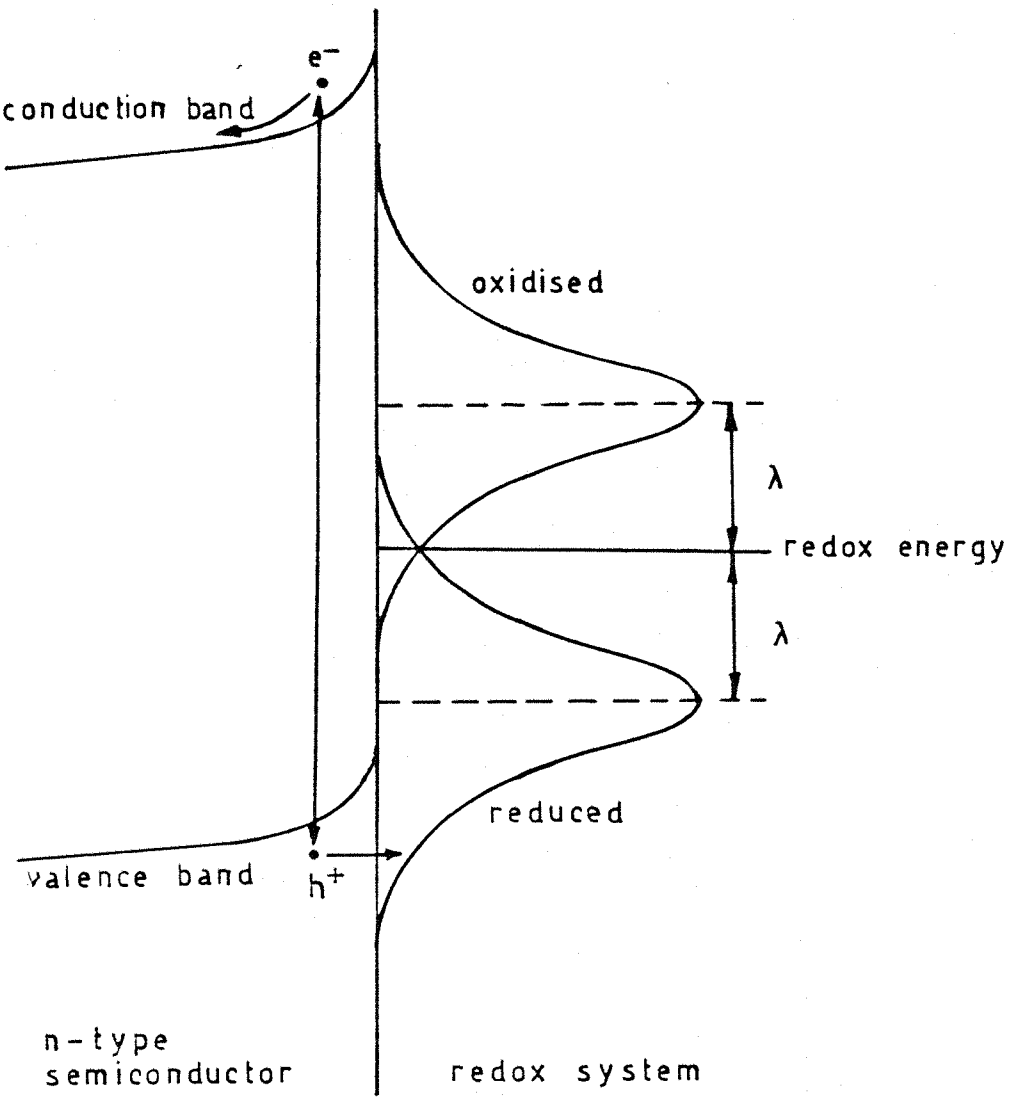
e⁻
conduction band
oxidised
λ
redox energy
λ
reduced
valence band
h⁺
n-type
semiconductor
redox system

ion-solvent interactions. The reorganisation energy is defined as half the distance of separation of the peaks of the two distributions, and is of the order of one eV. The mid point (the average energy at which the redox system can supply or receive an electron) is called the standard redox potential, and is the electrochemical potential or Fermi level for electrons in the redox system. Values of this are available from standard tables in many cases.

Suppose, finally, that a metal counter electrode is immersed in the electrolyte. This is followed by a further shift in the Fermi levels until they become equal throughout. Thus, the counter electrode can be responsible for changes in surface state occupation and adsorption on the photoelectrode.

The metal work function should approximate to the redox energy in the electrolyte for efficient cell operation, since charge transfer occurs most easily by isoenergetic tunnelling across the double layer at this interface. Inelastic tunnelling is permitted, but is kinetically less favoured.

Overall, then, the Fermi level equilibrates throughout the system in the dark (fig 2.6).

(2.3) THE EFFECT OF ILLUMINATION ON THE LIQUID JUNCTION CELL

Photogenerated minority carriers within a diffusion length of the junction field tend to be swept to the interface where, ideally, they undergo charge transfer reactions with the redox system in the electrolyte. Electrons excited into the conduction band may reduce the oxidised form of the couple if they reach the interface, whereas if the holes left in the valence band reach the surface, they may oxidise the reduced form. The efficiency of this charge separation

Fig. 2.6

in the dark

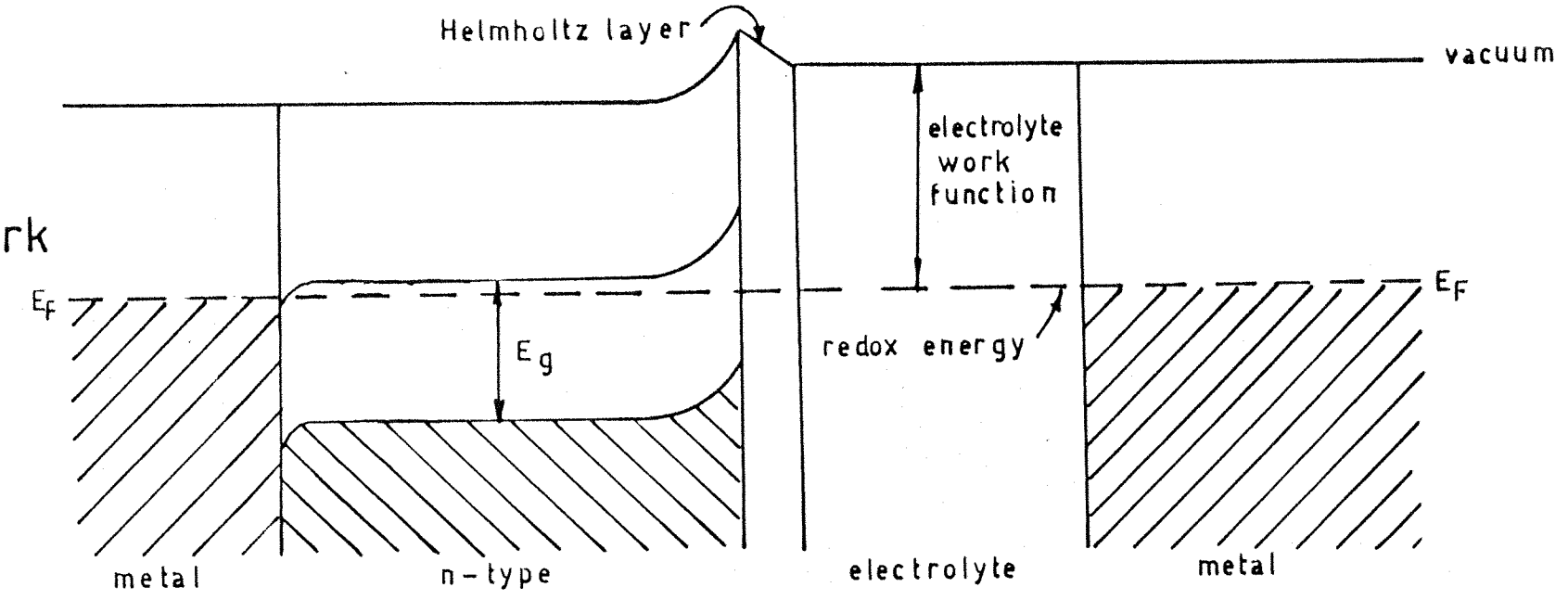

Fig. 2.7

illuminated

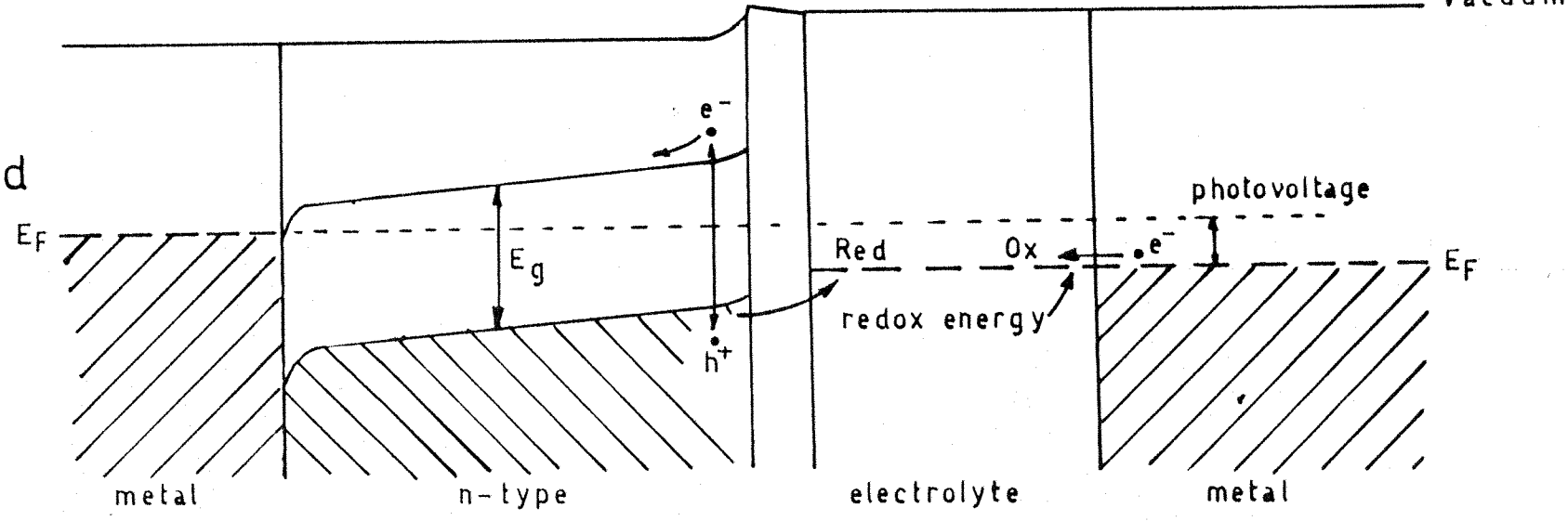

(minority carriers to the interface, majority carriers to the bulk) depends on the potential gradient near the interface (the degree of band bending), the carrier mobility and lifetime, and the optical absorption coefficient of the electrode. Majority carriers leave the bulk through the back ohmic contact, give up some of their energy to do work in an external load, and then pass to the counter electrode.

From here, they fall in to the redox energy levels of the electrolyte, to be transported across to the photoelectrode for reaction at the minority carrier band edge, or at surface states (fig 2.7). Defects such as grain boundaries, inclusions, vacancies, and dangling bonds at surfaces (Tamm states) act as recombination centres which reduce the conversion efficiency.

Ideally, the light should be absorbed over as short a distance as possible near the junction. This requires a high optical absorption coefficient α, which is characteristic of direct band gap semiconductors such as GaAs. In such materials, the valence band maximum and the conduction band minimum occur at the same value of the wave (momentum) vector, k.

Indirect gap materials such as Si do not have a steep absorption edge, due to the need for phonon (quantised lattice vibration) participation in absorption to conserve momentum; these materials therefore require relatively defect-free material to a depth of as much as 100 microns for optimum solar absorption. In practice, the absorption edge is pulled out in to a quasi-exponential tail due to transitions between band edge states perturbed by the local fields of charged impurities.

There are less efficient modes of optical excitation, found mainly in direct gap materials. These may involve excitons (interactive groups of electrons, holes, and sometimes atoms) that are

eventually either quenched by recombination or decomposed to free carriers in localities of high field strength, such as the interface. Also, photons may interact with excitons, phonons, and plasmons (quantised free carrier vibrations) to form polaritons [26].

The drift of photoexcited holes to the interface in the case of an n-type illuminated semiconductor tends to neutralise the excess negative surface charge, reducing the band bending, and raising the Fermi level in the bulk (fig 2.7). If a load is placed across the cell, the flow of current reduces this effect, and causes a potential gradient in the semiconductor bulk so that the measured photovoltage is less than that generated at the interface. The band edges are changed slightly on illumination due to modification of the charge in interfacial states as the Fermi level changes.

The photovoltage, in the absence of non-radiative recombinations, is the difference between the chemical potential of electrons in the redox system (the redox potential) and that in the semiconductor (the Fermi level).

While a large photopotential could in theory be achieved by heavily doping the semiconductor so that its Fermi level is very close to the edge of the band gap, the disadvantages of using heavily doped material for the electrode outweigh these gains.

The maximum photovoltage is obtained at higher light intensities as soon as the minority carrier density approaches the majority carrier density, and the energy bands in the semiconductor become flat. The photovoltage can never exceed the flat band potential, since this would reverse the band bending, and hence reverse the flow of charge carriers.

If the cell is shorted externally, the band bending is not altered by illumination, and the photocurrent depends linearly on the

light intensity. However, if the redox couple is at a high ionic concentration, interfacial charge transfer becomes the rate limiting step in the passage of current round the circuit, and "photocurrent suppression" occurs. Ion transport may become a factor limiting cell current flow at high illumination intensities.

(2.4) THE GÄRTNER THEORY OF ILLUMINATED SEMICONDUCTOR CONTACTS

A theoretical model of the photocurrent-voltage characteristic of a semiconductor Schottky barrier photodiode in reverse bias, accounting for the generation of carriers within the depletion region, and bulk recombination, was described in a generic paper by Gärtner [66], and was subsequently developed by several authors including Butler [67], Reichman [68], Albery et.al. [69], McCann et.al. [70], and Lemasson et.al. [71] for the semiconductor-electrolyte contact.

Consider an (n-type) semiconductor with a surface carefully prepared to be representative of the bulk, in contact with an electrolyte in the manner shown previously in Figs 2.6 and 2.7, such that the majority carriers are depleted at the surface.

Absorption of light of sufficient energy generates minority carriers. If these are depleted at the surface by reactions with the redox electrolyte, an electrochemical potential gradient is formed which draws futher minority carriers through the depletion region towards the interface. The observed photocurrent at any point equals the net flow of current due to minority and majority carriers through that point.

The Gärtner model assumes that the limiting processes for charge transfer at the surface are dependent only on the properties of the semiconductor and that charge transfer from the semiconductor to the redox species is not a rate determining step. Many factors could

invalidate this assumption, including retarded diffusion of the electroactive species in soluton, their adsorption (specific or not) at the semiconductor surface, the relative positions of acceptor/donor states in the electrolyte, etc. In some cases, however, the assumption is justified. This can be verified experimentally by determining whether the observed photocurrent is in direct proportion to the illumination intensity.

The Gärtner model assumes that there is no interaction between the electrolyte and the incident light, and that the band edges are pinned at the surface, with the flat band potential unaltered under illumination. The latter may be justified at low light intensities, but larger photon fluxes tend to shift the edges and so alter the band bending from the classical value.

It is assumed that there is unit quantum efficiency in the space charge region, negligible thermal generation of carriers or recombination there, that the minority carrier density falls to zero at the boundary of the SCR with the bulk of the material, and that the photocurrent is entirely due to minority carriers efficiently separated by a relatively large degree of band bending (greater than about 0.1V).

More recently, the Gärtner model has been extended [68,69] to take into account some of the factors neglected in the simple model, such as diffusion of minority carriers generated in the SCR to the bulk (where they recombine), recombination in the SCR itself, recombination via surface states, and the effect of the opposing dark current: these are described briefly in a later section.

Fig. 2.8 shows the model used in the simple Gärtner theory for the energy bands in the semiconductor at the electrolyte interface.

Fig. 2.8

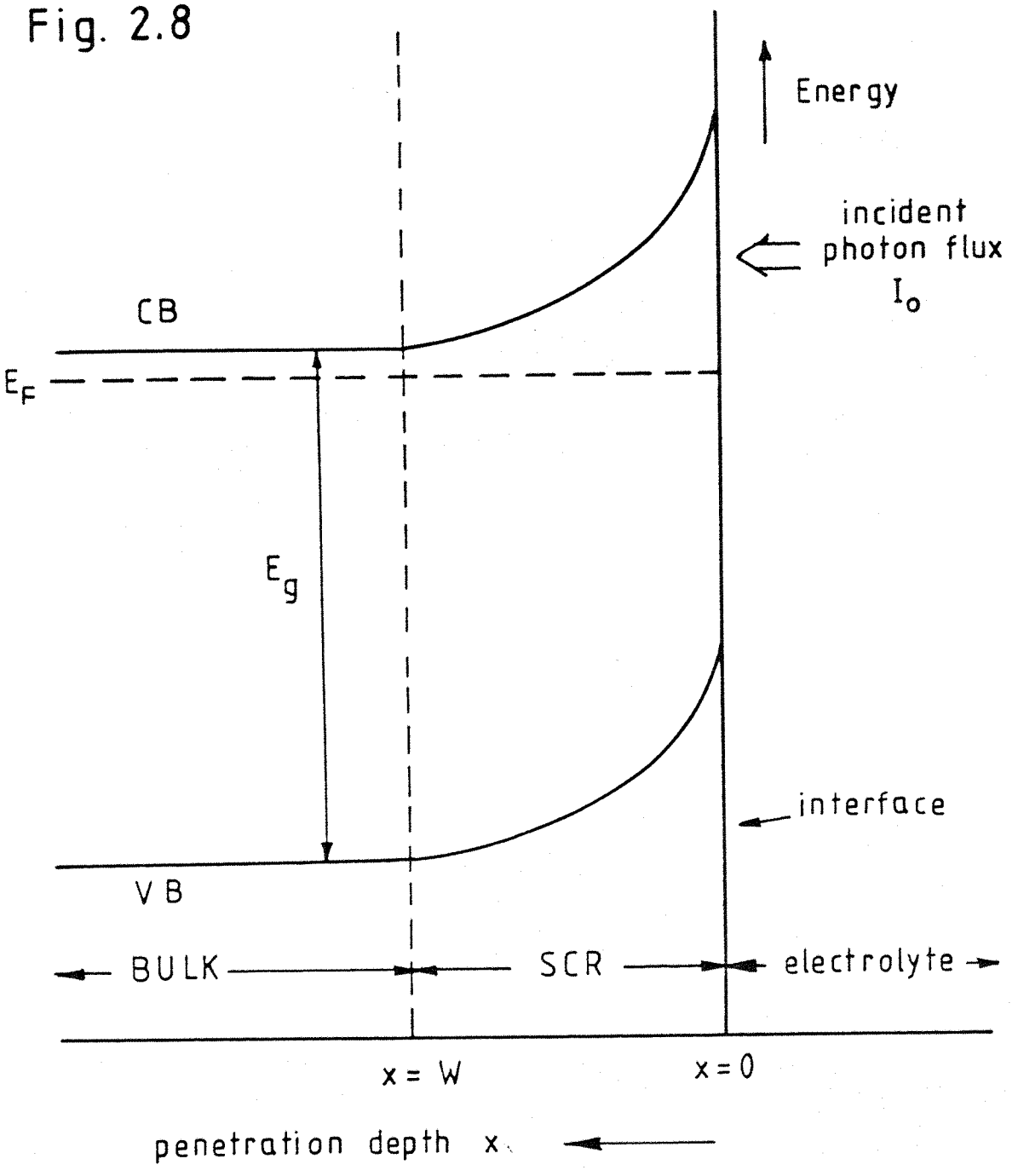
Energy
incident
photon flux
I_o
CB
E_F
E_g
interface
VB
BULK
SCR
electrolyte
x = W
x = 0
penetration depth x

The Gärtner theory is formulated as follows:

In the steady state, the total minority carrier flux through the depletion layer is the sum of the contributions from those generated in the space charge region J(scr) and those diffusing in to this region from the bulk J(bulk):

$$J = J(scr) + J(bulk) \qquad (2.1)$$

The rate of formation of electron-hole pairs due to photons absorbed at a distance x from the surface which is less than the penetration depth of the light in to the material (a few units of the reciprocal of the monochromatic absorption coefficient α) is

$$g(x) = I(0).\alpha.\exp(-\alpha x) \qquad (2.2)$$

where I(0) is the incident photon flux corrected for reflection.

J(scr) in the absence of recombination is the integral of this expression over the range x=0 at the surface to x=W at the boundary of the space charge region with the bulk, so that

$$J(scr) = I(0).[\exp(-\alpha W) - 1] \qquad (2.3)$$

Assuming that the potential drop across the Helmholtz layer remains constant, so that all changes in applied potential appear across the space charge region, (which is reasonable because of the relative narrowness of the Helmholtz layer), the depletion layer width W is given by

$$W = W(0).(E-Efb)^{1/2} \qquad (2.4)$$

where W(0) is a constant, E is the applied potential relative to a reference electrode, and Efb is the flat band potential relative to the same reference electrode. Note that

$$W(0) = (2.\varepsilon.\varepsilon(0)/e.Nd)^{1/2} \qquad (2.5)$$

where ε is the dielectric constant of the material and $\varepsilon(0)$ is the dielectric constant of free space.

For an n-type semiconductor, the flux of holes into the depletion layer from the bulk, J(bulk), is given by the solution of the diffusion equation for holes in the neutral region, under the given boundary conditions:

$$D.d^2p/dx^2 - (p-p(0))/\tau + g(x)=0 \qquad (2.6)$$

where D is the diffusion coefficient of the minority carrier (hole), and τ (tau) its average lifetime. p and p(0) are the density of holes at distance x from the surface and the equilibrium value in the bulk respectively, and so the second term is a measure of the recombination rate.

The Gärtner model has as boundary conditions that p = p(0) at x = infinity, that p=0 at x=W. This approximation is valid for larger W values. In these circumstances, it is found that:

$$J(bulk)=-(\alpha.L.I(0).\exp(-\alpha.W))/(1+\alpha.L) - p(0).D/L \qquad (2.7)$$

where the minority carrier diffusion length

$$L=(D.\tau)^{1/2} \qquad (2.8)$$

Then, adding the results for J(scr) and J(bulk),

$$J= -I(0).[1-\{\exp(-\alpha.W)/(1+\alpha.L)\}] - p(0).D/L \qquad (2.9)$$

For relatively large band bending, when the concentration of holes at the edge of the depletion layer tends to zero, the second term in (2.9) can be dropped.

Converting to current i, (2.9) reduces to

$$i = e.I(0).[1-\{\exp(-\alpha.W)/(1+\alpha.L)\}] \qquad (2.10)$$

where e is the electronic charge. Rewriting this in terms of the photocurrent conversion efficiency

$$\underline{\Phi} = i/(e.I(0)) \qquad (2.11)$$

we obtain one form of the Gärtner equation:

$$\underline{\Phi} = 1 - \{\exp(-\alpha.W)/(1+\alpha.L)\} \qquad (2.12)$$

In many cases, then, the behaviour of electrolyte junctions with semiconductors having sufficiently wide energy gaps and high enough doping densities may be accurately described at moderate illumination intensities by the Gärtner equation in the potential range which excludes the onset of the photocurrent. For sub-band gap photons, the model is not accurate, since it is necessary to take into account the high electric field in the space charge region,

which, through the Franz-Keldysh and/or Poole-Frenkel mechanisms, may give an extension of the energy range of the photoresponse.

In cases where the doping density is relatively small, the photocurrent can no longer be assumed to be due only to excess minority carriers. There is a contribution due to excess majority carriers flowing against the potential gradient to the interface, and reducing the net photocurrent (the dark current).

For materials in which the minority carrier diffusion length L is much less than the space charge width W at a given potential, the photocurrent will derive mainly from carriers generated in the depletion layer. As the carrier concentration Nd increases, for example through greater doping levels, the depletion layer becomes narrower, and consequently the quantum efficiency falls, as less minority carriers can be transported to the interface before they recombine. As Nd is reduced, the quantum efficiency increases, as the space charge region extends deeper in to the material, and provides a separating field in the region where lower energy photons, near the band gap, are absorbed. However, the Ohmic drop through the semiconductor bulk increases as the doping level falls, placing a lower practical limit on Nd.

There is an optimum carrier concentration which maximises the depletion layer width without increasing the Ohmic drop to the point where it limits the overall efficiency of the device. This value is a function of the dielectric constant, the minority carrier diffusion length, the flat band potential, and the nature of the optical transition involved (direct or indirect).

(2.5) SIMPLIFICATION OF THE GÄRTNER EQUATION

Fig 2.9 summarises the several possible rearrangements and simplifications of the Gärtner equation, making various assumptions.

(1) The first course is to take natural logarithms and rearrange:

$$-\ln(1-\Phi) = \ln(1+\alpha.L) + \alpha.W \qquad (2.13)$$

This contains no more assumptions than (2.12).

If, in certain conditions, the term $\alpha.L$ is much less than unity then (2.13) can be simplified to:

$$-\ln(1-\Phi) = \alpha.W \qquad (2.14)$$

Using photocurrent conversion efficiency spectra determined at various known potentials, and the corresponding curves of α versus wavelength for the given material, equation (2.14) may be used to determine values of W, and hence Nd via equations (2.4) and (2.5), as a function of potential, assuming a value for the flat band potential.

Alternatively, since the capacitance per unit area of the space charge region is

$$C(sc) = \varepsilon.\varepsilon(0)/W \qquad (2.15)$$

it is possible to construct Mott-Schottky plots (see later) from these values of W, and obtain flat band potentials from their intercepts on the capacitance axis, and Nd values from their gradients.

$$\Phi = 1 - \frac{\exp(-\alpha W)}{1+\alpha L}$$

$\alpha W \ll 1$

$$\Phi = \frac{\alpha (W+L)}{1+\alpha L}$$

$\alpha L \ll 1$

$$\Phi = \alpha (W+L)$$

$L \ll W$

$$\Phi = \alpha W$$

$$\Phi^2 = \frac{2\alpha^2 \varepsilon \varepsilon_o (E - E_{fb})}{e N_D}$$

$$-\ln(1-\Phi) = \ln(1+\alpha L) + \alpha W$$

$\alpha L \ll 1$

$$-\ln(1-\Phi) = \alpha W$$

$$-\ln(1-\Phi) = \left[\frac{2\alpha \varepsilon \varepsilon_o (E - E_{fb})}{e N_D} \right]^{1/2}$$

(25)

Fig 2.9 Simplification of Gärtner Equation

It is also possible to calculate values of α using equation (2.14), deriving W from known values of W(0) and Nd using (2.4) and (2.5), and hence to plot the dependence of α on photon energy hv. Using equations (2.4) and (2.5) for the width of the space charge region W at a given potential in (2.13):

$$-\ln(1-\Phi) = \ln(1+\alpha.L) + \alpha\{2.\varepsilon.\varepsilon(0)/e.Nd\}^{1/2} \cdot (E-Efb)^{1/2} \qquad (2.16)$$

Again, making the assumption that $\alpha.L$ is much less than unity,

$$-\ln(1-\Phi) = \alpha\{2.\varepsilon.\varepsilon(0)/e.Nd\}^{1/2} \cdot (E - Efb)^{1/2} \qquad (2.17)$$

Hence firstly, a plot of $-\ln(1-\Phi)$ against $(E-Efb)^{1/2}$ should be a straight line passing through the origin, with a slope inversely proportional to $Nd^{-1/2}$, and secondly, a plot of $\{-\ln(1-\Phi)\}^2$ versus E should be a straight line intercepting the potential axis at the flat band potential. The data for these plots can be derived from experimental curves of conversion efficiency versus potential.

(2) The Gärtner equation (2.12) can also be simplified by expanding the exponential to its first two terms, which is a reasonable approximation if $\alpha.W \ll 1$, that is if the space charge thickness W is small compared to the penetration depth of the light. The approximation, which will be more true for lower energy photons than for higher energy ones is:

$$\exp(-\alpha.W) = 1 - \alpha.W \qquad (2.18)$$

This gives

$$\Phi = \alpha.\{W+L\} / \{1 + \alpha.L\} \qquad (2.19)$$

Further, in conditions where $\alpha.L \ll 1$, we have

$$\Phi = \alpha.\{W+L\} \qquad (2.20)$$

This equation allows one to determine L from a plot of Φ versus W. If the conditions are such that it is justifiable to assume also that $L \ll W$, then

$$\Phi = \alpha.W \qquad (2.21)$$

and, substituting for W from (2.4) and (2.5) and squaring,

$$\Phi^2 = 2.\alpha^2.\varepsilon.\varepsilon(0).(E - Efb)/e.Nd \qquad (2.22)$$

which is a linear relationship between Φ^2 and E, from which Efb is obtained as the intercept at $\Phi = 0$.

(2.6) EXTENSIONS OF GÄRTNER THEORY

Reichman [68] pointed out that recombination in the neutral and space charge regions has a greater effect on the photocurrent characteristic of a semiconductor-electrolyte junction than it does for a p-n junction or a Schottky barrier photovoltaic junction, due to the rate limiting effect of charge transfer kinetics in the 'wet' cell. He obtained the minority carrier current density at the depletion edge, Jw by solving (2.6) under the new boundary conditions p=p(0) at x=infinity and p=pw at x=W:

$$Jw = -J(0).\{pw/p(0)-1\} + e.I(0).\alpha.L.\exp(-\alpha.W)/(1+\alpha.L\} \quad (2.23)$$

where the saturation current density

$$J(0) = e.p(0).L/\tau \quad (2.24)$$

He then made the so-called quasi-equilibrium approximation, namely that the electrons and holes are separately in translational equilibrium, and he assumed that their quasi-Fermi levels are flat and parallel in the SCR. This cannot be true in fact, since some driving gradient must exist, as McCann and Haneman [70] have pointed out.

Initially neglecting recombinations in the SCR and at the interface, Reichman obtained for the hole current across the interface:

$$Jp = [Jg - J(0).\exp\{eV/kT\}] \;/\; [1 + (J(0).\exp\{eV/kT\}/I(0)p] \quad (2.25)$$

where V is the photovoltage. I(0)p is a hole exchange current parameter determined by the degree of overlap of the bands in the semiconductor and of the interfacial states with the redox states in solution, and by the probabilities for charge transfer.

Jg is the Gärtner expression:

$$Jg = J(0) + e.I(0).[1 - \exp(-\alpha.W)/(1 + \alpha.L)] \quad (2.26)$$

When the expression

$$J(0).\exp\{eV/kT\}/I(0)p$$

is of the order of unity, the hole current across the electrode/ solution interface rapidly decreases. This can be due to increasing photovoltage, and a decrease in the band bending, leading in turn to greater hole density at the depletion edge and greater recombination rates there. It can also be due to slower interfacial charge transfer kinetics, giving a lower value of I(0)p. When the minority carrier concentration near the surface exceeds the majority carrier concentration, we have surface charge inversion, and SCR recombination is the dominant photocurrent loss mechanism.

Reichman determined the dark current due to majority carrier transfer across to the electrolyte species to be

$$Jn = -I(0)n.[\exp\{eV/kT\} - 1] \qquad (2.27)$$

which must be added as a correction to (2.25).

Following the method of Sah et.al. [72], Reichman made further corrections for recombination in the SCR.

A comparison of the photocurrent-voltage curve shapes predicted by the simple Gärtner equation, and its extensions to account for the dark current and recombination shows that the Gärtner expression is a good approximation at lower photovoltages, but that the photocurrent rapidly becomes less than this expression predicts at higher photovoltages.

Albery et.al. [69] have again refined the theory to show how the dominant recombination zone may vary with the intensity of the incident light.

(2.7) THE NATURE OF THE ELECTRONIC TRANSITION IN THE SEMICONDUCTOR ELECTRODE SIDE OF THE LIQUID JUNCTION

The fundamental process involves the transition of an electron from the valence band to the conduction band caused by the absorption of a photon of energy greater than or equal to the band gap Eg (fig.2.10). The onset of this effect occurs at the absorption edge.

The total energy and momentum of the electron-photon system is conserved. Since the momenta of optical photons are negligible compared to that of the electron, this part of the rule can be reduced to conservation of electron momentum, with only vertical transitions in momentum space allowed.

For direct gap materials, the maximum of the valence band in momentum space coincides with the minimum of the conduction band, and so electrons near the top of the valence band are able to make transitions in accord with the above selection rule.

In indirect band gap semiconductors, the electron must absorb both a photon and a phonon (quantised lattice vibration) simultaneously to conserve energy and momentum.

The behaviour of the optical absorption coefficient near the band edge is a complex function of the band detail and selection rules, but if we assume that the wave (momentum) vector k=0 in allowed transitions, then

$$\alpha = A.\{h\nu - Eg\}^{n} / h.\nu \qquad (2.28)$$

where A is a constant and n is 1/2 for a direct allowed transition, 3/2 for a direct forbidden transition, 2 for an indirect allowed transition, and 3 for an indirect forbidden transition.

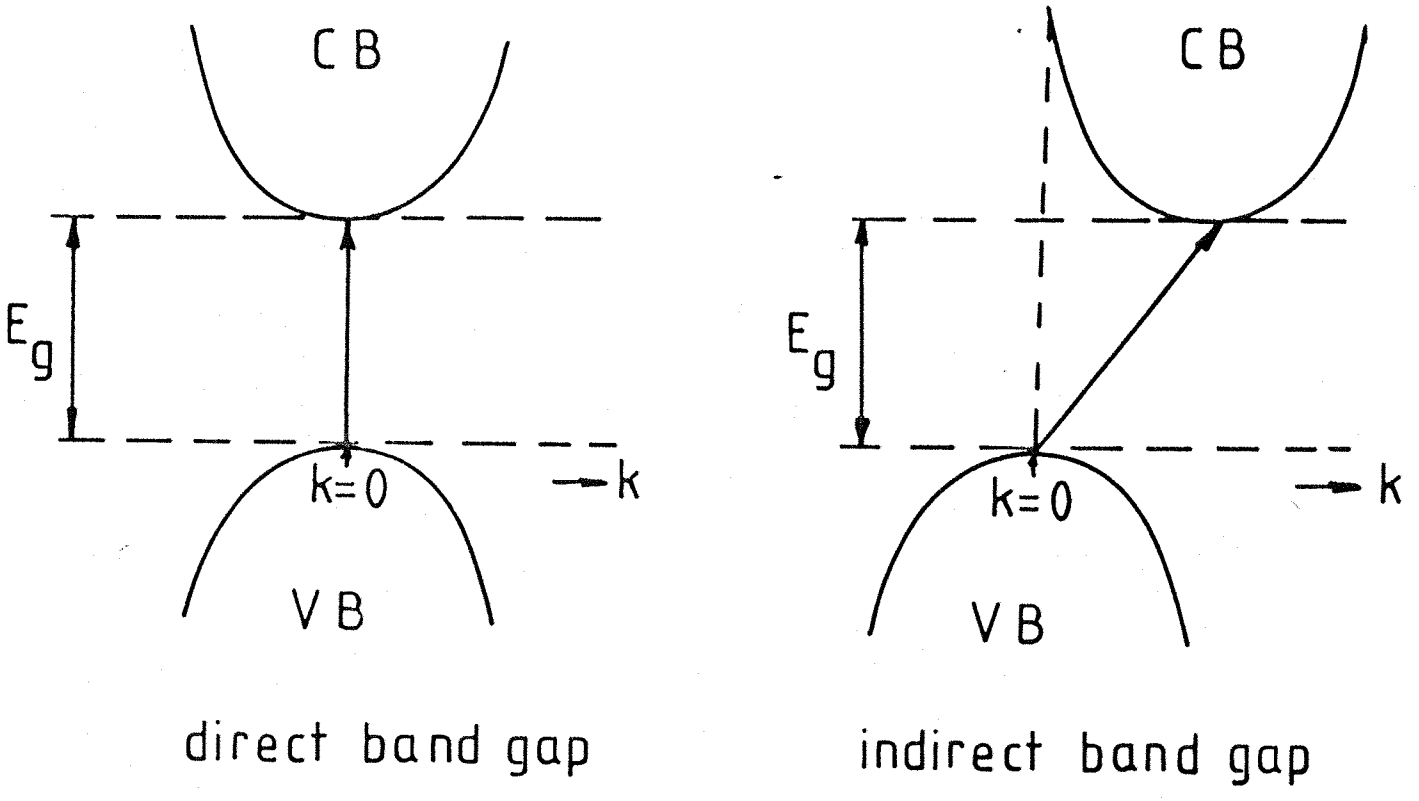

Fig 2.10 Optical Transitions in Semiconductors

For direct transitions (n=1/2), α rises steeply from the threshold to as much as 10^6 per cm, in contrast to indirect ones (n=2) where it rises only slowly.

Thus, either using values of alpha derived from (2.14), or values from the literature, plots of $\{\alpha.h\nu\}^{1/n}$ versus hv can be made to determine Eg.

From (2.20) and (2.28)

$$\Phi.h\nu = \{W + L\}.A.\{h\nu - Eg\}^{n} \qquad (2.29)$$

and so

$$\log(\Phi.h\nu) = \log\{A.(W + L)\} + n.\log\{h\nu - Eg\} \qquad (2.30)$$

which enables n to be determined from the slope of $\log(\Phi.h\nu)$ versus $\log(h\nu - Eg)$.

Alternatively, if n=2, as it will for an indirect transition, (2.29) gives

$$\Phi.h\nu = \{W + L\}.A.\{h\nu - Eg\}^{2} \qquad (2.31)$$

and a plot of $(\Phi.h\nu)^{1/2}$ versus hv gives Eg.

(2.8) THE EFFECTS OF SURFACE RECOMBINATION AT THE LIQUID JUNCTION

Surface states at the semiconductor-electrolyte interface can be thought of as energy states lying across the semiconductor band gap at the surface such that charge transfer can occur between them and the conduction and valence bands on the one side, and between them and

electrolyte adsorbed and solvated species on the other side. If charge exchange with the semiconductor is the more rapid process, then the surface states will trap minority carriers and act as recombination centres. If charge exchange with the redox species is the more rapid, then the surface states will act as charge transfer intermediates in promoting current flow across the interface.

When the occupancy of the surface states is sufficiently high (above 10^{13} per square cm), a redistribution of potential occurs through the interface such that the Fermi level becomes more and more influenced by these states, and ultimately becomes pinned to them, while all changes in applied potential appear across the Helmholtz layer. This will produce anomalous flat band potentials derived from Mott-Schottky plots (q.v.) unless these are obtained in the potential region in which the surface state occupancy is zero.

On the other hand, at high illumination intensities, or for surface states far from the band edges where the kinetics of recombination is less favoured, photogenerated minority carriers may accumulate at the surface, unpinning the band edges.

A number of authors have investigated the effect of these surface states on the photocurrent equations including R.H.Wilson [73], J.J.Kelly and R.Memming [74], J.-N.Chazalviel [75], K.Rajeshwar [76], and J.Li, R.Peat, and L.M.Peter [77].

It is found that the photocurrent is further reduced, as expected, for the potential region in which the surface states are partially occupied, but rises steeply when the Fermi level passes the surface states i.e. when they are fully occupied.

(2.9) SPACE CHARGE CAPACITY IN THE SEMICONDUCTOR NEAR THE LIQUID JUNCTION

The potential distribution in the space charge region is given by Poisson's equation

$$d^2\Phi/dx^2 = -e.N(sc)/\varepsilon.\varepsilon(0) \qquad (2.32)$$

where Φ is the potential at a distance x from the surface in to the electrode, e is the electronic charge, N(sc) is the charge density in the space charge region (SCR), ε is the sample's relative permittivity, and $\varepsilon(0)$ is the permittivity of free space.

This can be integrated twice, with the boundary condition that

$$d\Phi/dx = 0 \text{ at } x=W$$

where W is then the width of the SCR. It follows that

$$W = [2.\varepsilon.\varepsilon(0).(\Delta\Phi(sc)-kT/e)/e.Nd]^{1/2} \qquad (2.33)$$

where $\Delta\Phi(sc)$ is the band bending and Nd is the doping density. It then follows that the capacity of the SCR is

$$Csc = \varepsilon.\varepsilon(0)/W = [e.\varepsilon.\varepsilon(0).Nd/2.(\Delta\Phi(sc)-kT/e)]^{1/2} \qquad (2.34)$$

where the term kT/e is relatively small at room temperatures, being 25.7 mV at 298 K.

Hence, to a good approximation for this work,

$$1/Csc^2 = 2.(E - Efb) / e.\varepsilon.\varepsilon(0).Nd \qquad (2.35)$$

using

$$\Delta\phi(sc) = E - Efb \qquad (2.36)$$

A plot of C_{sc}^{-2} against E should therefore be a straight line whose slope is a function of the doping density, and whose intercept is the flat band potential.

For an electrolyte-semiconductor interface, any change in applied potential is realised across the Helmholtz layer, and thus affects the capacity in accord with equation (2.34), provided that the concentration and occupation of surface states is unaffected.

The differential capacity of the SCR is assumed negligible compared to that of the Helmholtz layer, and the effects of the Gouy double layer (the layer of electrolyte next out from the Helmholtz layer, containing an excess of one charge) are ignored.

(2.10) EFFICIENCY OF LIQUID JUNCTION CELLS

The energy output of a photoelectrochemical cell is related to the amount of band bending at the semiconductor-electrolyte interface, since this is the maximum voltage drop experienced by an electron passing round the circuit. Such cells are quantum converters with a certain threshold energy, the band gap Eg, below which photons are not absorbed in the ideal system, and above which relaxation of the carriers to the band edges dissipates the fraction

$$(Ephoton - Eg) / Ephoton \qquad (2.37)$$

of the incident energy. The photocurrent conversion efficiency is defined as:

$$\text{Efficiency} = N(e) \,/\, N(hv) \qquad (2.38)$$

where N(e) = Number of electrons flowing in external circuit

N(hv)= Number of incident photons of energy hv

Archer [15] defines the ultimate quantum efficiency in terms of the number of charge carrier pairs generated by the incoming light that is actually absorbed:

$$\left(Eg. \int_{E_g}^{\infty} A(E).P(E)\, d\ln E \right) / \left(\int_{o}^{\infty} P(E)dE \right) \qquad (2.39)$$

which is

$$\left(Eg. \int_{E_g}^{\infty} A(E).N(E)dE \right) / \left(\int_{o}^{\infty} E.N(E)dE \right) \qquad (2.40)$$

where P(E) is the spectral irradiance and N(E) is the photon flux density. A(E) is the optical absorbance for photons of energy E.

The efficiency should be close to unity in the ideal case, though values greater than unity are possible due to "current doubling" whereby one incident photon produces two electron-hole pairs.

There is a further, thermodynamic limitation to the efficiency of a solar converter such as we are considering. This is a Carnot limiting efficiency related to the difference in temperature between the sun's radiation and the radiation field with which the semiconductor electrode is in equilibrium.

Other unavoidable energy losses are those resulting from the band bending necessary to drive apart the charge carriers, and the energy lost through the potential drop at the back contact to the semiconductor.

The power delivered to a load is the product of the cell

current (I) and the cell voltage (V). Typical I-V curves in the dark and under illumination are shown in fig 2.11. The shape reflects the voltage dependence of the current, and the fact that the delivered power depends strongly on the load. With zero or infinite loads, the delivered power is zero; between these the power reaches a maximum near the "knee" of the curve. The curve for the illuminated device is essentially the forward biassed diode dark characteristic displaced in to the fourth quadrant by an amount equal to the photocurrent.

The power efficiency is usually reported as the ratio of maximum electrical power output to the total incident solar energy:

$$\text{Power Efficiency} = (V_{oc}.I_{sc}.FF) / P \qquad (2.41)$$

where P is the power density illuminating the device, Voc is the open-circuit voltage, Isc is the short-circuit current, and FF is the fill factor. FF is a measure of the "rounding" of the power curve at the knee, and ideally should be unity; it is defined as the ratio of the maximum output power to the product Isc.Voc . The curve becomes more rounded, and FF decreases, if the ohmic losses, which arise from high series resistance in surface contacts and the semiconductor bulk, increase. FF is also decreased by a tendency to lower diffusion lengths or higher recombination rates.

The fact that the efficiency increases with increasing Voc favours materials with large band gaps, but since these absorb a lower fraction of the sun's spectrum than materials with lower band gaps, there is an optimum range of values of Eg, ranging from 1.0 to 1.5 eV. Typical semiconductor band gaps are GaAs (~1.4 eV), InP (~1.3eV), CdTe (~1.5eV), Bi_2S_3 (~1.2eV) [79,80], and CdS (~2.4eV).

The mean solar irradiance just outside the earth's atmosphere

Fig. 2.11

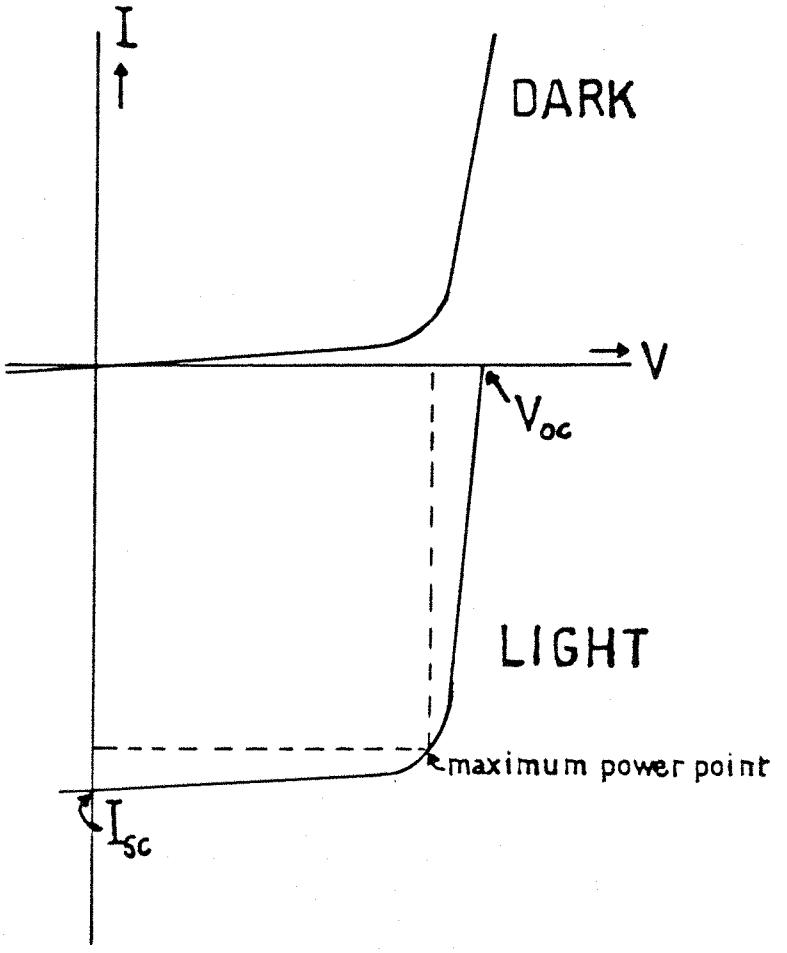

Fig. 2.12

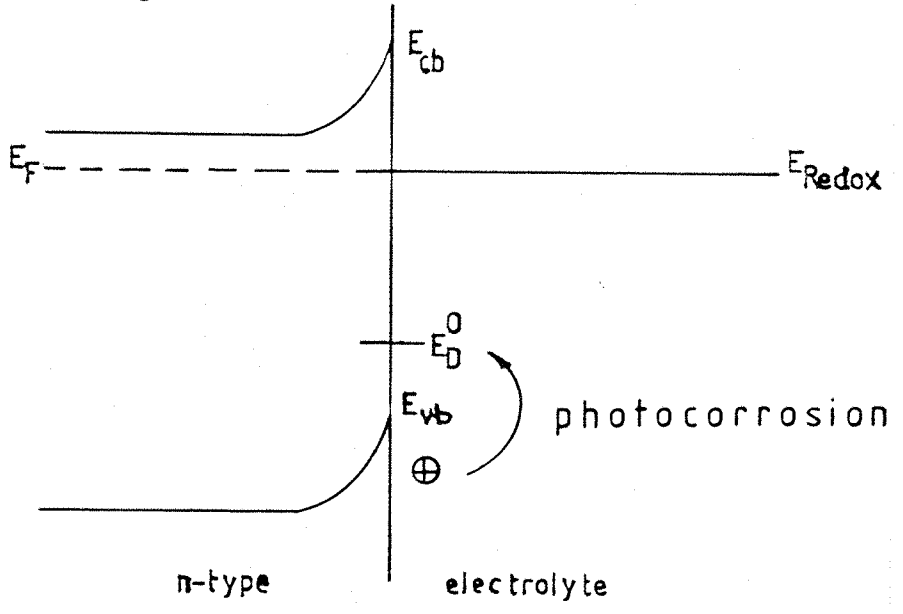

is 1353 watts per square metre, and the solar spectrum approximates fairly closely below 1250nm to that of a standard blackbody radiator at 6000K. The spectral distribution of sunlight reaching the earth's surface is modified by scattering, ozone absorption of the ultraviolet, and carbon dioxide and water vapour absorption in the infrared. The extent of these effects depends mainly on the so-called Air Mass Ratio, which is the ratio of the optical path length through the atmosphere of a ray of sunlight illuminating a point on the surface, to the optical path length to that point when the sun is at its zenith. The spectra for any given AM number are understood to be measured in cloudless conditions with no particulate pollution. Thus AM1 is the spectrum of the sun when it is directly overhead relative to the given point on the earth's surface, AM2 refers to a sun at 30 degrees altitude above the horizon, while at the other end of the scale, AM25 is a typical rising or setting sun's spectrum. Extra-terrestrial sunlight is said to have an AM0 spectrum. The higher the air mass ratio, the greater the absorption in the u/v and i/r, and the greater the proportion of visible wavelengths in the sunlight.

Standardisation of solar reference spectra for laboratory simulations has been slow, but there is some concensus that AM 1.5 be adopted. It is not essential in the early developmental stage of new solar cells to simulate actual solar spectra precisely. AM 1 conditions can be approximated by filtering through water the light from a tungsten-halogen lamp with a 3200K colour temperature, adjusting the intensity by means of a reference radiometer to achieve a power density of 100 mW per sq.cm.

A full thermodynamic treatment shows that the maximum solar cell efficiency is 31% for a single absorber (corresponding to an

absorption edge at 950nm) in AM0 conditions, changing to 33% (absorption edge at 1100nm) in AM1.5 sunlight. Efficiencies over 50% have been calculated for cells with multiple junctions, each junction absorbing a different part of the solar spectrum. Efficiency increases linearly with the logarithm of the light intensity, but decreases as the temperature increases.

There may be additional efficiency losses due to absorption in the electrolyte. For example, the sulphide/polysulphide system absorbs in the region up to 470nm. The photocurrent may also be reduced by reflection at the interface: the surface can be dulled by etching it slightly.

Slow electrode kinetics does not reduce Voc, and may or may not reduce Isc, but it always reduces FF. Unless the rate of arrival of minority carriers at the interface substantially exceeds their recombination rate, the current efficiency near the maximum power point drops, until it is zero when the recombination rate equals the photogeneration rate. At this limit, Voc no longer depends on the redox potential in the electrolyte, and is said to be "pinned" by the surface or defect states assisting recombination.

(2.11) PHOTOCORROSION AND ELECTROLYTIC DECOMPOSITION OF ELECTRODES IN LIQUID JUNCTION CELLS

Photoanodes (n-type materials) are subject to oxidation by surface holes, since the formal potential for oxidation of the semiconductor, E_D°, is always more negative than the potentials of holes at the valence band edge. The more negative this decomposition potential is from the band edge, the less stable is the electrode. If the holes have been produced by the absorption of light quanta, then the process is called photocorrosion. Relatively

stable semiconductor photoanodes such as TiO_2 unfortunately often have too large a band gap for efficient absorption of the solar spectrum. In a p-type electrode (photocathode), electrons in the conduction band may reduce the surface.

If the redox potential of one of the electrolyte species in a liquid junction solar cell is more positive than E_D^o then spontaneous oxidation of the electrode by the electrolyte is possible in the dark.

Fig 2.12 shows a junction which is thermodynamically stable to oxidation by the electrolyte (the redox potential is more negative than the surface decomposition potential) but which is not thermodynamically stable to oxidation by surface holes.

To a first approximation, whether or not a system is stable enough to be used in a practical solar cell depends on the kinetics of the desired interfacial redox reaction being much faster than the semiconductor decomposition reaction. For an n-type surface, this requires good overlap between the valence band edge and the occupied states of the reduced form of the redox couple.

It has been found, however, that a redox process may compete sucessfully with the anodic dissolution of an n-type semiconductor even when the potential of the reduced form of the redox couple is some distance negative of the valence band edge (fig 2.13), due to the mediation of surface states which accept electrons from the reduced species in solution and thermalise them so that they eventually drop in to holes in the valence band.

One possible origin for such surface states is as intermediates in dissolution of the surface by photocorrosion (fig 2.14). A free hole may break a bond, leaving an unpaired electron in an energy state (A*) above the band edge. A further hole may then be trapped to completely remove the surface group. This second step can

Fig. 2.13

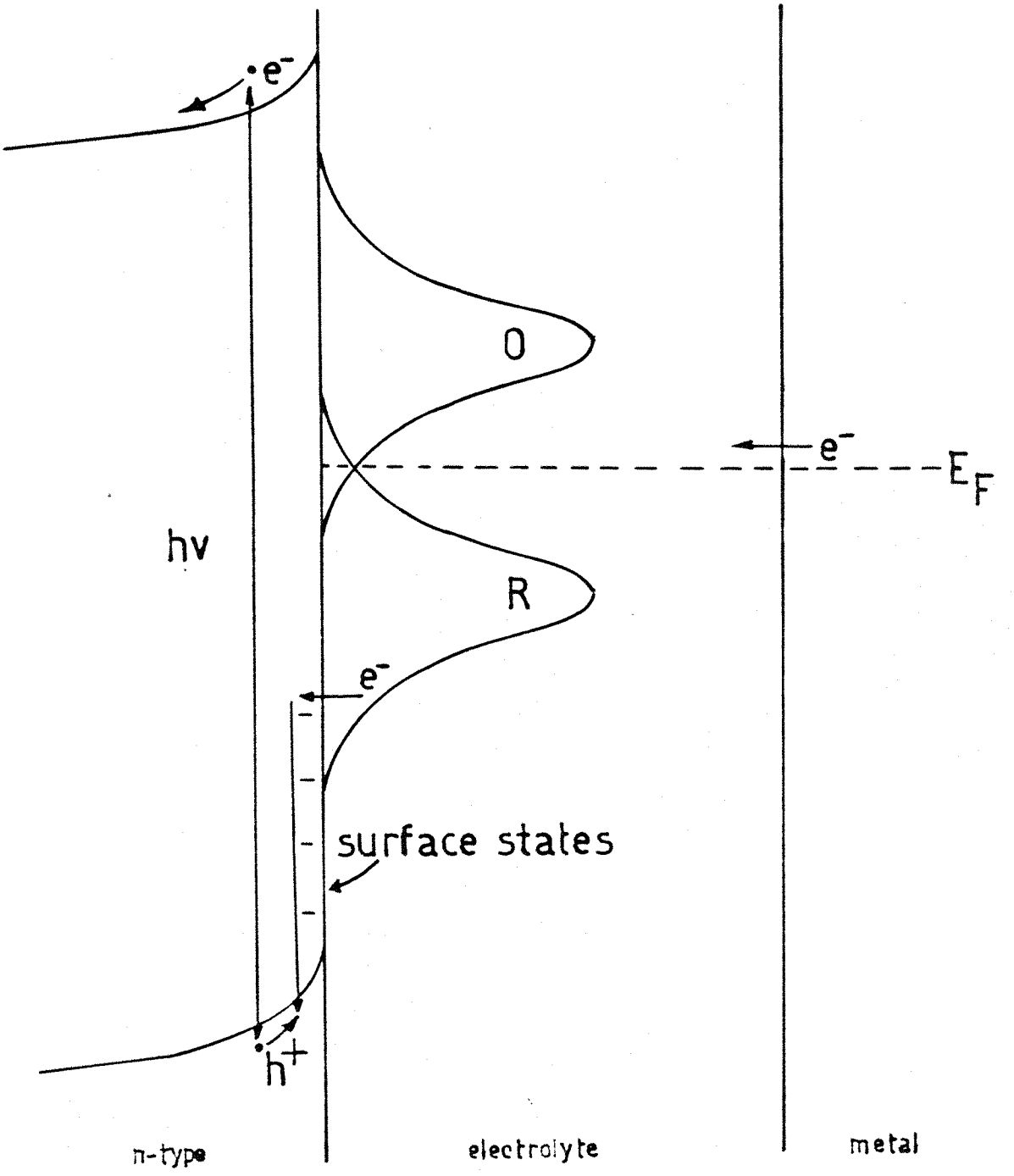

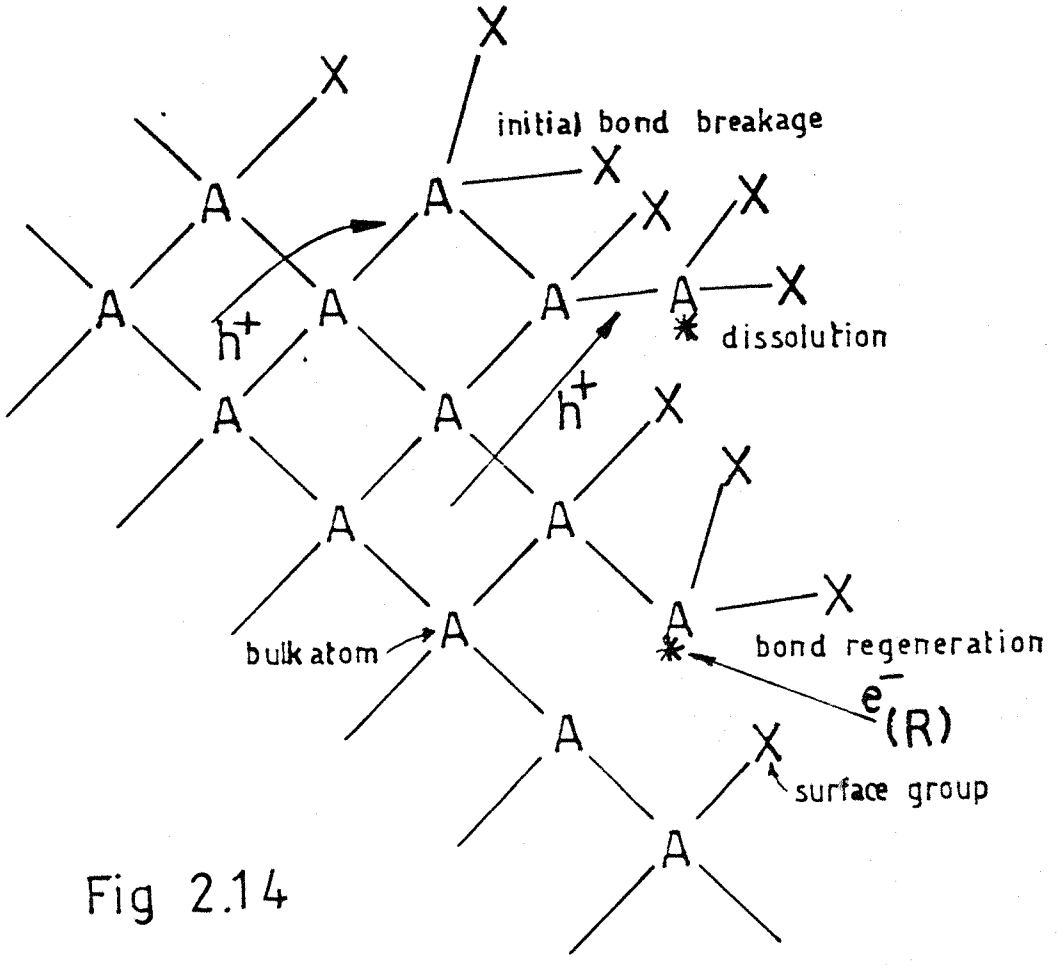
initial bond breakage
dissolution
bulk atom
bond regeneration
e⁻(R)
surface group

Fig 2.14

be prevented by the transfer of an electron from a suitable redox system to the surface group which has a broken bond, to restore the bond. A practical example is the use of sulphide/polysulphide and selenide/diselenide redox systems with chalcogenide electrodes. These systems have the additional advantage that any tendency to deposit insulating films of the chalcogen is reduced by the high solubility of these in the polyelectrolyte.

The strength of surface bonds is not simply the bulk bond dissociation energy, and is usually less than this due to lower coordination at defect sites. These higher energy atoms are particularly susceptible to photocorrosion.

In the case of p-type materials, photocorrosion is less severe, since the required redox charge transfer process can easily compete with the hydrogen evolution side reaction; however, the photovoltage is usually much lower than expected from predictions based on the known band bending, probably due to high recombination rates via surface states.

An alternative approach to prevent photocorrosion is to use transition metal chalcogenide electrodes, in which the optical transitions are to non-bonding rather than antibonding orbitals, so that there is stronger bonding between the surface atoms; this also reduces the surface recombination rate by lowering the density of surface states.

(2.12) SURVEY OF PLATING METHODS AND PREVIOUS RESULTS

The processes of nucleation and crystal growth are affected by the nature of the electrolyte, the temperature, the current density, the rate of agitation, the nature of the substrate, and the presence of additives such as supporting electrolytes, surfactants, brighteners,

and levellers.

Higher nucleation rates are, in general, induced by higher overpotentials and current densities, whereas the nucleation rate is decreased by increased metal ion concentration,increased temperature, and increased stirring rates. The more nuclei that form per unit area, the smaller will be the grain size, and the stronger and denser the deposit.

There is therefore a compromise to be reached between the need for a mechanically strong, firmly attached deposit, characteristic of deposits with a small grain size, and deposits with less lattice distortion and discontinuities, i.e. a larger average grain size, which have a higher minority carrier diffusion length.

Distortion "frozen" into the lattice during rapid deposition can cause internal stresses which lead to cracking and poor corrosion resistance. Organic additives can reduce this, but also alter the electrical properties of the layers.

There are three basic methods established for the deposition of thin-film chalcogenides.

One method involves oxidising the metal anodically in a solution of the chalcogenide ion, which deposits the insoluble metal chalcogenide on the substrate electrode [35-39]. Growth of such films has the disadvantage of requiring ion transport through the film, which is liable to create pores of electrolyte which short out the photocurrent.

Another method involves coreducing the metal ion and a chalcogen oxyanion in aqueous solution [40-44]. This has the advantage that the reaction to produce the film occurs at the semiconductor-solution interface. However, the mechanism is complicated by the need to dissociate the oxyanion.

A third method, which is being further investigated in this project, avoids this complication, and produces more homogeneous films, with better adherence to the substrate. It involves the cathodic coreduction of the metal ion and the elemental chalcogen from a non-aqueous solvent.

Most of the investigations made so far in to this method [46-51] have been lead by Baranski and Fawcett, who have deposited galvanostatically such semiconductors as CdS, HgS, PbS, Tl_2S, Bi_2S_3, Cu_2S, NiS, CoS, and CdSe, variously on Pt,Au,Ni,Zn, stainless steel, and glass coated with a conducting film of tin oxide. The non-aqueous solvent was usually dimethylsulphoxide (DMSO), but they have also used dimethylformamide (DMF) and diethylene glycol. These latter two high boiling non-aqueous solvents were selected for the present investigation. There are general reviews of their electrochemical and physical properties in the literature [52,53]. Apart from DMSO [54], other suitable solvents for future investigation include sulpholane (B.Pt. 285°C), propylene carbonate (B.Pt.242°C) [55,56] and N-methylacetamide (B.Pt. 206°C) [57].

The mechanism of the cathodic codeposition of CdS from a DMSO solution of $CdCl_2$ and elemental S must be complex for several reasons. There is a high activation energy for the single-step discharge of Cd^{++}, involving the simultaneous transfer of two electrons across the interface; an intermediate step involving Cd^+ is more likely. Also, the nature of the substrate on to which the deposition is taking place changes from metal (e.g. Pt) to semiconductor as the first few monolayers are deposited. Finally, there may be a strong contribution from chemisorbed impurities prior to and during the deposition, particularly in the case of substrates with high surface

energy such as Pt.

The reduction reactions of sulphur and cadmium have been studied separately in DMSO. Sulphur is reduced in two steps, each involving two electrons, via the polysulphide species S_8^{--}, S_6^{--}, and S_4^{--} [58-61]. Solvated Cd^{++} is reduced via Cd^{+}, or via specific adsorption of Cd^{++} with partial charge transfer.

Roe et.al. [50] studied the deposition of CdS on gold from DMSO, and concluded that the initial layer of CdS is formed by underpotential deposition of cadmium, followed by reaction of this with elemental sulphur. Further growth, they suggested, involves reaction between sulphur fragments and deposited cadmium, or between reduced sulphur and Cd(II) ions. This is in accord with the work of Kolb, who found that the redox process

$$Cd(II) + 2e^{-} \rightarrow Cd$$

on a solid electrode usually involves underpotential deposition.

However, Humphrey [63] found that the metal sulphide was formed initially on mercury in methanol. Baranski and Fawcett [49] also found strong chemisorption of sulphur at mercury, gold, and (probably) platinum in DMSO, as sulphide layers. They found that, in the codeposition from DMSO, the platinum surface was not uniformly covered with sulphide, and predicted that nucleation would occur preferentially on the more active sites. From cyclic voltammetry they concluded that the mechanism of the process did not alter as the temperature was raised to 110°C., although the current efficiency increased over this range from 50% to 81%. It was expected that better quality films would be obtained at higher temperatures because of the very fast chemical reaction rate needed at the surface in order to maintain deposit stoichiometry.

(2.13) COMPARISON OF PROSPECTS FOR LIQUID JUNCTION CELLS AND OTHER SOLAR CELL TECHNOLOGIES

The materials used in a commercial solar cell must be abundant enough to meet the projected demand economically, with an energy pay-back period much shorter than the expected system lifetime. The associated mining and manufacturing industries must have an acceptable social impact [27,28,45].

The expansion in the market for silicon solar cells has always been held back by the high financial and energy costs in the production of pure single-crystal silicon, despite continuing attempts to find cheaper solutions. Investigations are continuing in to large-crystal, polycrystalline, and hydrogenated amorphous silicon electrodes [29-31].

An alternative is to use small, costly, but efficient materials made from rarer substances such as GaAlAs. These are best used with solar concentrators.

Another solution is to use thin polycrystalline layers of semiconductors in solid state cells, the earliest and most exploited example being the cuprous sulphide/cadmium sulphide cell. Such layers can have a higher optical absorption coefficient than single-crystal silicon, so that less material is needed, and its purity is less critical, since the minority carriers have less distance to travel to the junction field, reducing recombination losses. These considerations can reduce manufacturing costs by making a continuous "conveyor belt" process possible.

However, thin-layer semiconductors are often fragile, easily degradable, and have somewhat variable electronic properties due to the difficulties of controlling the precise doping levels in techniques such as evaporation, spraying, and sputtering [32 - 34].

Such methods are also costly and energy consuming, since high temperatures are usually required.

Investigations of the properties of electrodeposited semiconductor thin films, such as this study of cadmium and bismuth sulphides, will hopefully lead eventually to a cheap manufacturing process producing mechanically and chemically durable photoelectrodes. The production process will then be carried out at much lower temperatures than before, and it will be possibe to codeposit the dopants from the plating bath, giving accurate control over the doping levels by adjusting their concentrations in the bath during manufacture.

CHAPTER 3

EXPERIMENTAL PROCEDURE

(3.1) THIN LAYER SEMICONDUCTOR ELECTRODEPOSITION SYSTEM

A plating cell was designed (figs 3.1 and 3.2), together with an oil bath and temperature controller (fig 3.3), to enable deposition of thin film semiconductors at elevated temperatures under a nitrogen blanket. The oil used was Dow-Corning silicone oil, stable up to about 200 °C. The settling time and temperature stability of the bath were examined, and found to be approximately one hour heating time from room temperature to 150 °C., and +/- 4 °C. regulation in the range 100-170 °C. This was tolerable for preliminary experiments, but a commercial oil bath was obtained subsequently which provided closer temperature regulation for the main body of the investigation.

A module was designed, constructed, and calibrated (fig 3.4) to enable a commercial potentiostat to be used as a galvanostat, to control the growth of the films.

A detachable electrode system was designed (fig 3.5) to allow several films to be grown on a series of buttons, storing them when necessary before analysis of their photocurrent properties, or surface structure by electron microscopy. The working surface of each button was a platinum disc 6 mm in diameter set in to a glass holder 1 cm high, and connected inside the button to a gold plated sub-miniature socket for electrical contact to the upper tube of the device, which was terminated by a corresponding pin. The connection between the two parts of the electrode was sealed by heat-shrinkable tubing. Due to attack of this by hot DMSO, the tubing was replaced after the growth of each film. Hot glycol did not attack the tubing so much.

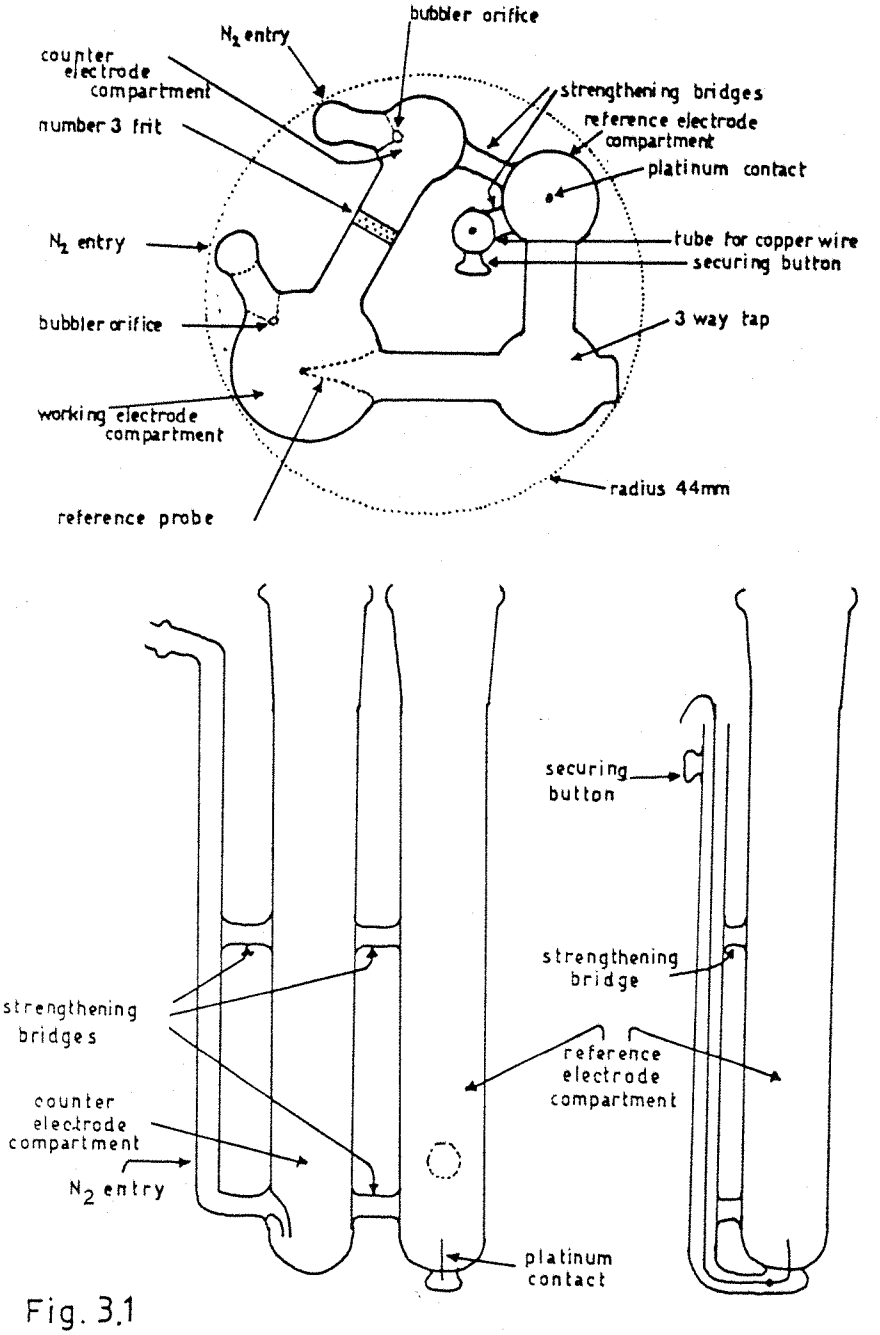
bubbler orifice
N_2 entry
counter electrode compartment
strengthening bridges
number 3 frit
reference electrode compartment
platinum contact
N_2 entry
tube for copper wire
securing button
bubbler orifice
3 way tap
working electrode compartment
radius 44mm
reference probe
securing button
strengthening bridge
strengthening bridges
reference electrode compartment
counter electrode compartment
N_2 entry
platinum contact

Fig. 3.1

Fig. 3.2

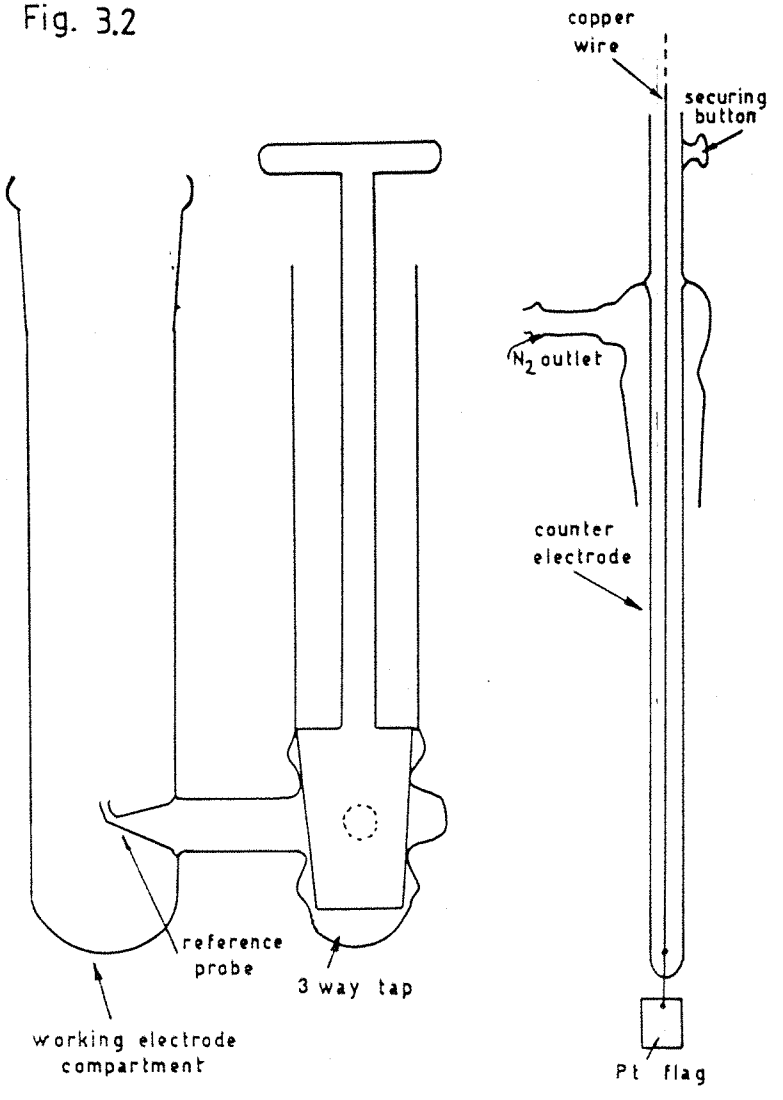
copper wire
securing button
N_2 outlet
counter electrode
reference probe
3 way tap
working electrode compartment
Pt flag

Fig. 3.3

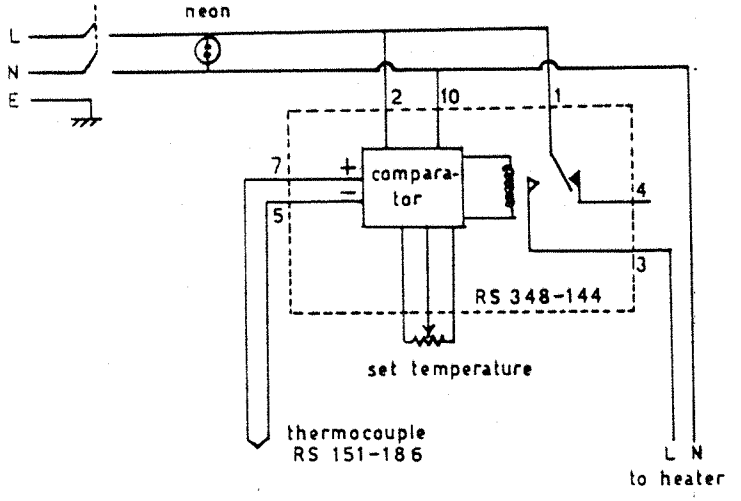

Fig. 3.4

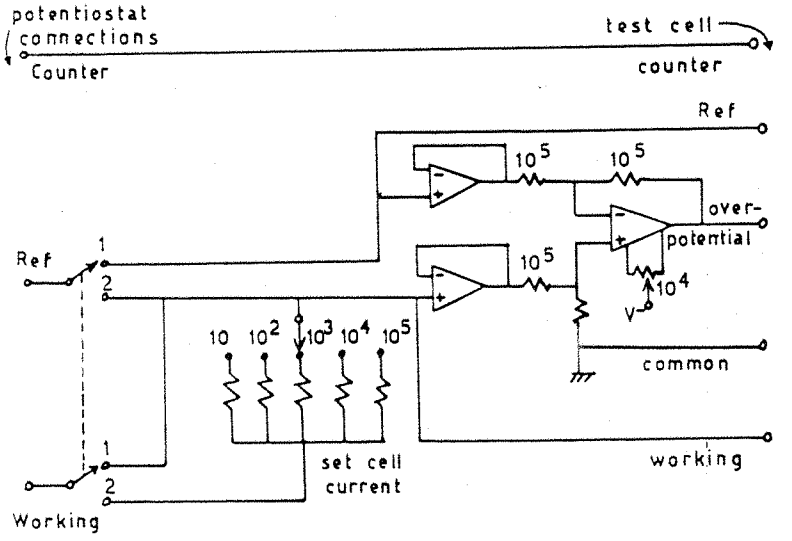

1 = Potentiostatic mode
2 = Galvanostatic mode

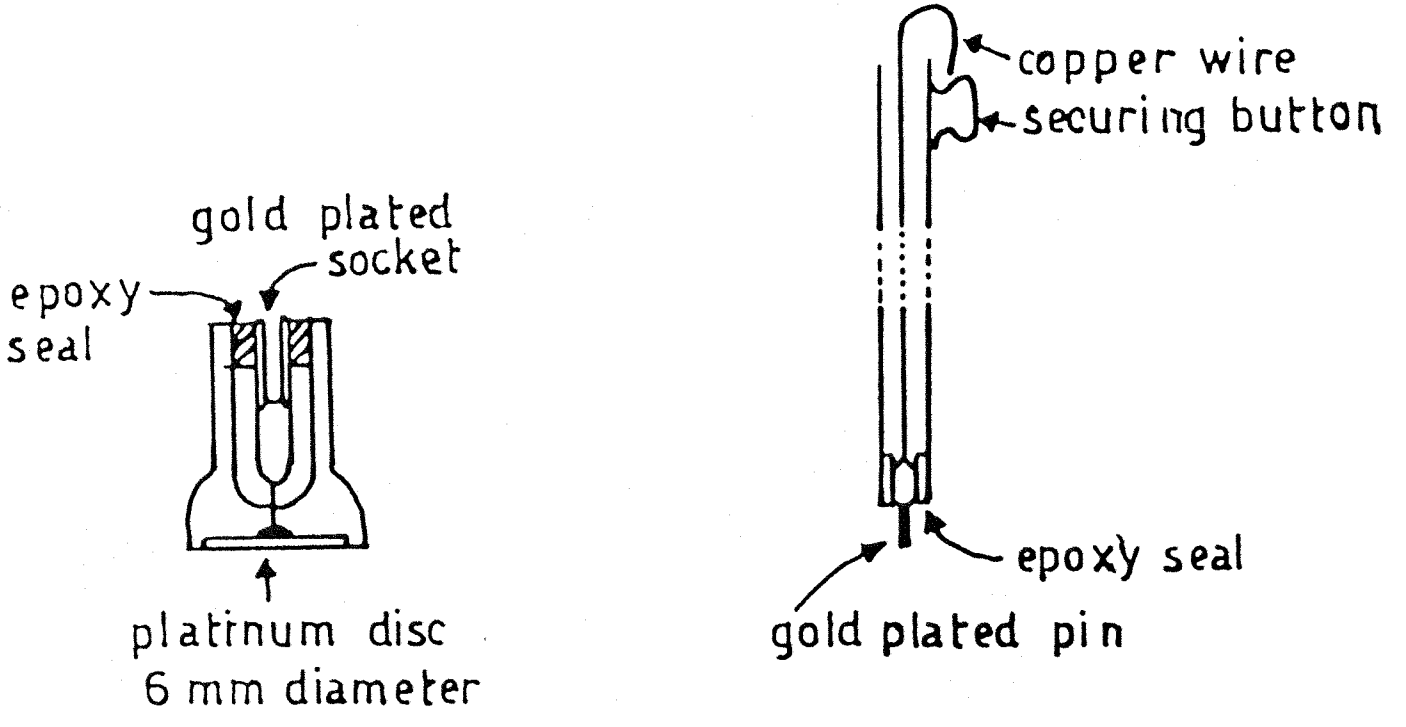
gold plated
socket
epoxy
seal
platinum disc
6 mm diameter
copper wire
securing button
epoxy seal
gold plated pin

Fig. 3.5

The button was of the correct dimensions for insertion in the vacuum chamber of the Cambridge Stereoscan electron microscope used, and a set of pin connectors was produced to facilitate the mounting of the button on the microscope platform.

When it was not necessary to have a detachable electrode tip, a one-piece electrode with a platinum disc of similar dimensions was used.

The discs used were polished on alumina powder of successively finer particle sizes , ending with 0.1 micron. A small amount of the powder was sprinkled on to a felt pad and moistened with distilled water. Then the pad was rotated mechanically under the stationary electrode which was supported in a clamp and pressed against the pad with a small adjustable pressure. The electrode was rotated to a few different angles during the polishing to offset any misalignment from the horizontal to the pad. Care was taken to avoid contamination of the surface from deposits left on the pad by previous polishing (the thin film semiconductor layers were removed by this apparatus after investigation).

All chemicals used were of AR grade, without further purification, unless indicated otherwise.

(3.2) OVERVIEW OF SYSTEM FOR AUTOMATIC MEASUREMENT OF PHOTOCURRENTS (AMP)

The purpose of the system is to provide the photocurrent conversion efficiency, as a function of the wavelength of the incident light, of a given test substance. A thin layer of the latter is made the working electrode in a conventional three-electrode cell arrangement, with the facility to illuminate the test substance by a

xenon or tungsten lamp, via a grating monochromator and an optical chopper (fig 3.6). The chopper provides the reference which is used in the phase sensitive detection of that small part of the total cell current due to the illumination.

Prior to the its automation, the experimental system used by the research group could only display the photocurrent as a function of wavelength on a simple X-Y recorder. It was therefore necessary to construct the conversion efficiency spectrum using point by point calculation from the test substance spectrum and a photodiode calibration spectrum. This manual method was tedious, wasteful of time, prone to errors of calculation, and of low resolution.

The new system developed for this project, and subsequently used extensively by other researchers in the group, is controlled by a BBC microcomputer via a custom-built interface, which controls the monochromator stepper motor, and scales the outputs from the psd and the photodiode prior to feeding them to the BBC micro's analogue to digital converter.

The reference photodiode and test spectra are held in memory blocks, and can be combined, together with the necessary correction factors, to give the photocurrent conversion efficiency spectrum. The correction factors include the calibration data for the secondary reference photodiode's own conversion efficiency spectrum, and also rescaling factors necessitated by amplifier range changes made by the operator during spectrum acquisition.

There is a wide range of facilities for data display and manipulation. Initially, the uncorrected spectrum is displayed on the monitor screen, usually as it is measured, although this may be delayed until after completion of data acquisition. Consecutive spectra of similar type may be displayed on the screen together. The

Fig. 3.6

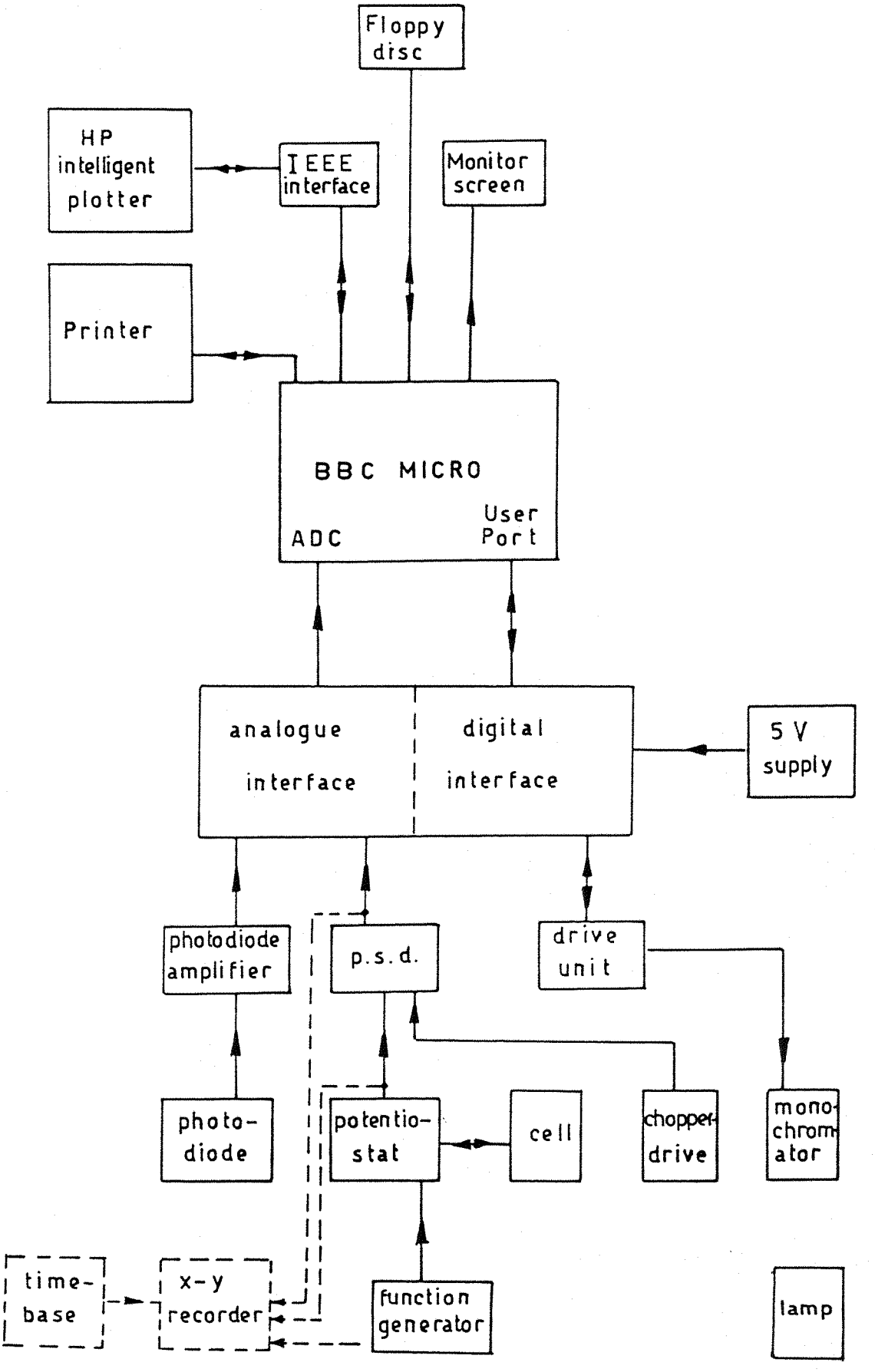
Floppy disc
HP intelligent plotter
IEEE interface
Monitor screen
Printer
BBC MICRO
User Port
ADC
analogue interface
digital interface
5 V supply
photodiode amplifier
p.s.d.
drive unit
photo-diode
potentio-stat
cell
chopper-drive
mono-chrom-ator
time-base
x-y recorder
function generator
lamp

spectrum can be edited point by point on the screen. The logarithm of the photocurrent conversion efficiency may also be displayed as a function of photon energy if required. Hard copy of any of these spectra is available as tabular printout and/or from an intelligent plotter via an IEEE interface.

All photodiode calibration spectra and test spectra may be saved as files on floppy discs, so that they can be recalled at a later date, either for display as above, or for averaging prior to display. A planned selection of spectra can thus be plotted on a single sheet of paper, with automatic plot symbol variation.

Two versions of the software allow different wavelength ranges to be covered.

(3.3) AMP SYSTEM HARDWARE

One of the light sources used was a 150 watt high pressure Xenon lamp driven by a constant current power supply, both manufactured by Applied Photophysics Ltd. The supply (model 406/01) generated a high voltage starting pulse, whose value was regulated by adjustable arc contacts. The arcs produced in the supply and the lamp were partially suppressed electrically by their metal housings, but sufficient high frequency radiation escaped to endanger nearby unprotected amplifier inputs, such as those of the potentiostat. As a precaution, these inputs were disconnected during lamp start-up.

The second light source was a tungsten lamp in a custom built housing (fig 3.7). This was needed to investigate wavelengths above 700nm. The lamp was designed to use a projector bulb mounted at the focus of a concave mirror, and supported in a blackened housing fitted with a light-tight ventilation duct at the top, and an iris diaphragm over a side exit. The lamp holder was fixed to a

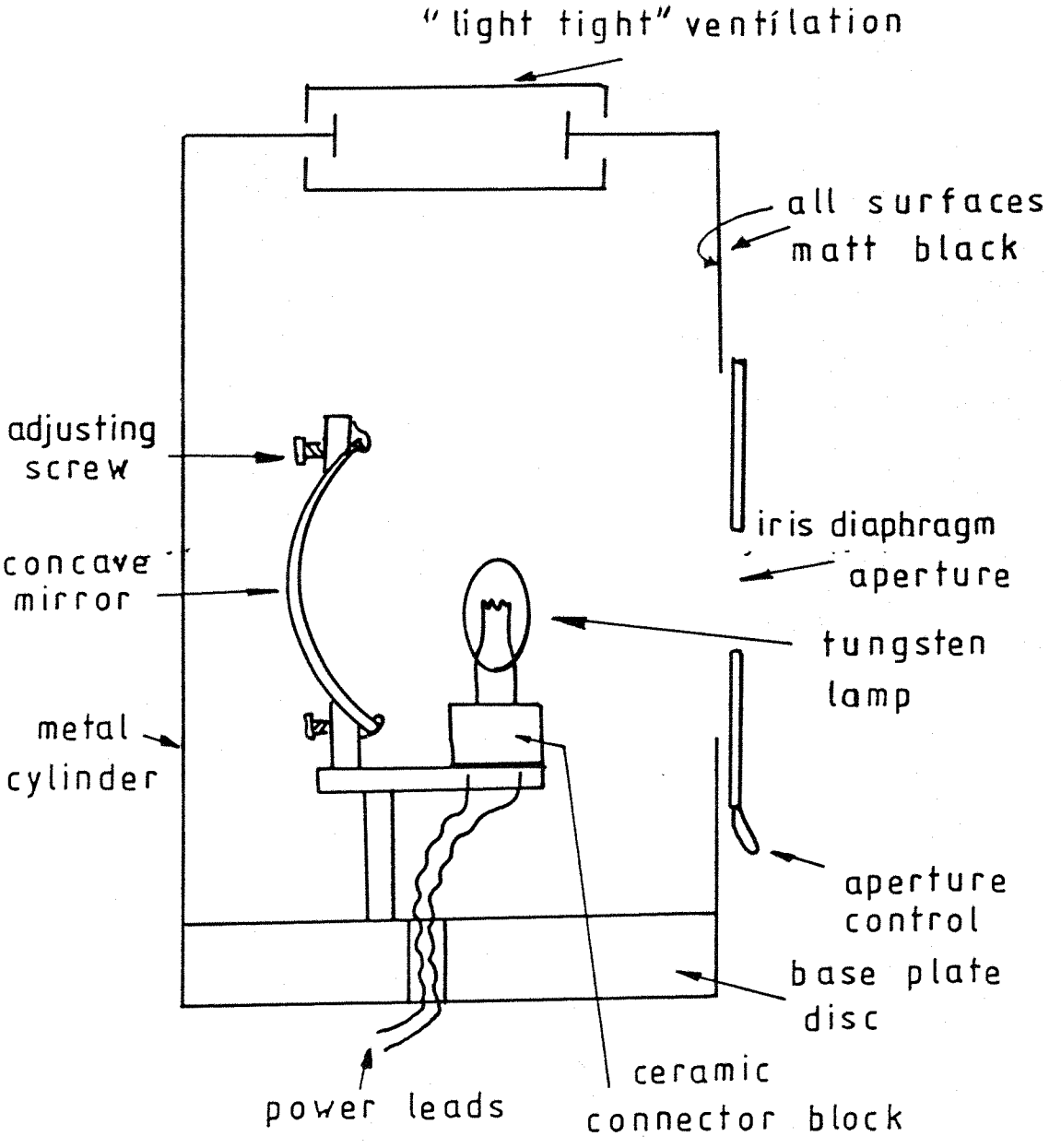

Fig 3.7 Tungsten Lamp

thick aluminium base plate fitted with support rods allowing accurate and stable positioning on the optical axis. The lamp was driven by a high current d.c. supply (also designed and constructed for the purpose by the author). The tungsten lamp intensity was about 50% lower at 500nm than that of the xenon lamp but it was found that the psd system was capable of producing smooth, accurate photocurrent outputs nevertheless, provided that the psd time constant was increased slightly, and the system allowed to settle for a sufficiently long time between readings.

The xenon lamp power spectrum was obtained at 1 nm intervals and at various exit slit width settings of the monochromator (fig 3.8) to check its operation. The latter is an Applied Photophysics model with a diffraction grating blazed at 300 nm. This ensures that the power transmission of the monochromator reaches a maximum in this region, to compensate for the reduced output power of the lamp in the ultra violet.

The shape of the power spectrum reaching the test electrode depends on the lamp spectrum, the monochromator power transmission characteristic, the reflection losses due to the mirror and lenses used, and the losses due to the cell walls and the electrolyte. The first three of these are compensated for by calibrating the system with a photodiode substituted for the cell. The fourth factor can be assumed to be negligible when using effectively clear solutions such as 0.1M sodium sulphide.

An exit slit width of 2.5 mm. was chosen for most of the experiments, since this was judged to be the best compromise in the trade off between high resolution (favoured by small slit widths) and high power throughput (favoured by large slit widths). The relatively flat power transmission spectrum at the chosen slit width

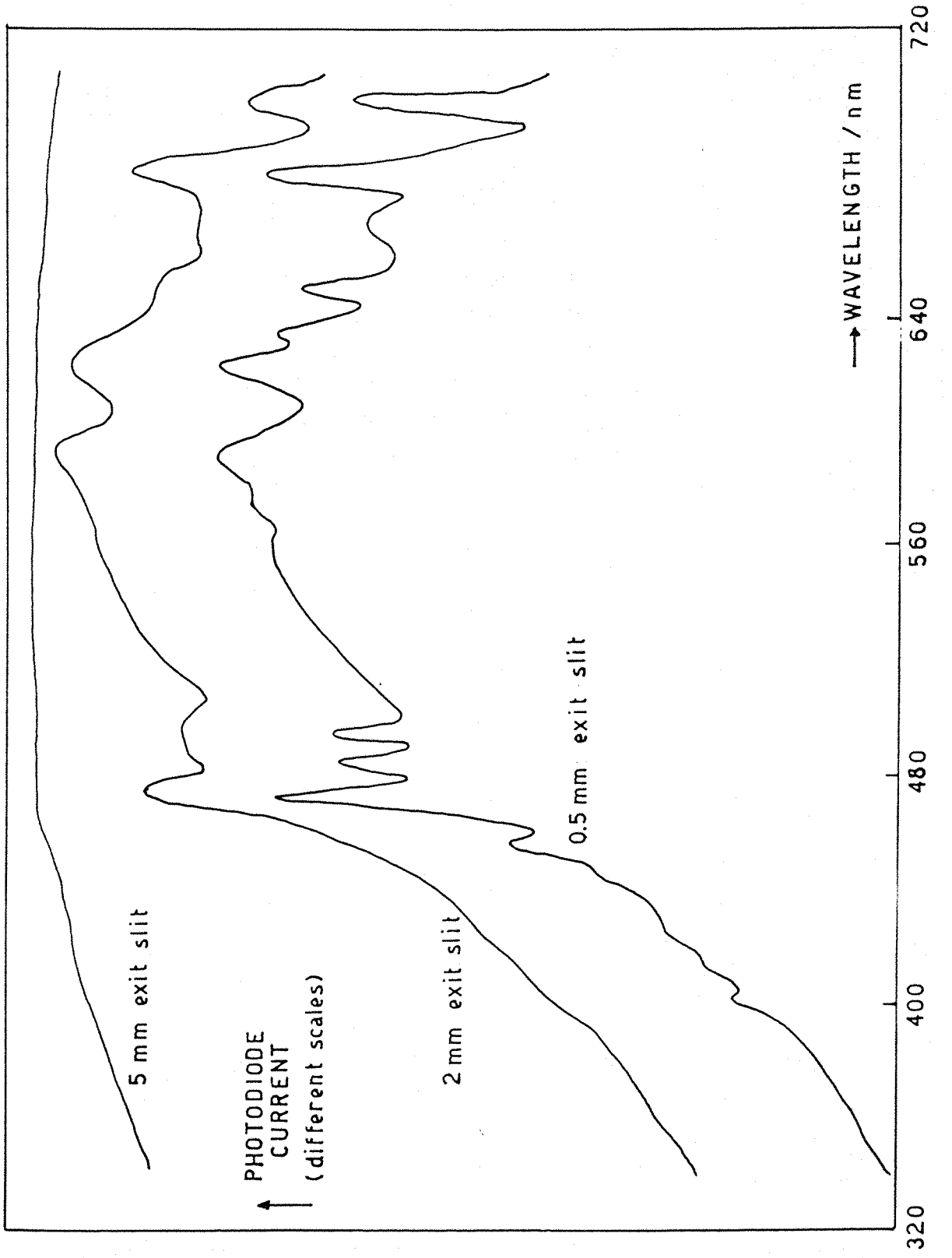
5 mm exit slit
2 mm exit slit
0.5 mm exit slit
PHOTODIODE CURRENT (different scales)
320
400
480
560
640
720
WAVELENGTH / nm

Fig.3.8

reduces difficulties resulting from inexact initial setting of the monochromator wavelength.

Due to the differing angular dispersions of the different orders in grating spectra, a first order primary maximum will overlap with a secondary maximum, produced by a lower wavelength entering the monochromator, in the second order. The unwanted light due to lower wavelengths from the lamp was therefore prevented from entering the monochromator (and hence the cell) by inserting an optical filter with a wavelength cut-off beyond which the filter was opaque. Provided that the filter was inserted at the same wavelength in every test and calibration spectrum, the intensity reduction of the desired wavelengths by the filter could be assumed to be compensated.

The monochromator was calibrated by a 5mW laser at 632.8nm using various exit slit widths (fig 3.9). Neutral density filters were used to reduce the beam intensity at the entrance slit, and the beam at the exit slit was detected by the normal photodiode and BBC micro automated system. However, the controlling program was modified slightly to display the relative intensity at the exit slit as a function of wavelength at 0.1nm intervals. This experiment showed that the the monochromator dial was within 1nm of the correct wavelength in this region.

To minimise the effects of mechanical backlash, the starting wavelength was always set by approaching from a lower value when adjusting the monochromator. The latter was driven by an Applied Photophysics stepping motor control unit, which could be operated either manually, or remotely via the BBC micro User Port.

The light beam was chopped by a Bentham optical chopper, whose rotation rate was set by the Bentham 218F control unit. The rotating disc had four sectors of equal area, alternately open and blocked,

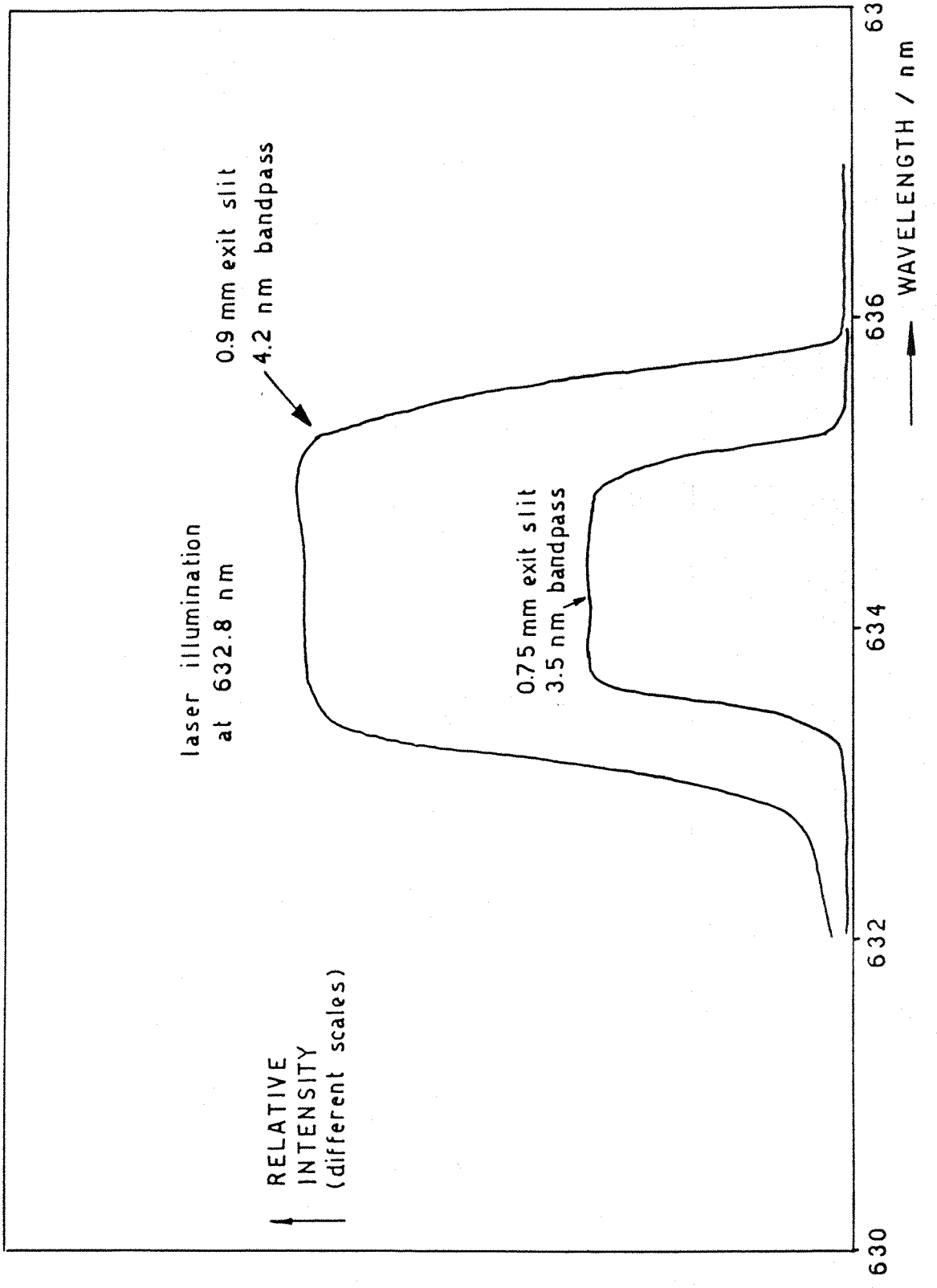
RELATIVE
INTENSITY
(different scales)
laser illumination
at 632.8 nm
0.9 mm exit slit
4.2 nm bandpass
0.75 mm exit slit
3.5 nm bandpass
630
632
634
636
638
WAVELENGTH / nm

Fig 3.9

with an effective transmission of 50% of the incident intensity. A reference output from the control box allowed phase locked detection of signals varying in phase with the chopper. Harmonics of mains frequency were avoided.

From the chopper, the light passed in to a metal dark box containing the cell, and via lenses and a mirror to focus the beam on the 6 mm diameter working electrode surface. Some ad hoc use of spherical aberrations in the lenses made it possible to produce an evenly illuminated spot of the right diameter. The mirror was front-silvered and the lenses were quartz.

Thin film electrodes which were to have their photocurrent properties examined were transferred to a specially designed cell (figs 3.10 and 3.11) containing aqueous 0.1M sodium sulphide.

The cell was the conventional three-electrode type, controlled by a low noise operational amplifier potentiostat; a variable gain current follower provided the cell current as a proportional output voltage. The potentiostat was programmed from a Hitek PPR1 function generator, which could provide pulses or ramps for e.g. cyclic voltammetry.

When a display was required of the total cell current versus the working electrode potential, a connection was made from the current follower output to the Y-axis of the Gould Advance X-Y recorder, with the X-axis driven in parallel with the potentiostat input program. By using a very slow chopper frequency (about 1 Hz) it was possible to show the photocurrent effects superimposed on the total cell current.

If the photocurrent alone was to be investigated, the total cell current was passed to an Ortec Brookdeal phase sensitive detection system, comprising a model 9542 precision a/c amplifier (to

Fig. 3.10

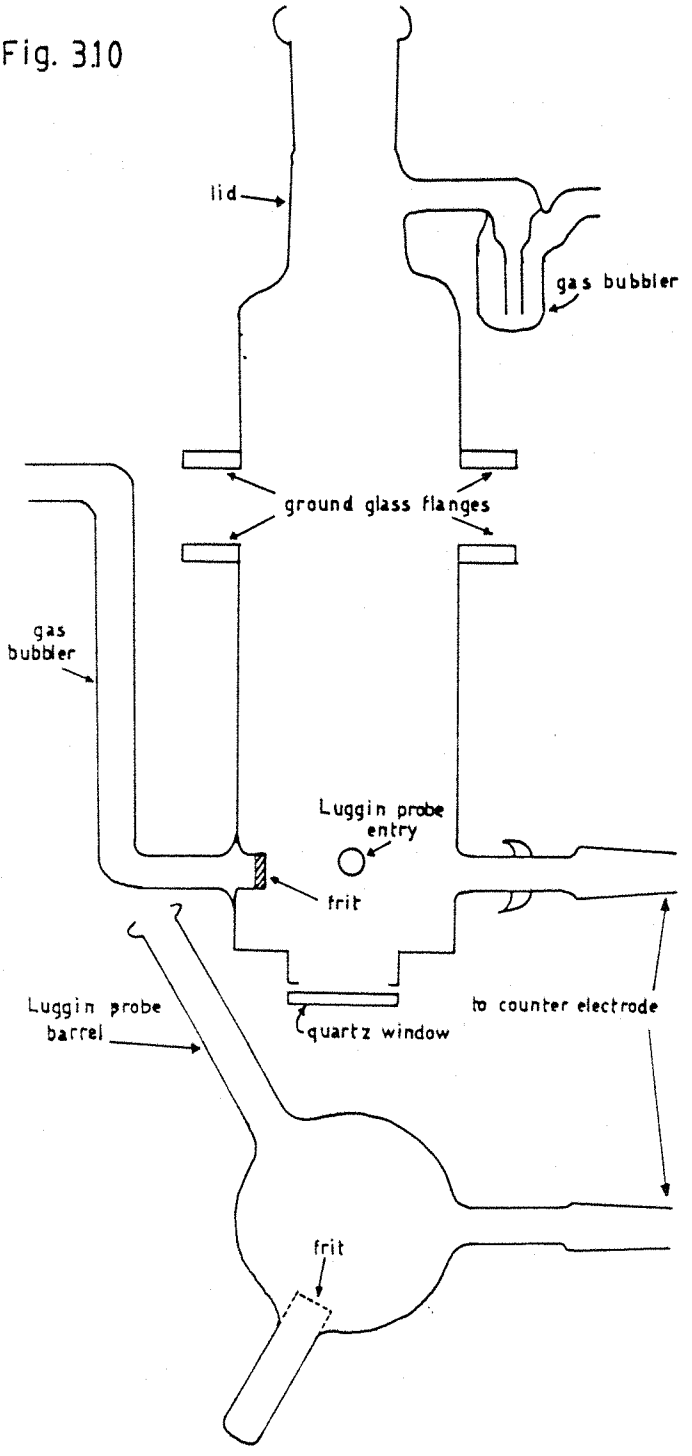
lid
gas bubbler
ground glass flanges
gas bubbler
Luggin probe entry
frit
Luggin probe barrel
quartz window
to counter electrode
frit

Fig. 3.11

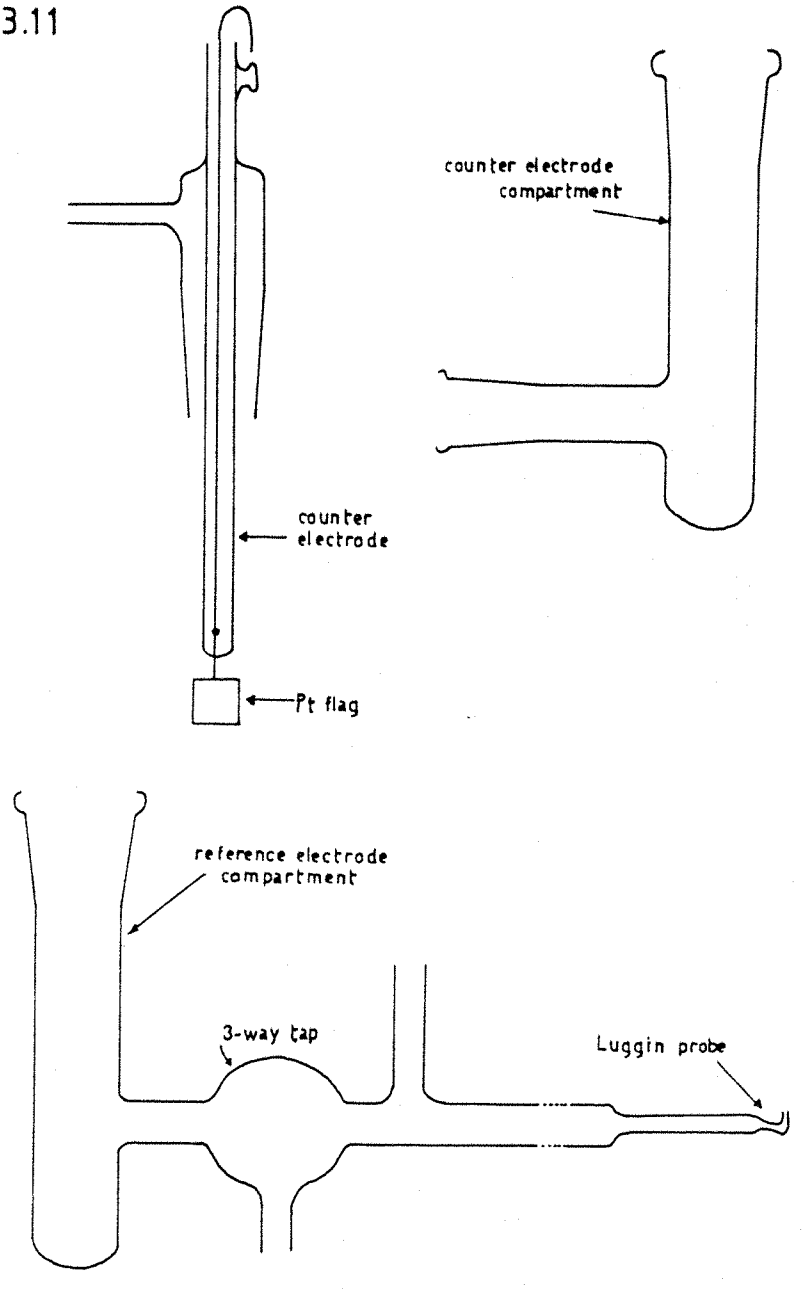
counter electrode
compartment
counter
electrode
Pt flag
reference electrode
compartment
3-way tap
Luggin probe

act as a signal preamplifier and conditioner), a model 9422 reference unit (to lock in to the chopper frequency), and a model 9412A psd (to detect the in-phase component of the total cell current). The preamplifier gain was used to set the necessary input level to the psd, rather than using a high gain in the current follower module, which because of its relatively unsophisticated circuitry would be more inclined to introduce distortion.

Before computer automation, the psd output signal was passed to the Y-axis of the X-Y recorder, enabling display of the photocurrent versus either the cell voltage or the wavelength of the incident light (driving the X-axis from a timebase module). In the latter case, it was necessary to manually synchronise the start of the ramp with the start of the monochromator drive motor.

After automation using the BBC micro, the psd output voltage was fed to a differential amplifier in an analogue interface (fig 3.12) which was designed to scale the psd signal before feeding it to one of the four 12-bit analogue to digital converter channels of the microcomputer. These have a cycle time of ten milliseconds per channel. A differential input was used to minimise the possibilities of ground loop currents disturbing the input signal. The earths of the microcomputer and the rest of the apparatus were connected by only one route through the mains earth wires.

A second amplifier (with fractional gain) in the analogue interface conditioned the the signal from the photodiode preamplifier (used when calibrating the system) before passing it to a second ADC channel in the microcomputer. A single-ended input amplifier could be used for the photodiode channel because its preamplifier box was battery powered, and isolated from mains ground.

Both ADC channels were protected from incorrect input voltages

Fig. 3.12

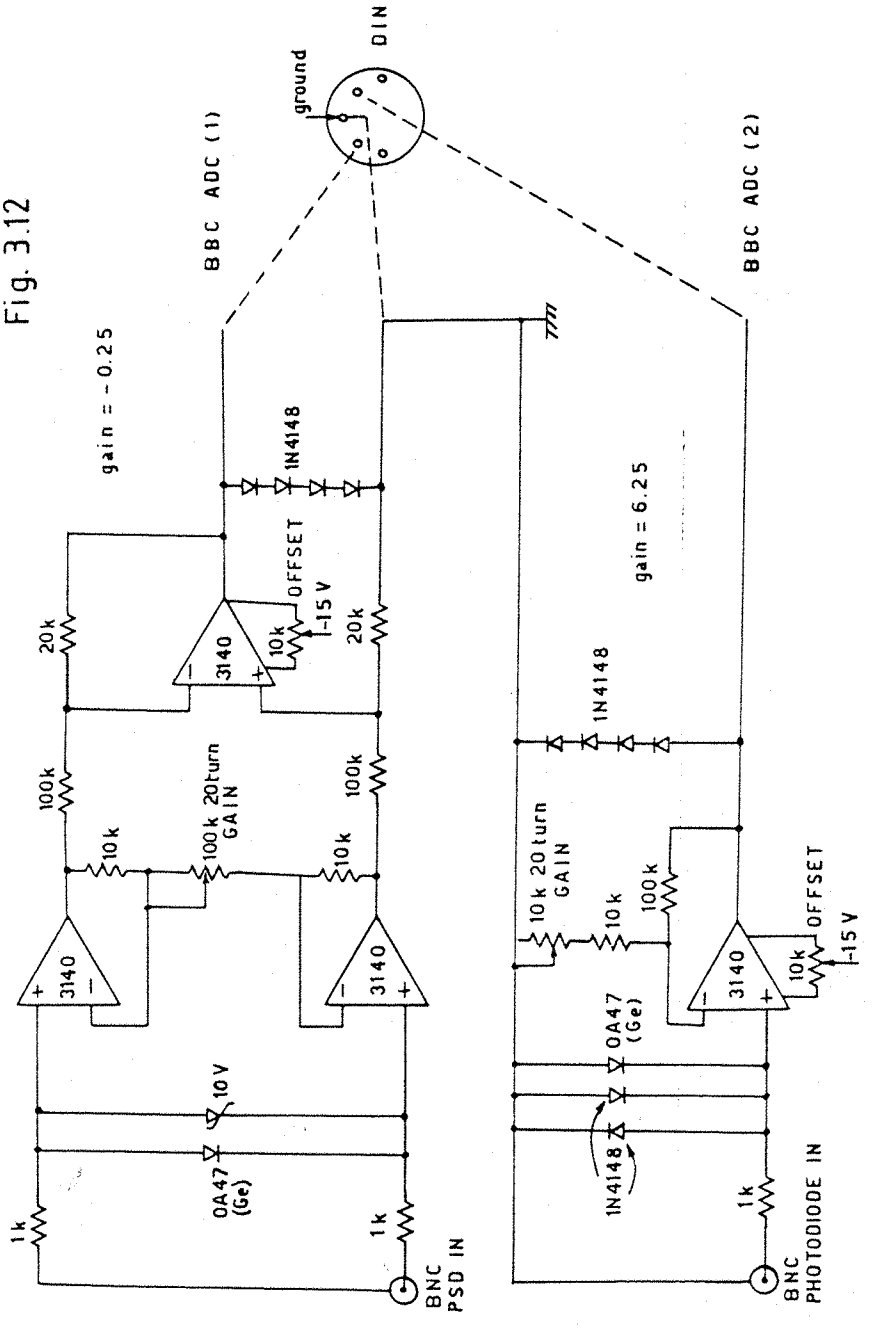
BBC ADC (1)
BBC ADC (2)
DIN
ground
gain = -0.25
gain = 6.25
1N4148
OFFSET
-15 V
20k
10k
3140
100k
100k 20turn GAIN
10 V
OA47 (Ge)
1k
BNC PSD IN
BNC PHOTODIODE IN
10k 20 turn GAIN

by diode shunt circuits in the interface.

A digital interface designed by the author (fig 3.13) allowed the microcomputer to send signals to, and receive signals from, the monochromator control box. The interface performed three basic functions. First, it set up a stable, predictable, initial condition when the equipment was switched on, which protected the microcomputer from transients, and held the wavelength stationary. Second, it converted the voltage levels in both directions between the microcomputer's 5V logic and the monochromator's 12V logic. Third, it isolated the microcomputer's ground line from that of the monochromator by use of opto-isolators.

All monochromator drive functions were individually addressed by the ten 6522 VIA (versatile interface adaptor) signal lines available at the User Port of the computer. The two User Port control lines were wired to establish a handshake control loop with the monochromator drive stepper motor. For future developments, one bit of the VIA was set up to count the stepper motor pulses.

The microcomputer was a BBC model B with a specified 32K of RAM. After the machine, disc, and IEEE operating systems have taken their share of this, the actual user memory runs from hex locations 1B00 to 7C00 in mode 7 or to 5800 in mode 4, i.e. the maximum program lengths are about 24K in mode 7 and 16K in mode 4. In fact, the AMP program suite has been written to avoid this limitation by loading sub-programs in to the screen workspace from floppy disc under control of the main program, in between the graphics displays generated.

The microcomputer controlled a Microvitec Cub VDU, an NEC printer with buffer memory, and a disc drive, through its dedicated interface busses. The 1MHz bus was connected to a Procyon

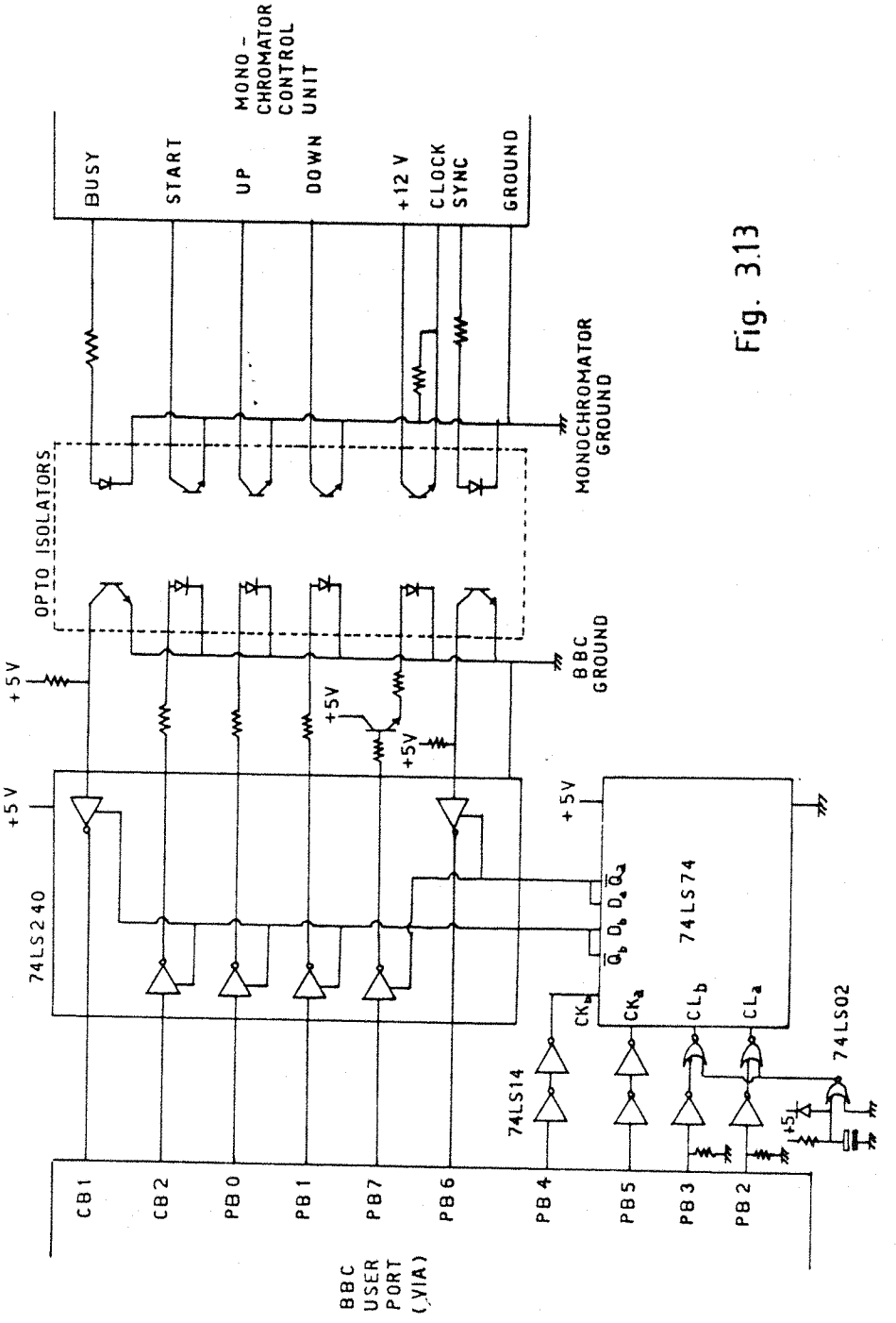
MONO-
CHROMATOR
CONTROL
UNIT
BUSY
START
UP
DOWN
+12 V
CLOCK
SYNC
GROUND
MONOCHROMATOR
GROUND
OPTO ISOLATORS
BBC
GROUND
+5V
74LS240
74LS74
74LS14
74LS02
BBC
USER
PORT
(VIA)
CB1
CB2
PB0
PB1
PB7
PB6
PB4
PB5
PB3
PB2

Fig. 3.13

IEEE interface controller, which can interface up to 30 devices to the computer using standard cables and commands. In the system used, a Hewlett-Packard intelligent X-Y plotter was controlled in this way.

(3.4) AMP SYSTEM SOFTWARE

Fig 3.14 is a memory map of the program specially written to control the system. The current photodiode calibration and psd test spectra are stored in two segments of six pages of 256 bytes per page. At the top of the permanently available user RAM is an assembled version ASS1 of an assembly code program which is used in a fast sampling routine, which transforms voltages at the analogue to digital converter inputs to numbers in the memory.

When disc procedures are requested by the user, either to store current spectra, or to recall previous results for data manipulation, then a program discop4 is loaded in to graphics workspace, and uses a further six pages there for temporary storage of the working spectrum. The latter can be transferred to the appropriate section of permanent memory, after compiling a running average with other spectra on disc if required, before handing back control to the main program which overwrites this area of memory. Parameters are passed automatically between the program overlays by storing them in the system integer variables and in free zero page locations, neither of which are overwritten by the movement of programs in and out of the normal work space.

Error trapping routines are incorporated which prevent program crashes due to incorrect operator input, and return the user to a suitable reentry point.

A listing of the program version which operates in the wavelength region 340 to 720nm is included in Appendix 1.

Fig. 3.14

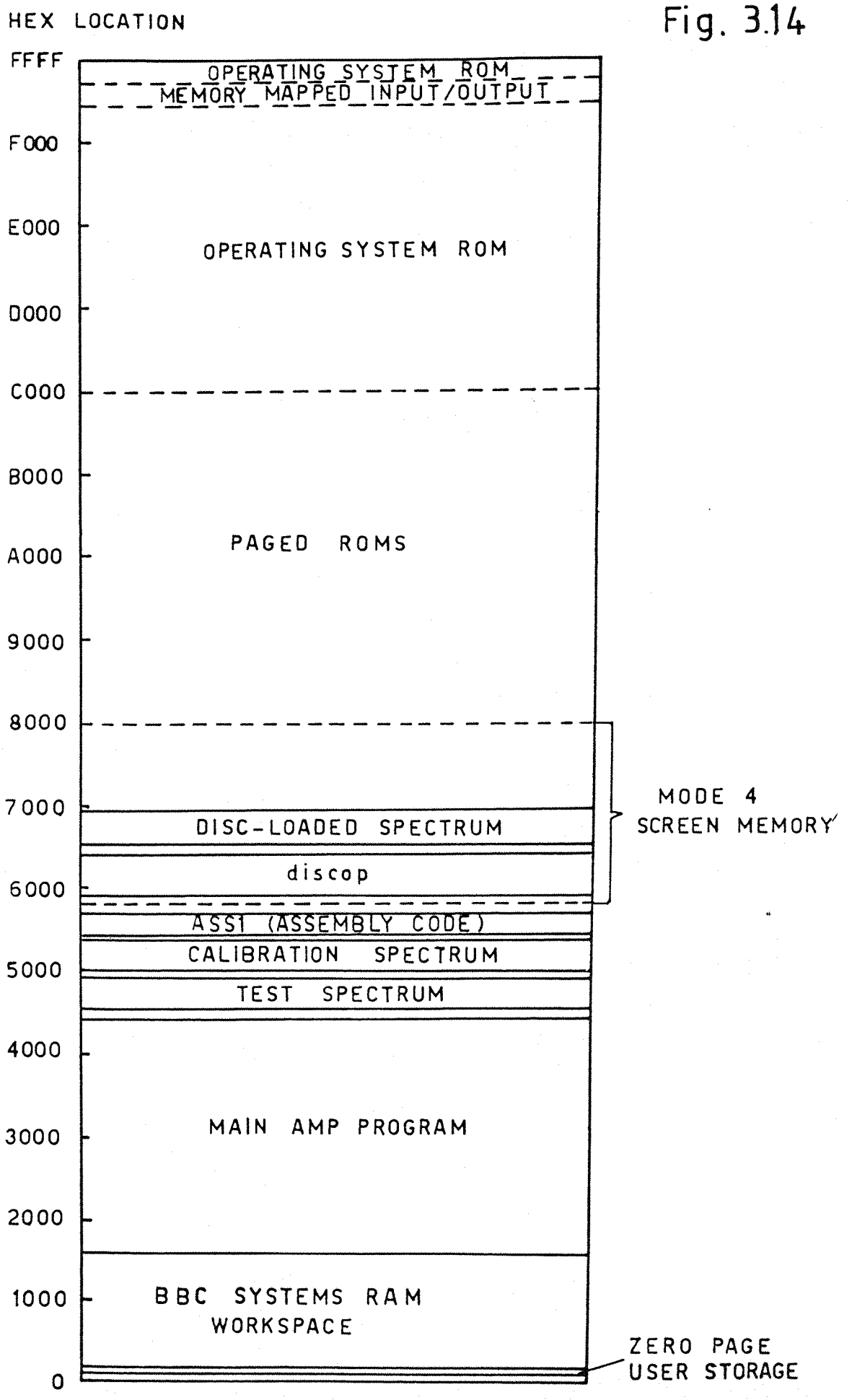
HEX LOCATION
FFFF
OPERATING SYSTEM ROM
MEMORY MAPPED INPUT/OUTPUT
F000
E000
OPERATING SYSTEM ROM
D000
C000
B000
PAGED ROMS
A000
9000
8000
7000
DISC-LOADED SPECTRUM
discop
6000
ASS1 (ASSEMBLY CODE)
CALIBRATION SPECTRUM
5000
TEST SPECTRUM
4000
MAIN AMP PROGRAM
3000
2000
1000
BBC SYSTEMS RAM
WORKSPACE
0
MODE 4
SCREEN MEMORY
ZERO PAGE
USER STORAGE

CHAPTER 4

INVESTIGATION OF ELECTROCHEMICALLY DEPOSITED CADMIUM SULPHIDE

(4.1) PRELIMINARY ATTEMPT TO PREPARE ELECTRODEPOSITED CADMIUM

Since it was considered possible that the direct deposition of cadmium sulphide on to a platinum electrode might not produce a proper mechanical or electrical (ohmic) contact, an attempt was made to plate the platinum with metallic cadmium first, before covering this with electrodeposited sulphide.

Many plating baths for the deposition of Cd have been investigated, all more or less empirically developed, to produce the best quality layers. Those based on cyanides and fluoroborates have obvious safety problems, and were not investigated in this project.

The plating solution chosen for a brief investigation over a range of temperatures and current densities was:

Material	g/250ml
$3CdSO_4.8H_2O$	16
$(NH_4)_2SO_4$	8.25
$Al_2(SO_4)_3.18H_2O$	7
Gelatine	0.125
Nickel sulphate	0.025
Ethanolamine	0.25
pH 3 to 5	

Also, three brighteners were tried:

Brightener A

1 vol% HNO_3

	g/250ml
Brightener B	
CrO_3	25
H_2SO_4(conc)	0.5

	g/250ml
Brightener C	
30% H_2O_2	7.5
H_2SO_4(conc)	1.25

Whilst some current densities tried were obviously too high, producing rough, dark, dendritic Cd layers on the platinum flag substrate, lower values, around 1 mA per sq cm, gave fairly smooth and adherent, rather dull grey films, However, even the best of these were found to have small cracks over much of the surface when viewed through an optical microscope, some apparently reaching through to the Pt substrate.

All of the brighteners were tried out on the best of the films. Whilst it was apparent that they were indeed improving the surface smoothness a little, it was also clear that areas of the Cd deposit were being raised from the substrate, perhaps due to poor adherence of the films in the first place.

The decision was made to proceed with the planned non-aqueous codeposition experiments, to produce CdS directly on the Pt, and to check the mechanical and electrical contact so produced.

(4.2) NON-AQUEOUS DEPOSITION EXPERIMENTS

A Hitek potentiostat was used with the galvanostat conversion module described in the previous chapter, set to the 1 kilohm position to give a constant output of 1 mA/V, to grow thin films of CdS in the high temperature deposition apparatus also described above. To display the growth transients on an X-Y recorder, the "overpotential" output of the galvanostat module was connected to the Y-axis, and the X-axis was fed from a ramp generator providing a simple timebase.

The cell contained 0.055M $CdCl_2$ solution in DMSO contacting a 1 atom % cadmium amalgam in the reference electrode compartment, and a 0.055M $CdCl_2$ + 0.1M S solution in DMSO in the working and counter electrode compartments.

Tetra-n-butyl ammonium perchlorate (TBAP) was prepared for use as a supporting electrolyte by the neutralisation of tetra-n-butyl ammonium hydroxide with perchloric acid. The product was washed with water to remove soluble perchlorate impurities such as the potentially explosive ammonium compound, and then recrystallised from ethyl acetate, and stored in a desiccator. The melting point was 210-211°C which agrees with the value quoted in the literature. The yield was 63-65%. However, it was decided that it would be interesting to see what results could be obtained without adding the perchlorate, and this was stored for future work.

Cadmium sulphide films of a number of thicknesses were deposited at various current densities under galvanostatic control on a platinum disc working electrode of 6mm diameter.

Some curves of overpotential against time, typical of those obtained, are shown in fig 4.1. The form of the curves can be analysed in to four segments.

Initially, there is a sharp rise in potential due to the

Fig. 4.1

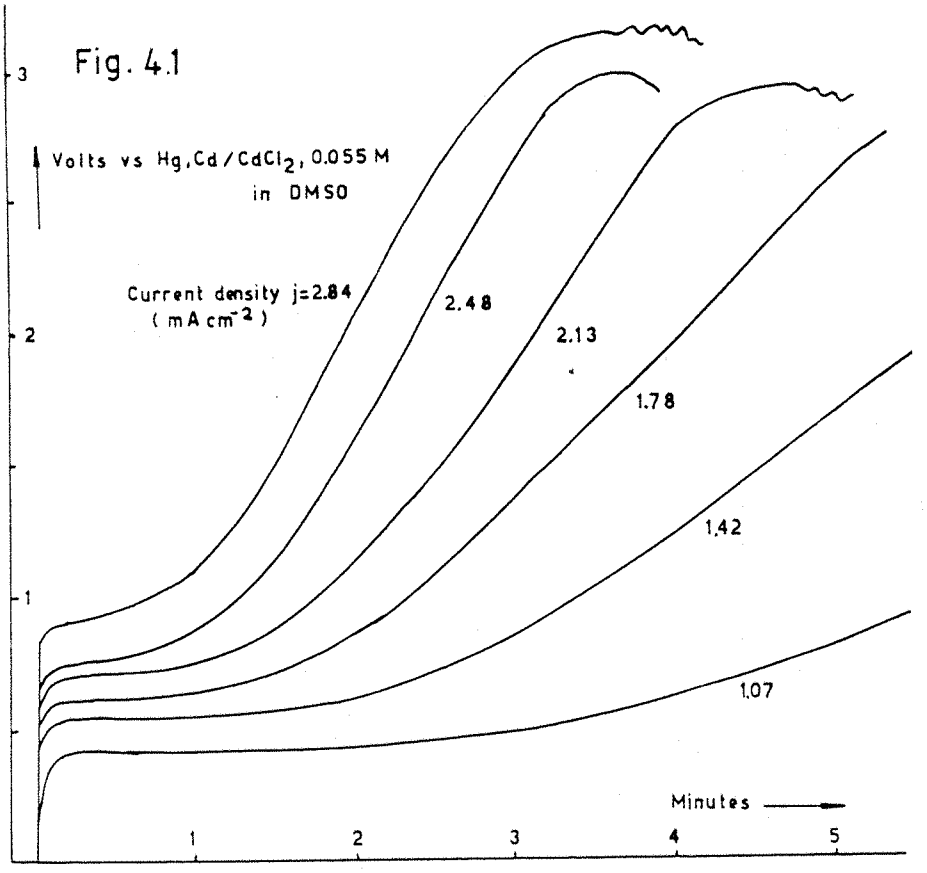
3
2
1
Volts vs Hg,Cd/CdCl2, 0.055 M
in DMSO
Current density j=2.84
(mA cm-2)
2.48
2.13
1.78
1.42
1.07
Minutes
1
2
3
4
5

Fig. 4.2

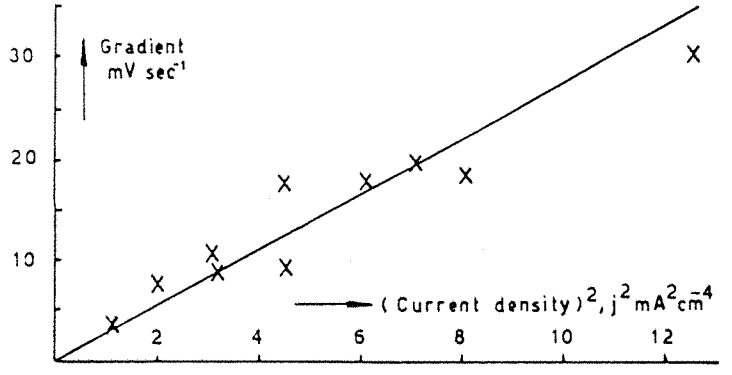
30
20
10
Gradient
mV sec-1
(Current density)2, j2 mA2 cm-4
2
4
6
8
10
12

charging of the double layer capacitance by a portion of the applied constant current. Under steady state conditions, a given potential difference at an electrified interface corresponds to a given structure of the interface, in terms of the excess charge densities in the various components of the double layer, and when current flows to or from the interface, the shift in charge densities causes a corresponding shift in potentials across the polarisable double layer.

As the structure of the double layer tends toward an equilibrium state, the proportion of the applied current which is taken up by charging the layer reduces towards zero, and a correspondingly greater proportion of the current is used in the charge-transfer reaction occurring at the surface.

This behaviour is reminiscent of the charging of an electrical capacitor and resistor in series, where the capacitor represents the double layer and the resistor represents the charge transfer reaction, although here the double layer capacitance is a function of the potential.

In practice, some of the initial charging current is also taken up by the adsorption of charged species at the surface, which contribute some pseudo-capacity in parallel with the double layer capacity.

The charge-transfer reaction(s) become dominant in the second phase of the transient, which is a relatively flat portion.

It is possible that a side-reaction competing with the electrodeposition process required is driven by the applied current in this phase, until perhaps some component for the reaction is depleted near the interface, allowing the CdS deposition to take over at higher potentials.

During CdS deposition, cadmium and sulphur ions are arriving

at the surface, and migrating across it to form and grow nuclei which eventually coalesce in successive layers of the compound.

It is likely that nuclei form and start to grow for the next layer before those for a given layer have extended fully across the surface; this, in the time scale of the observations (the layers are forming very rapidly), tends to even out the overpotential required for the growth, since the higher driving forces needed in sites where nucleation is occuring are compensated by the lower ones needed for the extension laterally of the growth centres. Therefore, an alternative explanation for the flat galvanostatic transient during this phase of deposition is that during this phase, film growth occurs with a near constant driving potential. This corresponds to a model for the growth in which species codepositing from solution can, for some time, find a constant electrical environment at the interface.

The third segment is a straight line of some positive slope, reflecting uniform increase with time of the potential necessary to maintain the same current flow across the interface. The deposit at this stage has exceeded a critical thickness, and the discharge of species from solution now involves a greater overpotential to drive the electron transport between the substrate and the depositing species, through the resistive semiconductor layer. which is steadily increasing in thickness (and hence resistance). The gradient of the segment increases as the galvanostatic current is increased, as one would expect if the growing deposit were acting as an ohmic resistance.

Finally, in the fourth segment, the film insulation breaks dowm at a critical value of the voltage across it, seen as an irregular horizontal trace in the overpotential curves, and as dark

scars in the yellow CdS on the electrode itself.

Assuming a current efficiency of 100% for the reaction

$$Cd^{++} + S \xrightarrow{2e^-} CdS$$

the film thickness d is given by:

$$d = j.M.t \;/\; n.F.\rho \qquad (4.1)$$

where j is the current density, M is the molecular weight (CdS=144.5), t is the time of deposition current flow, n is the number of electrons transferred in the reaction (2 here), F is the Faraday constant, and ρ is the density of the deposit
(CdS= 4.82 g/cm^{-3})

The resistance, R, of the film is given by:

$$R = K.d \;/\; A \qquad (4.2)$$

where K is the resistivity of the film and A is its area of cross section. Hence

$$R = K.j.M.t \;/\; A.n.F.\rho \qquad (4.3)$$

Using Ohm's Law to relate R to the voltage V across the film at time t:

$$dV/dt = j.A.\, dR/dt = K.M.\, j^2 \;/\; n.F.\rho \qquad (4.4)$$

Hence a plot of dV/dt versus j^2 should be a straight line of slope:

$$K.M / n.F.\rho \qquad (4.5)$$

passing through the origin, if the film grows under Ohmic control.

Fig 4.2 is such a plot using data from fig 4.1 and similar experiments.

The slope of the line shown is 2.8 mV $S^{-1}mA^{-2}cm^4$ which gives a value for K of about 1.8×10^7 ohm.cm.

Since $K = N.e.u$ where N is the carrier density, e is the electronic charge, and u is the carrier mobility, then, assigning a typical value of 1 cm $V^{-1}S^{-1}$ to u, N turns out to be about 6×10^{11} per cc. This is typical of an insulating film, which may be the result of compensation in the semiconductor, or due to a high density of electron traps. In the latter case, the effective mobility u (eff) would be given by:

$$u\ (eff) = u.\Theta \qquad (4.6)$$

where Θ is the fraction of the electrons which are free in the conduction band, and which may be as low as 10^{-3}.

Below the film breakdown limit, the galvanostatic deposition method produced excellent films of high brightness and even texture seen under an optical microscope. This was in spite of the radially symmetrical interference pattern seen on films less than half a micron thick. Several films were examined and photographed using a Cambridge Stereoscan 150 electron microscope (fig 4.3). This instrument is ideal for surface grain structure investigations, since it has a great depth of field as well as a useful magnification up to

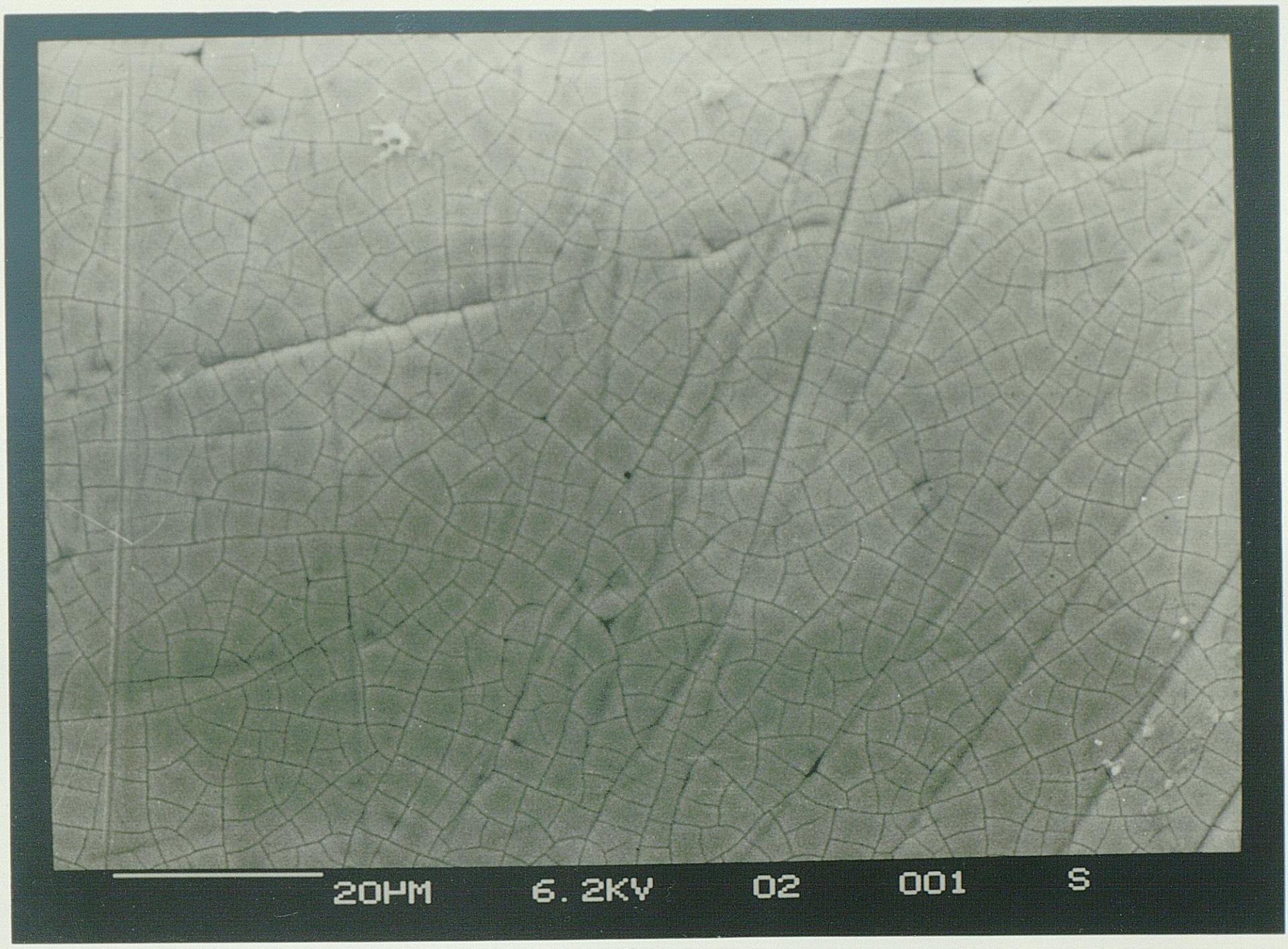

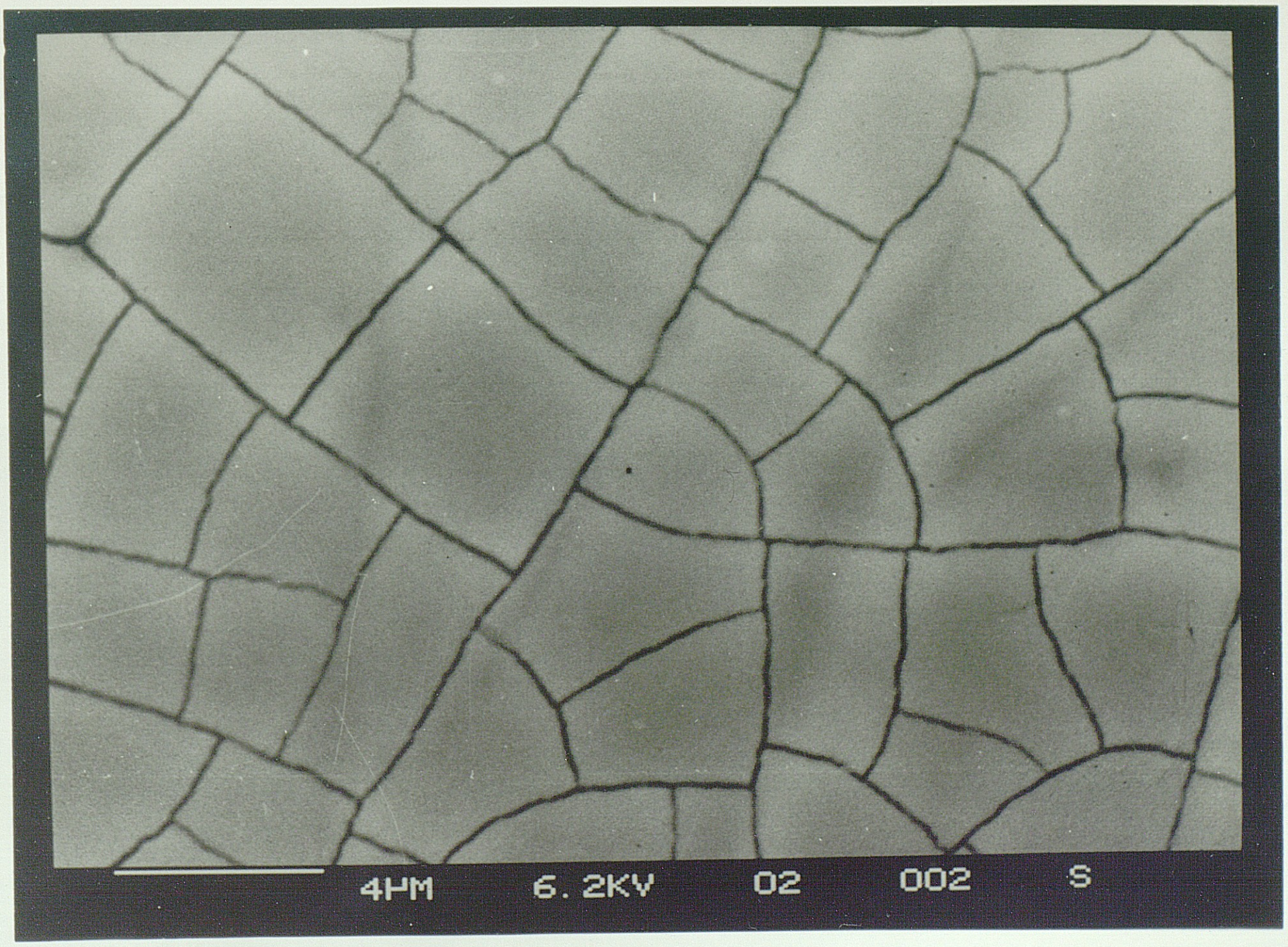

Fig 4.3 Electron micrographs of 1 micron layer of CdS on Pt

50 000 times. It was thus confirmed that the grains were evenly sized and not cracked through to the substrate.

It was decided that a cathodic deposition current of 0.5 mA (current density 1.78 mA cm^{-2}) produced the best films on the basis of their appearance, so this current was used to grow a large number of films of various thicknesses in the range 0.05 to 2 microns, at various DMSO temperatures in the range 80 to 180°C. Some films were, however, grown at 0.75 and 1.0 mA (2.67 and 3.55 mA cm^{-2}) for comparison.

(4.3) CHARACTERISATION OF THE CdS THIN FILMS

The thin CdS films were tested for their photocurrent response as a function of wavelength and potential, initially using the manual calculation method, and later automatically using the AMP computer-controlled system.

The films were immersed in 0.1 M sodium sulphide, in the measuring cell, and potentiostatted at 0.0 V versus a saturated calomel electrode. It was established (referring forward briefly to fig 4.14) that this potential was in the saturation photocurrent range for the films.

A number of experiments to determine the photcurrent response as a function of wavelength are summarised in figs 4.4 to 4.11. Each figure shows results for films of CdS of a given thickness, grown under various conditions of temperature and deposition current density as detailed in Table 4.1.

The thin films for which the highest quantum efficiencies were obtained have spectra of the general form shown in fig 4.12 as curve (3), which is the result obtained for a 0.1 micron film deposited from DMSO at 140 °C. The figure also shows two 'ideal'

TABLE 4.1

Film Number	Thickness/ micron	Temperature/ °C	Current/ mA
(1)	0.1	164	0.5
(2)	0.1	137	0.5
(3)	0.1	102	0.5
(4)	0.1	139	1.0
(5)	0.1	114	0.75
(6)	0.1	116	1.0
(7)	0.2	168	0.5
(8)	0.2	143	1.0
(9)	0.2	136	0.5
(10)	0.2	125	1.0
(11)	0.2	108	0.5
(13)	0.3	133	0.5
(14)	0.3	110	0.5
(15)	0.3	105	0.5
(16)	0.4	170	0.5
(17)	0.4	136	1.0
(18)	0.4	133	0.5
(19)	0.4	122	1.0
(20)	0.4	109	0.5
(21)	0.4	104	0.5
(22)	0.6	170	0.5
(23)	0.6	135	1.0
(24)	0.6	136	0.5
(25)	0.6	125	1.0
(26)	0.6	102	0.5

TABLE 4.1 (continued)

Film Number	Thickness/ micron	Temperature °C	Current/ mA
(27)	0.8	170	0.5
(28)	0.8	139	1.0
(29)	0.8	134	0.5
(30)	0.8	120	1.0
(31)	0.8	105	0.5
(32)	1.0	170	0.5
(33)	1.0	142	1.0
(34)	1.0	133	0.5
(35)	1.0	128	1.0
(36)	1.0	107	0.5
(37)	1.0	140	1.0
(38)	1.0	117	0.75
(39)	1.5	169	0.5
(40)	1.5	139	1.0
(41)	1.5	114	0.75

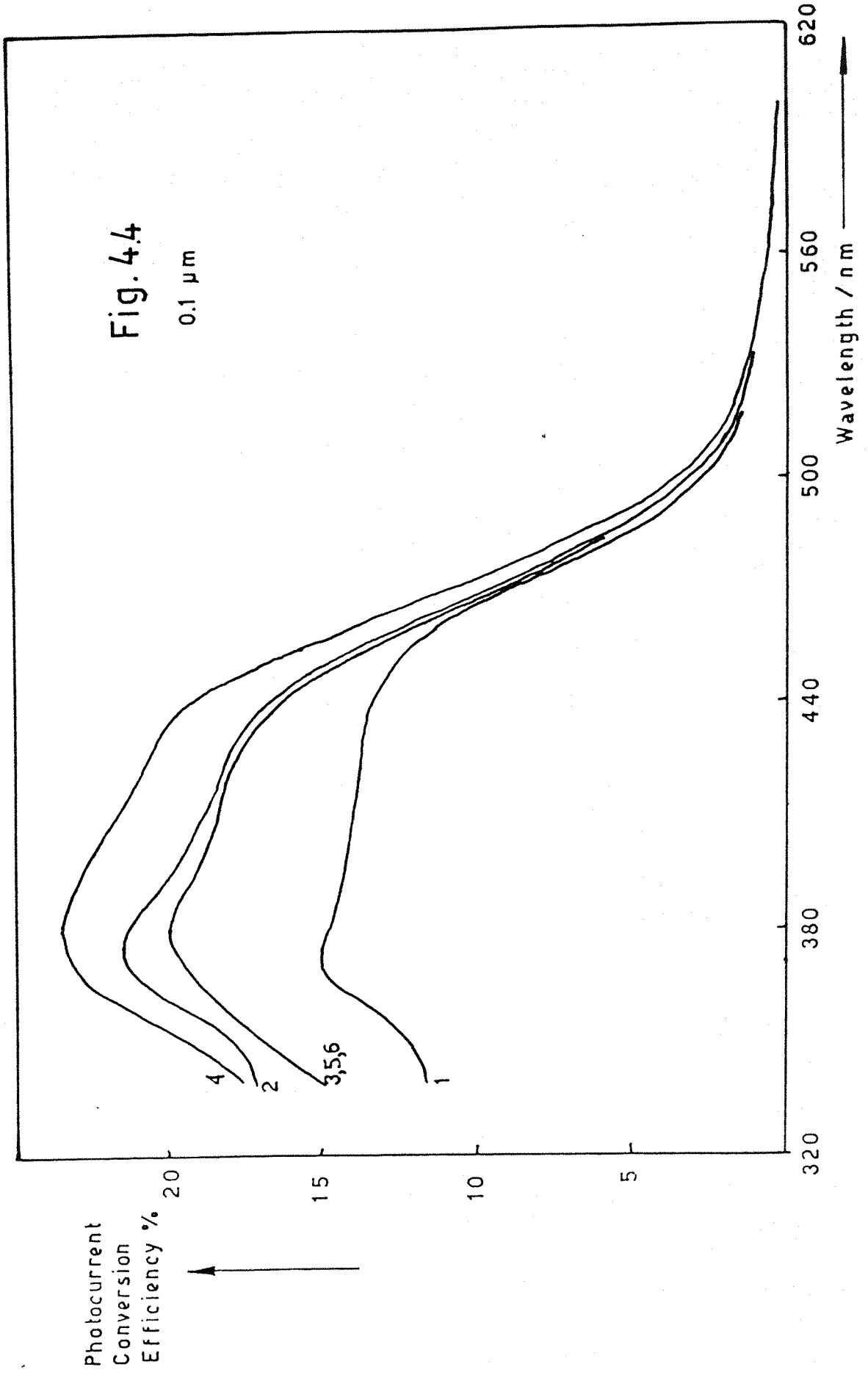
Fig. 4.4
0.1 µm
Photocurrent Conversion Efficiency %
20
15
10
5
320
380
440
500
560
620
Wavelength / nm
4
2
3,5,6
1

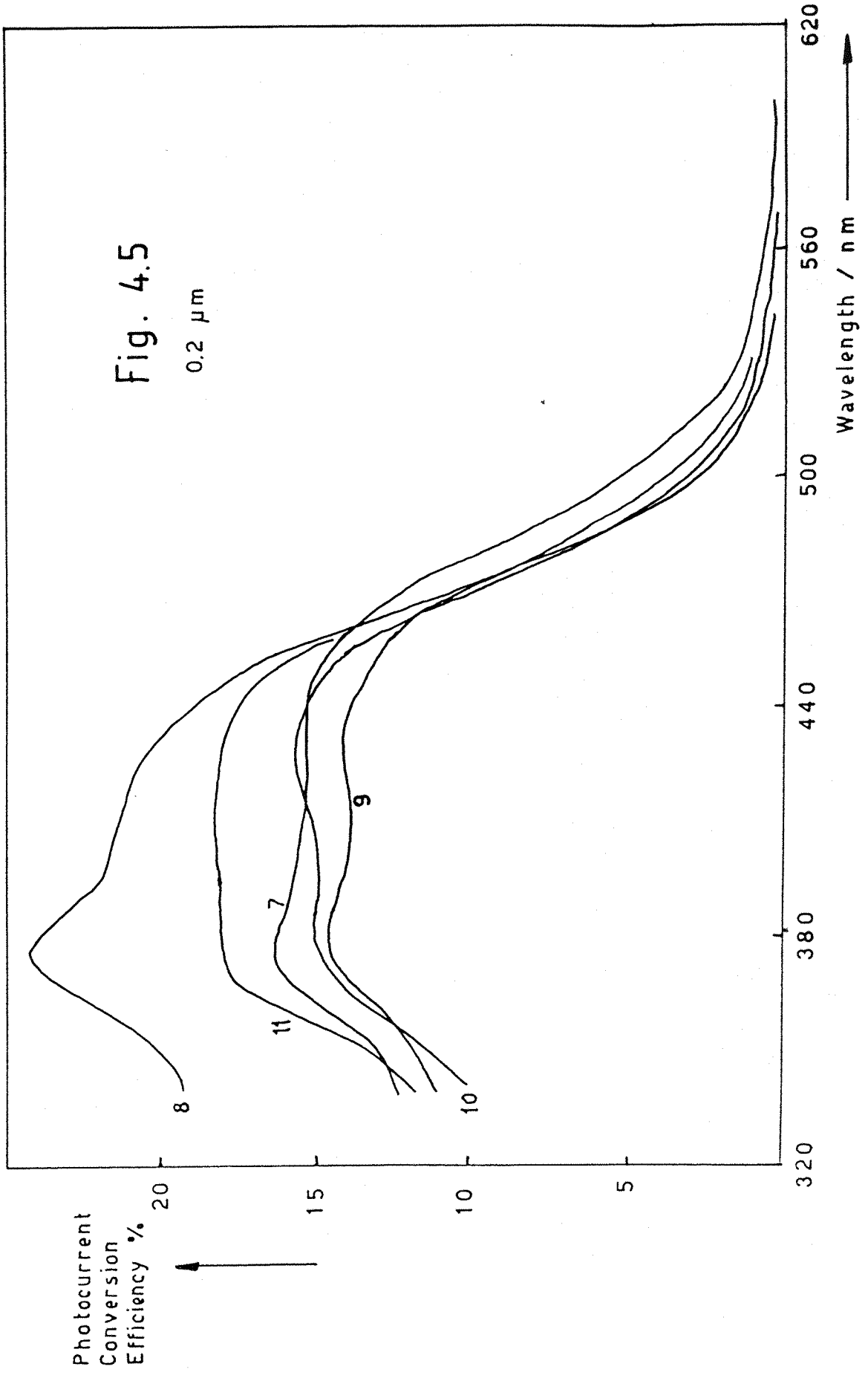
Fig. 4.5
0.2 µm
Photocurrent Conversion Efficiency %
20
15
10
5
320
380
440
500
560
620
Wavelength / nm
8
11
7
9
10

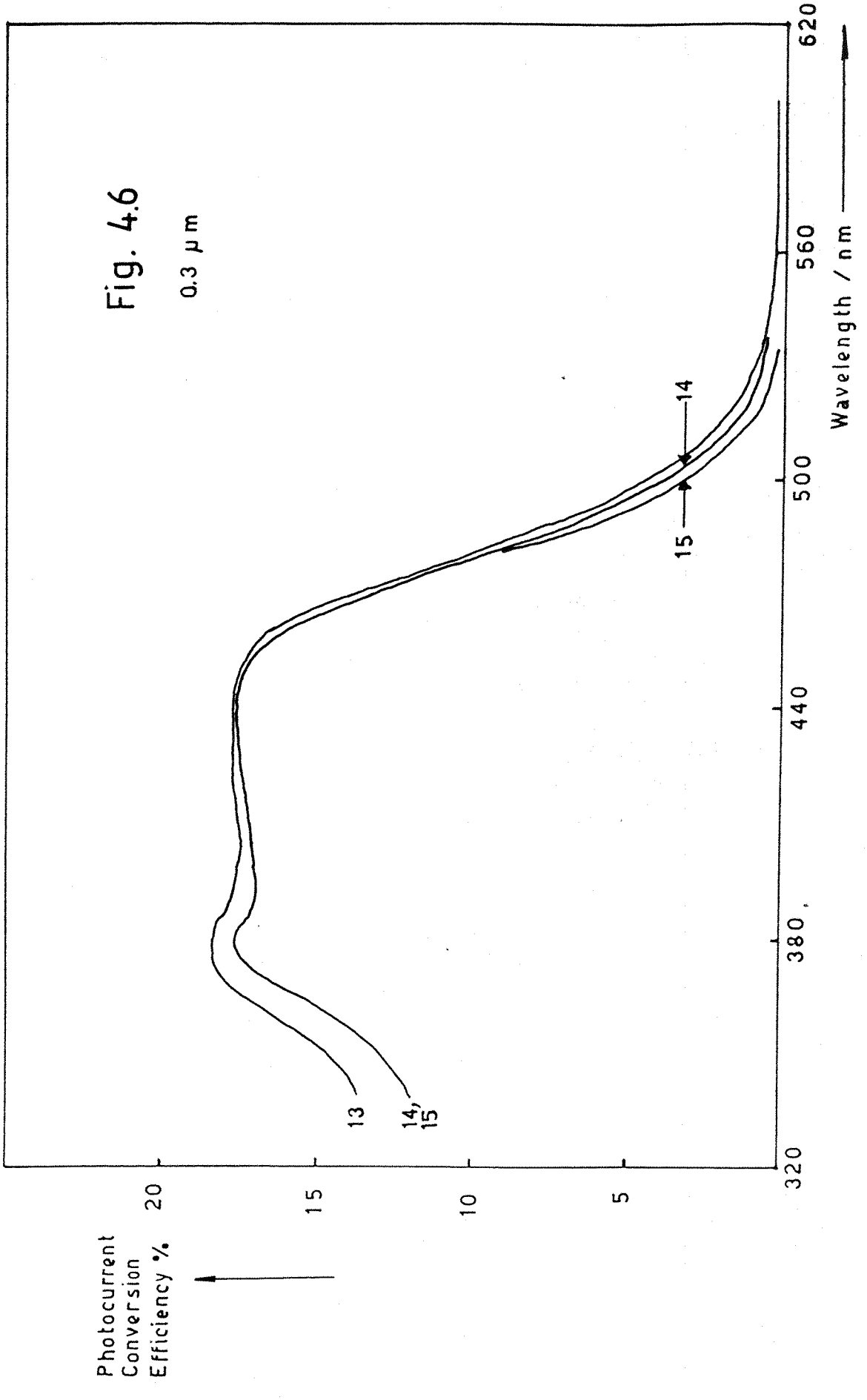
Fig. 4.6
0.3 μm
Photocurrent Conversion Efficiency %
20
15
10
5
320
380
440
500
560
620
Wavelength / nm
13
14, 15
14
15

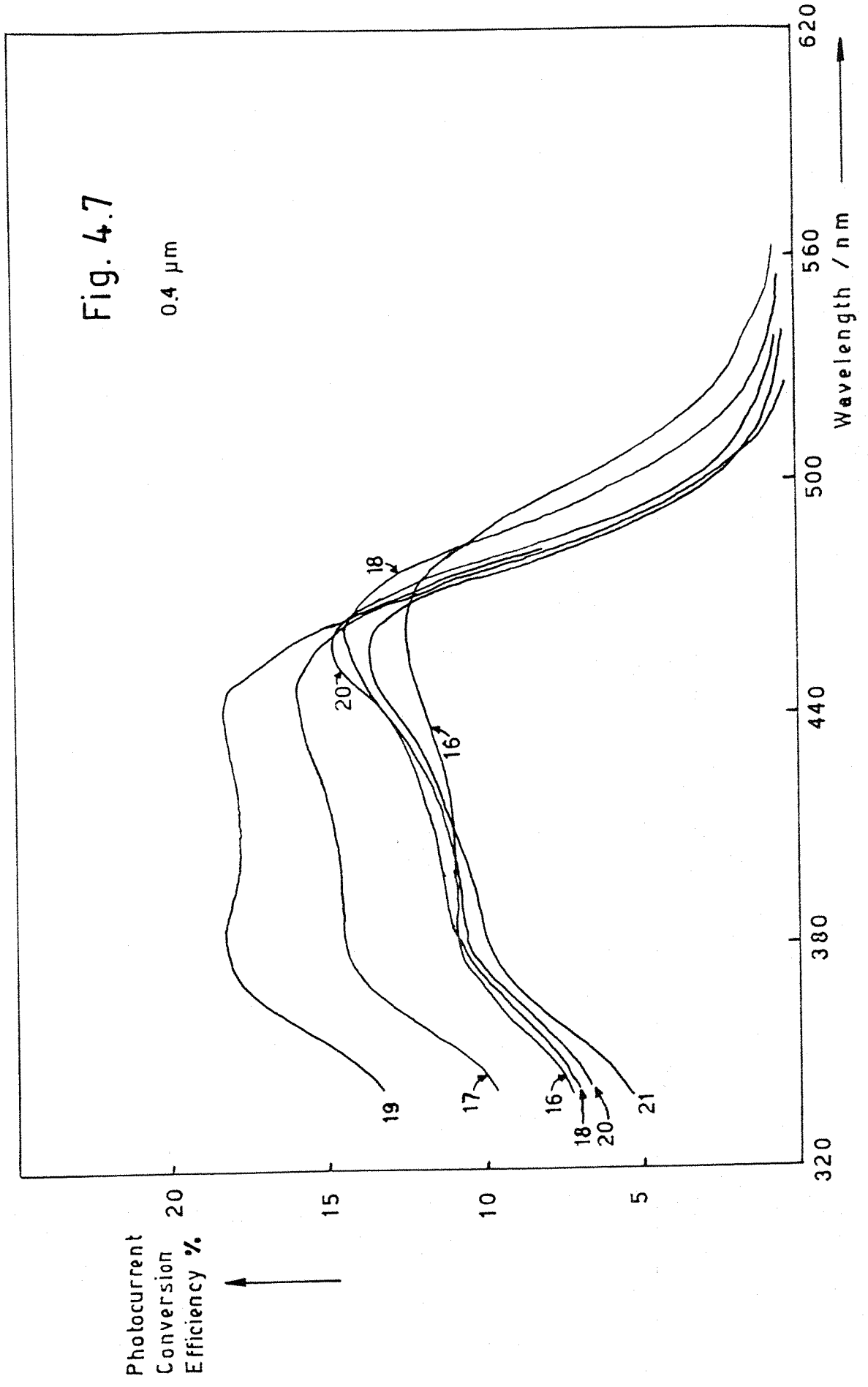
Fig. 4.7
0.4 µm
Photocurrent Conversion Efficiency %
20
15
10
5
320
380
440
500
560
620
Wavelength / nm
19
17
16
18
20
21
16
20
18

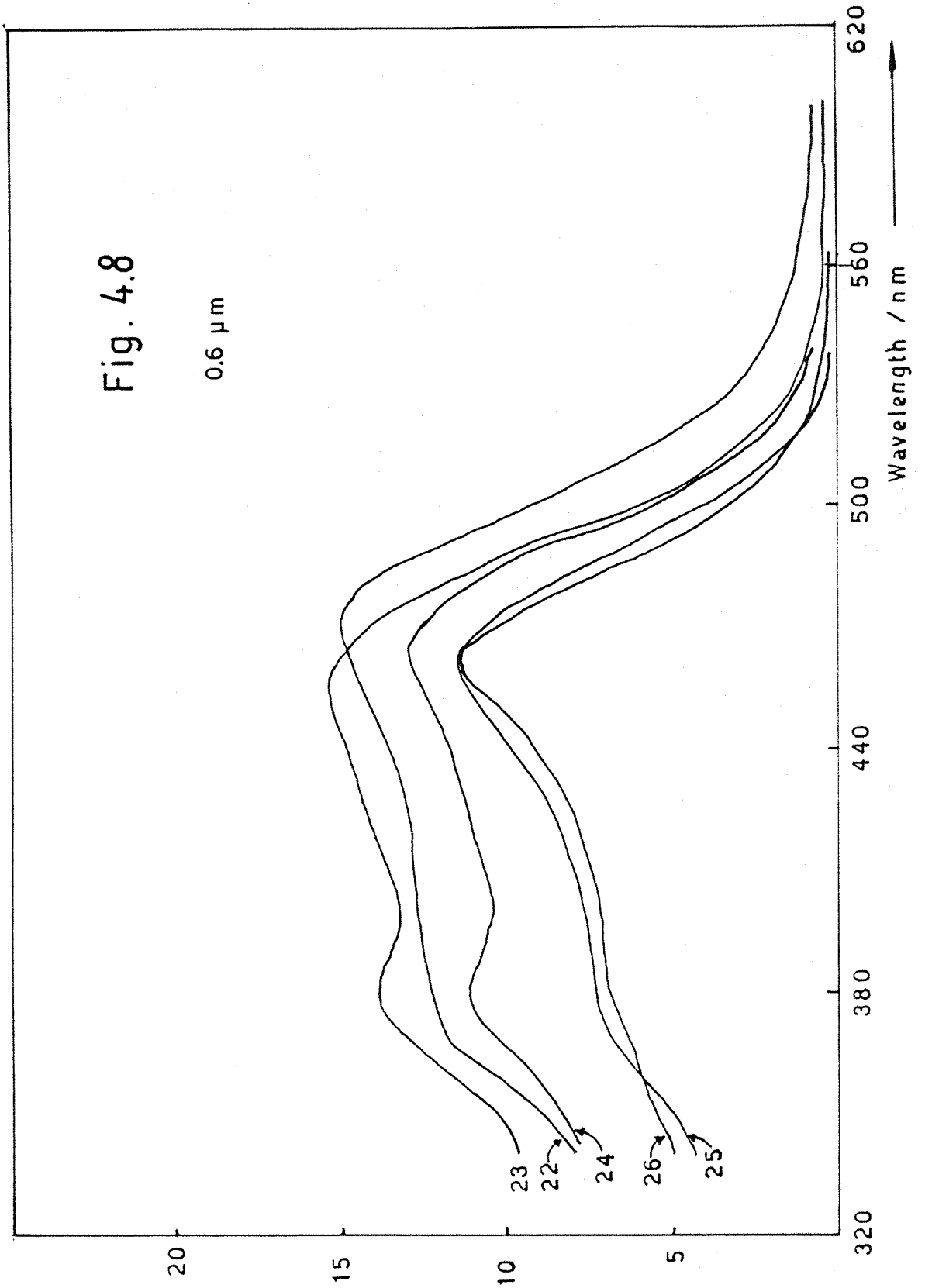
Fig. 4.8
0.6 µm
Photocurrent Conversion Efficiency %
20
15
10
5
320
380
440
500
560
620
Wavelength / nm
23
22
24
26
25

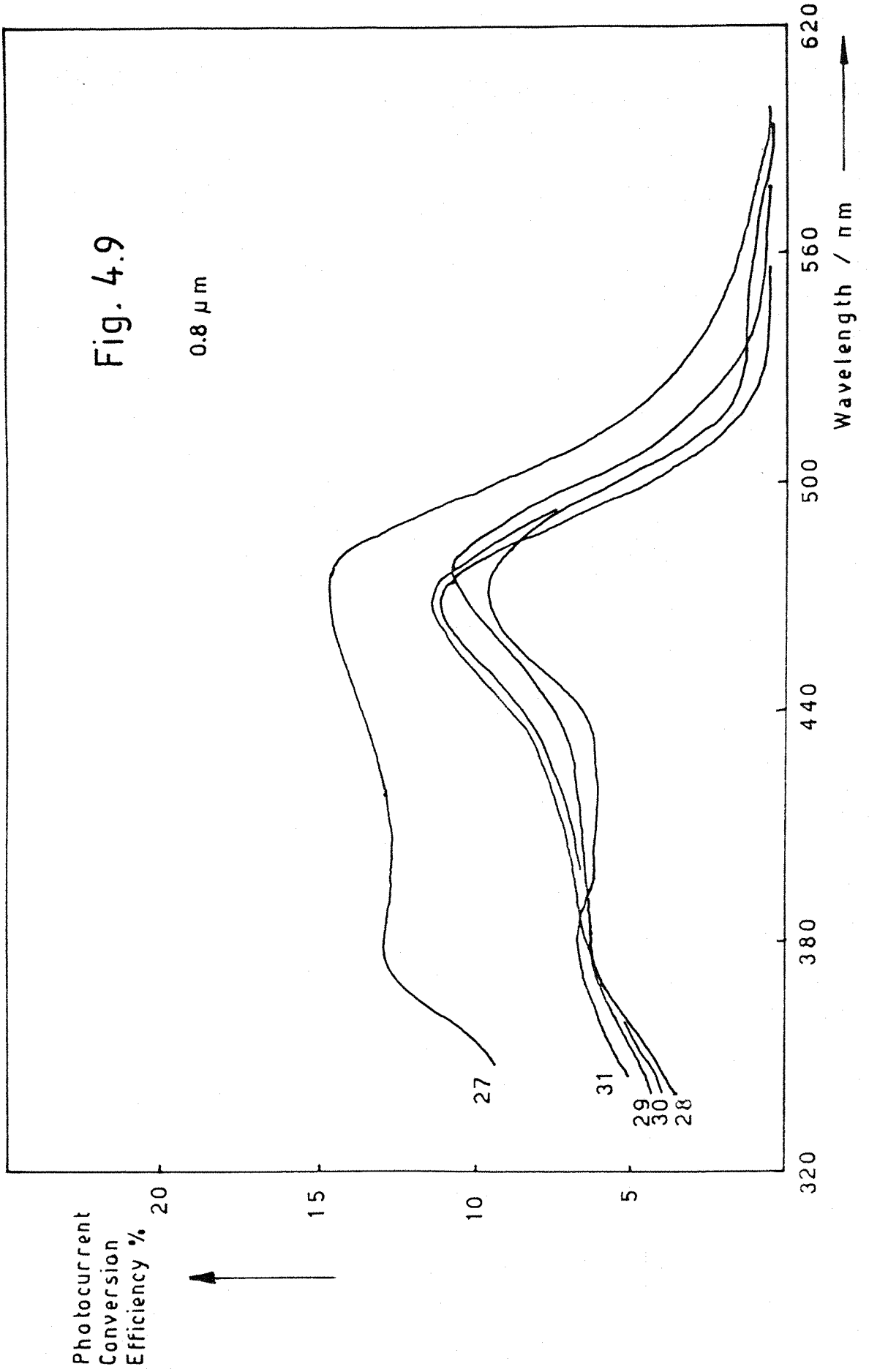
Fig. 4.9
0.8 μm
Photocurrent Conversion Efficiency %
20
15
10
5
320
380
440
500
560
620
Wavelength / nm
27
31
29
30
28

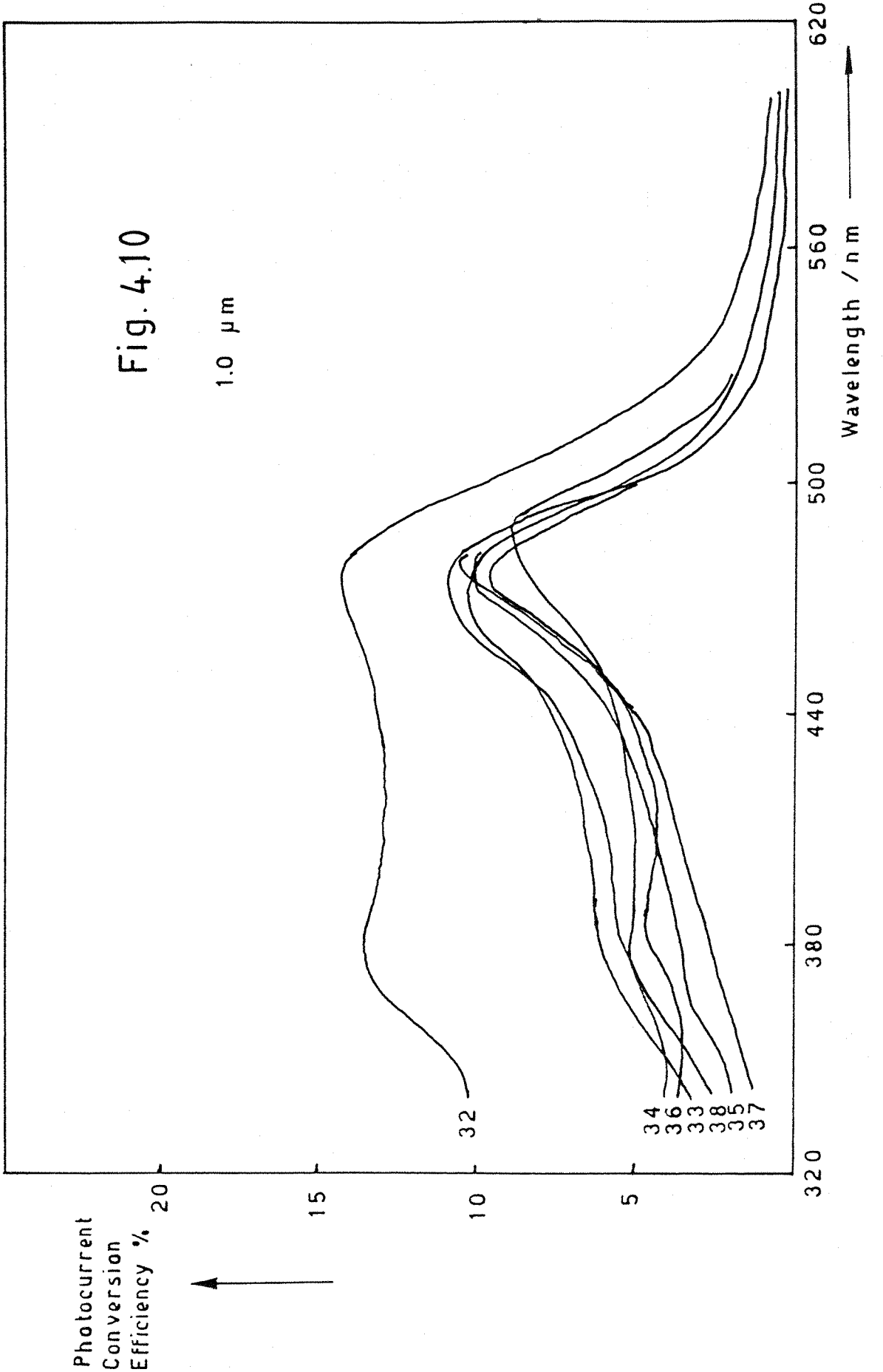
Fig. 4.10
1.0 μm
Photocurrent Conversion Efficiency %
20
15
10
5
320
380
440
500
560
620
Wavelength / nm
32
34
36
33
38
35
37

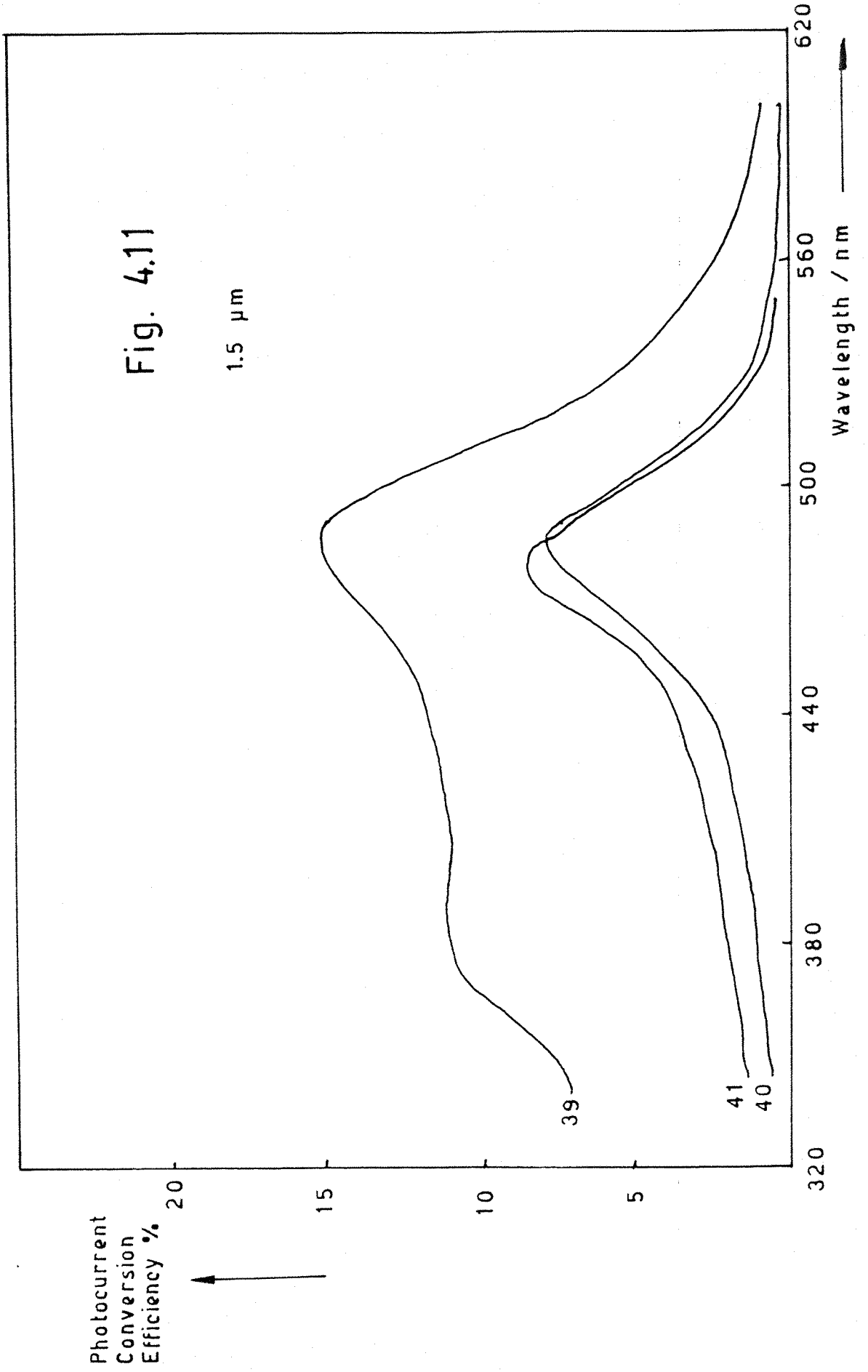
Fig. 4.11
1.5 µm
Photocurrent Conversion Efficiency %
20
15
10
5
320
380
440
500
560
620
Wavelength / nm
39
41
40

Fig. 4.12

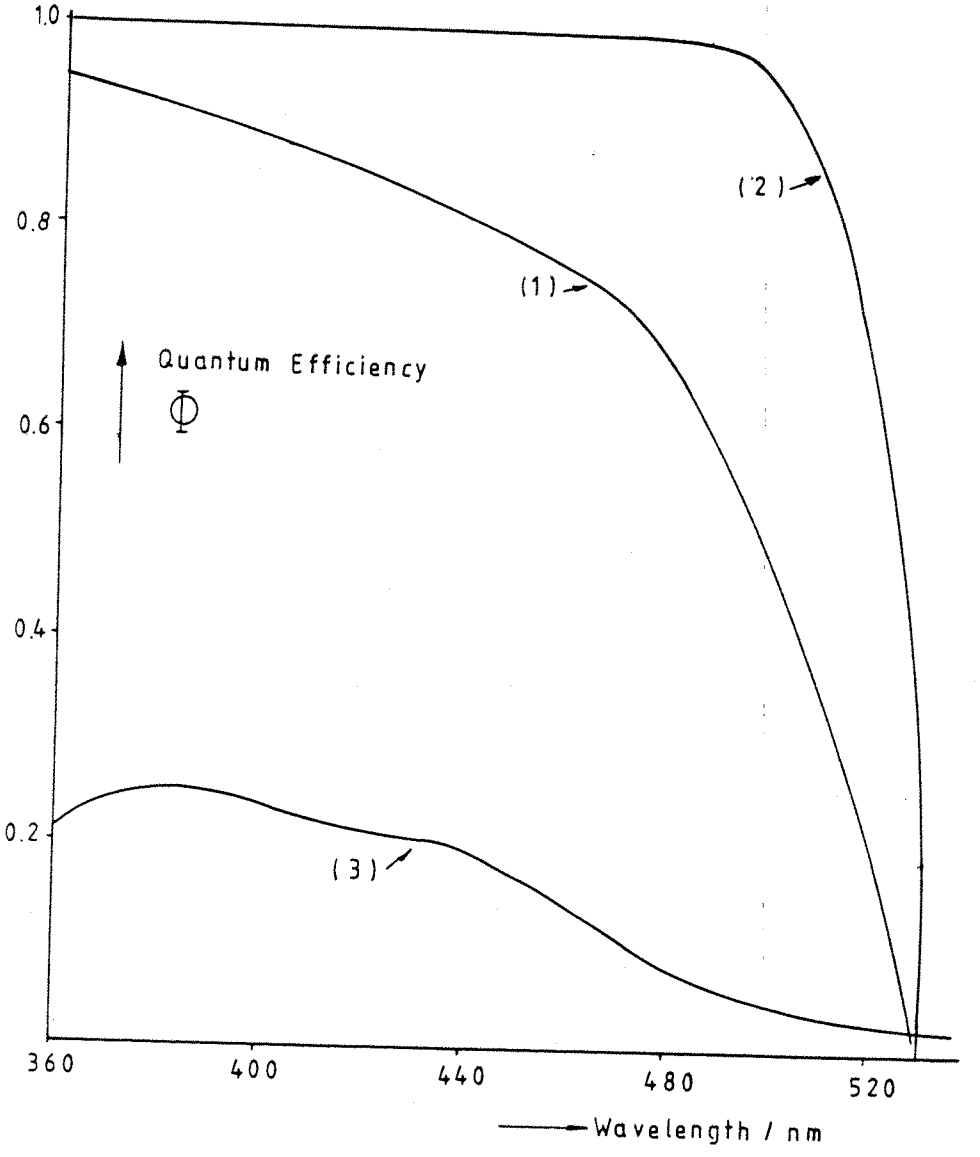
1.0
0.8
0.6
0.4
0.2
Quantum Efficiency
Φ
(1)
(2)
(3)
360
400
440
480
520
Wavelength / nm

response curves (1) and (2) for different film thicknesses, based on the Beer-Lambert Law and assuming 100% of the electron-hole pairs produced contribute to the photocurrent.

Two alternative hypotheses were used in constructing curves (1) and (2).

The first assumes that the incident light traverses the film in one direction only, with all photons that reach the semiconductor-substrate interface being absorbed and not reflected there. It is also assumed that the band bending extends throughout the film thickness d, so that there is a potential gradient throughout the film to separate the photogenerated electron-hole pairs with 100% collection efficiency at the contacts.

The equation that applies in this case is:

$$\Phi = 1 - \{\exp(-\alpha.d)\} \qquad (4.7)$$

The second hypothesis assumes that the incident light penetrates through to the back contact, and is totally reflected from it so that it can be absorbed in its second traverse of the film out towards the front surface, again with all electron-hole pairs produced in both traverses contributing to the photocurrent. We can then write:

$$\Phi = 1 - \{\exp(-2.\alpha.d)\} \qquad (4.8)$$

The absorption coefficient of cadmium sulphide as a function of wavelength was taken from the paper by Khawaja and Tomlin [81]. The values range from about 2×10^{7} m^{-1} at 360 nm to about 10^{6} m^{-1} at about 520 nm. This suggests that the thinner films tested do not

absorb all the incident light, even if it is reflected back through the film.

Thus curve (1) represents the theoretical quantum efficiency of either a 0.2 micron film using equation (4.7) or a 0.1 micron film using equation (4.8). Similarly, curve (2) represents either a 1.0 micron film using equation (4.7) or a 0.5 micron film using equation (4.8).

The gradual drop in quantum efficiency at lower wavelengths may be due to the variation in grain size from the platinum back contact (larger) to the solution interface (smaller): since higher energy quanta are absorbed over a shorter distance beneath the surface of the semiconductor, they are therefore absorbed in regions of smaller grain size, where the diffusion length is lower, due to the higher density of trapping centres; this produces lower conversion efficiencies.

The sub-band gap tail which extends the quantum efficiency to wavelengths beyond 540 nm is possibly due to transitions between states in the band gap induced by defects such as local charged impurities. These intermediate states within the "forbidden" energy region allow photons of lower energy than would otherwise be absorbed to excite an electron out of the valence band.

The general conclusions one can draw from these results are, firstly, that for a given film thickness, the efficiency of the layers improves as the deposition temperature is increased from 100 C to the region of 130 °C, but then declines if the deposition is carried out at higher temperatures still, up to 160 °C. Secondly, for a given deposition temperature, the quantum efficiency declined steadily as the film thickness was increased over the range 0.1 micron to 1.0 micron. Films less than 0.1 micron thick were uneven in appearance,

probably pierced with holes through to the substrate, and produced lower, variable quantum efficiency spectra. Films less than one micron thick showed an interference pattern of concentric rings of slightly different colours, radiating out from the centre of the disc electrode. This tends to confirm the idea that the films were graded in thickness, to a certain extent, across the face of the test electrode.

A similar set of photocurrent experiments were carried out for several CdS film thicknesses, grown at 130 °C. from DMSO, but substituting 5 millimolar potassium ferrocyanide and ferricyanide, dissolved in 0.1M potassium chloride in the optical test cell, in place of the sodium sulphide. It was observed that the films became detached from the platinum substrate after being immersed in the ferro/ferricyanide for more than a few minutes. The results of the experients are summarised in fig 4.13. The reduction in quantum efficiency, particularly at lower wavelengths, is likely to be a result of absorption of quanta by the oxidised iron species, whose molar extinction coefficient rises rapidly in this region.

Figs 4.14 and 4.15 show the effect on the photocurrent in 0.1M sodium suphide of the applied electrode potential, scanning at a rate of 10 mV per second towards the more negative potentials. It is seen that the photocurrent rises rapidly from the onset potential of about -1.2 V to its saturation value, and in this respect the form of the characteristic resembles the results obtained for a single crystal [81]. By contrast, it has been found that the rise to saturation values for more defective materials, such as titanium dioxide, is much slower. One can deduce from this that the thin film material has a fairly high degree of crystallinity. The peak which occurs just prior to the drop down to the onset potential in the negative-going

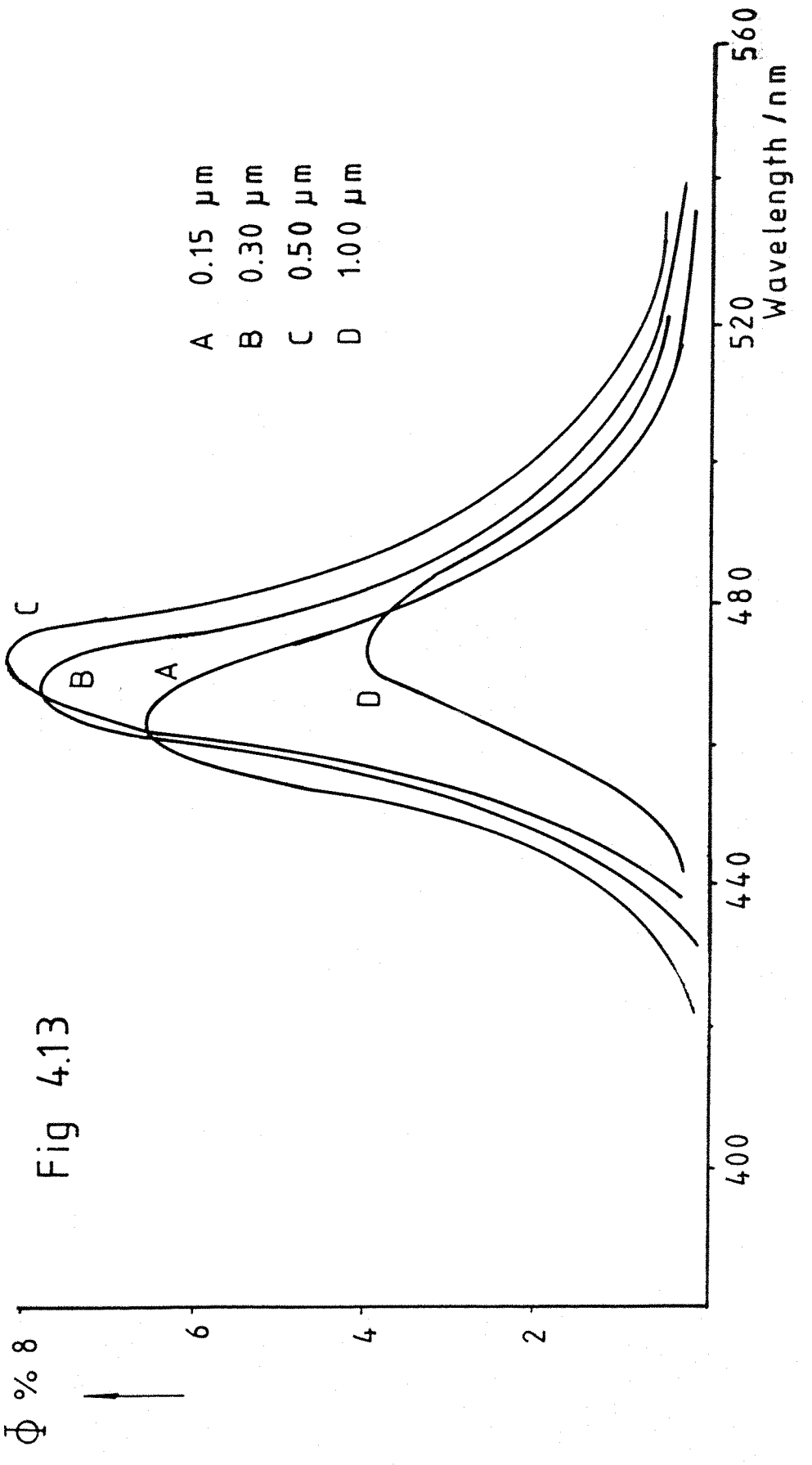
A 0.15 µm
B 0.30 µm
C 0.50 µm
D 1.00 µm
A
B
C
D
Φ %
8
6
4
2
400
440
480
520
560
Wavelength / nm

Fig 4.13

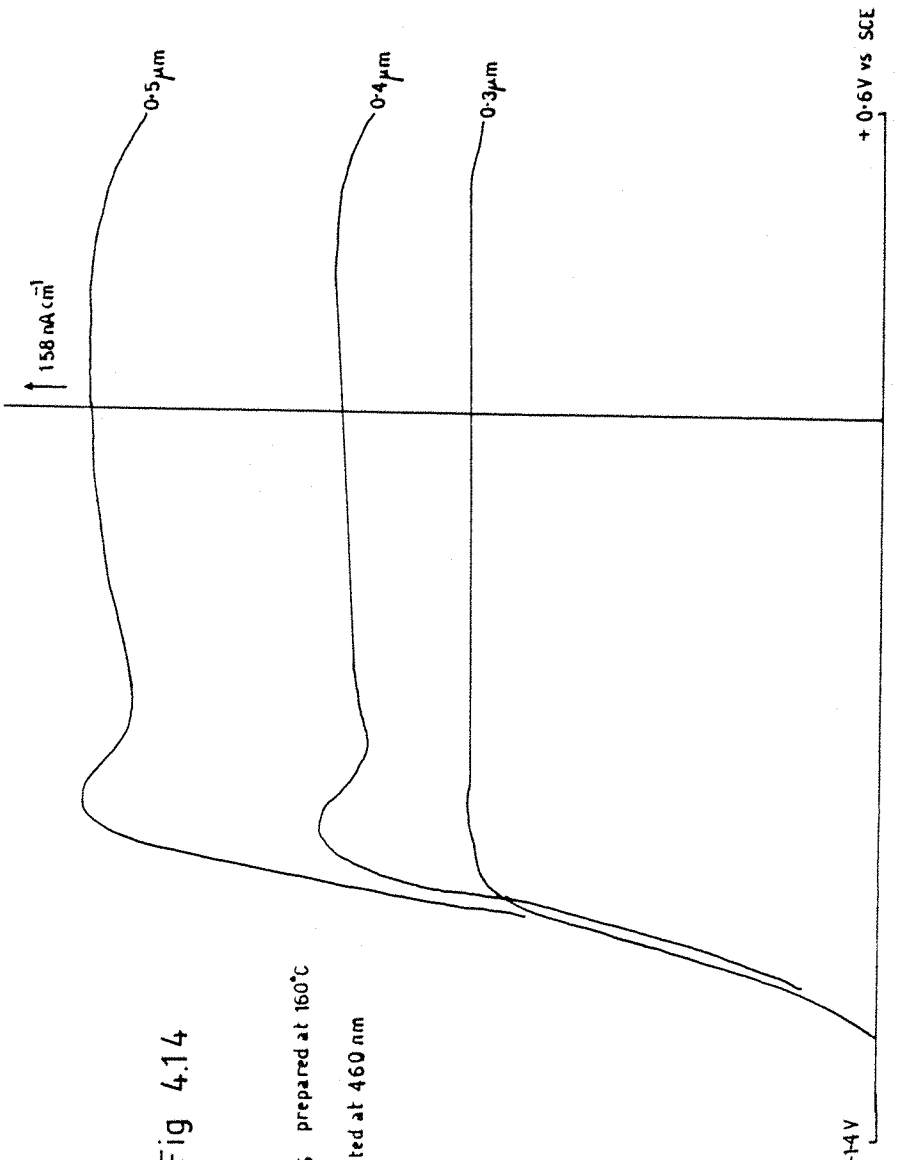

Fig 4.14

CdS prepared at 160°C

illuminated at 460 nm

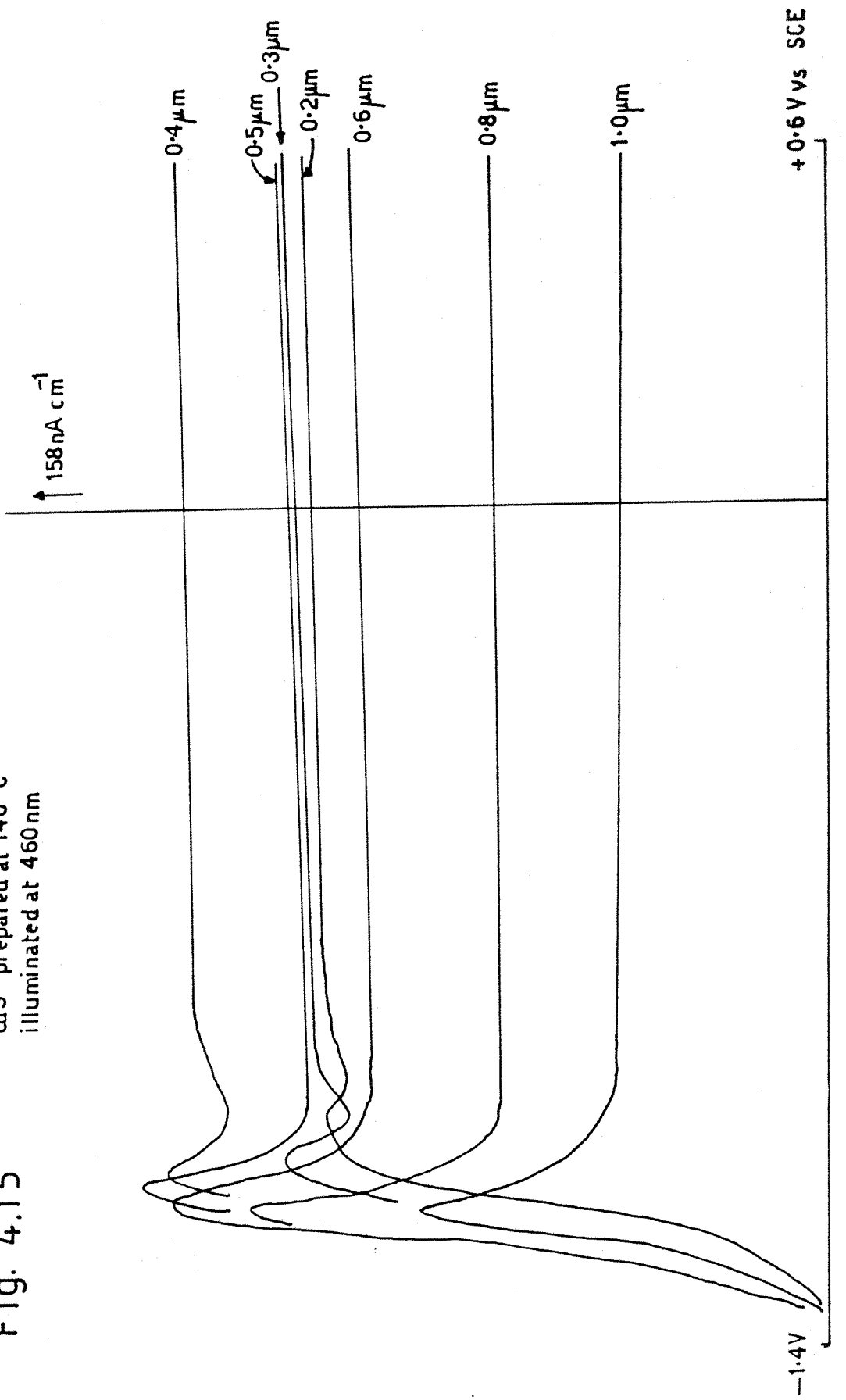

Fig. 4.15

CdS prepared at 140° c
illuminated at 460 nm

scan may be due to a reorganisation of the surface material.

Fig 4.16 shows the measured photocurrent conversion efficiency of a single crystal of CdS in the same electrolyte, at 0.0V with respect to SCE. It is seen that the peak efficiency is in the region of 80%, compared to the theoretical values of nearly 100% expected in the plateau region. Taking the refractive indices of water and cadmium sulphide to be 1.35 and 2.29 [82] respectively, we calculate the reflectivity of the CdS/solution interface to be around

$$((2.29 - 1.35)/(2.29 + 1.35)) = 0.067$$

which is high enough to account for a good part of the loss of efficiency observed.

Fig 4.17 shows a typical cyclic voltammogram of the CdS layers in 0.1M sodium sulphide, using slow chopping of the incident monochromatic light at the wavelength of maximum photocurrent to show the relation between the photocurrent and the background current.

It is clear that substantial dark current flows in addition to the plateau photocurrent, suggesting that the film is porous due to cracks, which probably appear in the film as it cools on removal from the plating bath. The cracks are probably not formed during the layer deposition, since the galvanostatic growth curve is smooth, and shows a steady increase in resistance up to the breakdown limit.

It should be mentioned here that every effort was made to cool the films down slowly afer completing the deposition, by raising the electrode about a centimetre above the hot electrolyte for a few minutes beore final removal from the apparatus.

The presence of cracks agrees with the observations of Baranski and Fawcett in their papers cited earlier.

The surface appearance of the CdS films altered after

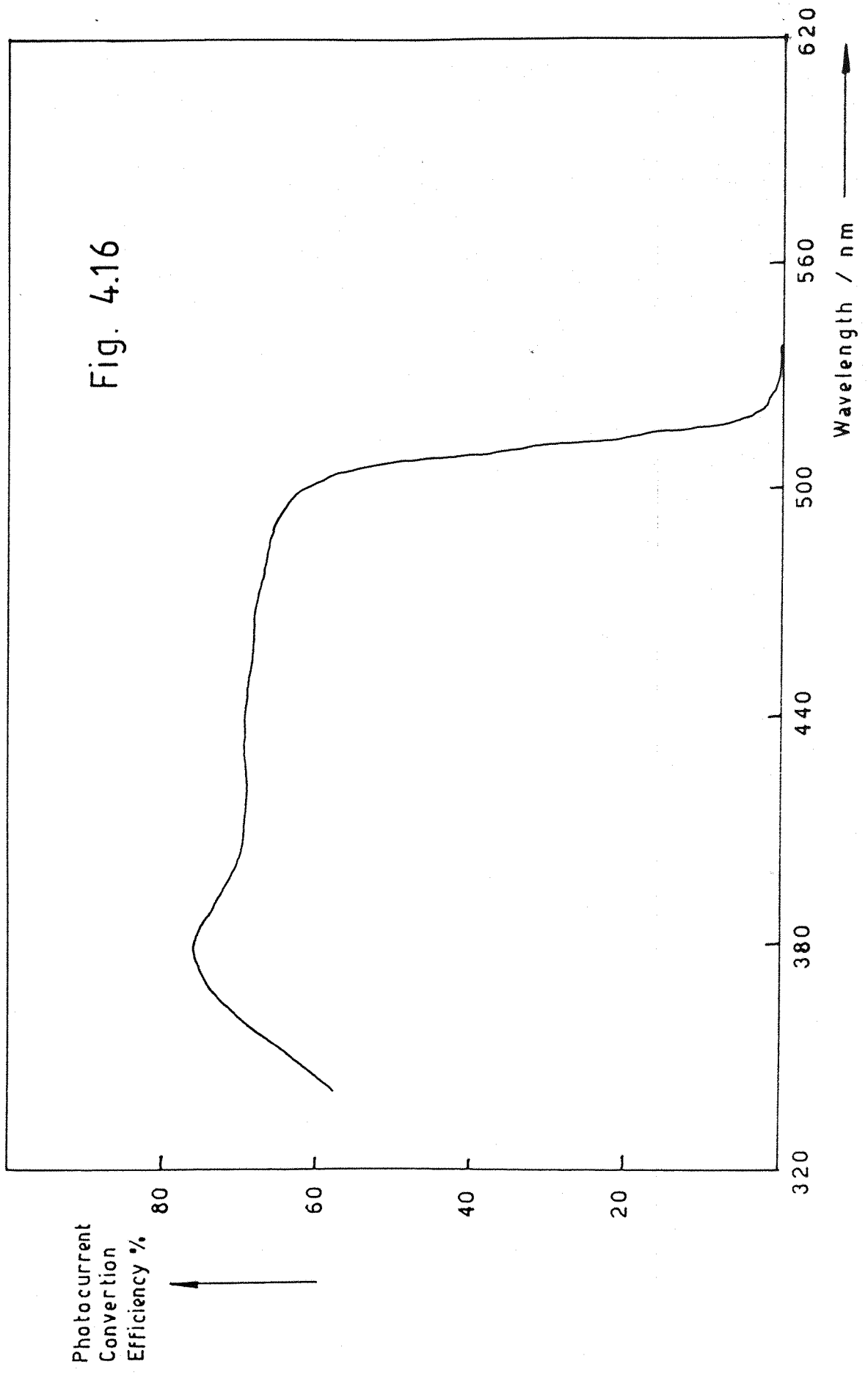
Photocurrent
Convertion
Efficiency %
80
60
40
20
320
380
440
500
560
620
Wavelength / nm

Fig. 4.16

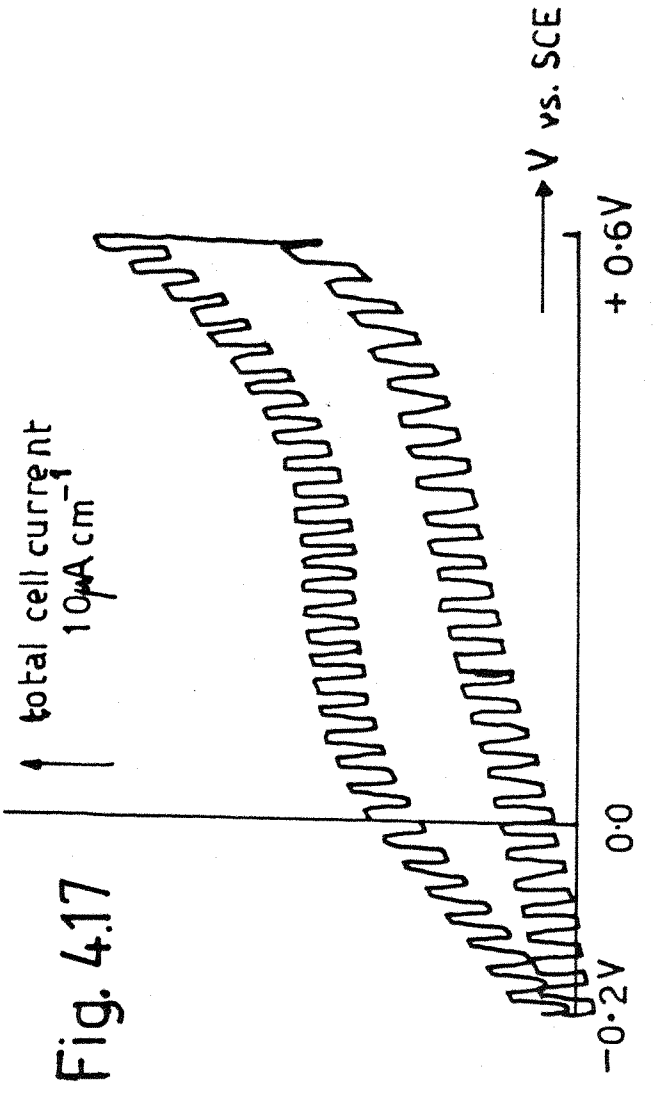

Fig. 4.17

prolonged cycling, becoming more even, and with less indication of interference patterns, which could be explained in terms of the dissolution and redeposition indicated in the CVs.

Figs 4.18 to 4.21 are CVs carried out in the dark on the bare substrate and on three thicknesses of CdS layers deposited on it, all in deoxygenated 0.1M sodium sulphide, and all at the same sweep rate of 20 mV per second. For bare Pt, there is a peak at about -0.1 V versus SCE. For the CdS films, the peak is shifted to 0.0 V, and a secondary peak appears at about -0.6 V. Both these peaks gradually increase in height with repeated scanning between +0.6 V and -1.2 V versus SCE. The arrows show the trends in peak magnitude with increasing scan number.

There are large currents on the coated electrodes, with the main features of platinum electrochemistry still visible, confirming once more that the films are cracked through to the substrate. The small peak at -0.6 V is most likely the reoxidation of cadmium to cadmium sulphide on the surface of the film in the anodic sweep.

Several CdS films of thicknesses from 0.1 to 1.0 microns were prepared on platinum and molybdenum flags for analysis using X-ray powder crystallography at the Materials Development Division, AERE, Harwell, by Mr. B.A.Bellamy.

The diffractograms are shown in figs 4.22 to 4.26. Marked on these in parentheses are the Miller indices of the the diffracting planes, and added as a subscript are the expected relative intensities of the peaks for random crystal orientation. All the figures indicate that the material becomes progressively more crystalline than amorphous as the film thickness is increased up to 1 micron, and that the hexagonal form is dominant on both substrates, with the c-axis oriented perpendicular to the substrate.

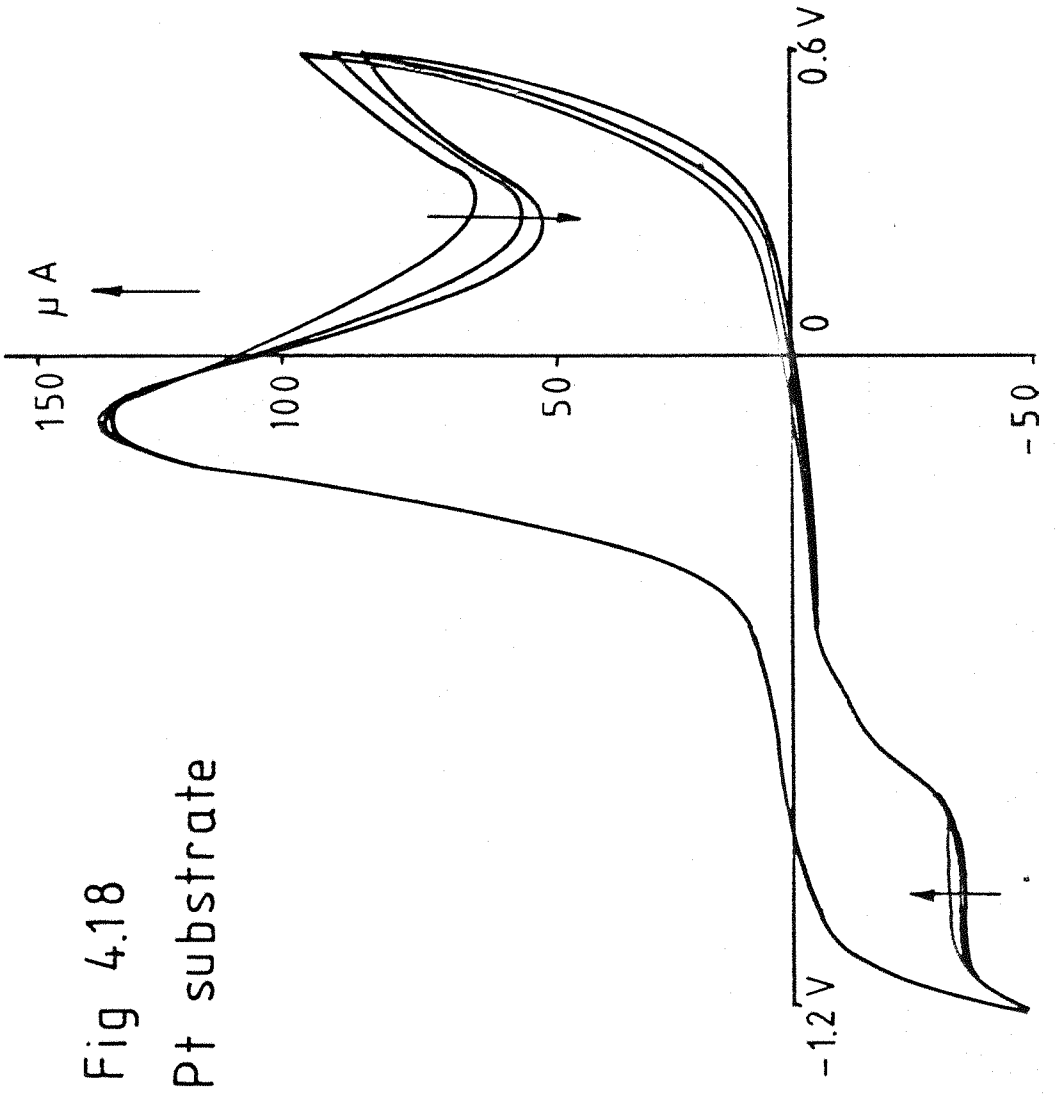

Fig 4.18
Pt substrate

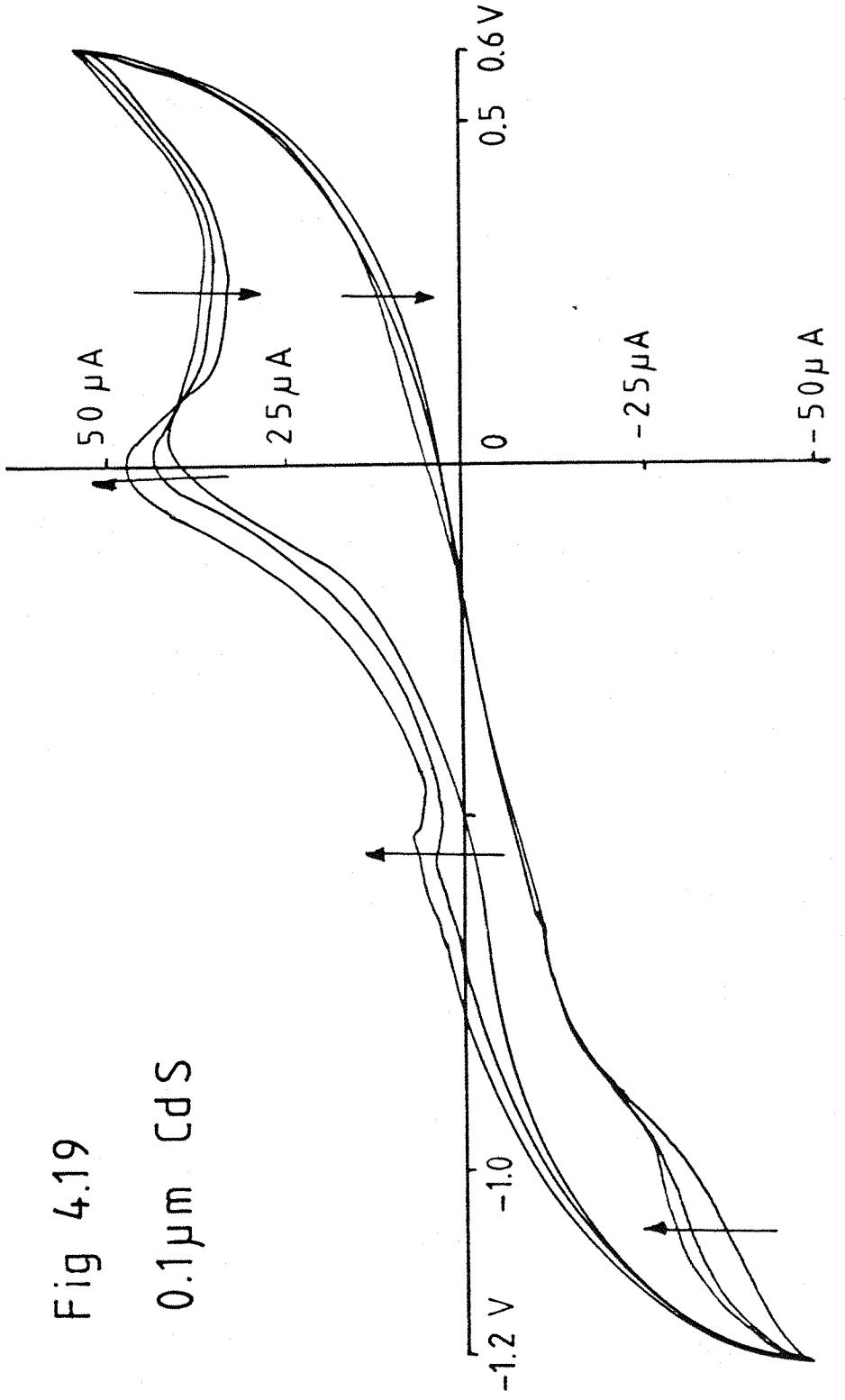

Fig 4.19
0.1µm CdS

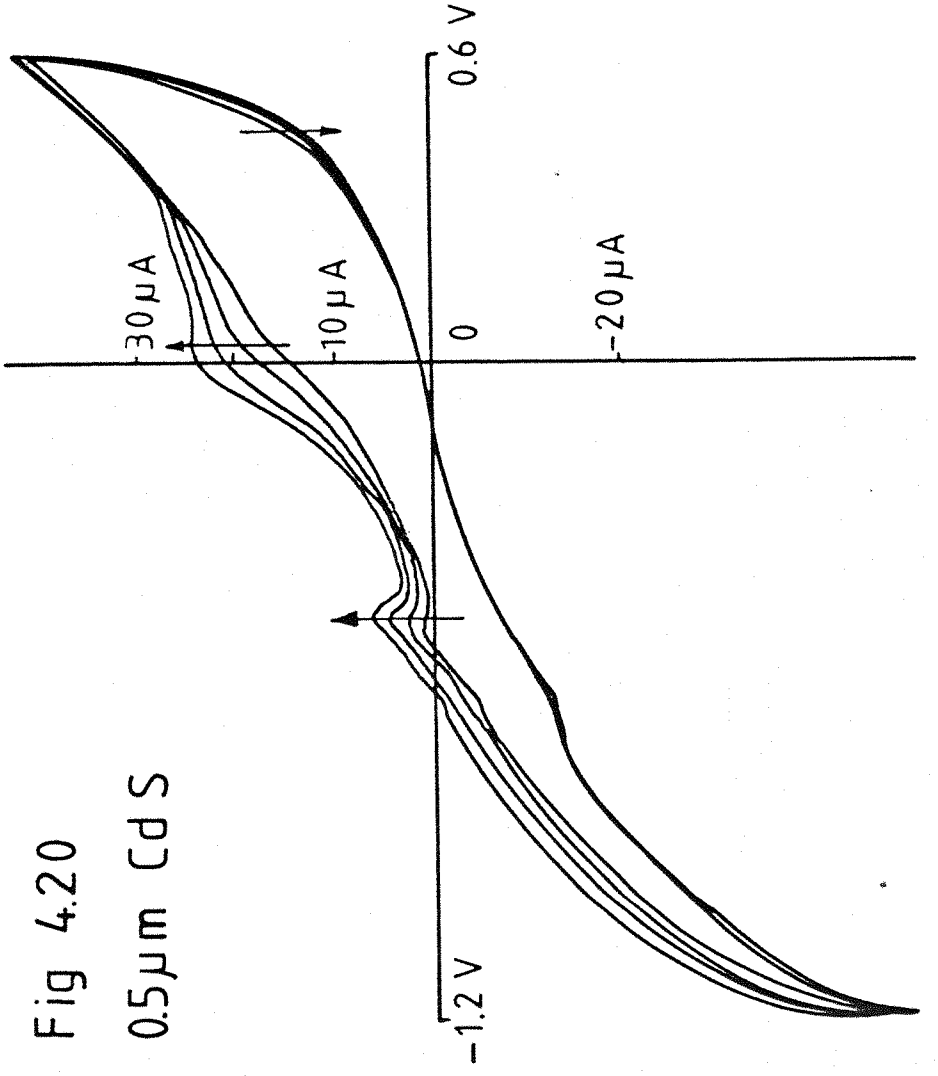

Fig 4.20
0.5µm CdS

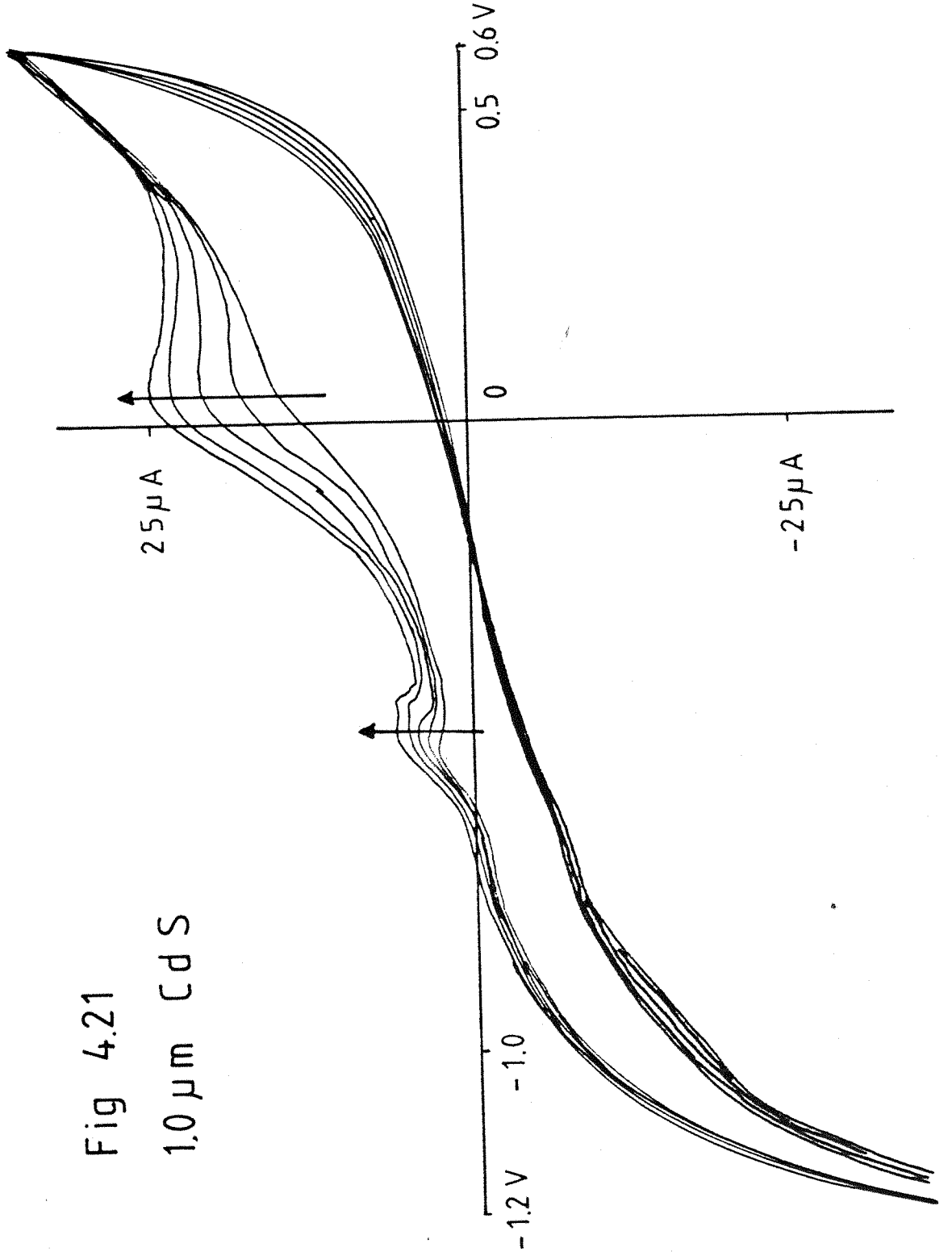

Fig 4.21
1.0 μm CdS

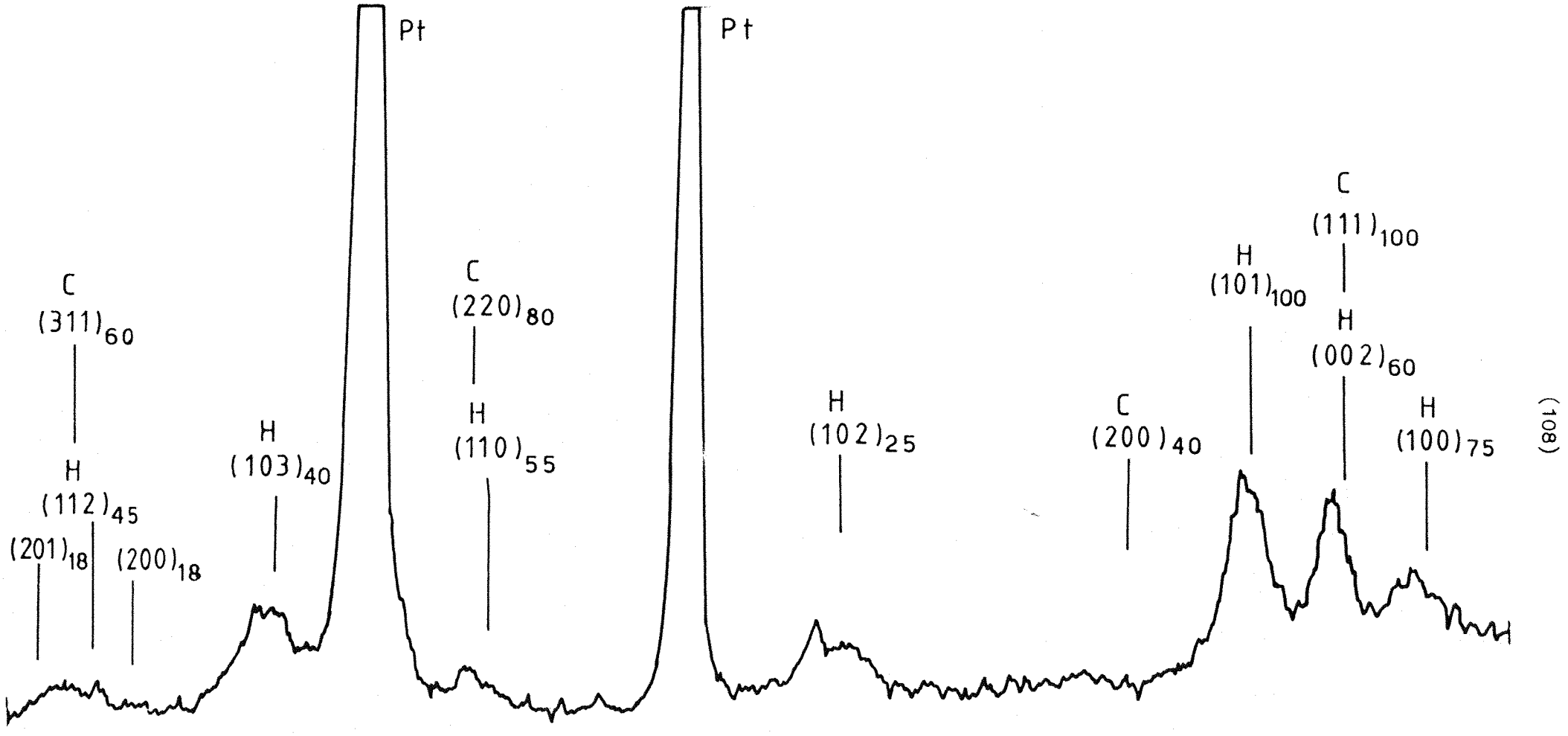

Fig 4.22 0.2 μm CdS on Pt

C = Cubic H = Hexagonal

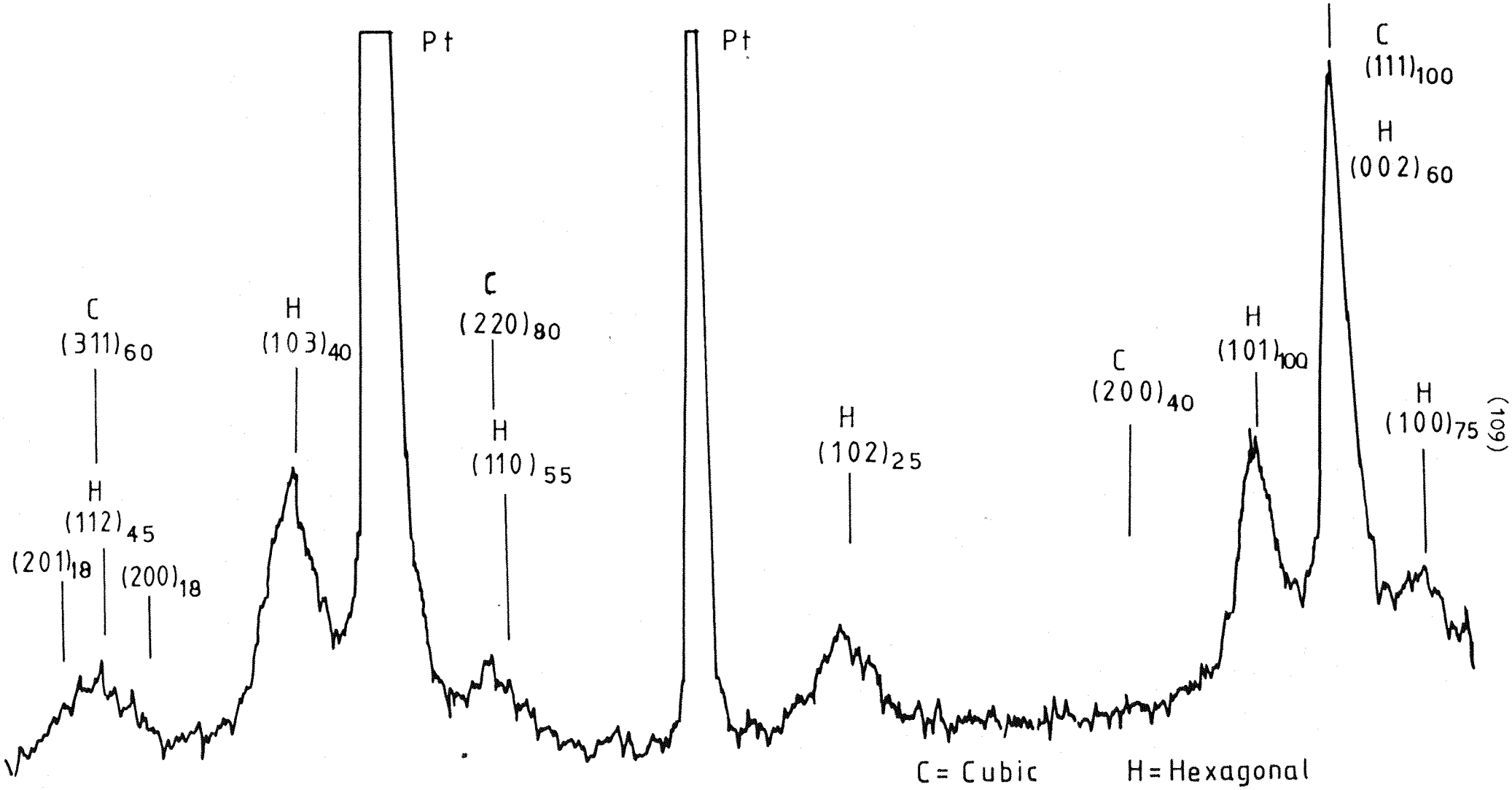

Fig 4.23 0.5 µm CdS on Pt

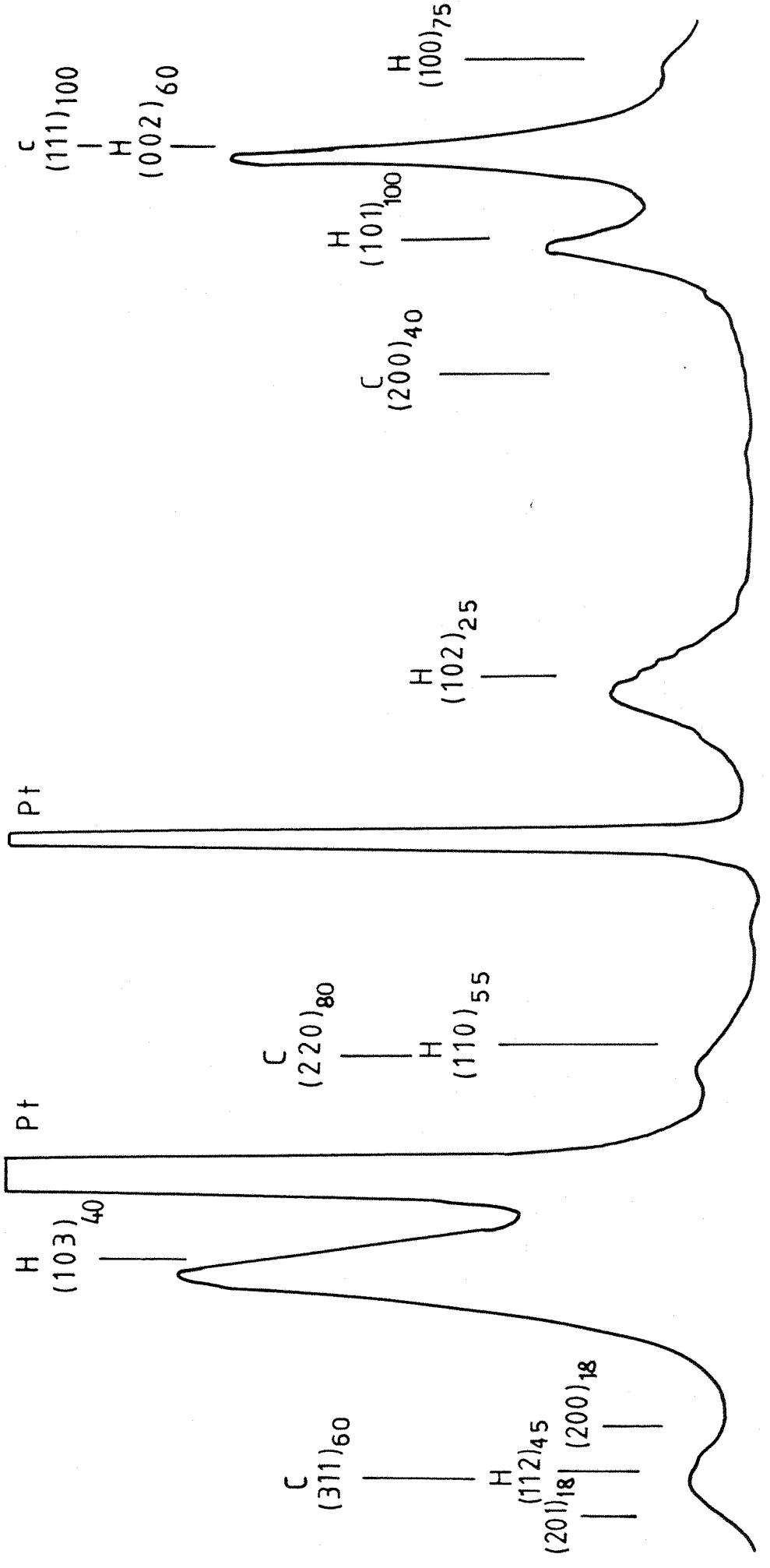

Fig 4.24 1.0 µm CdS on Pt

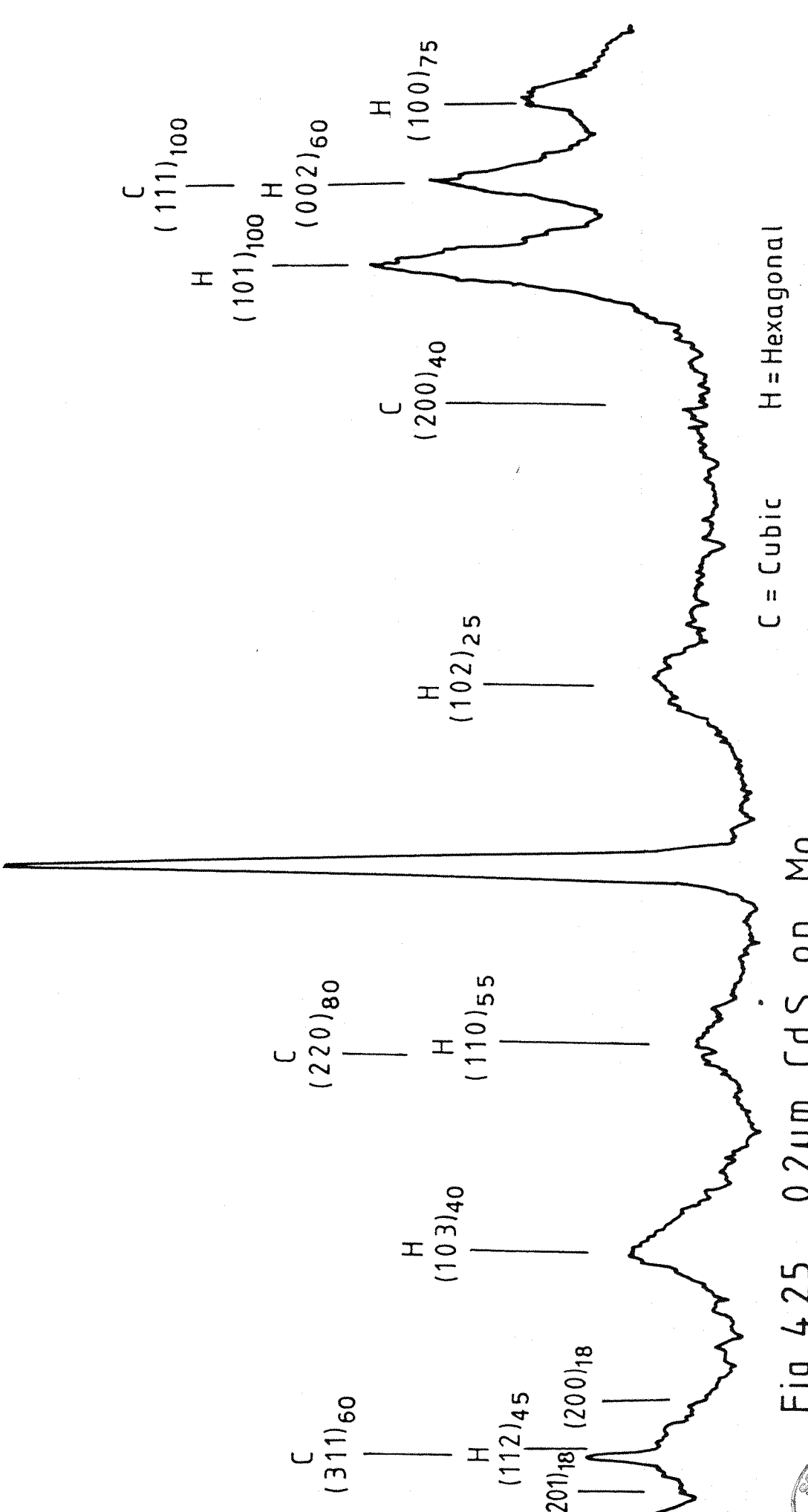

Fig 4.25 0.2μm CdS on Mo

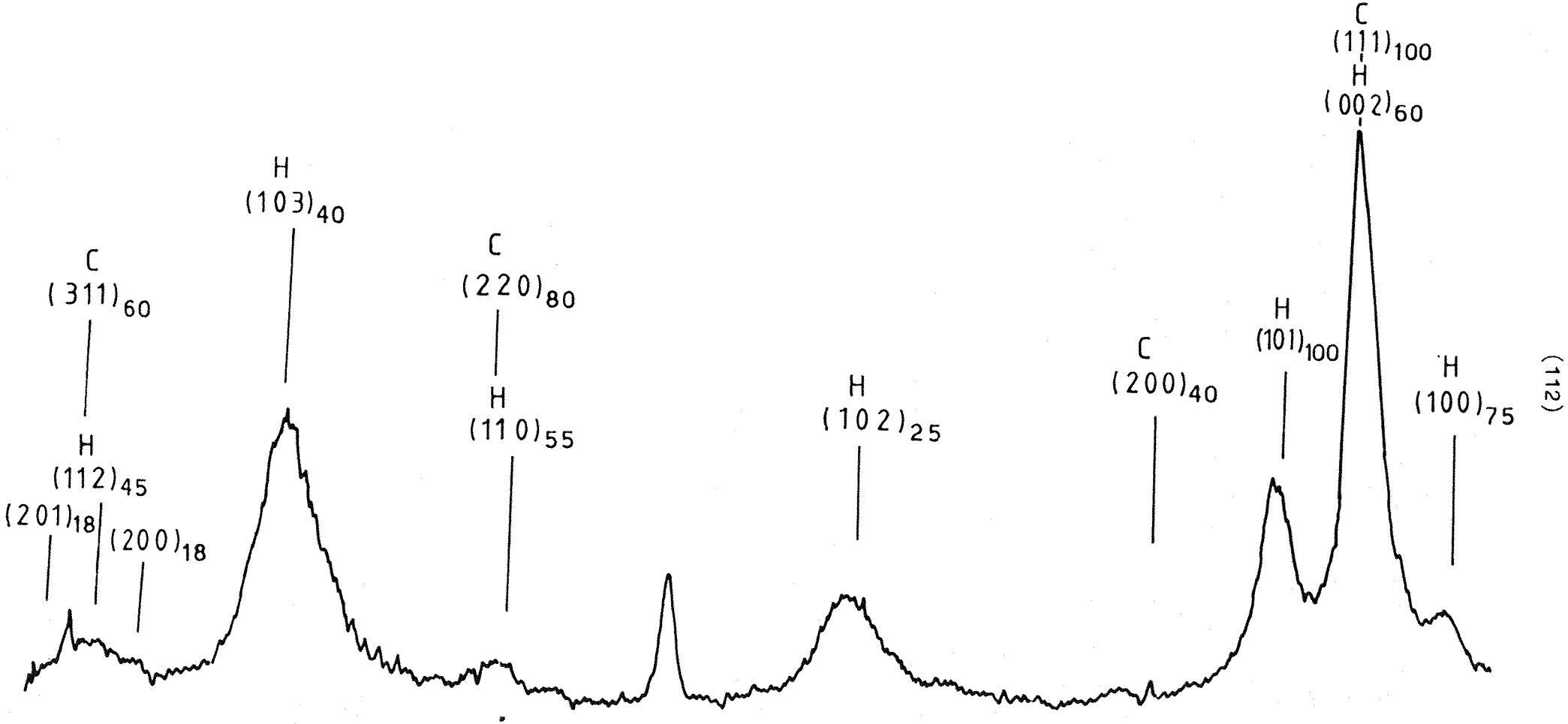

Fig 4.26 1.0 µm CdS on Mo C = Cubic H = Hexagonal

CHAPTER 5

INVESTIGATION OF ELECTROCHEMICALLY DEPOSITED BISMUTH SULPHIDE

(5.1) PROPERTIES OF FILMS DEPOSITED ON A Pt SUBSTRATE

Baranski and Fawcett [49] have deposited thin layers of bismuth sulphide from a solution of 0.032M bismuth trichloride, 0.0008M sulphur, and 0.93M ammonium chloride, in diethylene glycol (DEG), using a current density of 2 mA per sq.cm. Their investigation was extended in this part of the project to analyse the dependence of the photocurrent quantum efficiency of the thin layers on the deposition conditions, and to correlate their measured optical and electrical properties with their physical structure, in the light of the current theory.

DEG was chosen as a solvent for the plating bath because of its high boiling point (198°C. at STP), and relatively low toxicity. It is a colourless, rather viscous liquid at normal laboratory temperatures.

Most of the films investigated were deposited on to a 0.59 sq.cm. platinum disc electrode from a bath containing 0.03M bismuth trichloride, 0.1M ammonium chloride, and 0.01M sulphur in DEG. This sulphur concentration was approximately the solubility limit at 80°C. The reference electrode used in the bath was mercury / bismuth amalgam (1 atom%) / 0.1M ammonium chloride in DEG. The cell and control equipment were the same as had been used in the study of cadmium sulphide.

The films were deposited galvanostatically, recording the potential as a function of time. An interesting feature of the potential transients during the galvanostatic growth was that, after

the rapid initial rise to the required deposition potential (0.2V versus the amalgam reference electrode for 0.5mA per sq.cm.), there was no further increase in the potential throughout the growth for all film thicknesses tried. It is possible that this was due to cracks in the layer allowing contact from the deposition electrolyte to the substrate, or due to highly-doped inclusions providing a low ohmic resistance path across the layer, or due to the inclusion of chloride ion in the deposit: this latter explanation is the one suggested by Baranski, Fawcett, and Gilbert [46] who found the material of the layers to be highly conductive and to exhibit metallic behaviour. They found the material to be amorphous and photosensitive when grown below 100°C, and to be crystalline and photoinactive when grown above this temperature, in contradiction to this study.

The voltage at which the current plateau was observed was approximately proportional to the current density in the range investigated, and so it is probable that the value of the deposition voltage is being determined mainly by the solution resistance.

The apparatus used to measure the photocurrents was the same as that used for the investigation of cadmium sulphide, except that to investigate the effect of wavelengths above 700nm, the tungsten lamp was substituted for the xenon lamp.

A preliminary set of experiments was carried out to establish the effect on the photocurrent conversion efficiency of the layers, in 0.1M sodium sulphide, produced by changes in the current density and deposition temperature in the plating bath, and the thickness of the layer.

At current densities below 0.1 mA per sq.cm., the deposit could not be made to cover the whole of the platinum electrode surface. Above 1.5 mA per sq.cm., the deposit contained dark patches

which rubbed off easily with a soft tissue. In the range between these values, the deposit was light grey, and adhered very well to the substrate (it was slow to dissolve in acid, and so the samples were polished away, after investigation, with alumina powder on a felt pad). Some trial photocurrent spectra were obtained for a few films grown at 1.0 and 0.5 mA per sq.cm., those at the latter current density providing marginally higher conversion efficiencies. A value of 0.5mA per sq.cm. was therefore chosen for use in the project.

Fig 5.1 shows the effect of deposition temperature on the photocurrent conversion efficiency for a series of bismuth sulphide films of thickness 0.03 micron (a thickness chosen because of its good photocurrent in preliminary tests). It is seen that there is a rapid increase in efficiency with temperature between 60 °C. and 100 °C., but that then there is a decline in efficiency as the temperature is raised further. This peak in the photoresponse at a depositon temperature of 100 °C. coincides with the temperature at which Baranski et.al. noted a transition from amorphous to crystalline nature. Above 100 °C., the decreasing photoresponse could be due to increasing doping densities, which narrow the depletion layer thickness, and reduce the chances of photogenerated carriers reaching the interface. At lower temperatures, the doping density may be correspondingly reduced, which would therefore increase the ohmic losses in the layer, and reduce the conversion efficiency.

On the basis of these results, a deposition temperature of 100 °C. was chosen for subsequent experiments.

Fig 5.2 shows the effect of film thickness on the photocurrent conversion efficiency for a series of films grown at 100 °C. This confirms that 0.03 micron is the optimum thickness of those investigated. The results indicate that the thicker the film, the

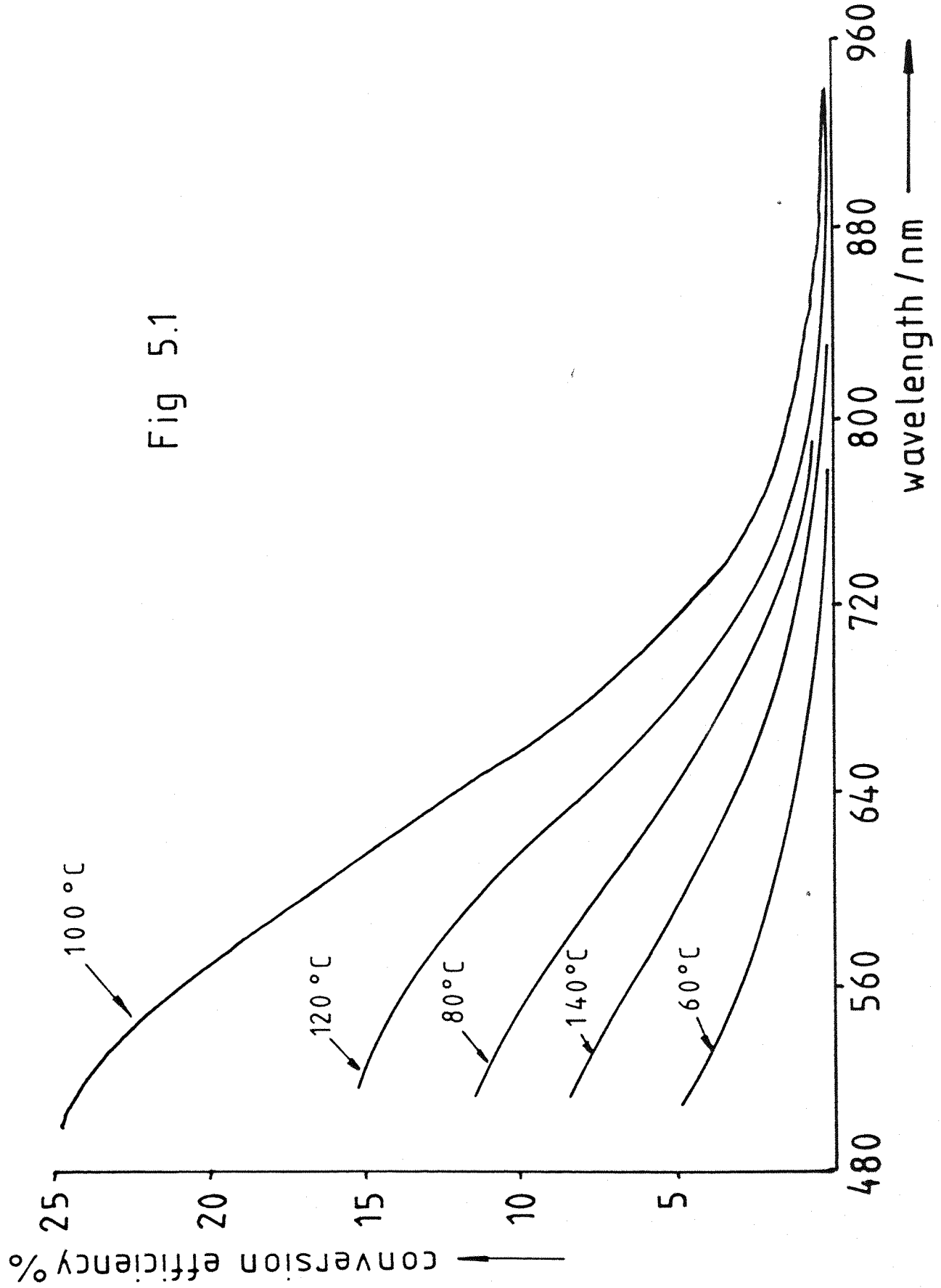
conversion efficiency %
25
20
15
10
5
480
560
640
720
800
880
960
wavelength / nm
100 °C
120 °C
80°C
140°C
60°C

Fig 5.1

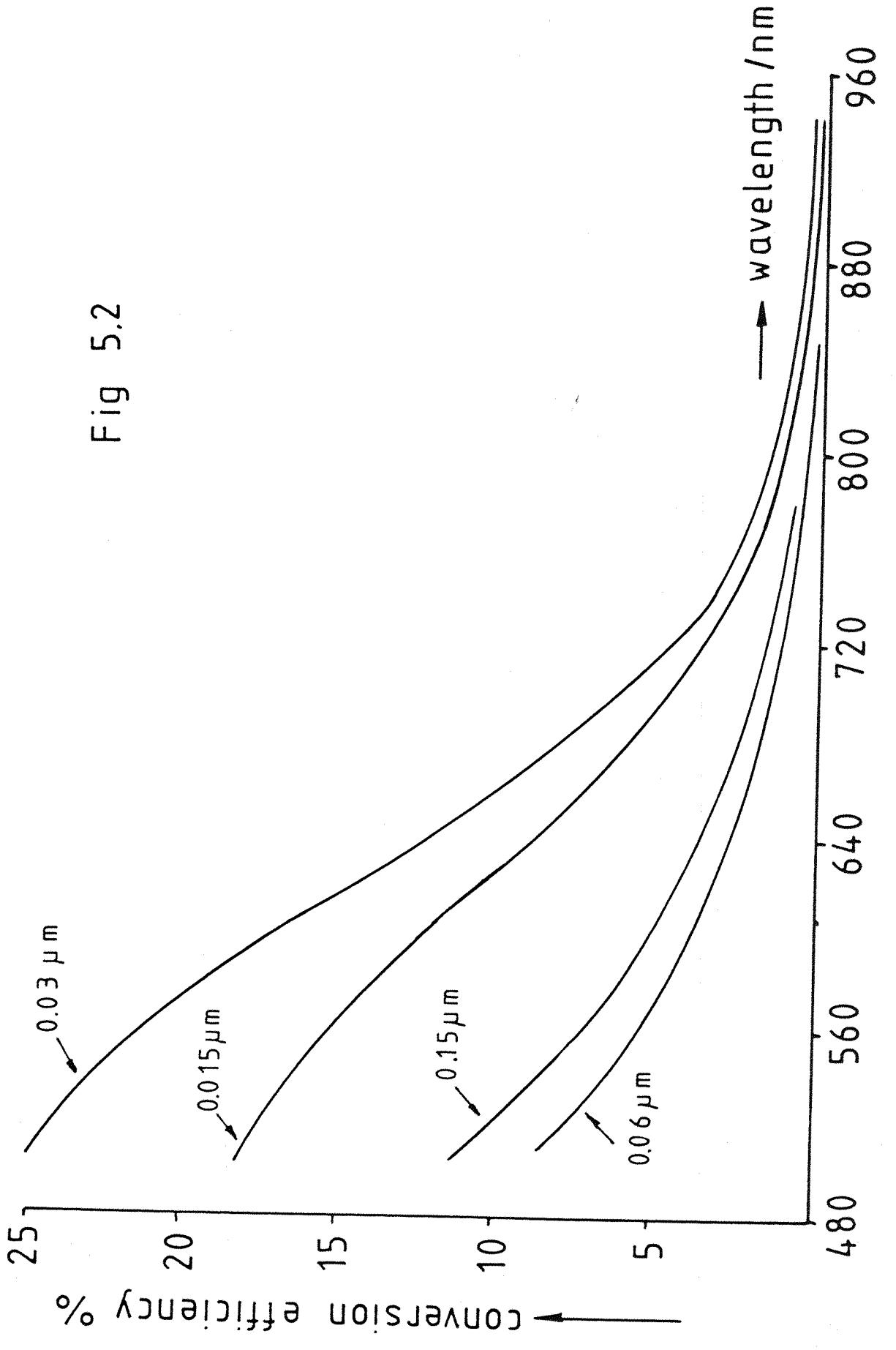
conversion efficiency %
25
20
15
10
5
480
560
640
720
800
880
960
wavelength/nm
0.03 µm
0.015µm
0.15µm
0.06 µm

Fig 5.2

less its efficiency, but when the film thickness is reduced below 0.03 micron, the efficiency ceases to rise.

Fig 5.3 shows amplified detail of the long wavelength response for the 0.03 micron film grown at 100 °C.

Recalling that, for an indirect transition, there is a linear relationship

$$\Phi.hv = \{W + L\}.A.\{hv - Eg\}^2 \qquad (2.31)$$

fig 5.3 was used to obtain Eg from a plot of $\{\Phi.hV\}^{1/2}$ versus hv. The graph (fig 5.4) is linear to a good approximation, and shows an indirect transition for this material occurs at 1.31 eV.

There was a general tendency for the conversion efficiency of a film to increase slowly over a period of hours if the specimen was allowed to stand in 0.1M sodium sulphide (with no electrical connection). Fig 5.5 shows the efficiency of the 0.03 micron film after 18 hours, and fig 5.6 shows the similar effect for a 0.15 micron film. There was some evidence that the efficiencies had stabilised at this time.

The effect is probably explained partly at least by the gradual oxidation of residual occluded bismuth metal to the sulphide by the sodium sulphide solution. It is also possible that there is a redistribution of the material of the film, through exchange with the electrolyte, which either creates a physically more effective surface for the absorption process (the roughness being of the same order of magnitude as the wavelength of the light), or that the crystal size and structure is affected in such a way as to facilitate the separation and collection of the charge carriers (highly doped regions in the bulk or along grain boundaries, and their associated trapping

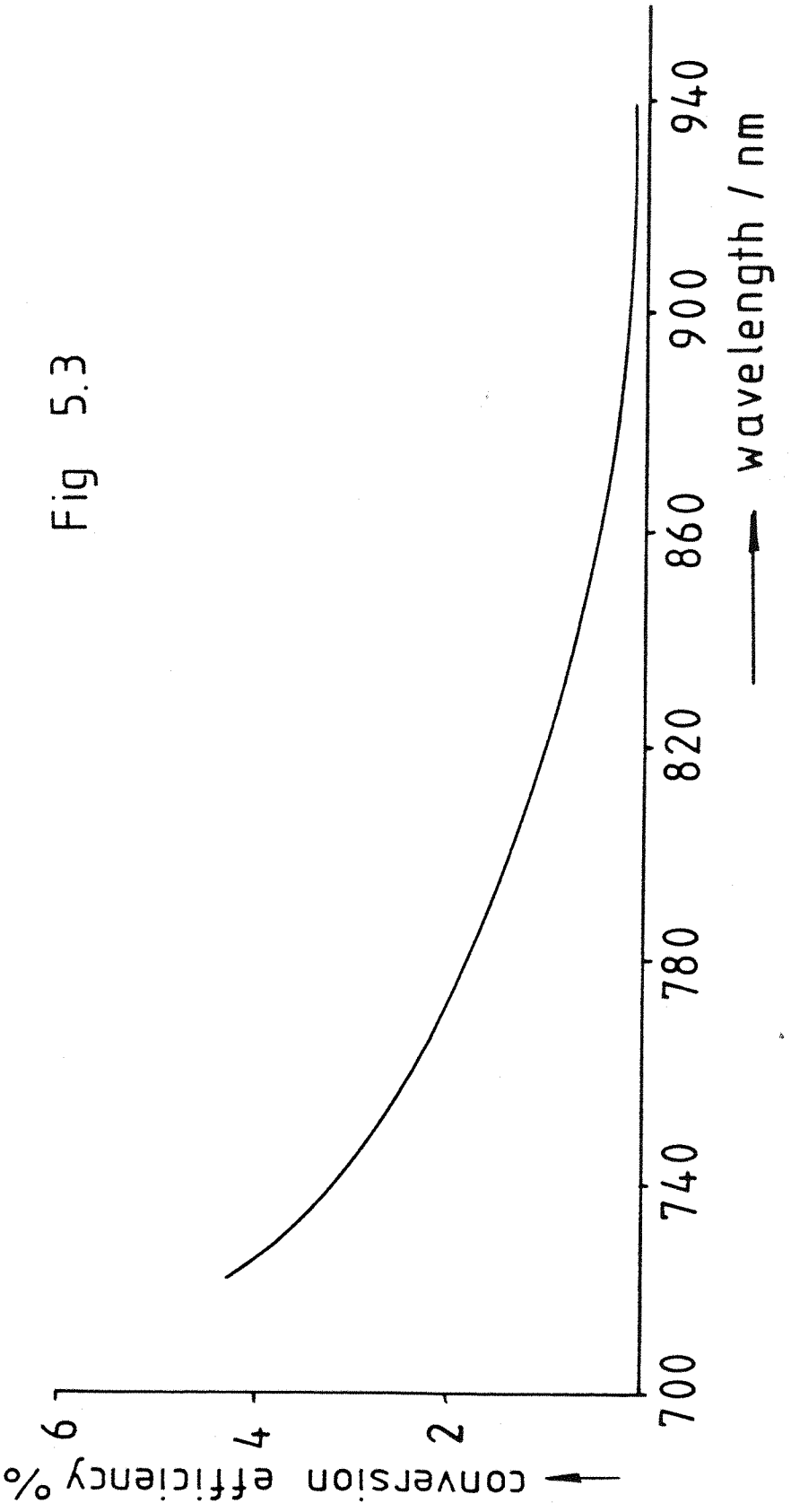
conversion efficiency %
6
4
2
700
740
780
820
860
900
940
wavelength / nm

Fig 5.3

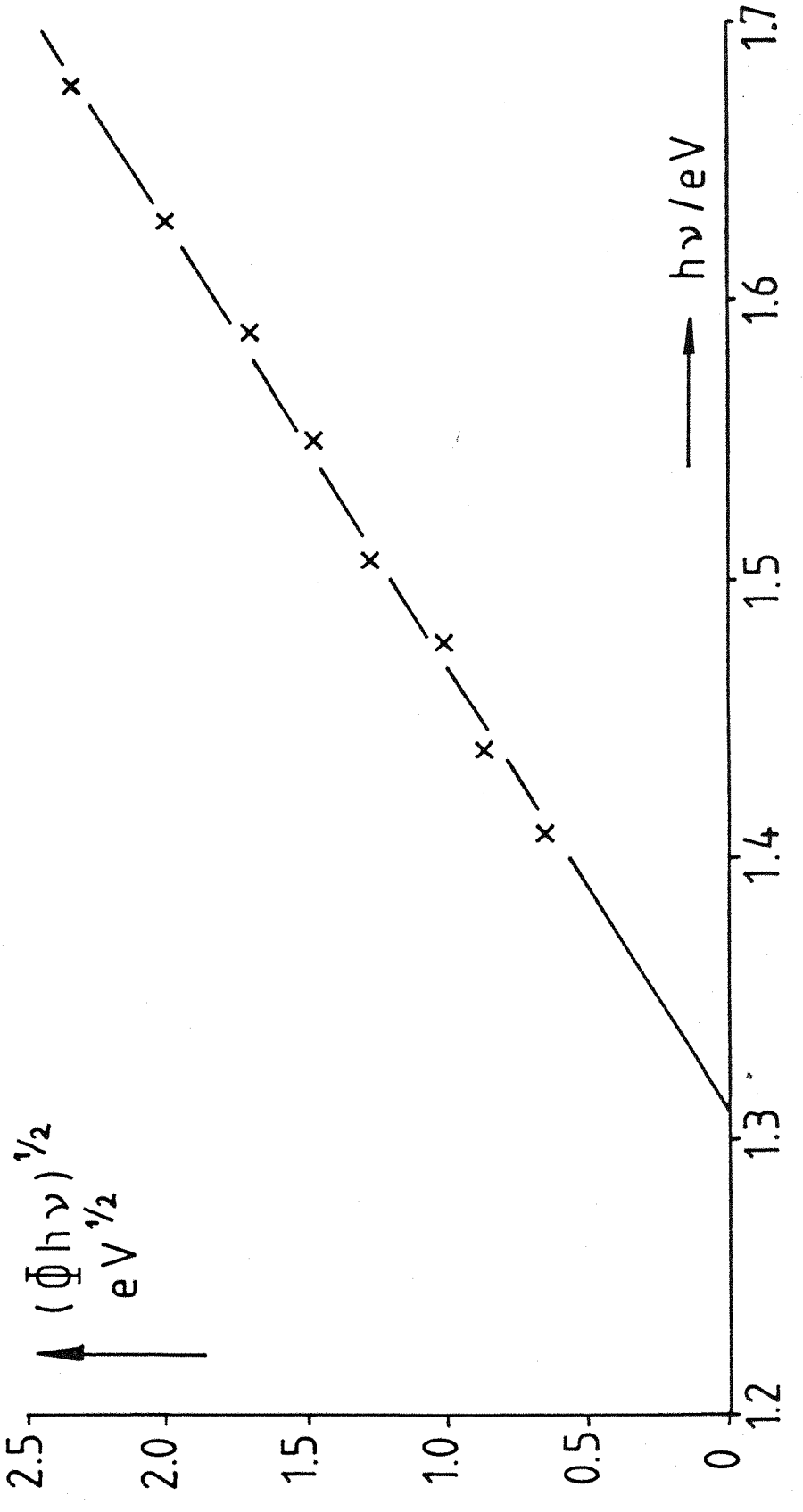

Fig 5.4

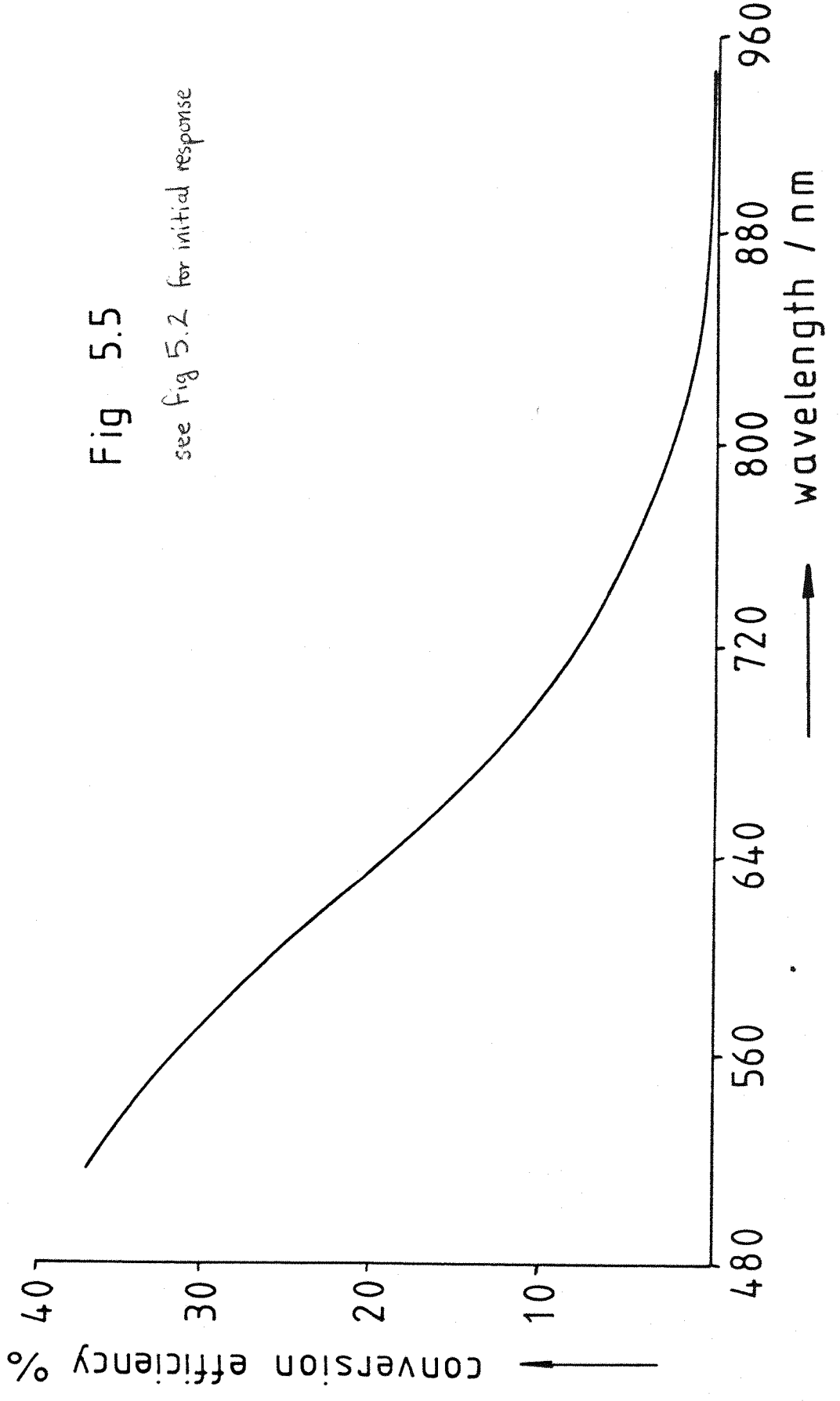

Fig 5.5

see Fig 5.2 for initial response

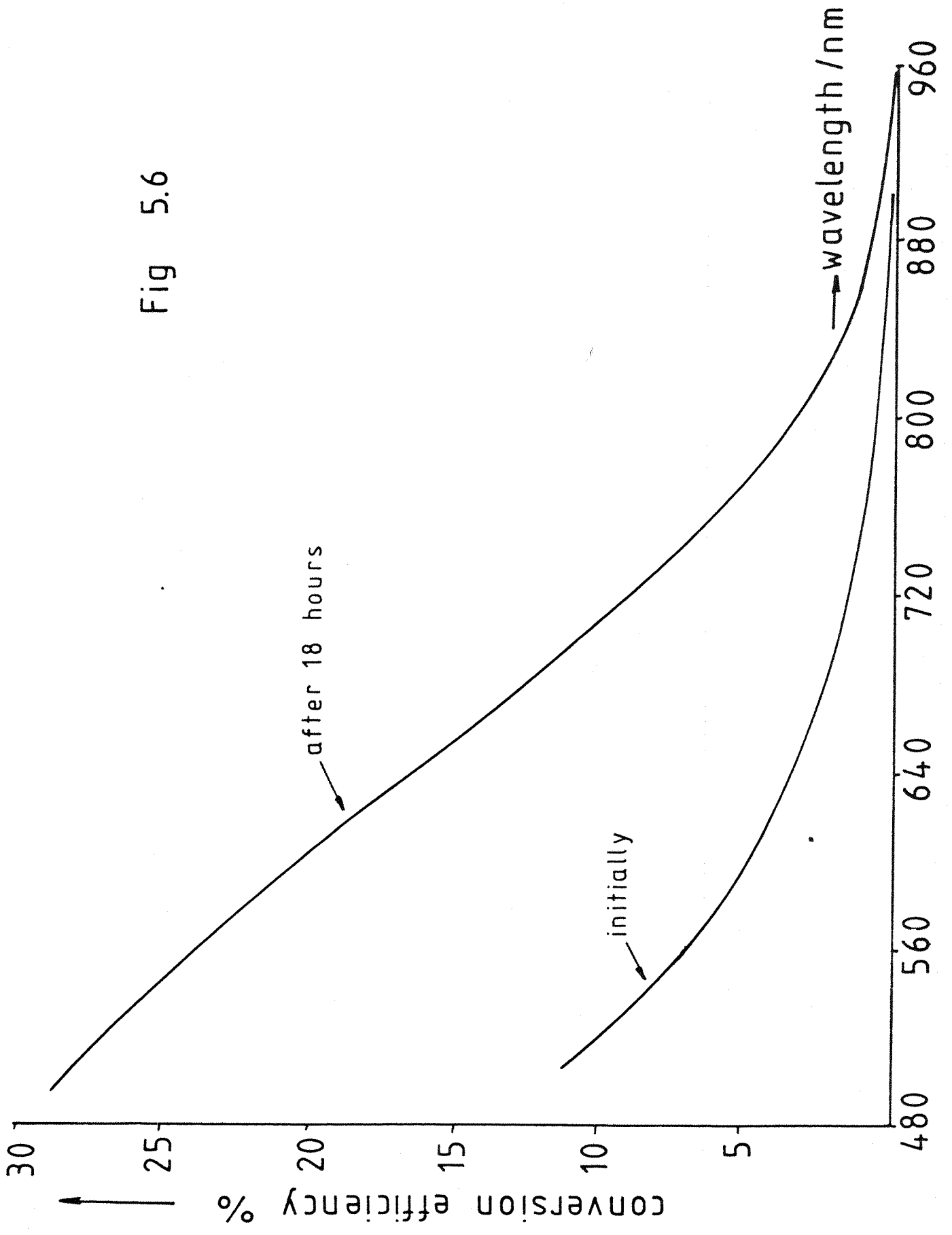
conversion efficiency %
30
25
20
15
10
5
480
560
640
720
800
880
960
wavelength/nm
after 18 hours
initially

Fig 5.6

sites could be partially eliminated if these are preferentially corroded).

A similar surface effect, perhaps involving the formation of bismuth oxychloride, could explain the increase in conversion efficiency observed after etching the samples in dilute hydrochloric acid (0.01M) for a few seconds. The enhancement of the photoresponse after etching in HCl was also noted by Peter [35]. A typical result is shown in fig 5.7, and fig 5.8 compares the results obtained for Eg before and after etching, using the same method as for fig 5.4, i.e. plotting $(\Phi.hv)^{1/2}$ versus hv. It was found that Eg decreased from 1.39 eV to 1.31 eV as a result of the etching. This represents an increase of about 55 nm in wavelength terms. By comparison, Peter [35] found the indirect transition to occur at 1.25 eV.

On the other hand, when a 0.03 micron film was potentiostatted at a positive voltage versus SCE, then after an initial slight fall, the photocurrent declined at a steady rate which was faster at higher potentials (fig 5.9). This is thought to be due to the formation of the photoelectrochemically inactive bismuth oxide. The effect is reversible, in that the photoresposnse returns almost completely over a period of hours at open circuit.

The dependence of the photocurrent, at the wavelength of maximum response, on the applied potential, is shown for a film deposited at a temperature of 80°C in fig 5.10. In both cases, the potential was scanned at 20mV per second from the more positive to the more negative potential.

Four such scans are shown, but the return sweeps, carried out at the same rate, are not shown for clarity. Due to noise on the

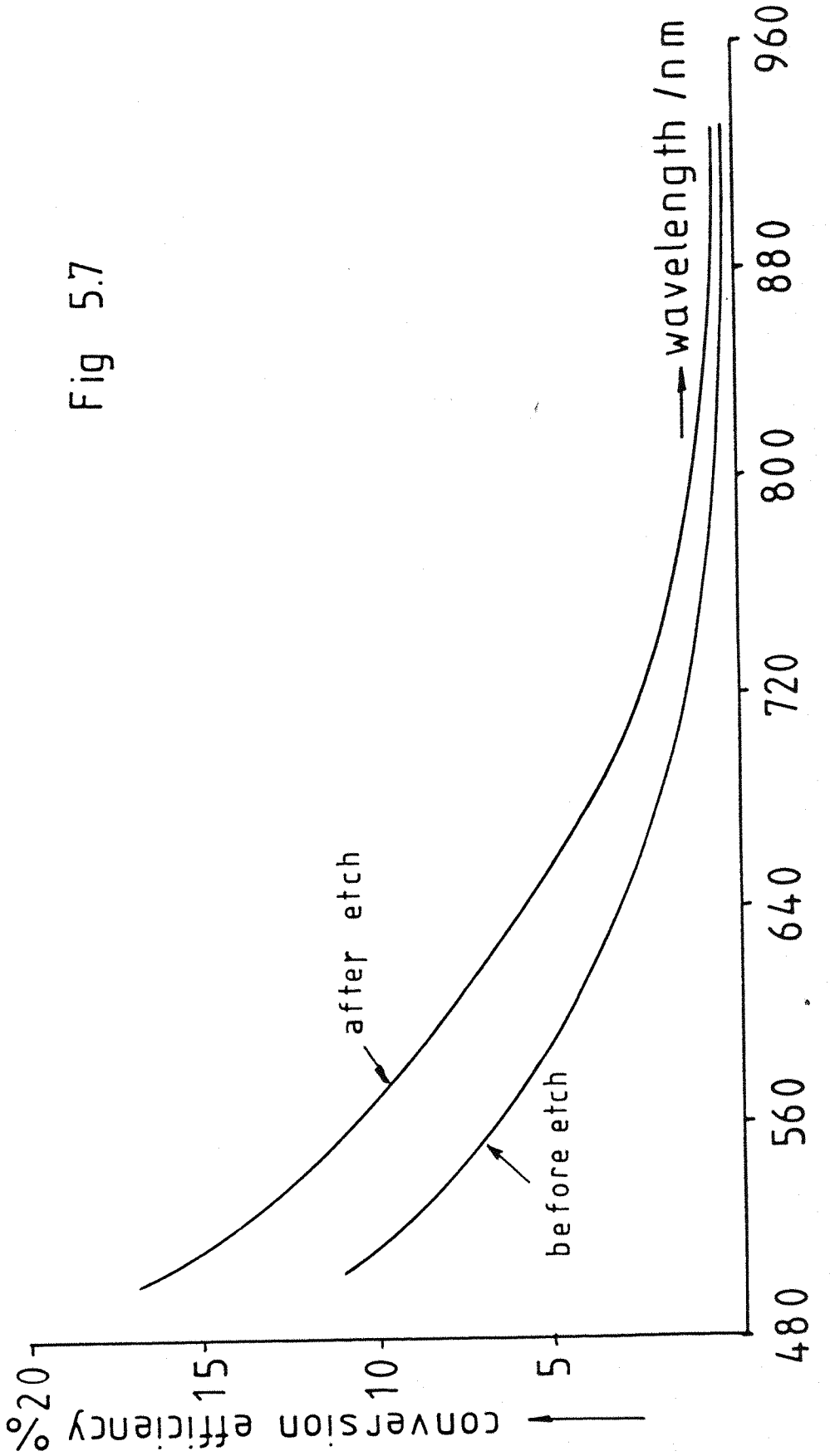
conversion efficiency %
20
15
10
5
480
560
640
720
800
880
960
wavelength /nm
after etch
before etch

Fig 5.7

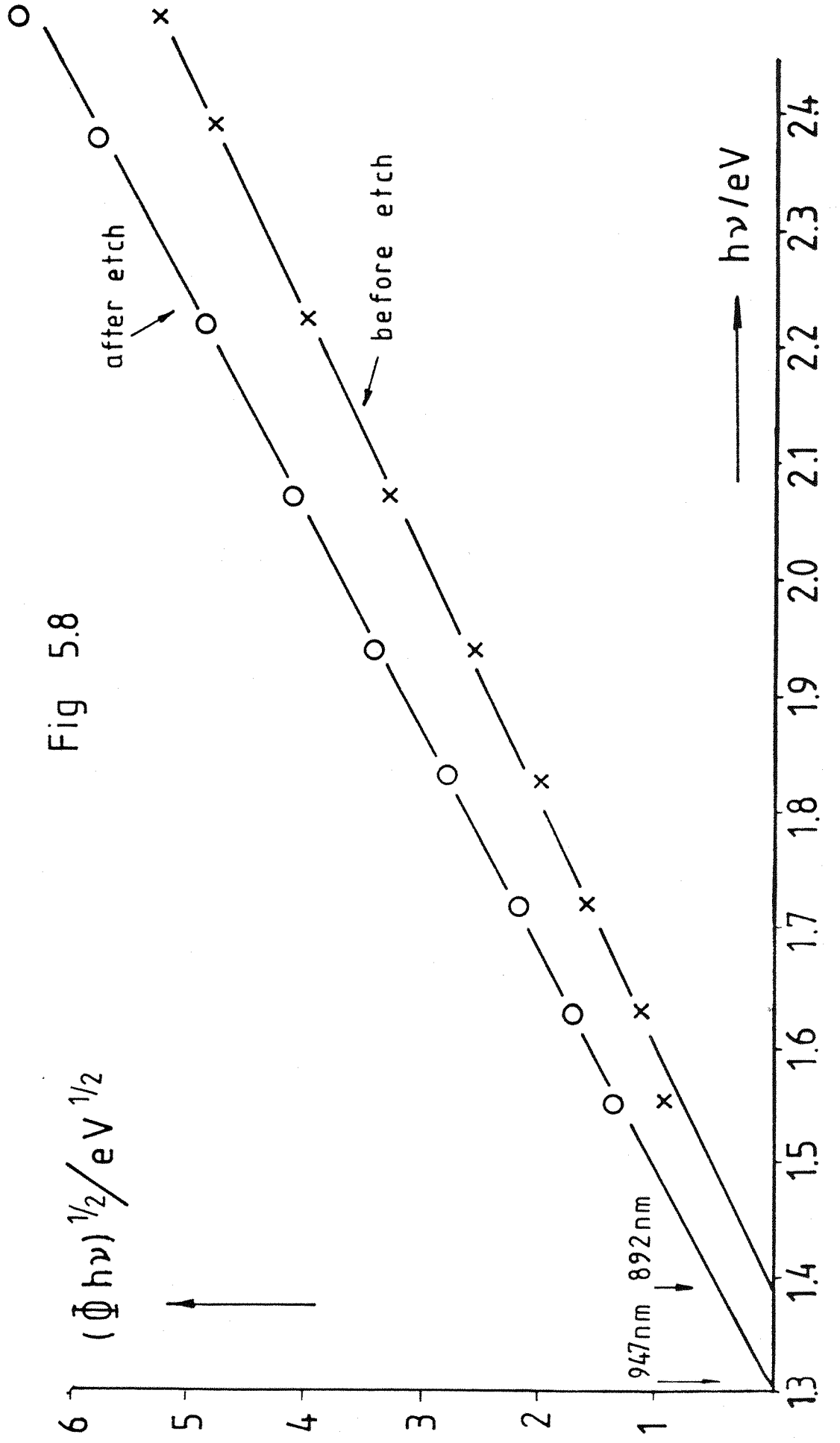
after etch
before etch
$(\Phi h\nu)^{1/2}/eV^{1/2}$
$h\nu/eV$
947nm
892nm
1
2
3
4
5
6
1.3
1.4
1.5
1.6
1.7
1.8
1.9
2.0
2.1
2.2
2.3
2.4

Fig 5.8

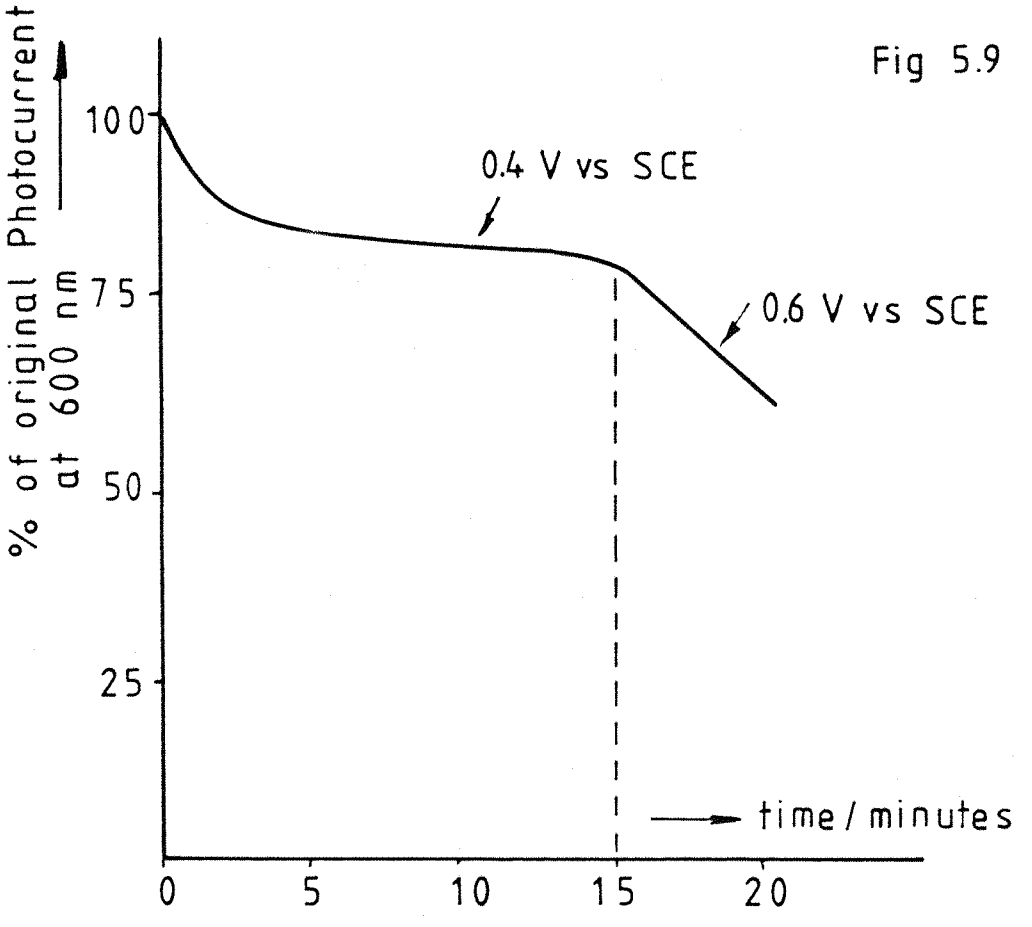
% of original Photocurrent at 600 nm
100
75
50
25
0.4 V vs SCE
0.6 V vs SCE
time / minutes
0
5
10
15
20

Fig 5.9

photocurrent signal at very low values, the actual signals obtained in this region have not been drawn, but rather the smooth trend from higher potentials has been extrapolated to the zero current axis, where the theory indicates it should meet it at the flat band potential. The intercepts obtained agree reasonably with the value of -0.95V versus SCE obtained by other methods.

Fig 5.11 shows a typical dark current cyclic voltammogram of the optimum bismuth sulphide film in 0.1M sodium sulphide, using a 20mV per second sweep rate. The peak at -0.2V versus SCE, and the plateau more positive of it, decrease in height with increasing scan number. There is a large dark current, suggesting that the film is porous, with substantial platinum electrochemistry occurring at the platinum back contact. A possible model of the surface structure is a bismuth sulphide deposit consisting of an array of blocks or stacks of the compound, separated by narrow vertical grooves and channels which often reach right down through the layer to the substrate.

(5.2) EFFECT OF CHANGING THE SUBSTRATE

All the work described in this section so far has been on a platinum substrate. In order to assess the effect of the substrate on the growth mechanism, and the properties of the thin films, several different substrate materials in the form of button electrodes were used in the plating bath.

Tantalum was the first substrate tried. The galvanostatic growth transient was flat. A charge equivalent to 0.1 microns of bismuth sulphide was passed, and a grey deposit was observed on the electrode. However, the cell current was very small when cyclic voltammetry was performed on the electrode between +1.0 and -1.0V versus SCE in 0.1M sodium sulphide. No photocurrent could be

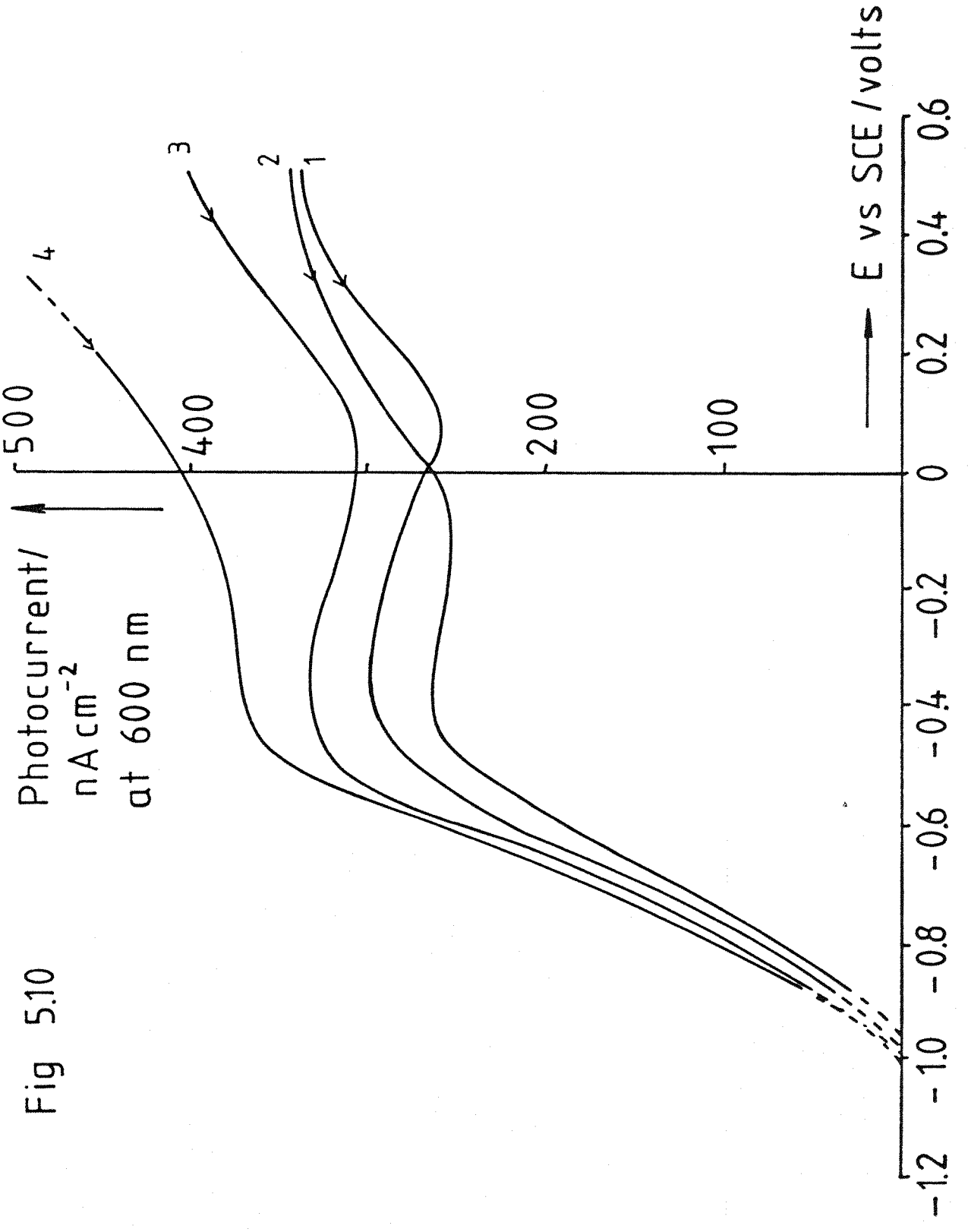
Photocurrent/
nA cm^{-2}
at 600 nm
500
400
200
100
0
1
2
3
4
E vs SCE / volts
0.6
0.4
0.2
0
-0.2
-0.4
-0.6
-0.8
-1.0
-1.2

Fig 5.10

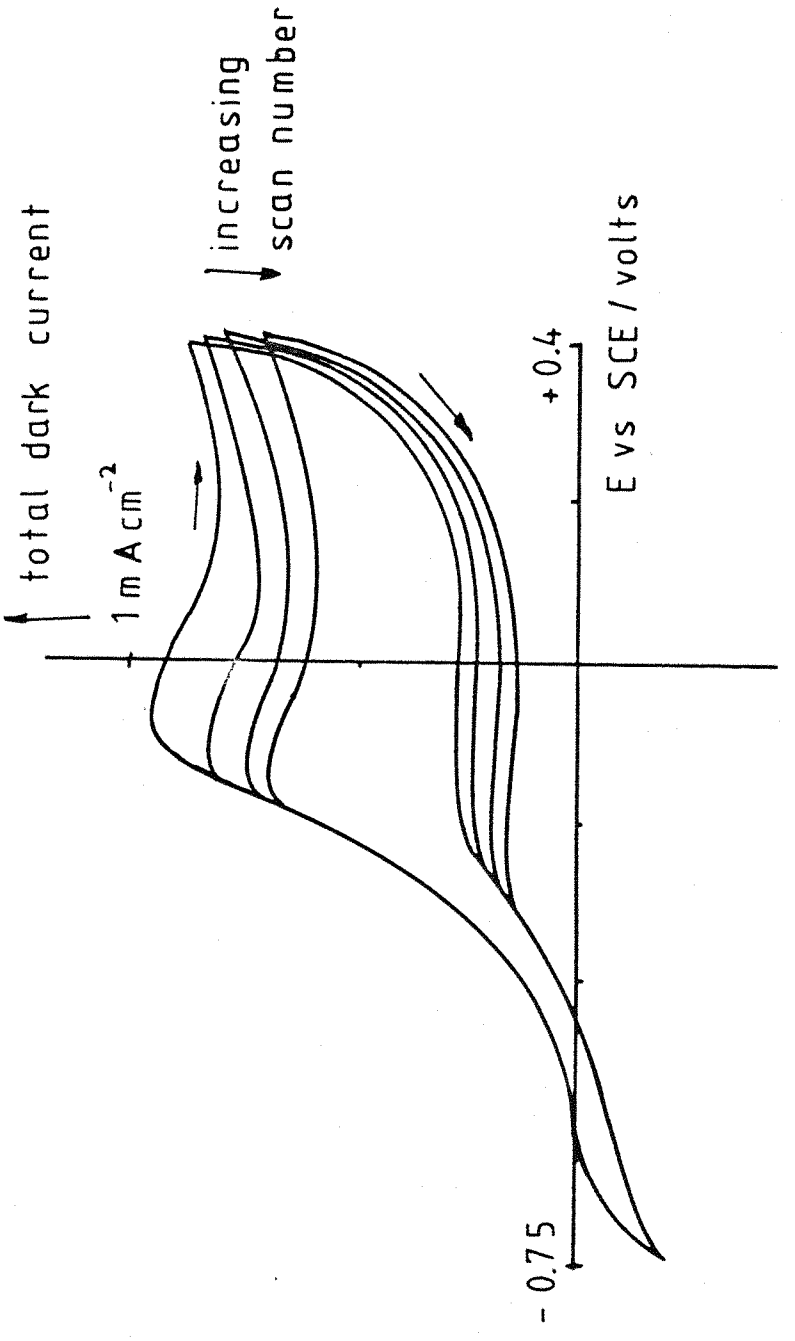
total dark current
1 m A cm^{-2}
increasing
scan number
+ 0.4
E vs SCE / volts
- 0.75

Fig 5.11

detected.

Niobium was then investigated. The results were much the same as for tantalum, with no detectable photocurrents, and a featureless voltammogram, although the dark current during cyclic voltammetry was larger, reaching 1 microamp per sq cm at +0.6 V versus SCE.

Vitreous carbon gave a more encouraging result. The galvanostatic growth curve remained flat during the deposition of 0.1 micron of bismuth sulphide. The deposit was light grey, and fairly smooth in appearance. A photocurrent conversion efficiency of about 2% at 500 nm was recorded (see fig 5.12). Again, Eg was estimatedby plotting $(\Phi.hv)^{1/2}$ versus hv, and was found to be 1.25 eV (fig 5.13).

The cyclic voltammograms of the bare substrate and the bismuth sulphide film on it are compared in fig 5.14, where it is seen that the rather large dark current at the bare carbon has been reduced by the application of the film.

(5.3) COMPARISON OF PHOTOCURRENT RESULTS WITH THOSE OF HIGH PURITY BISMUTH SULPHIDE GROWN BY THE BRIDGMAN METHOD

In order to assess the measured properties of electrodeposited thin films of polycrystalline bismuth sulphide, two samples of high purity crystalline bismuth sulphide were examined, using first the photocurrent spectroscopy apparatus, and then an apparatus to obtain the interfacial capacity of the crystals in 0.1M sodium sulphide, as a function of applied potential.

The crystals, which were dark, lustrous, and brittle, had been prepared by a previous member of the research group, Mohd. bin Kasiran, using the Bridgman method. A quartz ampoule containing

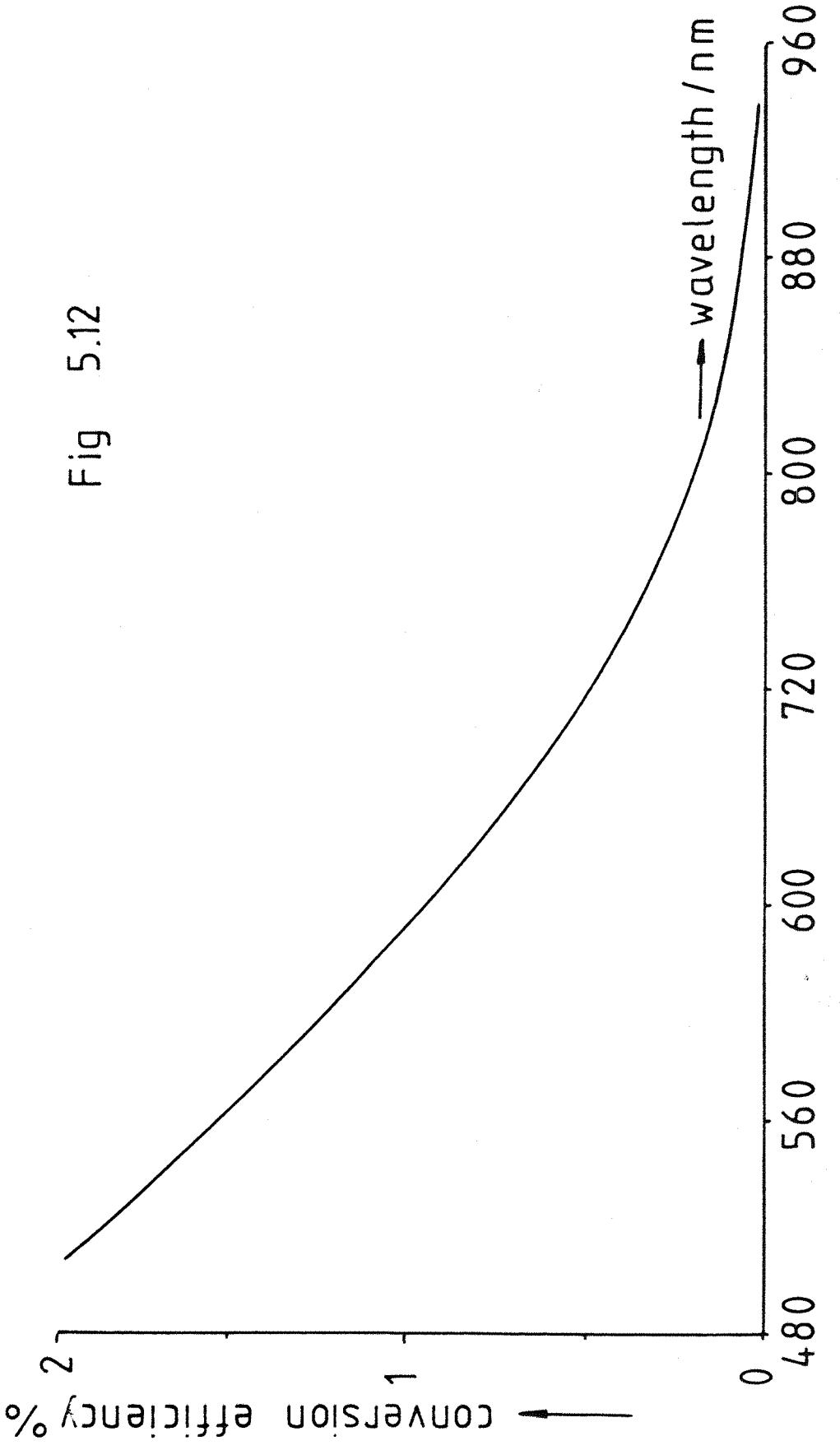
conversion efficiency %
2
1
0
480
560
600
720
800
880
960
wavelength / nm

Fig 5.12

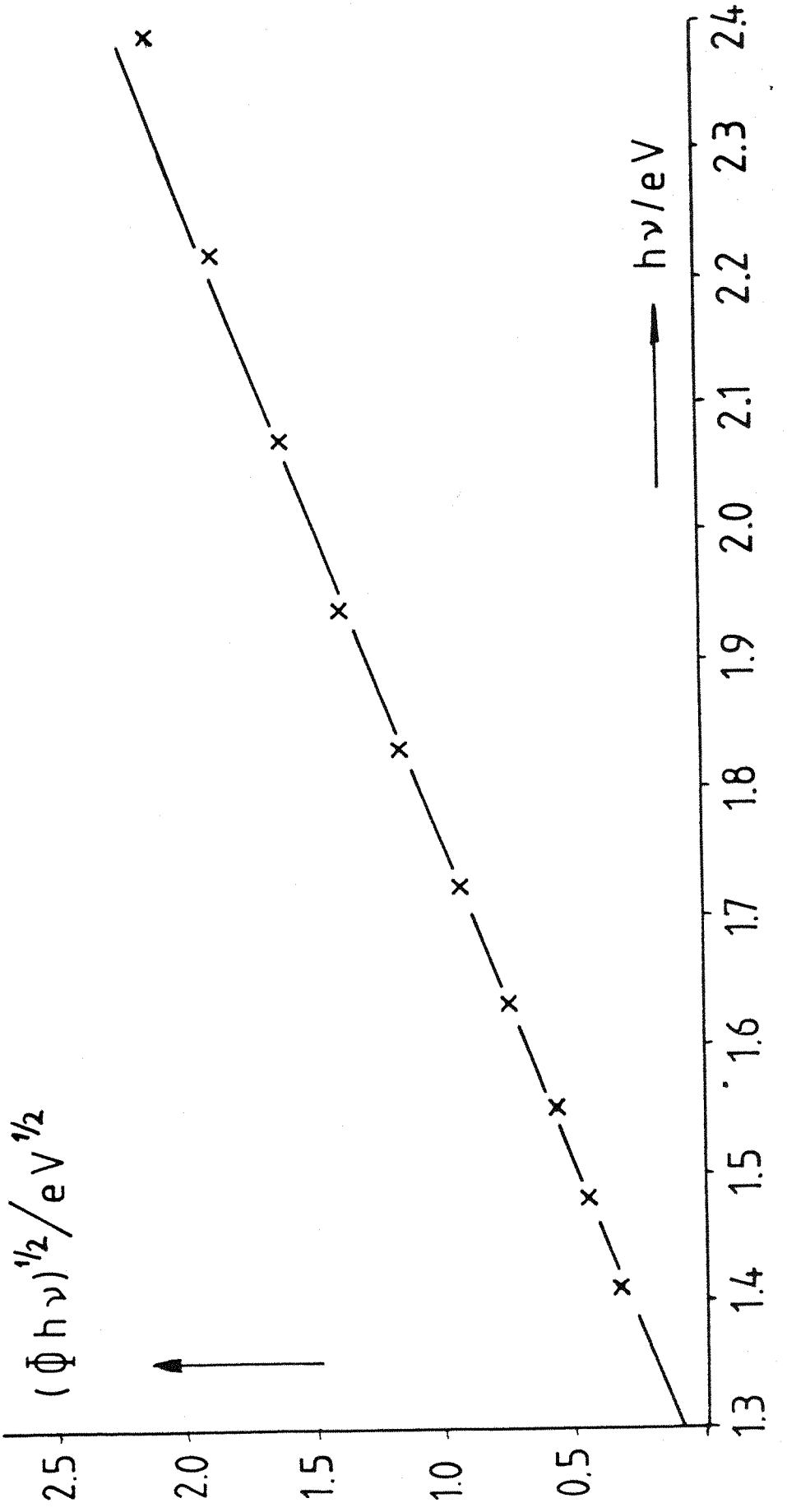

Fig 5.13

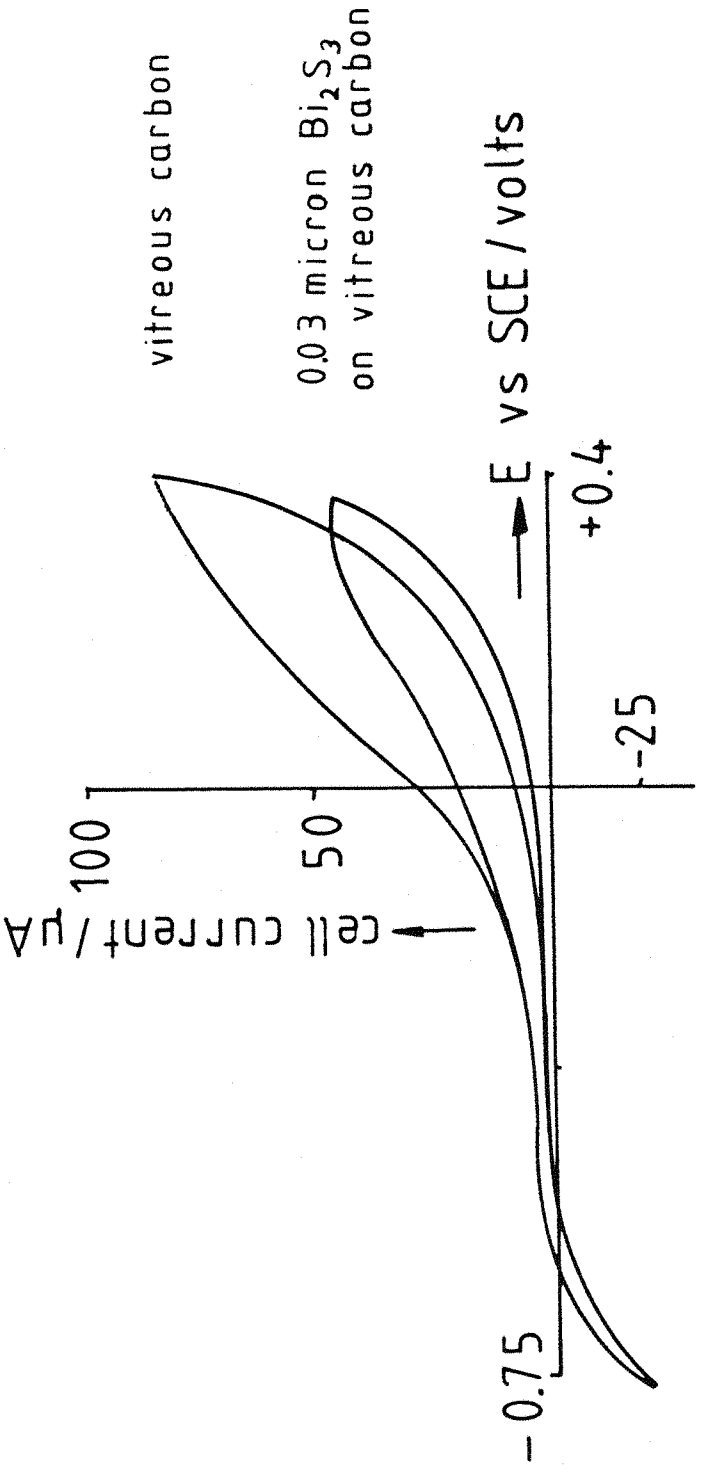
vitreous carbon
0.03 micron Bi_2S_3 on vitreous carbon
E vs SCE / volts
+0.4
-25
-0.75
100
50
cell current / μA

Fig 5.14

99.999% bismuth sulphide powder was suspended under 200 torr of nitrogen in a tubular oven wth a 50 °C. difference between top and bottom. After a few hours just above the melting point (685 °C.) the ampoule was lowered by motor at a rate of a few mm. per hour to recrystallise the compound.

Kasiran noted that the material appeared to be polycrystalline, and examination under an optical microscope confirmed that there were several individual grains in the pieces chosen for study.

Two batches of crystals were available, from each of which two button electrodes were made as shown in fig 5.15. A small hole of about 1mm. diameter was cut in a stiff sheet of plastic from a weighing boat, and the sample was fixed over this with epoxy adhesive. A thin film of indium metal was then evaporated under vacuum through the hole on to the exposed crystal, to give an ohmic contact. Next, a copper wire was attached to the indium using silver epoxy cement. The other end of the copper wire was then soldered to the copper disc which formed the recessed front surface of the button electrode mount. Finally, the rim of the plastic disc holding the sample was attached to the end of the button with silicone rubber glue. The button contained a recessed thread, into which a copper rod set in Kel-F could be screwed to give an electrode assembly long enough to protrude from the cell, allowing external wiring to be connected conveniently.

It was not possible to polish the crystals as much as would be preferred, due to their brittle nature, and so the suface was rough both macroscopically and microscopically.

The apparatus and method used to investigate the photoelectrochemistry of the samples were essentially the same as previously used to characterise the cadmium sulphide thin film

Fig 5.15

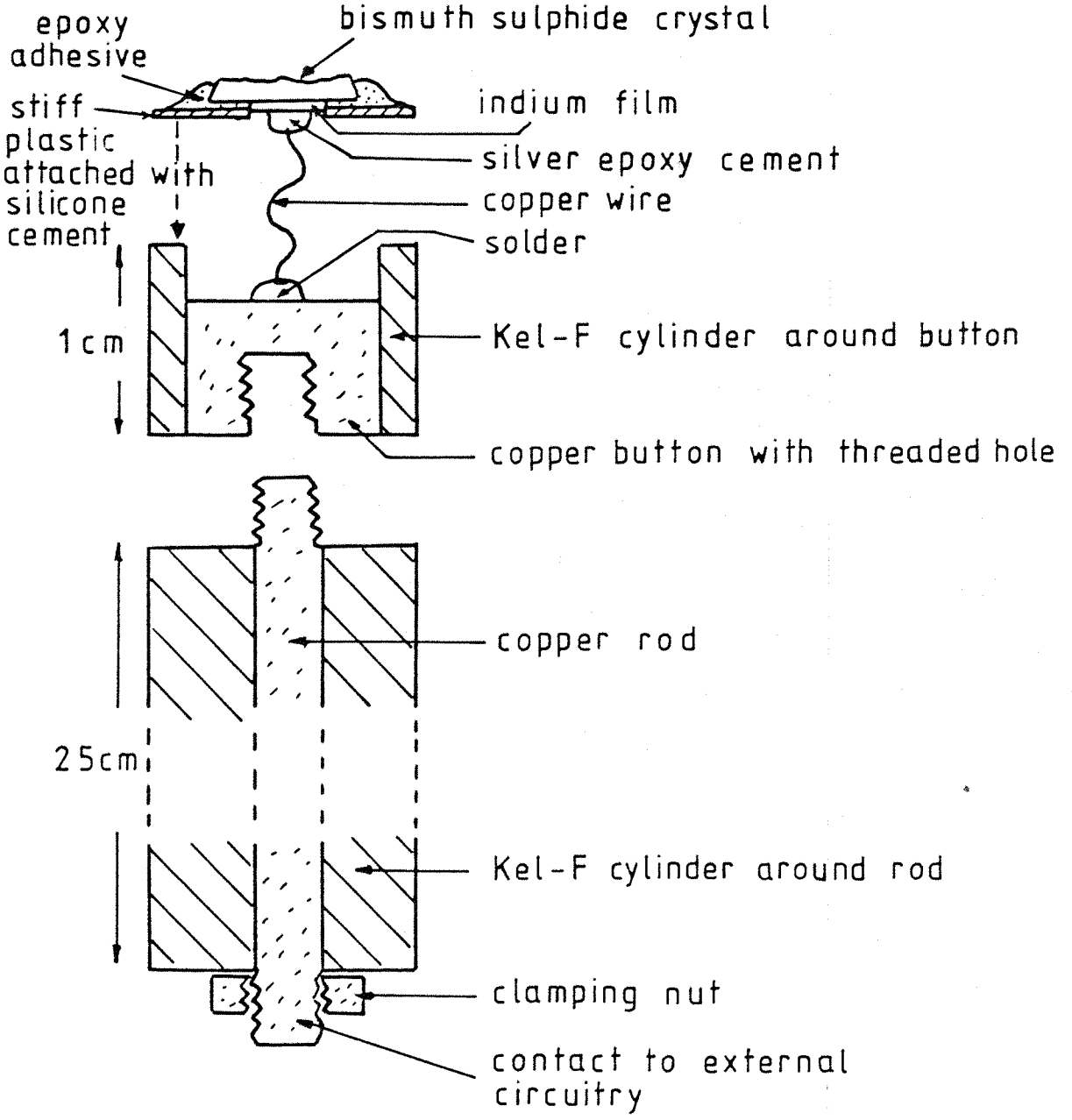
epoxy adhesive
bismuth sulphide crystal
stiff plastic attached with silicone cement
indium film
silver epoxy cement
copper wire
solder
1 cm
Kel-F cylinder around button
copper button with threaded hole
copper rod
25cm
Kel-F cylinder around rod
clamping nut
contact to external circuitry

semiconductors.

Fig. 5.16 shows the variation in photocurrent conversion efficiency of the samples with wavelength at various applied potentials.

Recalling equation 2.14 from the section dealing with the Gartner equation and its predictions, we have:

$$-\ln(1 - \Phi) = \alpha . W \qquad (2.14)$$

and hence

$$W = -\ln(1 - \Phi)/\alpha \qquad (5.1)$$

Hence we can use the curves in fig 5.16 to obtain plots of the space charge thckness W versus wavelength, at given potentials E, provided that we have values for the absorption coefficient. Using values of the latter from the paper by Peter [35], these plots were constructed, and are shown in fig 5.17: the average values of W as a function of potential are summarised in table 5.1.

From equations 2.4 and 2.5 we have that

$$W = (2.\varepsilon.\varepsilon(0)/e.Nd)^{1/2}. (E - Efb)^{1/2} \qquad (5.2)$$

so that we can obtain values for the doping density Nd at these potentials assuming values for the relative permittivity and the flat band potential Efb.

Assuming Efb= -0.90V and ε=10, average values of Nd were obtained from the plots in fig 5.17. These are also summarised in table 5.1. The values of Nd obtained are of the order of 1 to 6 x 10^{16} cm^{-3} ., showing a tendency to increase at potentials less than 0.0V vs the saturated calomel electrode, where the photocurrent is

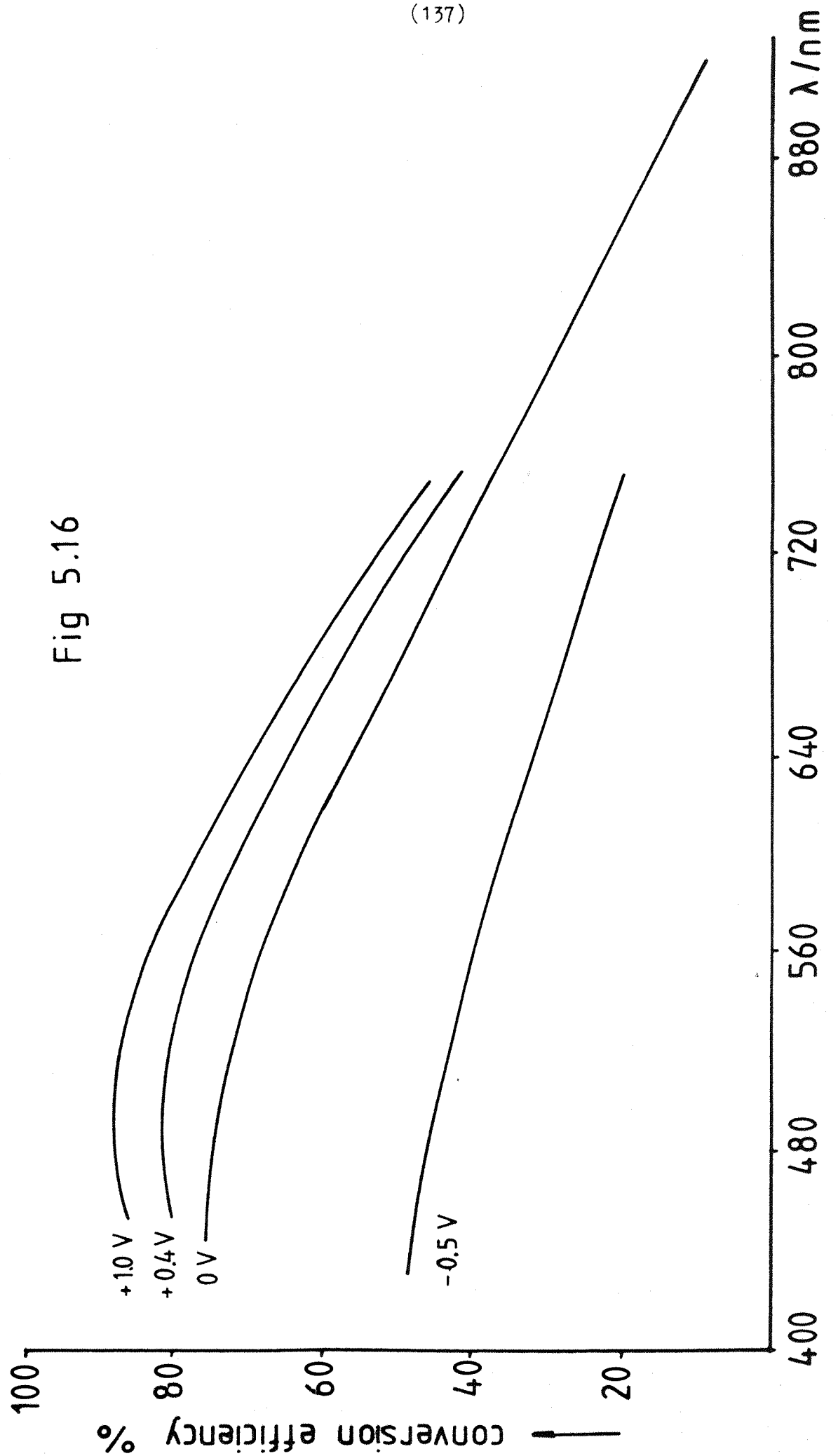
100
80
60
40
20
conversion efficiency %
400
480
560
640
720
800
880 λ/nm
+1.0 V
+0.4 V
0 V
-0.5 V

Fig 5.16

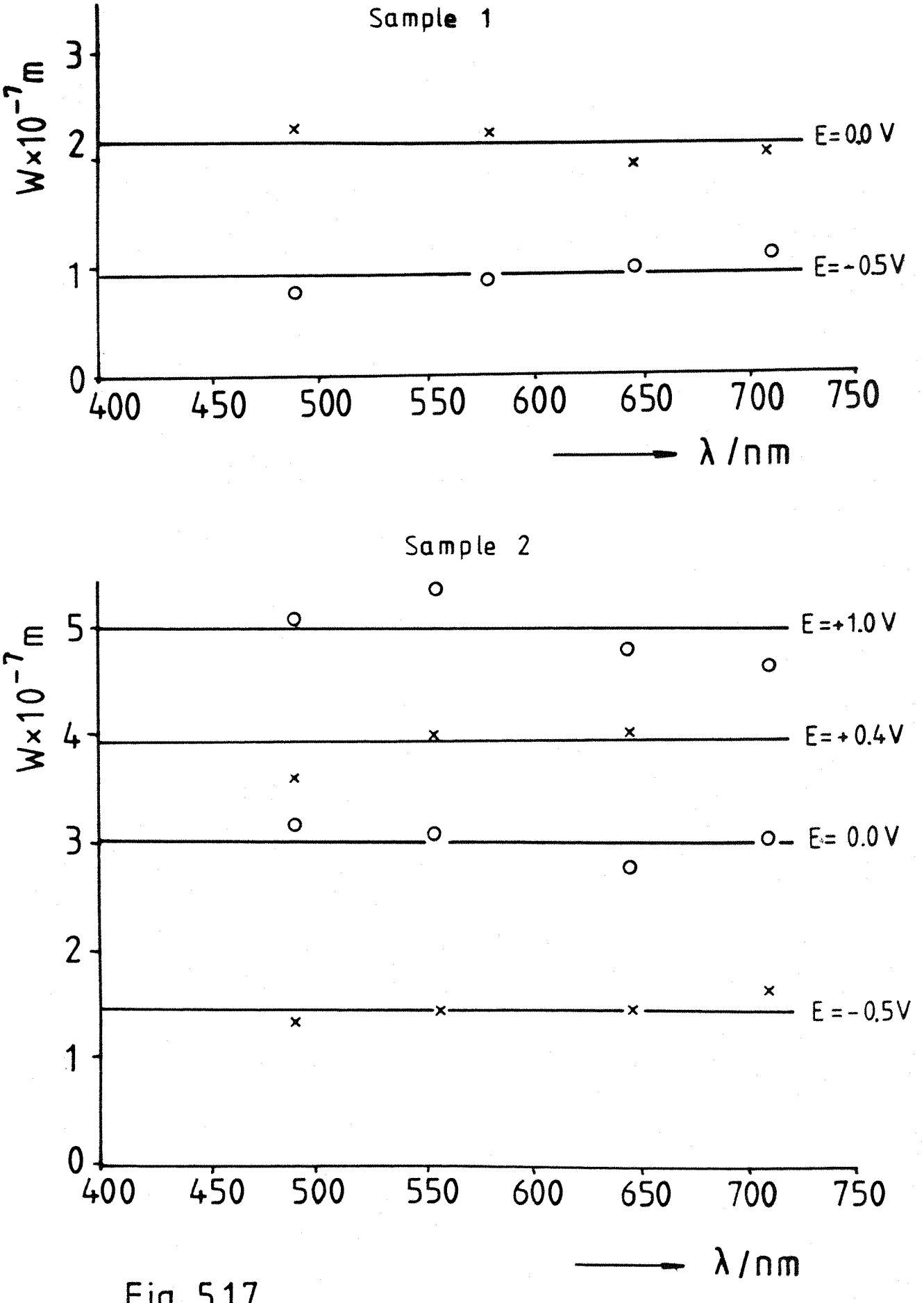
Sample 1
W×10⁻⁷m
3
2
1
0
E=0.0 V
E=-0.5V
400
450
500
550
600
650
700
750
λ/nm
Sample 2
W×10⁻⁷m
5
4
3
2
1
0
E=+1.0 V
E=+0.4V
E= 0.0 V
E=-0.5V
400
450
500
550
600
650
700
750
λ/nm

Fig 5.17

TABLE 5.1

SAMPLE NUMBER	POTENTIAL (VOLTS)	AVERAGE SPACE CHARGE THICKNESS (MICRONS)	CARRIER DENSITY cm^{-3}
1	-0.5	0.09	5.5×10^{16}
1	0.0	0.22	2.1×10^{16}
2	-0.5	0.15	2.0×10^{16}
2	0.0	0.30	1.1×10^{16}
2	0.4	0.39	0.9×10^{16}
2	1.0	0.50	0.8×10^{16}

TABLE 5.2

WAVELENGTH nm	SLOPE $V^{1/2}$	ABSORPTION COEFFICIENT cm^{-1}	CARRIER DENSITY cm^{-3}
400	0.60	5.5×10^{4}	9.2×10^{16}
500	0.75	4.2×10^{4}	3.4×10^{16}
700	0.30	1.5×10^{4}	2.8×10^{16}

less than that predicted by the Gartner equation.

Photocurrent-potential curves were also obtained for the samples over a range of wavelengths from 400 to 700nm (fig 5.18). The photocurrent axes of these curves were calibrated in terms of conversion efficiency by comparison with the relevant photocurrent-wavelength curves.

It has been shown that the simplified form of the Gartner equation, with the assumption that the diffusion length of the minority carriers is zero, can be rearranged to give Nd from the slope of a plot of $-\ln(1-\Phi)$ against the root of the band bending:

$$-\ln(1-\Phi) = \alpha\{2.\varepsilon.\varepsilon(0)/e.Nd\}^{1/2}.(E-Efb)^{1/2} \qquad (2.17)$$

Fig 5.19 shows these plots, and table 5.2 gives the calculated values of Nd assuming $\varepsilon=10$ and using the absorption coefficient values as above. The values of Nd obtained are again of the order of 10^{16} per cc.

Equation (2.17) can be squared on both sides, allowing $\{-\ln(1-\Phi)\}^2$ to be plotted against E to obtain Efb as the intercept on the E axis (see fig 5.20). The points more positive than -0.4V lie on straight lines, within experimental error, and give Efb values of -0.95V +/- 0.05V.

Assuming $\alpha.W \ll 1$, $\alpha.L \ll 1$, and $L \ll W$, we can use equation 2.22 to find Efb from a plot of Φ^2 versus E:

$$\Phi^2 = 2.\alpha^2.\varepsilon.\varepsilon(0).(E - Efb)/e.Nd \qquad (2.22)$$

The plot is given in fig 5.21, and the value of Efb obtained from the intercept is -0.90 V +/- 0.05V.

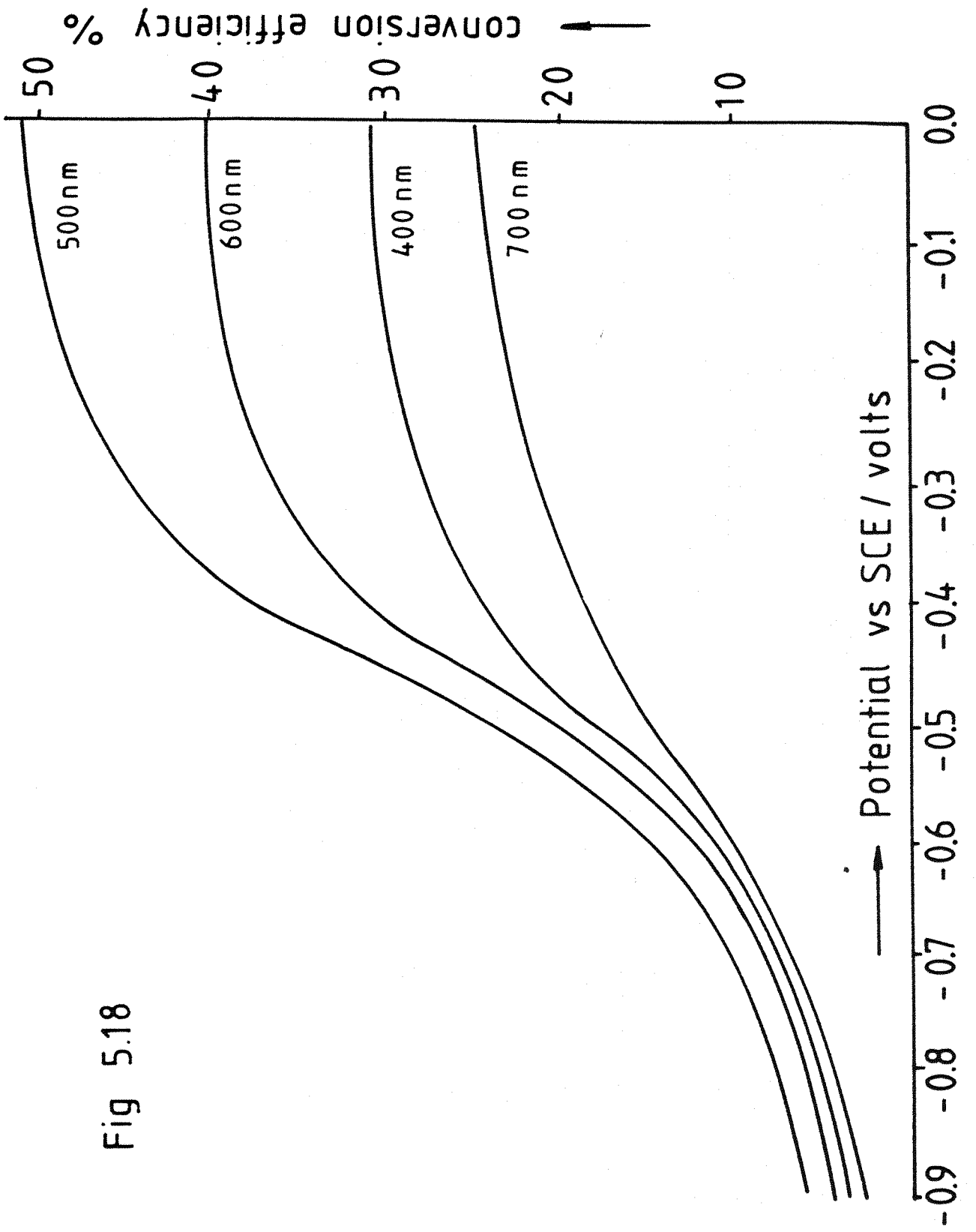
conversion efficiency %
50
40
30
20
10
500 nm
600 nm
400 nm
700 nm
Potential vs SCE / volts
0.0
-0.1
-0.2
-0.3
-0.4
-0.5
-0.6
-0.7
-0.8
-0.9

Fig 5.18

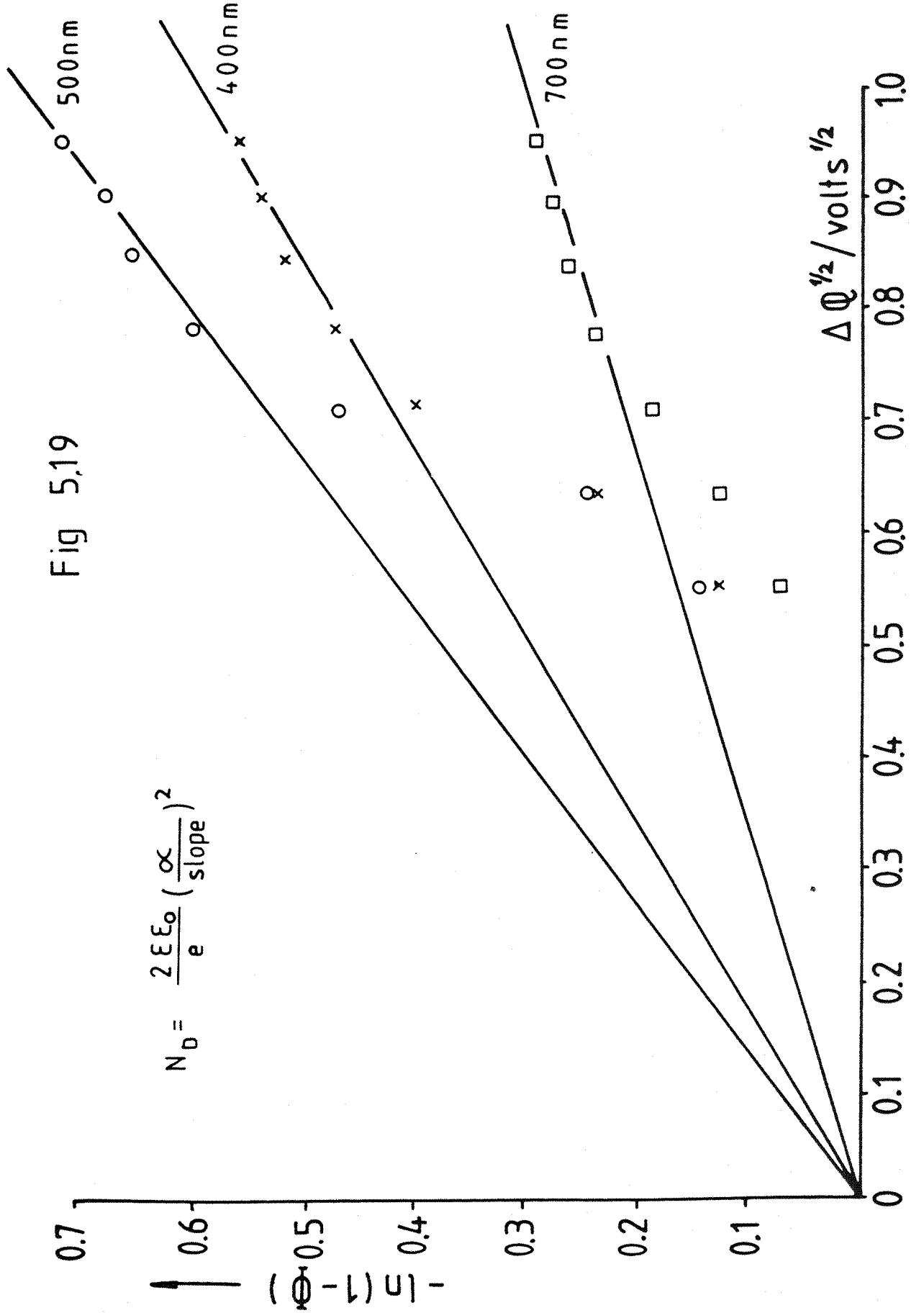
500nm
400nm
700nm
$\Delta Q^{1/2}$/volts$^{1/2}$
0
0.1
0.2
0.3
0.4
0.5
0.6
0.7
0.8
0.9
1.0
$-\ln(1-\Phi)$
$N_D = \frac{2\varepsilon\varepsilon_0}{e}\left(\frac{\alpha}{\text{slope}}\right)^2$

Fig 5.19

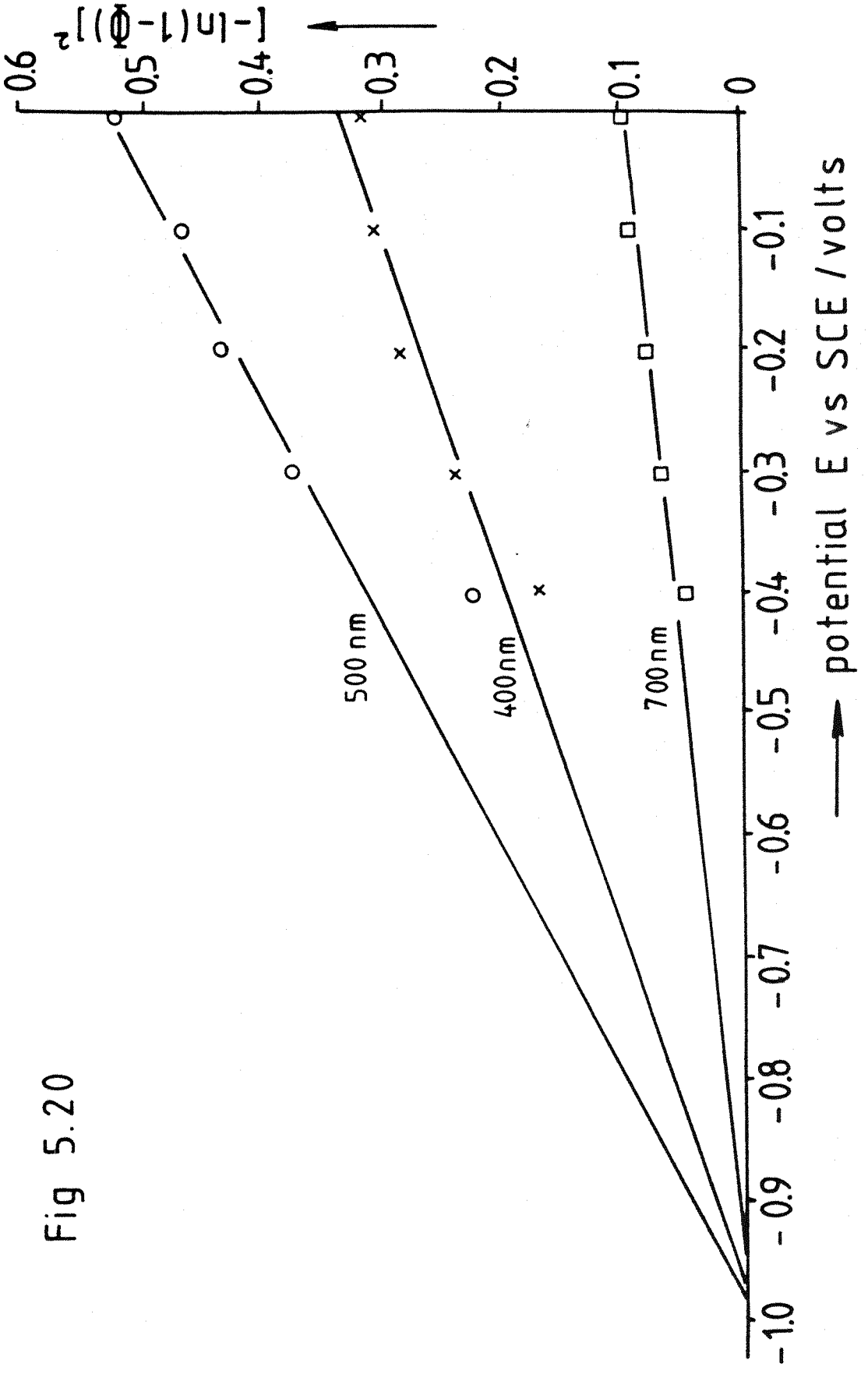
0.6
0.5
0.4
0.3
0.2
0.1
0
-0.1
-0.2
-0.3
-0.4
-0.5
-0.6
-0.7
-0.8
-0.9
-1.0
potential E vs SCE / volts
500 nm
400nm
700nm

Fig 5.20

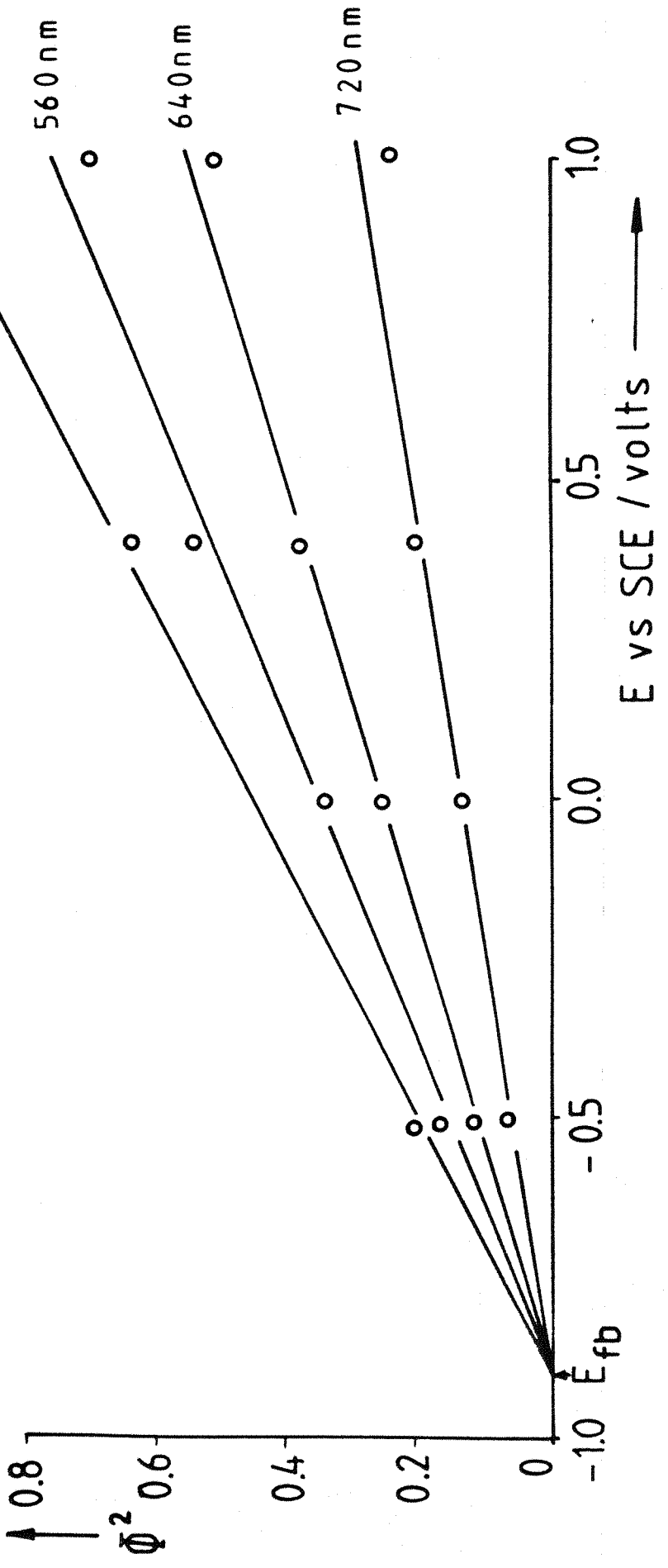
480 nm
560 nm
640 nm
720 nm
Φ^2
0.8
0.6
0.4
0.2
0
-1.0
E_{fb}
-0.5
0.0
0.5
1.0
E vs SCE / volts

Fig 5.21

The nature of the optical transition was investigated by inserting values for n of 1/2 and 2 in equation 2.28:

$$\alpha = A.(h\nu - Eg)^{n} \; / \; h\nu \qquad (2.28)$$

to test for a direct and indirect allowed transition respectively. These graphs are shown in figs 5.22 and 5.23. It is seen that the test for a direct transition is negative, whereas there is clearly an indirect transition, with an energy gap of 1.10 eV from the intercept.

Assuming an indirect transition, a plot of $(\Phi.h\nu)^{1/2}$ versus hv was plotted to determine the energy gap Eg from

$$\Phi.h\nu = \{W + L\}.A.\{h\nu - Eg\}^{2} \qquad (2.31)$$

The value of Eg was found to be 1.03 eV (fig 5.24). This is lower than the values found earlier, by similar calculations, for thin film bismuth sulphide samples. It is also lower than the value of around 1.2 eV found by other workers [79,80].

Fig 5.25 shows the dark current as a function of applied potential during the cyclic voltammetry of the bismuth sulphide samples in 0.1 M sodium sulphide. As can be seen, there is little hysteresis, indicating that there is no net deposition or dissolution. The dark current is about 250 microamps per sq. cm. at 0.0V vs calomel, rising to about 700 at +0.5V. The high values indicate that the layer is very imperfect, and not exhibiting blocking Schottky barrier behaviour. The presence of cracks would again account for this effect.

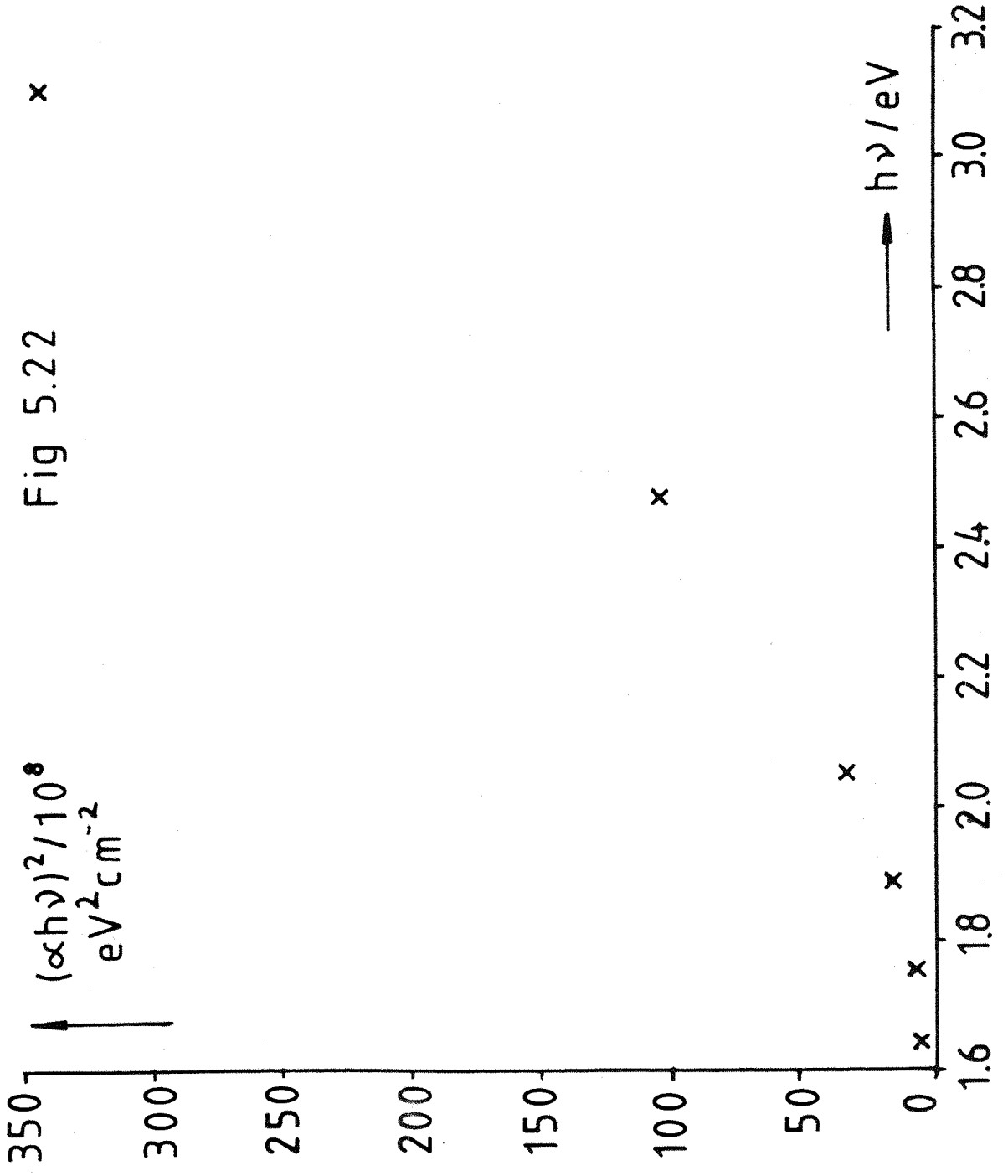
(αhν)²/10⁸
eV²cm⁻²
350
300
250
200
150
100
50
0
1.6
1.8
2.0
2.2
2.4
2.6
2.8
3.0
3.2
hν/eV

Fig 5.22

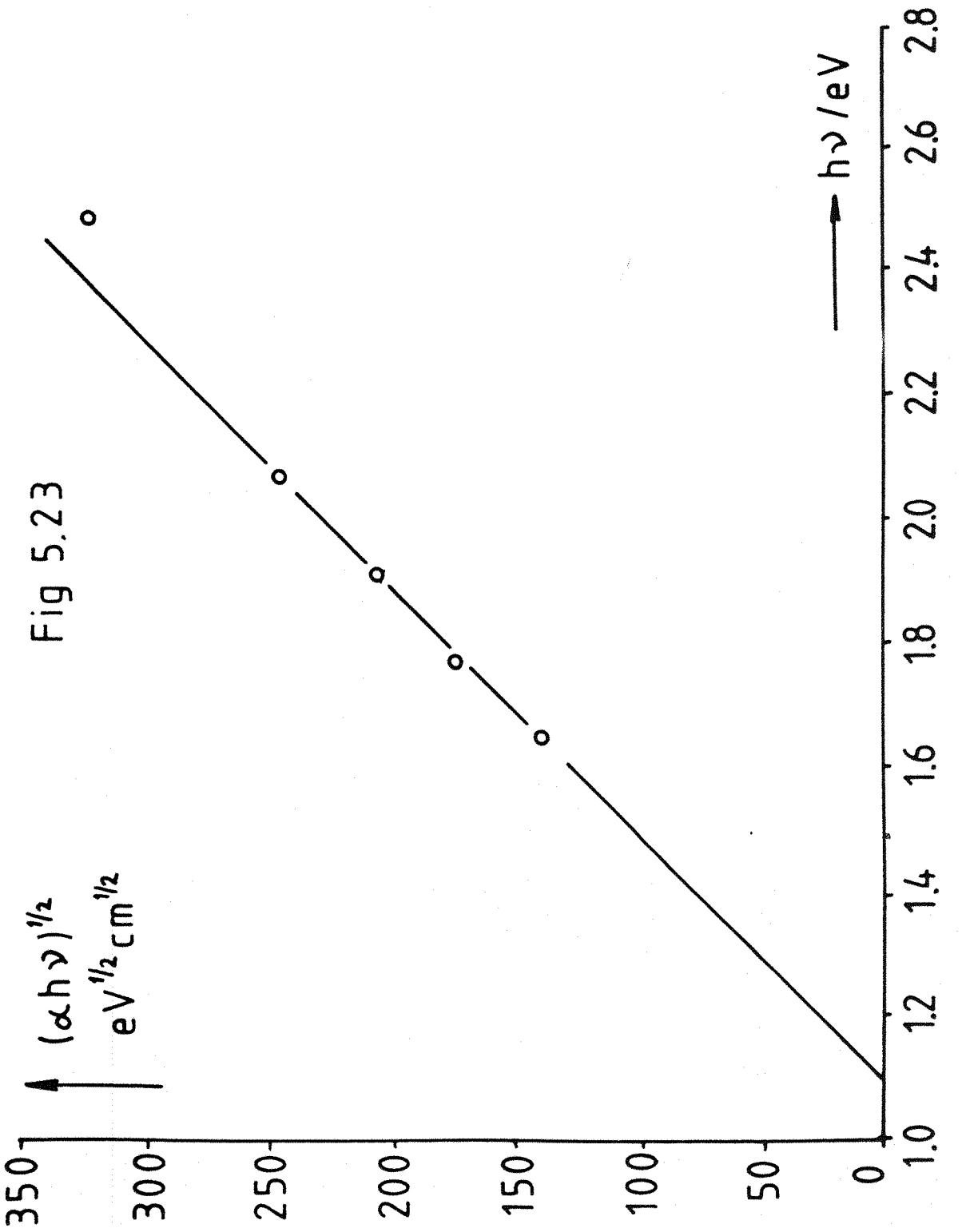
(αhν)^1/2
eV^1/2 cm^1/2
350
300
250
200
150
100
50
0
1.0
1.2
1.4
1.6
1.8
2.0
2.2
2.4
2.6
2.8
hν/eV

Fig 5.23

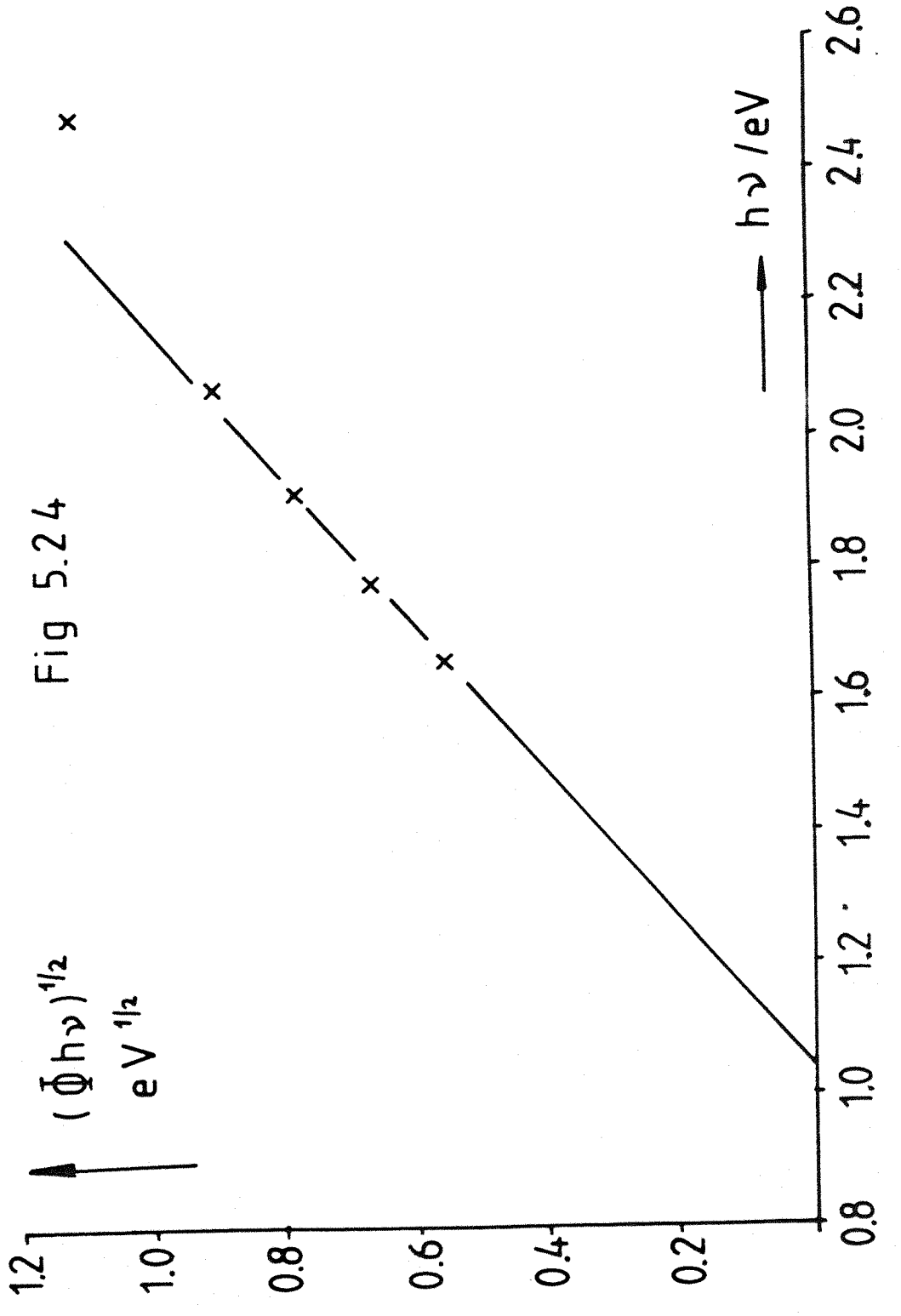

Fig 5.24

Fig 5.25

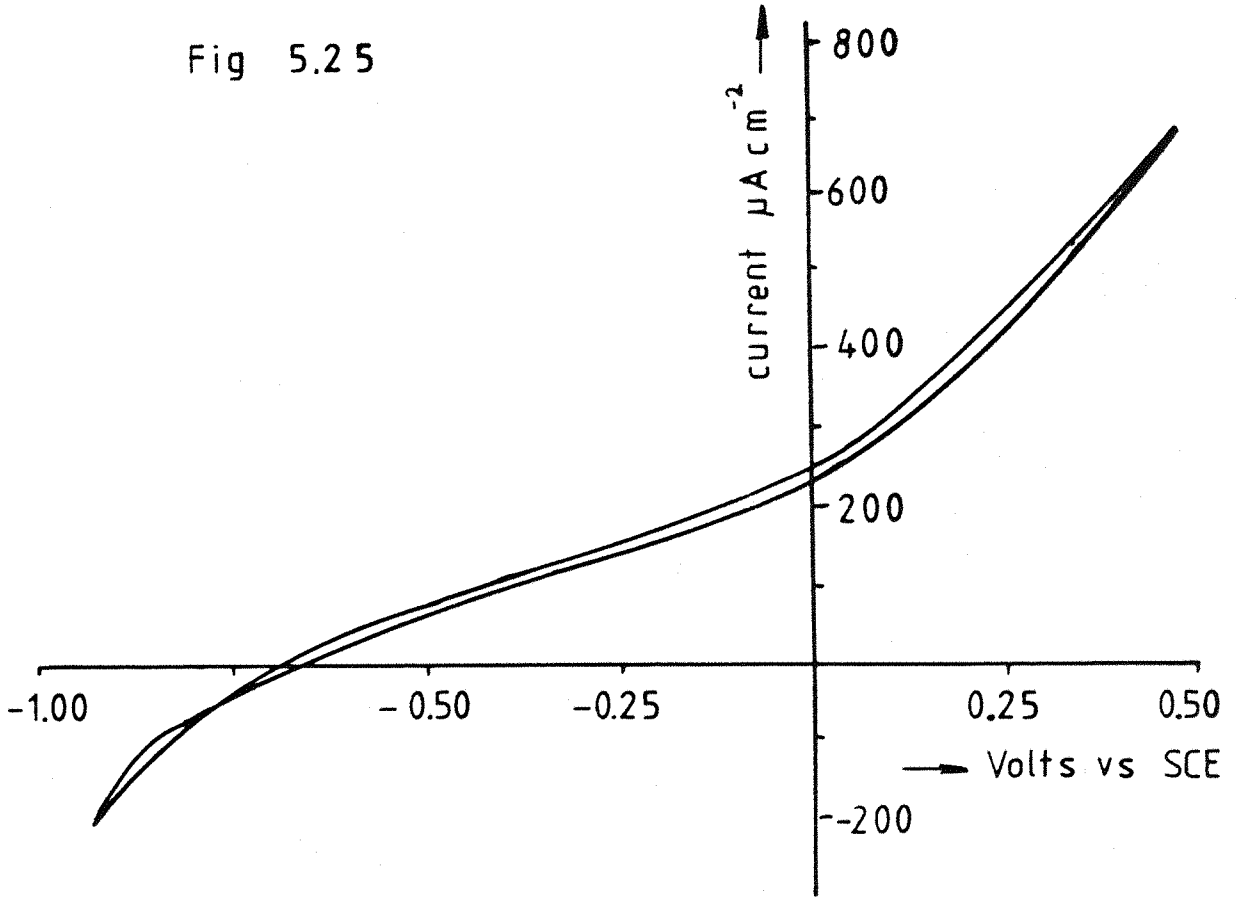
800
600
400
200
-200
current μA cm⁻²
-1.00
-0.50
-0.25
0.25
0.50
Volts vs SCE

(5.4) INTERFACIAL CAPACITY OF HIGH PURITY BISMUTH SULPHIDE

The interfacial capacity of the samples in 0.1M sodium sulphide was measured by applying a small sinusoidally varying potential of known frequency plus a d.c. offset to the bismuth sulphide electrode via a potentiostat in the standard three-electrode configuration, using a calomel reference electrode. The quadrature component of the cell current was displayed on an X-Y recorder as a function of working electrode potential over the range +0.4V to -0.8V versus SCE. The magnitude of this current is proportional to the electrode capacity, so the y-axis could be calibrated directly in microfarads by substituting a standard capacitance box for the cell. It has been shown that the if the capacity of the SCR is Csc, then to a good approximation for this work,

$$1/Csc^2 = 2.(E - Efb) / e.\varepsilon.\varepsilon(0).Nd \qquad (2.35)$$

and that so-called Mott-Schottky plots, of $1/Csc^2$ versus E, can be drawn to find Efb from their intercepts on the potential axis, and Nd from their slopes.

The capacitance results at several frequencies for one of the two crystal samples are shown in fig 5.26. There is relatively little hysteresis between the forward and reverse voltage scans over this potential range, but the hysteresis gets larger when the negative limit is increased to -0.9V.

Using electrode areas obtained from vernier microscope measurements, the Mott-Schottky plots shown in fig 5.27 were drawn. It is seen that there is frequency dispersion of the slopes, and a range of +/-0.08V about -0.9V in the intercepts on the potential axis, which would be the flat band potential if the material exhibited ideal

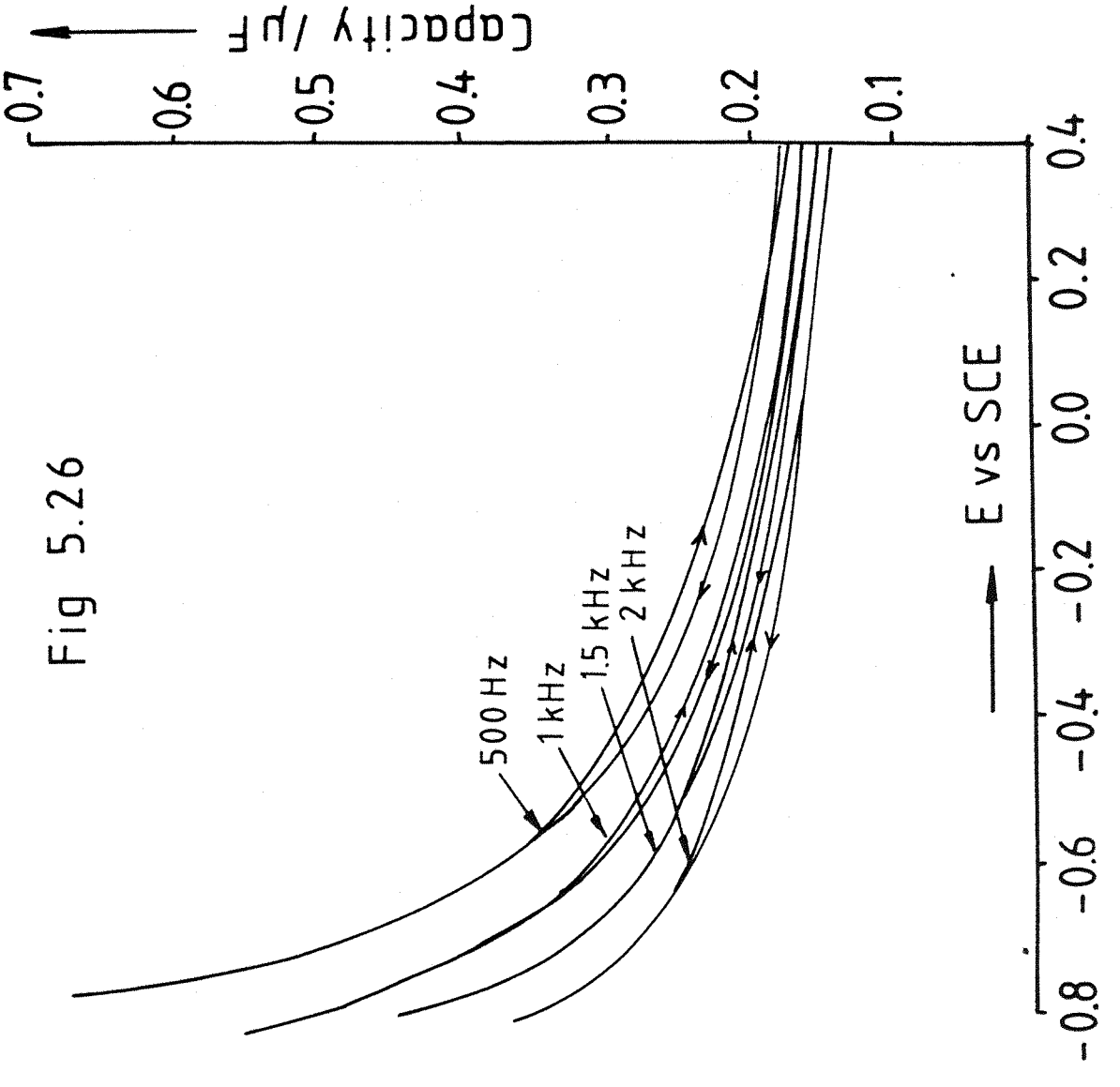
Capacity /μF
0.7
0.6
0.5
0.4
0.3
0.2
0.1
E vs SCE
0.4
0.2
0.0
-0.2
-0.4
-0.6
-0.8
500 Hz
1 kHz
1.5 kHz
2 kHz

Fig 5.26

Fig 5.27

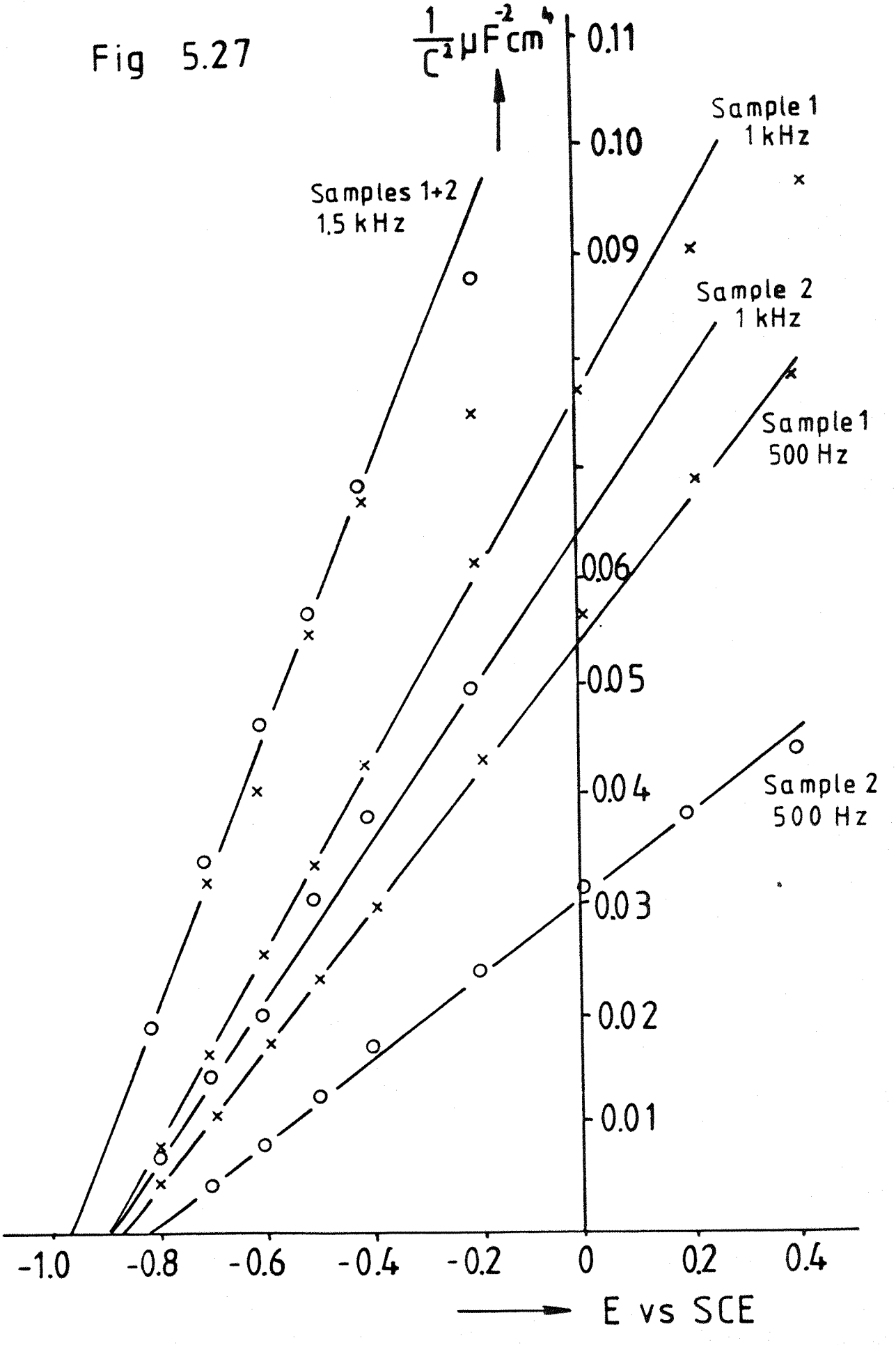
$\frac{1}{C^2}\mu F^{-2}cm^4$
0.11
0.10
0.09
0.06
0.05
0.04
0.03
0.02
0.01
Samples 1+2
1.5 kHz
Sample 1
1 kHz
Sample 2
1 kHz
Sample 1
500 Hz
Sample 2
500 Hz
-1.0
-0.8
-0.6
-0.4
-0.2
0
0.2
0.4
E vs SCE

blocking behaviour. The fact that the dark current varies with potential can be ignored if it changes only slowly. There is also some curvature at more positive potentials.

The frequency dispersion suggests some series resistance with the capacities of the double layer and space charge regions. This is not thought to arise from solution resistance since, given that the ionic strength of the electrolyte was fairly high and the Luggin probe was a few mm. from the working electrode, the value of this resistance could not have been higher than a few tens of ohms, whereas the impedance corresponding to the capacities measured was of the order of several hundreds of ohms. However, some resistance could have been caused by a less than ideal ohmic contact between the bismuth sulphide and the back layer of indium.

The curvature observed at higher potentials could be explained by high band bending, even to the point of charge carrier inversion (high density of holes at the interface), and a steeply rising dark current in this potential region.

In the first approximation, the gradient of these Mott-Schottky plots should be inversely proportional to the donor densities under the given conditions. Table 5.3 shows the values of Nd obtained from the plots assuming the relative permittivity of bismuth sulphide to be 10. The values of $1.0 - 3.5 \times 10^{20}$ per cc are higher by four orders of magnitude than those obtained by methods based on the photocurrent spectroscopy results.

It is believed that a part of this discrepancy can be explained by the high surface roughness of the samples, which gives them higher true surface areas than their geometric areas.

But the dominating factor could be the formation, during the recrystallisation process, of highly doped n+ regions at the

TABLE 5.3

SAMPLE NUMBER	FREQUENCY Hz	CARRIER DENSITY cm^{-3}
1	500	2.2×10^{20}
1	1000	1.6×10^{20}
1	1500	1.1×10^{20}
2	500	3.5×10^{20}
2	1000	1.9×10^{20}
2	1500	1.0×10^{20}

interface, which contain more excess bismuth than the normally doped n-type regions: these regions are believed to occur throughout the deposit as vertical channels, sometimes reaching back to the substrate, and would have a near-metallic behaviour. Relatively few photogenerated carriers from them would reach the interface, so they would make only a small contribution to the photocurrent, whose value would be largely determined by the normal n regions at the interface. Nevertheless, the n and n+ regions both contribute in parallel to the interfacial capacity, that of the n+ dominating in producing the readings found in the type of experiments described for the consruction of Mott-Schottky plots.

There may even be inclusions of metallic bismuth, which would act in much the same way, in reducing the photocurrents, and hence the values of Nd calculated from them, without correspondingly reducing the capacity at the interface, and the Nd values associated with the Mott-Schottky plots.

It has been mentioned that Mott-Schottky plots can be constructed from photocurrent conversion efficiency data, with known values of the absorption coefficient and dielectric constant. Rearranging equation 2.14 and substituting in 2.15:

$$-\ln(1 - \Phi) = \alpha.W \qquad (2.14)$$

$$Csc = \varepsilon.\varepsilon(0)/W \qquad (2.15)$$

$$Csc = -\alpha.\varepsilon.\varepsilon(0)/\ln(1 - \Phi) \qquad (5.3)$$

Assuming $\varepsilon = 10$, and using the data for α as before [35], values of Csc were calculated, and the Mott-Schottky plot of fig 5.28 was drawn. This gives a flat band potential of -0.63 V vs SCE, and a donor density Nd = 7×10^{15} per cm^3.

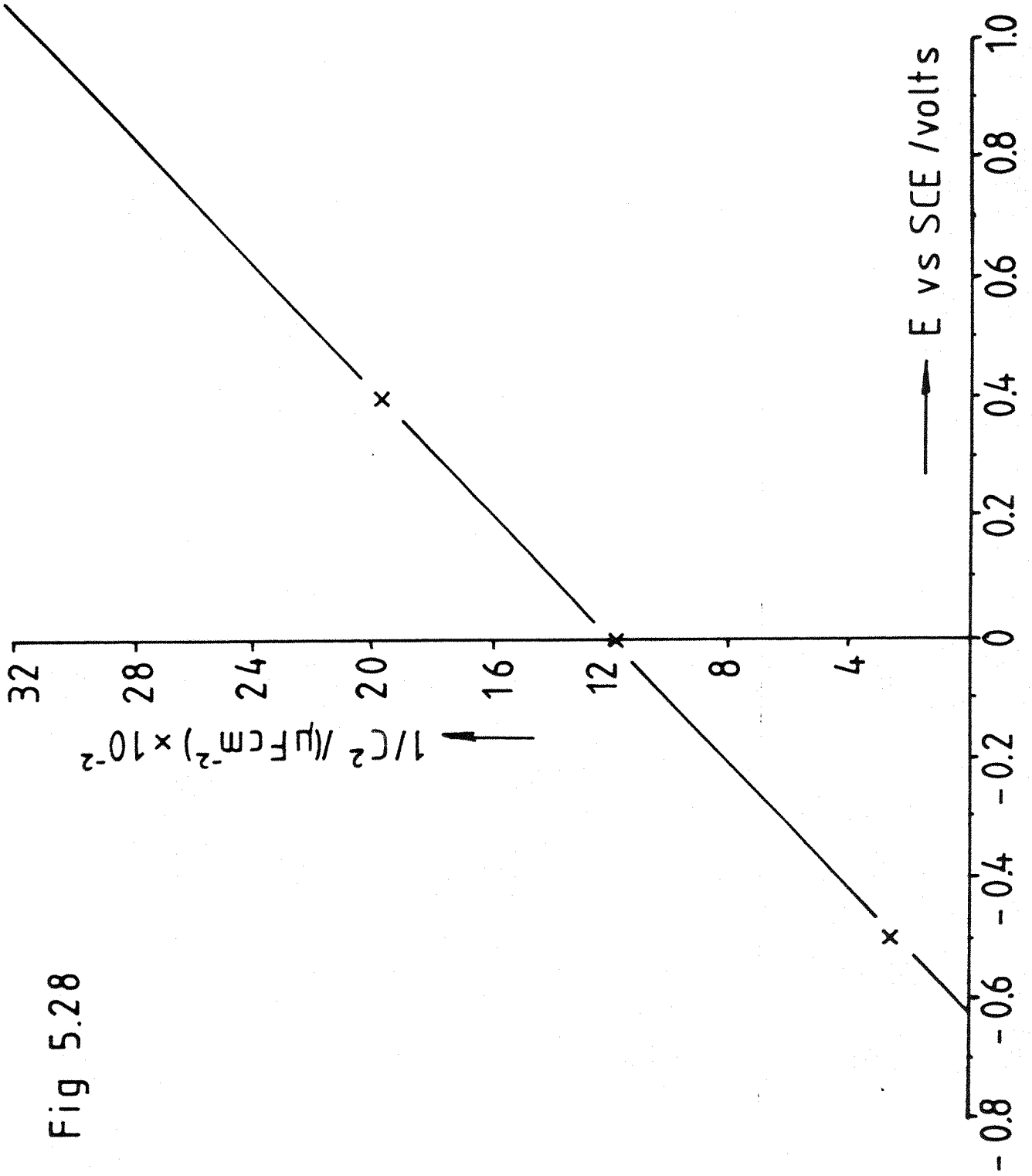
E vs SCE /volts
1.0
0.8
0.6
0.4
0.2
0
-0.2
-0.4
-0.6
-0.8
$1/C^2$ /(μF cm^{-2}) x 10^{-2}
32
28
24
20
16
12
8
4

Fig 5.28

REFERENCES

(1) "The Energy Question" G.Foley Penguin 1978

(2) "Fuel's Paradise" P.Chapman Penguin 1975

(3) "Sunlight to Electricity" J.A.Merrigan MIT Press 1982

(4) "Photovoltaic and Photoelectrochemical Solar Energy Conversion" Eds. F.Cardon,W.P.Gomes,W.Dekeyser Plenum 1981

(5) "Terrestrial Solar Cells- Present and Future" B.T.Debney, J.R.Knight Contemp. Phys. 19 (1978) 25

(6) "Solar Photovoltaic Energy" H.Ehrenreich,J.H.Martin Phys.Today (Sept.1979) 25

(7) "Electrochemical Solar Cells" A.Heller Solar Energy 29 (1982) 153

(8) "Photovoltaic Power Systems: A Tour through the Alternatives" H.Kelly Science 199 (1978) 634

(9) "Photovoltaic Materials" E.A.Perez-Albuerne,Y.S.Tyan Science 208 (1980) 902

(10) "Solar Cells- A Technology Assessment" J.R.Bolton Solar Energy 31 (1983) 483

(11) "Solar Energy Conversion by Photoelectrochemical Processes" R.Memming Electrochim. Acta 25 (1980) 77

(12) "Conversion of Sunlight into Electrical Power and Photoassisted Electrolysis of Water in Photoelectrochemical Cells" A.Heller Acc.Chem.Res. 14 (1981) 154

(13) "Energy Conversion in Photoelectrochemical Systems- A Review" K.Rajeshwar,p.Singh,J.DuBow Electrochim. Acta 23 (1978) 1117

(14) "Photoelectrochemistry- Applications to Solar Energy Conversion" A.J.Nozik Ann.Rev.Phys.Chem. 29 (1978) 189

(15) "Electrochemical Aspects of Solar Energy Conversion" M.D.Archer J.Appl.Electrochem. 5 (1975) 17

(16) "Surfaces for Photoelectrochemical Cells" D.Haneman Surface Science 86 (1979) 462

(17) "Photochemical Aspects of Solar Energy Conversion" L.M.Peter in Photochemistry, Vol.12 (1981) and Photochemistry, Vol.13 (1982) Royal Soc. of Chemistry

(18) "Photochemical Conversion and Storage of Solar Energy" C.Kutal J.Chem.Ed. 60 (1983) 882

(19) "Solar Scientists Go Green With Envy" L.Milgrom New Scientist (Feb.1984) 26

(20) "An Overview of the Progress in Photoelectrochemical Energy Conversion" B.Parkinson J.Chem.Ed. 60 (1983) 338

(21) "On the Design and Operation of Electrochemical Solar Cells" S.Kar,K.Rajeshwar,P.Singh,J.DuBow Solar Energy 23 (1979) 129

(22) "Photoelectrochemical Conversion of Optical Energy to Electricity and Fuels" M.S.Wrighton Acc.Chem.Res. 12 (1979) 303

(23) "Solar Fuels" J.R.Bolton Science 202 (1978) 705

(24) "Photoelectrochemical Cells" A.J.Nozik Phil.Trans. R.Soc.London A295 (1980) 453

(25) "Charge Transfer Processes at Semiconductor Electrodes" R.Memming in Electroanalytical Chemistry Vol.2 Ed. A.J.Bard Dekker 1979

(26) "Optical Processes in Semiconductors" J.I.Pankove Prentice-Hall 1971

(27) "The Social Costs of Solar Energy: A Study of Photovoltaic Energy Systems" T.L.Neff Pergamon 1981

(28) "Photovoltaic Energy Systems: Environmental Concerns and Control Technology Needs" U.S.Environmental Protection Agency EPA 600/57-82-066 March 1983

(29) "Theory of the Electrical and Photovoltaic Properties of Polycrystalline Silicon" A.K.Ghosh,C.Fishman, T.Feng J.Appl.Phys. 51 (1980) 446

(30) "Thin Film Amorphous Silicon Solar Cells" A.Madan Solar Energy 29 (1982) 225

(31) "Review of Amorphous and Polycrystalline Thin Film Silicon Solar Cell Performance Parameters" H.K. Charles Jr.,A.P.Ariotedjo Solar Energy 24 (1980) 329

(32) "Polycrystalline Thin Film CdS Liquid Junction Photovoltaic Cell" C.C.Tsou,J.R.Cleveland J.Appl. Phys. 51 (1980) 455

(33) "Electrochemical Solar Cell based on a Sprayed CdS Film Photoanode" M.Tsuiki,H.Minoura,T.Nakamura,Y.Ueno J.Appl.Electrochem 8 (1978) 523

(34) "CdS Thin Films for Terrestrial Solar Cells" L.M.Fraas, M.A.Yale J.Crystal Growth 39 (1977) 92

(35) "The Photoelectrochemical Properties of Anodic Bismuth Sulphide Films" L.M.Peter J.Electroanal.Chem. 98 (1979) 49

(36) "Anodic Formation of Thin CdS Films" L.-S. Yeh,P.G. Hudson, A.Damjanovic J.Appl.Electrochem. 12 (1982) 153

(37) "Anodic Formation of Thin CdS Films" A.Damjanovic, L.-S.R.Yeh,P.G.Hudson J.Appl.Electrochem. 12 (1982) 343

(38) "The Electrocrystallisation of Thin Cadmium Sulphide Films on Cadmium" L.M.Peter Electrochim.Acta 23 (1978) 165

(39) "Anodic Formation of Semiconductor Sulphide Films at Cadmium and Bismuth" B.Miller,S.Menezes,A.Heller J.Electroanal.Chem. 94 (1978) 85

(40) "Optimising the Photoelectrochemical Performance of Electrodeposited CdSe Semiconductor Electrodes" G.J.Houston,J.F.McCann,D.Haneman J.Electroanal.Chem 134 (1982) 37

(41) "Cathodic Deposition of CdTe from Aqueous Electrolytes" M.P.R.Panicker,M.Knaster,F.A.Kroger J.Electrochem. Soc. 125 (1978) 566

(42) "Photoelectrochemical Energy Conversion and Storage using Polycrystalline Chalcogenide Electrodes" G.Hodes, J.Manassen,D.Cahen Nature 261 (1976) 403

(43) "Energy Dependence of the Quantum Efficiency of CdSe Photoelectrochemical Cells" K.Colbow,D.J.Harrison, B.L.Funt J.Electrochem.Soc. 128 (1981) 547

(44) "Morphology, Properties, and Performance of Electrodeposited n-CdSe in Liquid Junction Solar Cells" M.Tomkiewicz,I.Ling,W.S.Parsons J.Electrochem.Soc 129 (1982) 2016

(45) "Solar Cell Materials and their Basic Parameters" E.Bucher Appl.Phys. 17 (1978) 1

(46) "The Structural and Compositional Characterisation of Bismuth Sulphide Films grown by Cathodic Deposition" A.S.Baranski,W.R.Fawcett,C.M.Gilbert J.Electrochem. Soc. 30 (1983) 2423

(47) "The Structural Characterisation of Cadmium Sulphide Films grown by Cathodic Electrodeposition" A.S. Baranski, W.R.Fawcett,A.C.McDonald,R.M.deNobriga J.Electrochem.Soc. 128 (1981) 963

(48) "The Electrodeposition of Metal Chalcogenides" A.S.Baranski,W.R.Fawcett J.Electrochem.Soc. 127 (1980) 766

(49) "The Mechanism of Electrodeposition of Cadmium Sulphide on Inert Metals from Dimethylsulphoxide Solution" A.S.Baranski,W.R.Fawcett,A.C.McDonald J.Electroanal. Chem. 160 (1984) 271

(50) "Electrochemical Deposition of Cadmium Sulphide from DMSO Solution" D.K.Roe,L.Wenzhao,H.Gerischer J.Electroanal.Chem. 136 (1982) 323

(51) A.S.Baranski,W.R.Fawcett,K.Gatner,A.C.McDonald, J.R.MacDonald,M.Solen J.Electrochem.Soc. 130 (1983) 579

(52) "Electrolysis of Non-Aqueous Systems" A.Brenner in Advances in Electrochemistry and Electrochemical Engineering Eds. Delahay,Tobias Vol.5 (1967)

(53) "Non-Aqueous Solvents for Electrochemical Use" C.K. Mann in Electroanalytical Chemistry Vol.3 Ed. A.J. Bard, Dekker (1969)

(54) "Electrochemistry in Dimethlsulphoxide" J.N.Butler J.Electroanal.Chem. 14 (1967) 89

(55) "Propylene Carbonate: A Versatile Solvent for Electrochemistry and EPR" R.F.Nelson,R.N.Adams J.Electroanal.Chem. 13 (1967) 184

(56) "Bibliography on the Uses of Propylene Carbonate in High Energy Density Batteries" R.Jasinski J.Electroanal.Chem. 15 (1967) 89

(57) "N-Methyl Acetamide as a Polarographic Solvent" L.A.Knecht,I.M.Kolthoff Inorg.Chem. 1 (1962) 195

(58) "Electrochemical Reduction of Elemental Sulphur in Aprotic Solvents" M.V.Merritt,D.T.Sawyer Inorg.Chem. 2 (1970) 211

(59) "Spectrophotometric Study of the Electrochemical Reduction of Sulphur in Organic Media" R.Bonnaterre, G.Cauquis J.C.S.Chem.Comm. (1972) 293

(60) "Further Studies of the Electrochemical Reduction of Sulphur in Aprotic Solvents" R.P.Martin,W.H.Doub Jr., J.L.Roberts Jr.,D.T.Sawyer Inorg.Chem. (1973) 1921

(61) "La Reduction du Soufre en Milieu Organique" J.Badoz-Lambling,R.Bonnaterre,G.Cauquis,M.Delamar, G.Demange Electrochim.Acta 21 (1976) 119

(62) D.M.Kolb Adv.Electrochem.Eng. 11 (1978) 125

(63) R.E.Humphrey Anal.Chem. 34 (1962) 167

(64) "Spectral Response and Efficiency Relations in Semiconductor Liquid Junction Solar Cells" A.Heller, K.C.Chang,B.Miller J.Electrochem.Soc. 124 (1977) 697

(65) "Photocurrent Spectroscopy of Semiconductor Electrodes in Liquid Junction Solar Cells" A.Heller,K.C.Chang, B.Miller J.Am.Chem.Soc. 100:3 (1978) 684

(66) "Depletion Layer Photoeffects in Semiconductors" W.W.Gartner Phys.Rev. 116 (1959) 84

(67) "Photoelectrolysis and Physical Properties of the Semiconducting Electrode WO M.A.Butler J.Appl.Phys. 48 (1977) 1914

(68) "The Current-Voltage Characteristics of Semiconductor-Electrolyte Junction Photovoltaic Cells" J.Reichman Appl.Phys.Lett. 36 (1980) 574

(69) "The Transport and Kinetics of Minority Carriers in Illuminated Semiconductor Electrodes" W.J.Albery, P.N.Bartlett,A.Hamnett,M.P.Dare-Edwards J.Electrochem.Soc. 128 (1981) 1492

(70) "Recombination Effects on Current-Voltage Characteristics of Illumnated Surface Barrier Cells" J.F.McCann,D.Haneman J.Electrochem.Soc. (1982) 1134

(71) "Analysis of Photocurrents at the Semiconductor-Electrolyte Junction" P.Lemasson,A.Etcheberry, J.Gautron Electrochim. Acta 27 (1982) 607

(72) C.-T.Sah,R.N.Noyce,W.Shockley Proc. IRE 45 (1957) 1228

(73) "A Model for the Current-Voltage Curve of Photoexcited Semiconductor Electrodes" R.H.Wilson J.Appl.Phys. 48 (1977) 4292

(74) "The Influence of Surface Recombination and Trapping on the Cathodic Photocurrent at p-type III - V Electrodes" J.J.Kelly,R.Memming J.Electrochem.Soc. 129 (1982) 730

(75) "Electrochemical Transfer via Surface States- A New Formulation for the Semiconductor-Electrolyte Interface" J.-N.Chazalviel J.Electrochem.Soc. 129 (1982) 963

(76) "Charge Transfer in Photoelectrochemical Devices via Interface States: Unified Model and Comparison with Experimental Data" K.Rajeshwar J.Electrochem.Soc. 129 (1982) 1003

(77) "Surface Recombination at Semiconductor Elecrodes Part II. Photoinduced "near-surface" recombination centres in p-GaP" J.Li,R.Peat, L.M.Peter J.Electroanal.Chem. 165 (1984) 41

(78) "On the Interpretation of Mott-Schottky Plots determined at Semiconductor-Electrolyte Systems" R.deGryse,W.P.Gomes,F.Cardon,J.Vennik J.Electrochem.Soc. 122 (1975) 711

(79) "Some Semiconducting Properties of Bismuth Trisulphide" L.Gildart,J.M.Kline,D.M.Mattox J.Phys.Chem.Solids 18 (1961) 286

(80) B.T.Kolomiets Zh.Tekhn. Fiz. 19 (1949) 126

(81) E.Khawaja, S.G.Tomlin J.Phys.D. 8 (1973) 581

(82) D.C.Reynolds et.al. Phys. Stat. Solidi 12 (1965) 3
referred to in the Handbook of the American
Institute of Physics

APPENDIX 1

LISTING OF PROGRAM SUITE FOR AUTOMATIC MEASUREMENT OF PHOTOCURRENTS (AMP)

PROGRAM 1 "AMP4"

```
   10*FX16,2
   20DIMyval(5)
   26IF?&7C=99ANDF%=&4900THENT$="N":A$="Y"
   27IF?&7C=99ANDF%=&5000THENT$="Y":A$="N"
   28IF?&86=1THENF$="N"ELSEF$="Y"
   29IF?&7E=99THEN?&7E=0:GOTO1170
   30plot=0:PLC$="0":A$="0":P$="0":?&89=0:KAL%=&FFFF:CLK%=0:HD$
="""
   40visible%=69:invisible%=71:diode%=1:psd%=2:QU$="":QU2$="":C
OR$=""
   50IF?&8C=1THEN1270
   80IF(?&8D=1AND?&8F=1)OR(?&8D=2AND?&8F=1)THENU%=U%:V%=V%:R%=S
%:G%=K%:?&77=D%
   90IF?&8D=1THENT$="Y":A$="N":GOTO170
  100IF?&8D=2THENA$="Y":T$="N":GOTO170
  105IF?&84=1THEN146
  106Z%=1
  107ONERRORGOTO110
  108IFQU7$="Y"THEN115
  110ONERROROFF:INPUT"DISC",disc$:IFdisc$="Y"THEN1250
  120*DISC
  130*LOAD"ASS1"
```

```
140ONERROROFF:%%=&E0E
144CHAIN"GETPARS"
146?&84=0
150IF?&7F=1THENT$="Y":A$="N"
160IF?&7F=2THENT$="N":A$="Y"
170IF?&86=1THENF$="N"ELSEF$="Y"
310PROCwavelength_bounds
320MODE4:PROCaxes_labels
330PROClabel_uncorr_and_test
340IF?&8D=1OR?&8D=2THENPROCsimple_plot:GOTO480
345?&71=0
350ONERRORGOTO380
360IFF$="N"THENCALL&5640
370ONERROROFF:GOTO470
380IFERR=17 THENVDU:MOVE200,980:PRINT"STOPPED":VDU4:VDU7:GOTO
370
400DEFPROCsimple_plot
410FORL%=340TO722
420IF!((L%-340)*4+F%)=0THEN440
430PROCpoint_plot(visible%)
440NEXTL%
450?&8D=0
460ENDPROC
470PROCscreenplot
472IFR%>G%THENINPUT"FINAL PSD NANOAMP/VOLT",V:V%=V*1000
480CLS:INPUT"EDIT",ED$
490IFED$="Y"THENPROCedit(0):GOTO480
491IFT$="Y"THEN500
492CLS:INPUT"SET RANGE CHANGE BREAK POINTS",RA$
```

```
  494IFRA$="Y"THEN?&71=0:PROCedit(1):GOTO492
  500CLS:INPUT"PLOTTER",PL$
  510IFPL$="N"THEN610
  515PRINT"HEADING?";:INPUTLINE HD$
  520CLS:INPUT"AXES",hpaxes$:IFhpaxes$="Y"THEN570
  530*IEEE
  540plot=?&8A:plot=plot+1:?&8A=plot
  550IFplot=1THENPRINT£5,"SM+;"ELSEIFplot=2THENPRINT£5,"SMX;"EL
SEIFplot=3THENPRINT£5,"SM£;"ELSEplot=1:GOTO550
  560GOTO600
  570CLS:PROChp_axes
  580PROChp_label
  590PROChp_label_symbol
  600PROChp_plot
  610CLS:INPUT"PRINTOUT",print$
  612IFprint$="Y"THENPRINT"HEADING";:INPUTLINEHD$
  620IFprint$="Y"ANDT$="Y"THENPROCprint(diode%)ELSEIFprint$="Y"
THENPROCprint(psd%)
  630GOTO860
  640DEFPROCprint(spectrum%)
  650*FX6
  660VDU2
  670IFspectrum%=diode%THENhead$="PHOTODIODE SPECTRUM"ELSEhead$
="TEST SPECTRUM"
  680PRINT''HD$:PRINT''TAB(30);head$
  690IFspectrum%=diode%THEN720
  700IFV%<100000THENunit$="PICOAMPS"ELSEunit$="NANOAMPS"
  710GOTO730
  720IFU%<40THENunit$="NANOAMPS"ELSEunit$="MICROAMPS"
```

```
730PRINT'TAB(2);"NM";TAB(30);unit$
740ONERRORGOTO840
755IFG%<R%THENJ%=-5ELSEJ%=5
760FORL%=R%TOG%STEPJ%
770FORloop%=0TO4
780yval(loop%)=P7%*(!((L%-340+loop%)*4+F%))/KAL%
790NEXTloop%
800%%=&E0E:PRINT;L%;"/";L%+4;
802%%=&20108:PRINTyval(0),yval(1),yval(2),yval(3),yval(4)
810NEXTL%
820%%=&E0E:VDU3:VDU7
830ENDPROC
840IFERR=17THENVDU3:%%=&E0E:ONERROROFF:GOTO860
860ONERROROFF:CLS:INPUT"CORRECTED SPECTRUM",COR$
870IFCOR$="N"THEN1192
880VDU5:GOSUB2440
890ONERROROFF:CLS:INPUT"EDIT",ED2$
900IFED2$="Y"THENPROCcalc(3):GOTO890
910CLS:INPUT"PLOTTER",PLC$
920IFPLC$="N"THEN1000ELSEPRINT"HEADING";:INPUTLINEHD$
930INPUT"AXES",hpaxes$:IFhpaxes$="Y"THEN980
940*IEEE
950plot=?&8E:plot=plot+1:?&8E=plot
960IFplot=1THENPRINT£5,"SM+;"ELSEIFplot=2THENPRINT£5,"SMX;"EL
SEIFplot=3THENPRINT£5,"SM£;"ELSEplot=1:GOTO960
970GOSUB3270
980PROChp_axes
990GOSUB3190
1000*FX6
```

```
 1010CLS:INPUT"PRINTOUT",print$
 1020IFprint$="N"THEN1192ELSEPRINT"HEADING";:INPUTLINEHD$
 1030ONERRORGOTO1180
 1040*FX6
 1050VDU2:PRINT''HD$:PRINT''TAB(30);"CORRECTED SPECTRUM":PRINT'
TAB(2);"NM";TAB(30)"CONV.EFF.%"
 1060?&7E=99
 1065*DISC
 1070CHAIN"logplt2"
 1170VDU3:VDU7:%%=&E0E:GOTO1192
 1180IFERR=17THENVDU3:%%=&E0E:ONERROROFF:GOTO1192
 1190VDU3:GOTO110
 1192IFT$="Y"THEN1210ELSEINPUT"LOG PLOT",log$:IFlog$="N"THEN121
0
 1194IFlog$<>"Y"THEN1192
 1195*DISC
 1196CHAIN"logplt2"
 1210INPUT"DISC",disc$
 1220COR$=""
 1230IFdisc$="N"THEN1270
 1240*DISC
 1250MODE7:PAGE=PAGE+&4500
 1260CHAIN"discop4"
 1270?&8C=0:INPUT"ANOTHER EXPERIMENT",QU7$
 1280IFQU7$="N"THEN1210ELSE30
 1290MODE7:GOTO110
 1690DEFPROCscreenplot
 1700VDU5
 1710IFG%<R%THENJ%=-(?&77):GOTO1730
```

```
1720J%=?&77
1730ONERRORGOTO1840
1740FORL%=R%TOG%STEPJ%
1750IF?&86=1THEN1770
1760?&86=2:CALL&5640
1770PROCpoint_plot(visible%)
1780IF?&86=1THEN1800
1790?&86=3:CALL&5640
1800NEXTL%
1810ONERROROFF
1820VDU4
1830ENDPROC
1840IFERR=17THENVDU5:MOVE200,980: PRINT"STOPPED AT ";L%-J%;" N
M":VDU4
1850IFERR<>17THEN110
1860ONERROROFF:GOTO480
1870DEFPROCwavelength_bounds
1880NUM20S=2:LAMBDADIFF=ABS(R%-G%)
1890IFLAMBDADIFF<20THEN1910
1900LAMBDADIFF=LAMBDADIFF-20:NUM20S=NUM20S+1:GOTO1890
1910LAMBDASPAN=NUM20S*20
1920IFR%<G%THEN1940
1930LOWLAMBDA=20*INT(G%/20):GOTO1950
1940LOWLAMBDA=20*INT(R%/20)
1950ENDPROC
1960DEFPROCaxes_labels
1970VDU28,0,31,39,30
1980VDU19,0,3;0;
1990VDU19,1,4;0;
```

```
2000COLOUR0:COLOUR129
2010FORY=100TO104STEP4
2020MOVE150,Y:DRAW1150,Y
2030NEXTY
2040FORX=150TO154STEP4
2050MOVEX,100:DRAWX,1000
2060NEXTX
2070IFNUM20S<8THEN2100
2080HY%=NUM20S/5
2090FORI=0TONUM20S STEPHY%:GOTO2110
2100FORI=0TONUM20S
2110MOVE150+1000*I/NUM20S,104:DRAW150+1000*I/NUM20S,128
2120NEXTI
2130VDU5
2140IFNUM20S<8THEN2170
2150HT%=NUM20S/5
2160FORI=0TONUM20S STEPHT%:GOTO2180
2170FORI=0TONUM20S
2180MOVE110+1000*I/NUM20S,94:IF110+1000*I/NUM20S<100THEN2190EL
SEPRINT;20*(I-1)+LOWLAMBDA
2190NEXTI
2200MOVE1170,140:PRINT"NM"
2210ENDPROC
2220DEFPROClabel_uncorr_and_test
2230IFT$="Y"THEN2260
2240IFV%<100000THENP7%=V%*10ELSEP7%=V%*.01
2250GOTO2270
2260IFU%<40THENP7%=U%*1000ELSEP7%=U%
2270VDU4
```

```
 2280IFP7%<1000THENP8%=10*INT(P7%/10)ELSEP8%=100*INT(P7%/100)
 2290FORI=0TOP8%STEPP8%/4
 2300MOVE154,104+900*I/P7%:DRAW178,104+900*I/P7%
 2310VDU5:MOVE0,104+900*I/P7%:PRINT;INT(I)
 2320NEXTI
 2330VDU5
 2340IFT$="Y"THEN2370
 2350IFV%<100000THENMOVE154,890:PRINT "I/PICOAMPS":VDU4:GOTO239
0
 2360MOVE154,890:PRINT"I/NANOAMPS":VDU4:GOTO2390
 2370IFU%<40THENMOVE154,890:PRINT"I/NANOAMPS":VDU4:GOTO2390
 2380MOVE154,890:PRINT"I/MICROAMPS":VDU4
 2390ENDPROC
 2400?&75=A3%+B1%:?&74=A1%*4
 2410IFG%<R%AND?&74=&FFTHEN?&74=0:?&75=(?&75)+1
 2420IFG%<R%AND?&74<&FFTHEN?&74=(?&74)+1
 2430RETURN
 2440CLG:PROCaxes_labels
 2445PROCmaxeff
 2448IF maxeff>10THEN%%=&E0E ELSEIF maxeff>1 THEN %%=&20208 ELS
EIF maxeff>.1 THEN %%=&20308 ELSEIF maxeff>.01 THEN %%=&20408 E
LSE%%=&20508
 2449VDU5:MOVE40,104:PRINT"0"
 2450FORI=maxeff/5 TOmaxeff STEPmaxeff/5
 2460MOVE154,104+I*900/maxeff:DRAW178,104+I*900/maxeff
 2470VDU5:MOVE0,104+I*900/maxeff:PRINT;I
 2480NEXTI
 2485%%=&E0E
 2490MOVE154,890:PRINT"CONV.EFF.%":VDU4
```

```
2500PROCcalc(1)
2520RETURN
2530DEFPROChp_axes
2540*IEEE
2550ZZ$=CHR$(3)
2560PRINT£5,"IN;SP1;IP1250,750,9250,6250;"
2570PRINT£5,"SC0,1000,0,900;"
2580PRINT£5,"PU0,0 PD0,900,1000,900,1000,0,0,0 PU"
2590PRINT£5,"SI.3,.3;"
2600AA$="PA0,1000;CP0,2.2;LB"
2610BB$=AA$+HD$+ZZ$
2620PRINT£5,BB$,CHR$(3)
2630IFT$="Y"THENTITLE$="PHOTODIODE SPECTRUM"ELSEIFCOR$="Y"THEN
TITLE$="CORRECTED SPECTRUM"ELSETITLE$="UNCORRECTED SPECTRUM"
2640AA$="PA0,1000;CP0,1;LB"
2650BB$=AA$+TITLE$+ZZ$
2660PRINT£5,BB$
2670PRINT£5,"SI.2,.3;TL1.5,0"
2680IFNUM20S<8THEN2710
2690HZ%=NUM20S/5
2700FORI%=0TONUM20S STEPHZ%:GOTO2720
2710FORI%=0TONUM20S
2720J%=1000*I%/NUM20S
2730HH$=STR$(J%):JJ$="PU":KK$=",0;XT;"
2740LL$=JJ$+HH$+KK$
2750PRINT£5,LL$
2760FF%=20*(I%-1)+LOWLAMBDA
2770NN$=STR$(FF%):VV$="CP-2,-1;LB"
2780CC$=VV$+NN$+ZZ$
```

```
 2790PRINT£5,CC$
 2800NEXTI%
 2810ENDPROC
 2820DEFPROChp_label
 2830FORI%=0TOP8%STEPP8%/4
 2840NN$=STR$(900*I%/P7%):VV$="PU0,":WW$=";YT;"
 2850CC$=VV$+NN$+WW$
 2860PRINT£5,CC$
 2870HH$=STR$(I%)
 2880IFI%<10THENJJ$="CP-2,-.25;LB"ELSEIFI%<100THENJJ$="CP-3,-.2
5;LB"ELSEIFI%<1000THENJJ$="CP-4,-.25;LB"ELSEJJ$="CP-5,-.25;LB"
 2890LL$=JJ$+HH$+ZZ$
 2900PRINT£5,LL$
 2910NEXTI%
 2920BB$="PA900,0;CP-13,-2.5;LBWAVELENGTH/NM"
 2930AA$=BB$+ZZ$:PRINT£5,AA$
 2940ENDPROC
 2950DEFPROChp_label_symbol
 2960BB$="PA0,1000;CP-5,-1;LBPHOTOCURRENT/"
 2970AA$=BB$+ZZ$:PRINT£5,AA$
 2980IFT$="Y"THEN3010
 2990IFV%<100000THENBB$="CP-13,-1;LBPICOAMPS"ELSEBB$="CP-13,-1;
LBNANOAMPS"
 3000GOTO3020
 3010IFU%<40THENBB$="CP-13,-1;LBNANOAMPS"ELSEBB$="CP-13,-1;LBMI
CROAMPS"
 3020AA$=BB$+ZZ$:PRINT£5,AA$
 3030PRINT£5,"SM*;"
 3040IFG%<R%THENJ%=-(?&77)ELSEJ%=?&77
```

```
 3050ENDPROC
 3060DEFPROChp_plot
 3070IFG%<R%THENJ%=-(?&77)ELSEJ%=?&77
 3080ONERRORGOTO3170
 3090FORL%=R%TOG%STEPJ%
 3100X$=STR$((L%-LOWLAMBDA+20)*1000/LAMBDASPAN)
 3110Y$=STR$(900*(!((L%-340)*4+F%))/KAL%)
 3120DD$="PU;PA":EE$=",":FF$=";"
 3130GG$=DD$+X$+EE$+Y$+FF$:PRINT£5,GG$
 3140NEXTL%
 3150ONERROROFF
 3160ENDPROC
 3170IFERR=17THENONERROROFF:GOTO610
 3180GOTO110
 3190FORI=0TOmaxeff STEPmaxeff/5
 3195CCX$=STR$(I*900/maxeff)
 3200NN$=LEFT$(CCX$,4):VV$="PU0,":WW$=";YT;"
 3210CC$=VV$+NN$+WW$:PRINT£5,CC$
 3212IFmaxeff<1THENJ=I*1000ELSEJ=I
 3214HH$=STR$(J):HH$=LEFT$(HH$,4):JJ$="CP-6,-.25;LB":LL$=JJ$+HH
$+ZZ$:PRINT£5,LL$
 3220NEXTI
 3230BB$="PA900,0;CP-13,-2.5;LBWAVELENGTH/NM":AA$=BB$+ZZ$:PRINT
£5,AA$
 3240IFmaxeff<1THENBB$="PA0,1000;CP-5,-1;LB(PHOTO.CONV.EFFICIEN
CY/%)*1000"ELSEBB$="PA0,1000;CP-5,-1;LBPHOTO.CONV.EFFICIENCY/%"
 3250AA$=BB$+ZZ$:PRINT£5,AA$
 3260PRINT£5,"SM*;"
 3270IFG%<R%THENJ%=-(?&77)ELSEJ%=?&77
```

```
3280PROCcalc(2):GOTO1000
3285DEFPROCcalc(CLK2%)
3290RESTORE
3300CLK%=0
3302IF?&71=0THENA%=722
3303factor=1:L%=340:REPEAT:GOSUB3330
3304L%=L%+1
3305UNTILL%=A%
3306IF?&71=1THENB%=722ELSEIF?&71=0THEN3460
3307factor=.001*M%:L%=A%:REPEAT:GOSUB3330
3308L%=L%+1
3309UNTILL%=B%
3310IF?&71=2THENE%=722ELSEIF?&71=1THEN3460
3311factor=.001*N%:L%=B%:REPEAT:GOSUB3330
3312L%=L%+1
3313UNTILL%=E%
3314IF?&71=3THENX%=722ELSEIF?&71=2THEN3460
3315factor=.001*O%:L%=E%:REPEAT:GOSUB3330
3316L%=L%+1
3317UNTILL%=X%
3318IF?&71=3THEN3460
3320factor=.001*Q%:L%=X%:REPEAT:GOSUB3330
3321L%=L%+1
3322UNTILL%=722
3325ENDPROC
3330IFCLK%=1THENCLK%=0:GOTO3350
3340READIPH:IPH=IPH*.01:CLK%=1
3350IF!((L%-340)*4+&5000)<=0OR!((L%-340)*4+&4900)<=0THEN3450
3360DV=.001*factor*(!((L%-340)*4+&4900))/(!((L%-340)*4+&5000))
```

```
*(V%/U%)*2*IPH
 3370IFCLK2%=2THEN3410
 3380XVAL%=(L%-LOWLAMBDA+20)*1000/LAMBDASPAN
 3385IFCLK2%=3THEN3462
 3390PROCcorrected_point_plot(visible%)
 3400GOTO3450
 3410X$=STR$((L%-LOWLAMBDA+20)*1000/LAMBDASPAN)
 3420Y$=STR$(DV*scale%)
 3430DD$="PU;PA":EE$=",":FF$=";"
 3440GG$=DD$+X$+EE$+Y$+FF$:PRINT#5,GG$
 3450RETURN
 3460GOTO3470
 3462CLS:PRINT"N FOR NEXT POINT,D TO DELETE,F TO FINISH";
 3463PROCcorrected_point_plot(invisible%):FORDD%=1TO100:NEXT:PR
OCcorrected_point_plot(visible%)
 3464QU2$=INKEY$(40)
 3465IFQU2$=""THEN3463ELSEIFLEFT$(QU2$,1)<>"N"ANDLEFT$(QU2$,1)<
>"D"ANDLEFT$(QU2$,1)<>"F"THEN3462
 3466IFLEFT$(QU2$,1)="D"THENPROCcorrected_point_plot(invisible%
):!((L%-340)*4+&4900)=0
 3467IF LEFT$(QU2$,1)="F" THEN 3470
 3468RETURN
 3470ENDPROC
 3510DEFPROCedit(range%)
 3515IFrange%=1AND?&71>0THEN3540
 3520J%=?&77
 3525IF R%>G% THENXX%=G% ELSEXX%=R%
 3530L%=XX%-J%
 3540L%=L%+J%:IFG%>R%ANDL%>G%THEN3700
```

```
 3550IFG%<R%ANDL%>R%THEN3700
 3560YSCREEN%=(L%-340)*4+F%
 3570IF!YSCREEN%<=0THEN3540
 3575IFrange%=1THENCLS:PRINT"N=NEXT,R=RANGE CHANGE,F=FINISH";:G
OTO3590
 3580CLS:PRINT"N FOR NEXT POINT,D TO DELETE,F TO FINISH";
 3590PROCpoint_plot(invisible%):PROCpoint_plot(visible%)
 3600QU$=INKEY$(20)
 3610IFQU$=""THEN3590ELSEIFLEFT$(QU$,1)<>"N"ANDLEFT$(QU$,1)<>"D
"ANDLEFT$(QU$,1)<>"F"ANDLEFT$(QU$,1)<>"R"THEN3580
 3615IFrange%=1ANDLEFT$(QU$,1)="D"THEN3575
 3620IFLEFT$(QU$,1)="D"THENPROCpoint_plot(invisible%):!YSCREEN%
=0
 3625IFrange%=1ANDLEFT$(QU$,1)="R"THENPROCrange_change
 3630IFLEFT$(QU$,1)="F"THEN3700ELSE3540
 3640DEFPROCpoint_plot(visible_or_not%)
 3650FORDF%=150TO154STEP4
 3660FORGF%=100TO104STEP4
 3670PLOTvisible_or_not%,DF%+((L%-LOWLAMBDA+20)*1000/LAMBDASPAN
),GF%+(900*(!((L%-340)*4+F%))/KAL%)
 3680NEXTGF%
 3690NEXTDF%
 3700ENDPROC
 3880DEFPROCcorrected_point_plot(visible_or_not%)
 3890FORDF%=150TO154STEP4
 3900FORGF%=100TO104STEP4
 3910PLOTvisible_or_not%,DF%+XVAL%,GF%+DV*scale%
 3920NEXTGF%
 3930NEXTDF%
```

```
3940ENDPROC
3941DEFPROCrange_change
3942?&71=?&71+1
3943IF?&71>4THENPRINT"TOO MANY RANGE CHANGES":GOTO3949
3944CLS:INPUT"NEW PSD NANOAMP/VOLT",V2:V2=V2*1000
3945IF?&71=1THENM%=1000*V2/V%:A%=L%
3946IF?&71=2THENN%=1000*V2/V%:B%=L%
3947IF?&71=3THENO%=1000*V2/V%:E%=L%
3948IF?&71=4THENQ%=1000*V2/V%:X%=L%
3949ENDPROC
4000DEFPROCmaxeff
4010RESTORE
4020CLK%=0:DV=0
4025FORL%=340TO722
4030IFCLK%=1THENCLK%=0:GOTO4050
4040READIPH:IPH=IPH*.01:CLK%=1
4050IF!((L%-340)*4+&5000)<=0OR!((L%-340)*4+&4900)<=0THEN4150
4060IF.001*(!((L%-340)*4+&4900))/(!((L%-340)*4+&5000))*(V%/U%)
*2*IPH>DV THENDV=.001*(!((L%-340)*4+&4900))/(!((L%-340)*4+&5000
))*(V%/U%)*2*IPH
4150NEXTL%
4160IFDV<0.0001THENmaxeff=0.0001ELSEIFDV<0.001THENmaxeff=0.001
ELSEIFDV<0.01THENmaxeff=0.01ELSEIFDV<0.1THENmaxeff=0.1ELSEIFDV<
1THENmaxeff=1ELSEIFDV<10THENmaxeff=10ELSEIFDV<25THENmaxeff=25EL
SEmaxeff=100
4165scale%=900/maxeff
4167Z%=maxeff*100000
4170ENDPROC
4940REM RS£2 DEC84 340 TO 720NM STEP 2NM
```

```
4950DATA0,0,0,0,0,9,9,9,9,9,9,9,9,9,9,10,10,11,11,12,14,15,16,
18,21,22,23,25,27,29,31,32,33,35,36,38,40,42,44,46,48,50,52,53,
54,55,55,56,58,59,60,61,62,62,63,64,64,65,65,66,66,67,67,68,68,
68,68,69,69,70,70,70
4960DATA70,70,71,71,71,72,72,72,72,72,72,73,73,73,73,73,73,73,
73,74,74,74,74,74,74,74,74,74,74,74,74,74,74,74,74,74,74,74,74,
74,74,74,74,74,74,74,74,74,74,74,74,74,74,74,74,74,74,73,73,
73,73,73,73,73,73,73,73,73,73,73,73,72,72,72,72
4970DATA72,72,72,72,72,72,72,72,71,71,71,71,71,71,71,71,71,71,
71,71,70,70,70,70,70,70,70,70,70,70,69,69,69,69,69,69,69,69,69,
69,69,68,68
```

PROGRAM 2 "GETPARS"

```
  150INPUT"PHOTODIODE",T$
  160IFT$="Y"THENA$="N":?&7F=1
  170IFT$="N"THEN?&7F=2:GOTO200
  180INPUT"RANGE",U%
  190U%=U%*2:GOTO230
  200INPUT"PSD",A$
  210IFA$="Y"THEN?&7F=2ELSE?&7F=0:GOTO150
  220INPUT"INITIAL PSD NANOAMP/VOLT",V:V%=V*1000
  230INPUT"SCREEN",F$
  240IFF$="N"THEN?&86=1ELSE?&86=0
  250IFA$="Y"THEN?&75=&49:F%=&4900:PROCmemory_test
  260IFA$="Y"THEN280
  270?&75=&50:F%=&5000:PROCmemory_test
  280IF?&8D=1OR?&8D=2THEN1680
 1380INPUT"STARTING WAVELENGTH (NM)",R:IF R<>INT(R)THENPRINT"IN
TEGER":GOTO1380
 1390R%=R:IFR%<340ORR%>722THENPRINT"340 TO 722 NM ONLY":GOTO138
0
 1400A1%=R%-340:B1%=0:A3%=?&75
 1410IFA1%<64THEN1440
 1420A1%=A1%-64:B1%=B1%+1
 1430GOTO1410
 1440?&74=A1%*4:?&75=?&75+B1%
 1450INPUT"FINISHING WAVELENGTH (NM)",G:IFG<>INT(G)THENPRINT"IN
TEGER":GOTO1450
 1460G%=G:IFG%<340ORG%>722THENPRINT"340 TO 722 NM ONLY":GOTO145
0
 1470A2%=G%-340:B2%=0
```

```
 1480IFA2%<64THEN1510
 1490A2%=A2%-64:B2%=B2%+1
 1500GOTO1480
 1510?&7A=A2%*4:?&7B=A3%+B2%
 1520IFG%>R%THEN?&76=2ELSE?&76=1
 1530IFG%=R%THENPRINT"NOT ALLOWED":GOTO1380
 1540INPUT"STEP HEIGHT IN NM",R$
 1550IFR$="1"THEN?&77=1ELSEIFR$="2"THEN?&77=2ELSEIFR$="5"THEN?&
77=5ELSEIFR$="10"THEN?&77=10ELSEIFR$="20"THEN?&77=20ELSE1540
 1560INPUT"CELL SETTLING TIME",T
 1570IFINT(T)<>T THENPRINT"INTEGER":GOTO1560
 1580T%=T:?&81=T%
 1590INPUT"PRESS 'G' TO START,ESCAPE TO INTERRUPT SPECTRUM",S$
 1600IFS$<>"G"THEN1590
 1610?&FE62=&3C:?&FE60=0:Z%=?&FE6C:Z%=(Z%OR&E0)AND&EF:?&FE6C=Z%
:?&FE62=&BF:Z%=?&FE60:Z%=Z%OR&F:?&FE60=Z%:FORI%=1TO100:NEXTI%:Z
%=?&FE60:Z%=Z%OR&30:?&FE60=Z%:FORI%=1TO100:NEXTI%
 1620IF?&76=2THEN1650
 1630Z%=?&FE60:Z%=Z%OR3:?&FE60=Z%:Z%=?&FE60:Z%=Z%AND&FD:?&FE60=
Z%:FORI%=1TO100:NEXTI%:Z%=?&FE60:Z%=Z%OR&02:?&FE60=Z%
 1640GOTO1660
 1650Z%=?&FE60:Z%=Z%OR3:?&FE60=Z%:Z%=?&FE60:Z%=Z%AND&FE:?&FE60=
Z%:Z%=Z%OR3:?&FE60=Z%:Z%=?&FE60:Z%=Z%AND&FE:?&FE60=Z%:FORI%=1TO
100:NEXTI%:Z%=?&FE60:Z%=Z%OR1:?&FE60=Z%
 1660IFG%<R%AND?&74=&FFTHEN?&74=0:?&75=(?&75)+1
 1670IFG%<R%AND?&74<&FFTHEN?&74=(?&74)+1
 1680?&84=1
 1690CHAIN"AMP4"
 2000DEFPROCmemory_test
```

```
 2010FORI%=0TO&5FCSTEP4
 2020!(F%+I%)=0
 2030IF!(F%+I%)<>0THENPRINT"MEM FAULT AT";~(F%+I%);"TO";~(F%+I%
+3)
 2040NEXTI%
 2050PRINT"TEST OK"
 2060ENDPROC
```

PROGRAM 3 "discop4"

```
   10INPUT"DISC DUMP",QU3$:IFQU3$<>"Y"ANDQU3$<>"N"THEN10
   20IFQU3$="N"THEN120
   30INPUT"FILENAME",filename$
   40A=OPENOUT(filename$)
   50IFF%=&4900THENPRINT"FILING YOUR LAST TEST SPECTRUM"ELSEPRI
NT"FILING YOUR LAST PHOTODIODE SPECTRUM"
   60PRINT£A,F%
   70FORLAMBDA%=340TO722
   80PRINT£A,!((LAMBDA%-340)*4+F%)
   90NEXTLAMBDA%
  100PRINT£A,V%:PRINT£A,U%:PRINT£A,R%:PRINT£A,G%:PRINT£A,?&77:P
RINT£A,M%:PRINT£A,N%:PRINT£A,O%:PRINT£A,Q%:PRINT£A,A%:PRINT£A,B
%:PRINT£A,E%:PRINT£A,X%:PRINT£A,?&71
  110CLOSE£A
  120INPUT"LOAD FROM DISC",QU5$:IFQU5$<>"Y"ANDQU5$<>"N"THEN120
  130IFQU5$="N"THEN?&8F=2:GOTO470
  140IFQU5$="Y"THEN?&8F=1
  150INPUT"FILENAME TO BE ACCESSED",accessfile$
  160B=OPENIN(accessfile$)
  165ONERRORGOTO274
```

```
170INPUT£B,F%
180CLOSE£B
190IFF%=&4900THENPRINT"THIS IS A TEST SPECTRUM"ELSEIFF%=&5000
THENPRINT"THIS IS A PHOTODIODE SPECTRUM"
200B=OPENIN(accessfile$)
210INPUT£B,F%
220FORLAMBDA%=340TO722
230INPUT£B,XX%
240!((LAMBDA%-340)*4+&6800)=XX%
250NEXTLAMBDA%
252IFF%=&4900THENINPUT£B,V%ELSEINPUT£B,temp
260IFF%=&5000THENINPUT£B,U%ELSEINPUT£B,temp
262INPUT£B,S%:INPUT£B,K%:INPUT£B,D%:INPUT£B,M%:INPUT£B,N%:INP
UT£B,O%:INPUT£B,Q%:INPUT£B,A%:INPUT£B,B%:INPUT£B,E%:INPUT£B,X%:
INPUT£B,TEMP%
265?&71=TEMP%
270CLOSE£B
272GOTO280
274ONERROROFF:?&71=0:Y%=Y%*1000
280INPUT"TRANSFER THIS SPECTRUM TO MAIN MEMORY",trans$:IFtran
s$="N"THEN320
290FORLAMBDA%=340TO722
300!((LAMBDA%-340)*4+F%)=!((LAMBDA%-340)*4+&6800)
310NEXTLAMBDA%
320IFF%=&4900THENPRINT"AVERAGE WITH RESIDENT TEST SPECTRUM";E
LSEPRINT"AVERAGE WITH RESIDENT PHOTODIODE SPECTRUM";
330INPUTQU9$:IFQU9$<>"Y"ANDQU9$<>"N"THEN320
340IFQU9$="N"THEN470
350INPUT"NUMBER OF SPECTRA USED TO CREATE RESIDENT AVERAGED S
```

```
PECTRUM (ANSWER 1 IF RESIDENT SPECTRUM HAS JUST BEEN OBTAINED B
Y EXPERIMENT)",numspectra%
  360IFF%=&4900THEN420
  370FORLAMBDA%=340TO722
  380XX%=(numspectra%*((!((LAMBDA%-340)*4+F%))*U%+(!((LAMBDA%-3
40)*4+&6800))*W%))/((numspectra%+1)*U%)
  390!((LAMBDA%-340)*4+F%)=XX%
  400NEXTLAMBDA%
  410GOTO120
  420FORLAMBDA%=340TO722
  430XX%=(numspectra%*((!((LAMBDA%-340)*4+F%))*V%+(!((LAMBDA%-3
40)*4+&6800))*Y%))/((numspectra%+1)*V%)
  440!((LAMBDA%-340)*4+F%)=XX%
  450NEXTLAMBDA%
  460GOTO120
  470INPUT"DISPLAY DATA",QU10$:IFQU10$<>"Y"ANDQU10$<>"N"THEN470
  480IFQU10$="N"THEN510
  490IFF%=&4900THEN?&8D=2ELSE?&8D=1
  500GOTO520
  510?&8C=1
  520PAGE=&1900
  530CHAIN"AMP4"
```

PROGRAM 4 "ASSEM"

```
  40 MEM =&74:ANALOG=&72:TEMP=&70:OSBYTE=&FFF4:OSRDCH=&FFE0:OS
WRCH=&FFEE:OSASCI=&FFE3
  50 FOR H%= 0 TO 2
  60 P%=&5640
  70 [OPT H%
  80 LDA &86
  90 CMP £3
 100 BEQ LAMBDAMOVE
 110 .LOOPADC
 120 JSR ADC
 130 .LAMBDAMOVE
 140 LDA &86
 150 CMP £2
 160 BNE NXTZ
 170 JMP TEXT
 180 .NXTZ
 190 LDA &76
 200 CMP £1
 210 BEQ WE
 220 JMP LAMBDAINC
 230 .WE
 240 LDX &77
 250 .LOOPDOWN
 260 JSR DECTEST
 270 JSR DECTEST
 280 JSR DECTEST
 290 DEX
 300 BEQ DONEDEC
```

```
310 JSR DECTEST
320 JMP LOOPDOWN
330 .DONEDEC
340 LDA &86
350 CMP £1
360 BEQ NXTY
370 JMP RNON
380 .NXTY
390 LDA MEM+1
400 CMP &7B
410 BEQ BYTETEST1
420 BCS NXTA
430 JMP TEXT
440 .NXTA
450 JMP RNON
460 .BYTETEST1
470 LDA MEM
480 CMP &7A
490 BEQ NXTM
500 BCS RNON
510 .NXTM
520 JMP TEXT
530 .RNON
540 LDA &FE6C
550 ORA £&C0
560 AND £&DF
570 STA &FE6C
580 LDX £&FF
590 .LOOP99
```

```
600 DEX
610 BNE LOOP99
620 LDA &FE6C
630 ORA £&E0
640 STA &FE6C
650 LDX &77
660 .WAITLAMBDASTEP
670 JSR DELAY250MS
680 DEX
690 BNE WAITLAMBDASTEP
700 LDX &81
710 .CELLSETTLE
720 BNE NXTDEL
730 LDA &86
740 CMP £1
750 BEQ G
760 JMP TEXT
770 .G
780 JMP LOOPADC
790 .NXTDEL
800 JSR DELAY250MS
810 DEX
820 BNE NXTDEL
830 LDA &86
840 CMP £1
850 BNE TE
860 JMP LOOPADC
870 .TE
880 JMP TEXT
```

```
 890 .LAMBDAINC
 900 LDX &77
 910 .LOOPUP
 920 JSR INCTEST
 930 JSR INCTEST
 940 JSR INCTEST
 950 DEX
 960 BEQ DONEINC
 970 JSR INCTEST
 980 JMP LOOPUP
 990 .DONEINC
1000 LDA &86
1010 CMP £1
1020 BEQ NXTW
1030 JMP RNON
1040 .NXTW
1050 LDA &7B
1060 CMP MEM+1
1070 BCC Y
1080 BEQ BYTETEST2
1090 JMP RNON
1100 .Y
1110 JMP TEXT
1120 .BYTETEST2
1130 LDA MEM
1140 CMP &7A
1150 BCC WO
1160 JMP TEXT
1170 .WO
```

```
1180 JMP RNON
1190 .ADC
1200 LDA &7F
1210 CMP £2
1220 BEQ PSD
1230 LDA £&11
1240 LDX £2
1250 JSR OSBYTE
1260 .ADCWAIT
1270 LDA £&80
1280 LDX £0
1290 JSR OSBYTE
1300 TYA
1310 CMP £2
1320 BNE ADCWAIT
1330 LDA £&80
1340 LDX £2
1350 JSR OSBYTE
1360 JMP LABEL2
1370 .PSD
1380 LDA £&11
1390 LDX £1
1400 JSR OSBYTE
1410 .ADCWAIT2
1420 LDA £&80
1430 LDX £0
1440 JSR OSBYTE
1450 TYA
1460 CMP £1
```

```
1470 BNE ADCWAIT2
1480 LDA £&80
1490 LDX £1
1500 JSR OSBYTE
1510 .LABEL2
1520 LDA &76
1530 CMP £1
1540 BNE ADCUP
1550 TYA
1560 LDY £0
1570 STA (MEM),Y
1580 JSR DECTEST
1590 TXA
1600 STA (MEM),Y
1610 JMP FINISH
1620 .ADCUP
1630 TXA
1640 STY ANALOG
1650 LDY £0
1660 STA (MEM),Y
1670 JSR INCTEST
1680 LDA ANALOG
1690 STA (MEM),Y
1700 .FINISH
1710 RTS
1720 .DELAY250MS
1730 TXA
1740 PHA
1750 LDX £&3D
```

```
1760 .DL2
1770 LDY £0
1780 .DL1
1790 INY
1800 BNE DL1
1810 INX
1820 BNE DL2
1830 PLA
1840 TAX
1850 RTS
1860 .DECTEST
1870 LDA MEM
1880 BEQ DOWNPAGE2
1890 DEC MEM
1900 JMP SAMEPAGE2
1910 .DOWNPAGE2
1920 DEC MEM+1
1930 LDA £&FF
1940 STA MEM
1950 .SAMEPAGE2
1960 RTS
1970 .INCTEST
1980 LDA MEM
1990 CMP £&FF
2000 BEQ UPPAGE2
2010 INC MEM
2020 JMP SAMEPAGE4
2030 .UPPAGE2
2040 INC MEM+1
```

```
2050 LDA £0
2060 STA MEM
2070 .SAMEPAGE4
2080 RTS
2090 .TEXT
2100 RTS:]
2110 NEXT H%
```

PROGRAM 5 "logplt2"

```
   2maxeff=Z%/100000
   3DIMyval(5)
   4IF?&7E=99THEN210
   5MODE7:PRINT"HEADING";:INPUTLINEHD$
   6%%=&E0E:visible%=69:invisible%=71:QU$=""
  10 MODE 4
  20PROClabelaxes
  30PROCplot
  40VDU4:CLS:INPUT"EDIT",ed$
  50IFed$="Y"THENPROCeditlog:GOTO40
  60CLS:INPUT"PLOTTER",pl$
  70IFpl$="N"THEN160
  80INPUT"AXES",hpaxes$:IFhpaxes$="Y"THEN130
  90*IEEE
 100plot=?&8E:plot=plot+1:?&8E=plot
 110IFplot=1THENPRINT£5,"SM+;"ELSEIFplot=2THENPRINT£5,"SMX;"EL
SEIFplot=3THENPRINT£5,"SM£;"ELSEplot=1:GOTO110
 120PROChp_plot:GOTO160
 130PROChp_axes
 140PROChp_plot
```

```
160CLS:INPUT"PRINTOUT",print$
170IFprint$="N"THEN340
190*FX6
200VDU2:PRINT''HD$:PRINT''TAB(30);"LOG SPECTRUM":PRINT'TAB(2)
;"NM";TAB(26)"LOG(CONV.EFF.)"
210RESTORE:CLK%=0
211IF?&71=0THENA%=717
213factor=1:L%=340:REPEAT:GOSUB238
214L%=L%+5
215UNTILL%>=A%
216IF?&71=1THENB%=717ELSEIF?&71=0THEN320
217factor=.001*M%:L%=A%:REPEAT:GOSUB238
218L%=L%+5
219UNTILL%>=B%
220IF?&71=2THENE%=717ELSEIF?&71=1THEN320
221factor=.001*N%:L%=B%:REPEAT:GOSUB238
222L%=L%+5
223UNTILL%>=E%
224IF?&71=3THENX%=717ELSEIF?&71=2THEN320
225factor=.001*O%:L%=E%:REPEAT:GOSUB238
226L%=L%+5
227UNTILL%>=X%
228IF?&71=3THEN320
229factor=.001*Q%:L%=X%:REPEAT:GOSUB238
230L%=L%+5
231UNTILL%>=717
232GOTO320
238FORloop%=0TO4
240IFCLK%=1THENCLK%=0:GOTO260
```

```
  250READIPH:IPH=IPH*.01:CLK%=1
  260IF!((L%-340+loop%)*4+&5000)=00R!((L%-340+loop%)*4+&4900)=0
THENyval(loop%)=0:GOTO280
  265IF?&7E=99THENyval(loop%)=factor*.001*(!((L%-340+loop%)*4+&
4900))/(!((L%-340+loop%)*4+&5000))*(V%/U%)*2*IPH:GOTO280
  270yval(loop%)=LOG(factor*.00001*(!((L%-340+loop%)*4+&4900))/
(!((L%-340+loop%)*4+&5000))*(V%/U%)*2*IPH)
  280NEXTloop%
  290IFyval(0)=0ANDyval(1)=0ANDyval(2)=0ANDyval(3)=0ANDyval(4)=
0THEN310
  300%%=&E0E:PRINT;L%;"/";L%+4;
  305IF?&7E=99 THEN %%=&20408 ELSEIF maxeff>10 THEN %%=&20208 E
LSEIF maxeff>1 THEN %%=&20308 ELSEIF maxeff>.1 THEN %%=&20408 E
LSEIF maxeff>.01 THEN %%=&20508 ELSEIF maxeff>.001 THEN %%=&206
08 ELSEIF maxeff>.0001 THEN%%=&20708 ELSE %%=&20808
  307PRINTyval(0),yval(1),yval(2),yval(3),yval(4)
  310RETURN
  320ONERROROFF:VDU3:VDU7:%%=&E0E:GOTO340
  325IFERR=17THENVDU3:%%=&E0E:ONERROROFF:GOTO340
  330ONERROROFF:VDU3:GOTO160
  340IF?&7E<>99THEN347
  341?&7C=99
  342CHAIN"AMP4"
  347INPUT"DISC",disc$
  350COR$=""
  360IFdisc$="N"THEN400
  370*DISC
  375ONERRORGOTO380
  380 PRINT"X":MODE7
```

```
 382PAGE=PAGE+&4500
 385ONERROROFF
 390CHAIN"discop4"
 400?&8C=0:INPUT"ANOTHER EXPERIMENT",QU7$
 410IFQU7$="N"THEN340
 420*DISC
 430CHAIN"AMP4"
1000DEFPROCLabelaxes
1010VDU28,0,31,39,30
1020VDU19,0,3;0;
1030VDU19,1,4;0;
1040COLOUR0:COLOUR129
1050FORY=100TO104STEP4
1060MOVE150,Y:DRAW1150,Y
1070NEXTY
1080FORX=150TO154STEP4
1090MOVEX,100:DRAWX,1000
1100NEXTX
1110eVR%=124100/R%
1120eVG%=124100/G%
1130eVdiff%=ABS(eVR%-eVG%)
1140num20s%=2
1150IFeVdiff%<20THEN1170
1160eVdiff%=eVdiff%-20:num20s%=num20s%+1:GOTO1150
1170eVspan%=num20s%*20
1180IFeVR%<eVG%THEN1200
1190loweV%=20*INT(eVG%/20):GOTO1210
1200loweV%=20*INT(eVR%/20)
1210IFnum20s%<8THEN1240
```

```
 1220hy%=num20s%/5
 1230FORI%=0TOnum20s%STEPhy%:GOTO1250
 1240FORI%=0TOnum20s%
 1250MOVE150+1000*I%/num20s%,104:DRAW150+1000*I%/num20s%,128
 1260NEXTI%
 1270VDU5
 1275%%=&20103
 1280IFnum20s%<8THEN1300
 1290FORI%=0TOnum20s%STEPhy%:GOTO1310
 1300FORI%=0TOnum20s%
 1310MOVE110+1000*I%/num20s%,94:IF110+1000*I%/num20s%<100THEN13
20ELSEPRINT;(20*I%+loweV%)/100
 1320NEXTI%
 1330MOVE1170,140:PRINT"eV"
 1400FORI%=0TO50STEP10
 1410MOVE154,104+18*I%:DRAW178,104+18*I%
 1420IF104+18*I%<130THEN1430ELSEIFI%=50THENMOVE50,104+18*I%:PRI
NT;(I%-50)/10:GOTO1430
 1425MOVE20,104+18*I%:PRINT;(I%-50)/10
 1430NEXTI%
 1440MOVE164,980:PRINT"LOG(CONV.EFF.)":VDU4
 1445%%=10
 1450ENDPROC
 2000DEFPROCplot
 2010RESTORE
 2020CLK%=0
 2022IF?&71=0THENA%=722
 2023factor=1:L%=340:REPEAT:GOSUB2050
 2024L%=L%+1
```

```
2025UNTILL%=A%
2026IF?&71=1THENB%=722ELSEIF?&71=0THEN2200
2027factor=.001*M%:L%=A%:REPEAT:GOSUB2050
2028L%=L%+1
2029UNTILL%=B%
2030IF?&71=2THENE%=722ELSEIF?&71=1THEN2200
2031factor=.001*N%:L%=B%:REPEAT:GOSUB2050
2032L%=L%+1
2033UNTILL%=E%
2034IF?&71=3THENX%=722ELSEIF?&71=2THEN2200
2035factor=.001*O%:L%=E%:REPEAT:GOSUB2050
2036L%=L%+1
2037UNTILL%=X%
2038IF?&71=3THEN2200
2039factor=.001*Q%:L%=X%:REPEAT:GOSUB2050
2040L%=L%+1
2042UNTILL%=722
2044ENDPROC
2050IFCLK%=1THENCLK%=0:GOTO2070
2060READIPH:IPH=IPH*.01:CLK%=1
2070IF!((L%-340)*4+&5000)<=0OR!((L%-340)*4+&4900)<=0THEN2150
2080DV=.001*factor*(!((L%-340)*4+&4900))/(!((L%-340)*4+&5000))
*(V%/U%)*2*IPH
2085IFDV<.00001THEN2150
2090XVAL%=((124100/L%)-loweV%)*1000/eVspan%
2100FORDF%=150TO154STEP4
2110FORGF%=100TO104STEP4
2120PLOT69,DF%+XVAL%,GF%+(900-(ABS(LOG(DV/100))*180))
2130NEXTGF%
```

```
2140NEXTDF%
2150RETURN
2200ENDPROC
2300DEFPROCeditlog
2310RESTORE
2315CLK%=0
2320IF?&71=0THENA%=722
2321factor=1:L%=340:REPEAT:GOSUB2349
2322L%=L%+1
2323UNTILL%=A%
2326IF?&71=1THENB%=722ELSEIF?&71=0THEN2460
2327factor=.001*M%:L%=A%:REPEAT:GOSUB2349
2328L%=L%+1
2329UNTILL%=B%
2330IF?&71=2THENE%=722ELSEIF?&71=1THEN22460
2331factor=.001*N%:L%=B%:REPEAT:GOSUB2349
2332L%=L%+1
2333UNTILL%=E%
2334IF?&71=3THENX%=722ELSEIF?&71=2THEN2460
2335factor=.001*O%:L%=E%:REPEAT:GOSUB2349
2336L%=L%+1
2337UNTILL%=X%
2338IF?&71=3THEN2460
2339factor=.001*Q%:L%=X%:REPEAT:GOSUB2349
2340L%=L%+1
2341UNTILL%=722
2343ENDPROC
2349IFCLK%=1THENCLK%=0:GOTO2360
2350READIPH:IPH=IPH*.01:CLK%=1
```

```
 2360IF!((L%-340)*4+&5000)<=0OR!((L%-340)*4+&4900)<=0THEN2450
 2370DV=.001*factor*(!((L%-340)*4+&4900))/(!((L%-340)*4+&5000))
*(V%/U%)*2*IPH
 2380XVAL%=((124100/L%)-loweV%)*1000/eVspan%
 2390CLS:PRINT"N FOR NEXT POINT,D TO DELETE,F TO FINISH";
 2400PROCpoint_plot(invisible%):FORDD%=1TO100:NEXT:PROCpoint_pl
ot(visible%)
 2410QU$=INKEY$(20)
 2420IFQU$=""THEN2400ELSEIFLEFT$(QU$,1)<>"N"ANDLEFT$(QU$,1)<>"D
"ANDLEFT$(QU$,1)<>"F"THEN2390
 2430IFLEFT$(QU$,1)="D"THENPROCpoint_plot(invisible%):!((L%-340
)*4+&4900)=0
 2440IFLEFT$(QU$,1)="F"THEN2460
 2450RETURN
 2460ENDPROC
 2470DEFPROCpoint_plot(visible_or_not%)
 2480FORDF%=150TO154STEP4
 2490FORGF%=100TO104STEP4
 2500PLOTvisible_or_not%,DF%+XVAL%,GF%+(900-(ABS(LOG(DV/100))*1
80))
 2510NEXTGF%
 2520NEXTDF%
 2525ENDPROC
 2530DEFPROChp_axes
 2535ONERRORGOTO2885
 2540*IEEE
 2550ZZ$=CHR$(3)
 2560PRINT£5,"IN;SP1;IP1250,750,9250,6250;"
 2570PRINT£5,"SC0,1000,0,900;"
```

```
2580PRINT£5,"PU0,0 PD0,900,1000,900,1000,0,0,0 PU"
2590PRINT£5,"SI.3,.3;"
2600AA$="PA0,1000;CP0,2.2;LB"
2610BB$=AA$+HD$+ZZ$
2620PRINT£5,BB$
2630TITLE$="LOG(PHOTO.CONV.EFF.) VERSUS PHOTON ENERGY"
2640AA$="PA0,1000;CP0,1;LB"
2650BB$=AA$+TITLE$+ZZ$
2660PRINT£5,BB$
2670PRINT£5,"SI.2,.3;TL1.5,0"
2680IFnum20s%<8THEN2710
2690HZ%=num20s%/5
2700FORI%=0TOnum20s% STEPHZ%:GOTO2720
2710FORI%=0TOnum20s%
2720J%=1000*I%/num20s%
2730HH$=STR$(J%):JJ$="PU":KK$=",0;XT;"
2740LL$=JJ$+HH$+KK$
2750PRINT£5,LL$
2760FF%=20*I%+loweV%
2765IFINT(FF%/100)=FF%/100THENXX$=".0"ELSEXX$=""
2770NN$=STR$(FF%/100):VV$="CP-2,-1;LB"
2780CC$=VV$+NN$+XX$+ZZ$
2790PRINT£5,CC$
2800NEXTI%
2810FORI%=0TO50STEP10
2820NN$=STR$(18*I%):VV$="PU0,":WW$=";YT;"
2830CC$=VV$+NN$+WW$:PRINT£5,CC$:HH$=STR$(5-I%/10)
2835IFI%=50THENJJ$="CP-3,-.25;LB"ELSEJJ$="CP-3,-.25;LB-"
2836LL$=JJ$+HH$+ZZ$:PRINT£5,LL$
```

```
2840NEXTI%
2845TITLE2$="PHOTON ENERGY/eV"
2850BB$="PA900,0;CP-13,-2.5;LB":AA$=BB$+TITLE2$+ZZ$:PRINT£5,AA$
2860BB$="PA0,1000;CP-5,-1;LBLOG(PHOTO.CONV.EFF.)"
2870AA$=BB$+ZZ$:PRINT£5,AA$
2880PRINT£5,"SM*;"
2885ONERROROFF:GOTO140
2890ENDPROC
3000DEFPROChp_plot
3010IFG%<R%THENJ%=-(?&77)ELSEJ%=?&77
3020RESTORE
3030CLK%=0
3040ONERRORGOTO3150
3042IF?&71=0THENA%=722
3043factor=1:L%=340:REPEAT:GOSUB3069
3044L%=L%+1
3045UNTILL%=A%
3046IF?&71=1THENB%=722ELSEIF?&71=0THEN3150
3047factor=.001*M%:L%=A%:REPEAT:GOSUB3069
3048L%=L%+1
3049UNTILL%=B%
3050IF?&71=2THENE%=722ELSEIF?&71=1THEN3150
3051factor=.001*N%:L%=B%:REPEAT:GOSUB3069
3052L%=L%+1
3053UNTILL%=E%
3054IF?&71=3THENX%=722ELSEIF?&71=2THEN3150
3055factor=.001*O%:L%=E%:REPEAT:GOSUB3069
3056L%=L%+1
3057UNTILL%=X%
```

```
 3058IF?&71=3THEN3150
 3059factor=.001*Q%:L%=X%:REPEAT:GOSUB3069
 3060L%=L%+1
 3062UNTILL%=722
 3064ENDPROC
 3069IFCLK%=1THENCLK%=0:GOTO3080
 3070READIPH:IPH=IPH*.01:CLK%=1
 3080IF!((L%-340)*4+&5000)<=0OR!((L%-340)*4+&4900)<=0THEN3140
 3090DV=.001*factor*(!((L%-340)*4+&4900))/(!((L%-340)*4+&5000))
*(V%/U%)*2*IPH
 3100X$=STR$(((124100/L%)-loweV%)*1000/eVspan%)
 3110Y$=STR$((900-(ABS(LOG(DV/100))*180)))
 3120DD$="PU;PA":EE$=",":FF$=";"
 3130GG$=DD$+X$+EE$+Y$+FF$:PRINT£5,GG$
 3140RETURN
 3150ONERROROFF:GOTO160
 3160ENDPROC
 4940REM RS£2 DEC84 340 TO 720NM STEP 2NM
 4950DATA0,0,0,0,0,9,9,9,9,9,9,9,9,9,9,10,10,11,11,12,14,15,16,
18,21,22,23,25,27,29,31,32,33,35,36,38,40,42,44,46,48,50,52,53,
54,55,55,56,58,59,60,61,62,62,63,64,64,65,65,66,66,67,67,68,68,
68,68,69,69,70,70,70
 4960DATA70,70,71,71,71,72,72,72,72,72,72,73,73,73,73,73,73,73,
73,74,74,74,74,74,74,74,74,74,74,74,74,74,74,74,74,74,74,74,74,
74,74,74,74,74,74,74,74,74,74,74,74,74,74,74,74,74,74,73,73,
73,73,73,73,73,73,73,73,73,73,73,73,72,72
 4970DATA72,72,72,72,72,72,72,72,71,71,71,71,71,71,71,71,71,71,
71,71,70,70,70,70,70,70,70,70,70,70,69,69,69,69,69,69,69,69,69,
69,69,68,68
```